RICE UNIVERSITY

Laser Cooling of Ions in a Neutral Plasma

by

Thomas Langin

A Thesis Submitted
in Partial Fulfillment of the
Requirements for the Degree

Doctor of Philosophy

Approved, Thesis Committee:

Thomas C. Killian, Chair
Professor of Physics & Astronomy

F. Barry Dunning
Sam and Helen Worden Professor of
Physics & Astronomy

Stephan Link
Professor of Chemistry & Electrical and
Computer Engineering

Houston, Texas

August, 2018

ABSTRACT

Laser Cooling of Ions in a Neutral Plasma

by

Thomas Langin

In this thesis, we present results from the first successful application of laser-cooling to a neutral plasma. Specifically, we laser-cool an ultracold neutral plasma (UNP) generated from the photoionization of a cold trapped gas of strontium atoms. After photoionization, the ions heat up to a temperature of $\sim 500\,\mathrm{mK}$ through a process known as disorder induced heating (DIH). After laser-cooling the plasma for 135μs, we observe a temperature of $50\,\mathrm{mK}$.

One main driver of interest in UNP systems is that, even after DIH, the thermal energy scale of the ions (k_BT) is less than the interaction energy scale ($E_c = e^2/4\pi\epsilon_0 a$, where $a = (3/4\pi n)^{1/3}$ is the distance between nearest neighbors). This places UNPs in the 'strongly coupled' regime, defined by $\Gamma = E_c/k_BT \gtrsim 1$. Other plasmas in this regime include dense astrophysical systems like white dwarf stars ($\Gamma > 10$) and laser-produced plasmas relevant for inertial confinement fusion experiments. Plasmas in this regime are not well-described by conventional plasma theory. UNPs are amenable to measurements of quantities that are important for modeling dynamics of more complex strongly coupled systems. These measurements can also be used to test new theories of strongly coupled plasma dynamics.

However, DIH limits Γ to values of 3 or lower in UNPs, which has historically limited their effectiveness as a test of these theories. It has also limited the use of

UNPs as a tool for obtaining greater understanding of strongly coupled plasma physics in general. Through laser-cooling, we are able to increase Γ to 11, the highest recorded in a UNP system. This brings UNPs deep enough into the strongly coupled regime to serve as a very stringent test of strongly coupled plasma theory. Moreover, this is comparable to values predicted to exist in white dwarf stars, and thus UNPs can be used to directly study the physics relevant to these exotic astrophysical systems.

The application of laser-forces to neutral plasmas opens the door to a number of interesting possibilities beyond laser-cooling. For example, these forces may be used to generate a shear-flow, from which one could obtain measurements of viscosity, or a thermal gradient, from which one could obtain measurements of thermal conductivity. We also show that laser forces can inhibit the expansion of the plasma, which should motivate future studies regarding the possibility of optical confinement of a plasma.

Acknowledgments

As I reflect back on my journey leading up to this point, thinking about all of the people that made it possible, things start to get a little blurry. Not from tears (well, maybe a little), but because there are so many people without whom this would not have been possible. Even still, there are a few people who stand out clearly amongst the blur.

First and foremost is my advisor, Prof. Tom Killian. Anyone who reads this thesis should thank him for his editing skills, particularly his keen sense regarding what is truly *important* about a result and how to write in a way that emphasizes that aspect. It has helped make this thesis *much* clearer than it otherwise would have been. Learning that skillset from him will undoubtedly help me in my future endeavors. In the lab, his ability to recognize when I truly needed some help solving a problem versus when I needed to be left alone to solve it on my own was much appreciated. After having to teach new students how to run the experiment and do data analysis I've realized that the impulse to 'take over' and do things myself is a powerful one, so I appreciate him letting go of that impulse even during the times when I was probably working very inefficiently.

This leads me to the next group of people I need to thank: my partners in the plasma lab, both past and present. Dr. Patrick McQuillen and Dr. Trevor Strickler both exhibited many of the same advisory skills as Prof. Killian, and were a big help during my first few years at Rice. My current labmates, Grant Gorman and Mackenzie Warrens, have also provided essential help to me over the past few years, and I sincerely hope that I have been as helpful to them as Patrick and Trevor were to me. I am excited about the future of the experiment with them at the helm,

and look forward to reading their work over the next few years. There have been a number of Rice undergraduate students and REU students that worked in the plasma lab: Nikola Maksimovic, Alex Wikner, Zhitao Chen, Kyle Chow, Ilian Plompen, and Miriam Matney who also deserve to be acknowledged here for their work over the years. Nikola in particular played a crucial role during the initial stages of the development of the Molecular Dynamics simulation toolkits referenced throughout the thesis.

I would also like to thank my compatriots working on Prof. Killian's other experiments. As members of my Rice cohort, Jim Aman and Roger Ding have been there throughout my entire journey, from early struggles through problem sets to excitement at new results from our work in the lab, and have been willing partners both in commiseration and in scientific discussion. Dr. Brian DeSalvo, Dr. Francisco Carmago, Joe Whalen, Josh Hill, and Soumya Kanungo have also shared in the struggles and successes of the Killian lab.

I would also like to thank a few 'theory' collaborators that have aided me in the work presented in this thesis: Prof. Thomas Pohl, Prof. Daniel Vrinceanu, and Dr. Jerome Daligault, each of whom made valuable contributions to the simulation results presented throughout the thesis.

A number of professors at Rice also deserve acknowledgment. Having taken three courses with Prof. Anthony Chan, I can with certainty say that he is one of the best teachers I have ever had, and is responsible for most of the knowledge I've acquired on plasma physics, a topic I was largely unfamiliar with before coming to Rice. Prof. Randy Hulet, assuming he forgets things at all, has most certainly forgotten more than I could ever hope to know about atomic physics. However, I must thank him for trying to rectify that situation by teaching me a bunch of atomic physics in his class. The knowledge I acquired through the advanced quantum physics classes taught by Profs. Han Pu and Kaden Hazzard is also invaluable. Conversations with Prof. Hazzard were also helpful during the early stages of the development of the quantum trajectories code discussed in the thesis. I must also thank Prof. Barry Dunning and Prof. Stephan Link for agreeing to serve on my thesis committee and for taking their time to read this thesis.

A few of my undergraduate professors also deserve acknowledgment here for inspiring me to undergo this journey in the first place. Prof. David Hall and Prof. Larry Hunter at Amherst College taught me what true laboratory research was really all about, and the knowledge I acquired while pursuing my undergraduate thesis in Prof. Hall's lab helped me start off my graduate school journey on the right foot.

Mom and Dad, thank you for supporting me throughout all of my life's journeys, and for always being there for me whenever I need you. Same goes to the rest of my family and friends. Lastly, I want to thank Rachel, for making the past 5 years much more enjoyable then they otherwise would have been, and for her love and support throughout this process. I am very excited to see what the future holds for us.

Contents

Illustrations

Chapter 1

Introduction

1.1 Ultracold Neutral Plasmas: An Overview

This thesis discusses the first successful implementation of laser cooling of ions in a neutral plasma system; specifically, a plasma created by the photoionization of a cold ($T \leq 10\,\mathrm{mK}$) gas. Such plasmas are commonly referred to as ultracold neutral plasmas (UNPs) [1, 2].

In 1999 the first UNP was created from a magneto-optically trapped (MOT) gas of metastable Xe atoms[3]. In the following decades, UNPs have been generated by photoionization of MOTs of Rb[4], Ca[5], and Sr[6] atoms.

Figure 1.1 helps to demonstrate what makes UNPs such an unique system: they are *much* colder than other neutral plasmas. This is because most other plasmas rely on collisions to provide enough energy for ionization ($\sim 1\,\mathrm{eV}$); temperatures must be $> 10^3\,\mathrm{K}$ for there to be enough ionizing collisions for plasma formation. UNPs are so cold, in fact, that the average ion kinetic energy ($k_B T$) is less than the energy of nearest neighbor coulomb interactions ($E_c = e^2/4\pi\epsilon_0 a$, where $a = (3/4\pi n)^{1/3}$). This places them in the strongly coupled plasma (SCP) regime, defined by:

$$\Gamma = \frac{E_c}{k_B T} \geq 1. \tag{1.1}$$

Other SCPs tend to be very dense systems, such as white dwarf stars ($\Gamma = 10 - 200$[8, 9]), the cores of gas giant planets ($\Gamma = 20 - 50$[8]), and laser-produced

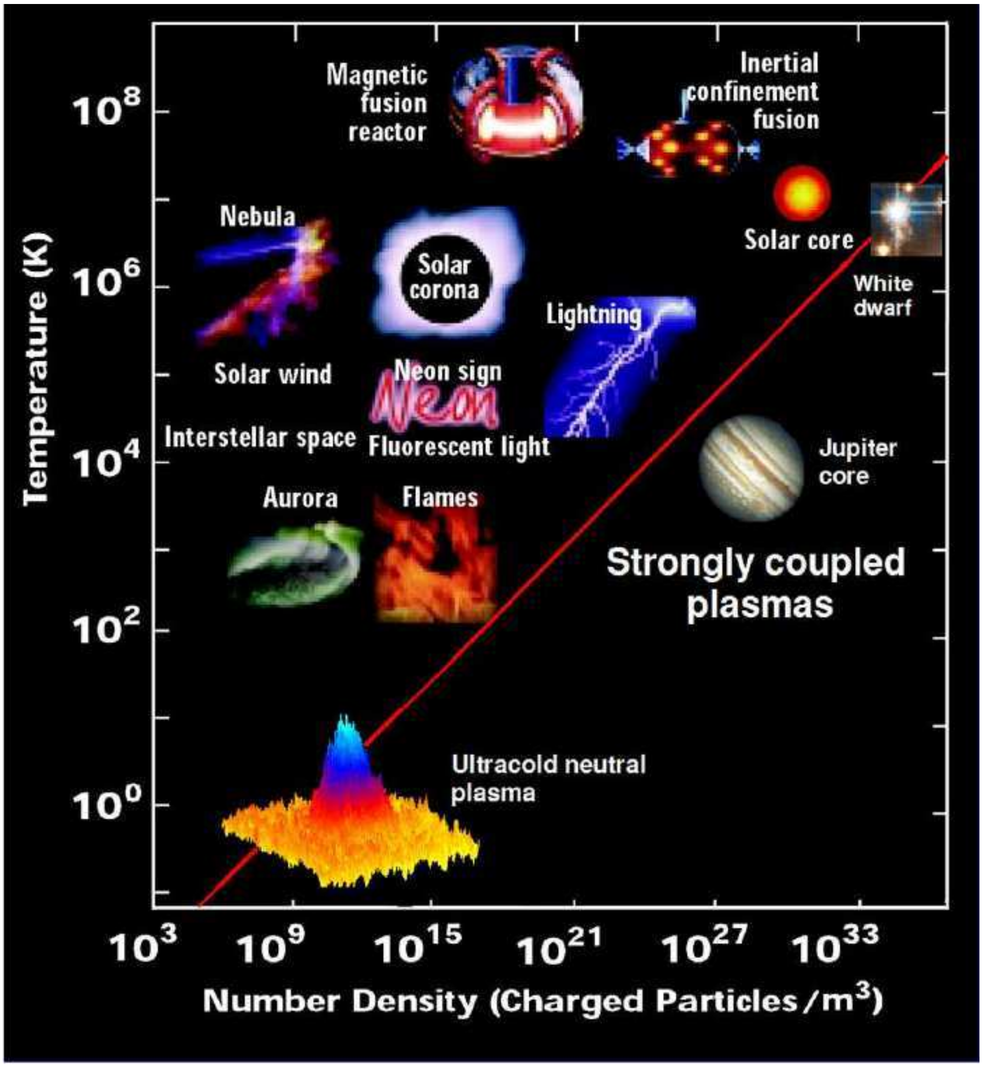

Figure 1.1 : Various plasmas plotted on $n - T$ phase diagram. The red line denotes $\Gamma = 1$ (Eq. 1.1). Adapted from [7]

plasmas important for studies of warm dense matter and inertial confinement fusion (ICF)[9, 10]. Dynamical timescales in plasmas tend to scale with the inverse of the ion plasma frequency $\omega_{pi} = \sqrt{e^2 n/m_i \epsilon_0}$ [11], which is on the order of 100 fs for dense SCPs, making the fundamental microscopic processes undergirding transport and collective behavior difficult to measure. These timescales in UNPs are extended to the $\sim$ 100 ns level, making these studies more tractable. The SCP regime is not well described by conventional plasma theory, as we discuss in Sec. 1.2, so the ability to study fundamental SCP physics using UNP systems has been of great interest for the benchmarking of new theories [1, 2].

Another important aspect of UNPs is their connection to the physics of cold Rydberg gases. Various ionization processes in systems of atoms or molecules excited to high-n ‘Rydberg’ states can result in the formation of UNPs. This has been realized in NO molecules[12] and in Rb[13, 14, 15], Sr [16], and Cs atoms [13]. Conversely, inelastic three body collisions between two electrons and an ion in UNPs can result in the formation of Rydberg atoms: $2e^{-}+A^{+} \rightarrow e^{-}+A^{*}$, where the A represents the ionic element, * indicates a Rydberg atom, and the electron carries away the binding energy.

The interplay between UNPs and gases of Rydberg atoms has been a source of interest for a number of reasons. For example, it is possible that a rydberg gas in the presence of a UNP can serve as a robust source for molecular ions [17]. Another proposal suggests that forming plasmas from Rydberg blockaded systems can yield very strongly coupled plasmas [18]. Finally, plasma formation processes in rydberg gases are a major source of instability, and may serve as a limiting factor in the quantum information capabilities of Rydberg gases[19].

One attractive feature of UNPs is their controllability; for example, the electron temperature can easily be varied by changing the wavelength of the photoionization beam and the initial spatial profile can easily be modified by either changing the structure of the photoionization beam or of the atomic gas. This controllability has allowed researchers to generate ion acoustic waves and measure how the dispersion relation depends on T_e[20], study the dynamics of the electron thermal pressure driven expansion of the plasma into vacuum[21, 22] and how the expansion can be modified by magnetic fields[23], study how the three-body recombination rate depends on electron temperature[24, 25], and create streaming plasmas[26, 27].

There are a number of ways to probe both the electron and ion components of these systems. The level of simplicity in a typical ‘cold atom’ experiment makes it relatively easy to use a combination of electrodes and charged particle detectors to manipulate and diagnose electrons. This has allowed for the study of collective modes [28, 29, 30] and electron-ion collisions[31, 32]. The ability to make UNPs of alkaline earth ions, which retain a valence electron, and thus an ‘alkali’-like level structure with optically accessible electronic transitions, provides a means to study the ion component using ‘standard’ atomic physics techniques like spectroscopy and pump-probe measurements. This has allowed for studies of ion equilibration after a rapid quench in the ion-ion interaction potential[33, 34, 35, 36] and the ion-electron thermalization rate[22].

Measurements of ion-ion collision rates in the SCP regime are particularly valuable because, as we will see in the next section, the nature of collisional transport changes dramatically in the SCP regime. This behavior has been previously studied in the context of trapped non-neutral plasmas [37], for which measured ion-ion collision rates in the SCP regime were observed to be a factor $\exp(\Gamma)$ higher than the rates predicted from formulas derived under the assumption $\Gamma \ll 1$ [38]. Similar measurements have also been performed in UNPs [39, 40], extending these observations to neutral plasmas free from external fields. Experiments like these are critical for the benchmarking of new SCP theories.

1.2 Strongly Coupled Plasmas: Exotic Systems that Challenge Theoretical Description

A number of the 'textbook' assumptions regarding the equation of state and collisional transport properties of plasmas break down in the SCP regime. These properties are generally derived from an underlying kinetic equation (e.g. the Boltzmann Equation) that handles collisions between the constituent particles. Under certain approximations, combining kinetic theory with Maxwell's equations and the equations of fluid flow lead to the magneto-hydrodynamic (MHD) equations used for design and diagnostics of magnetic fusion reactors, such as tokamaks and stellarators, and for studies of the solar corona, among other things[11].

In plasmas, interactions are modified by the Debye-Huckel effect, in which the potential from a constituent ion at $r = 0$ becomes $\phi(r) = e/4\pi\epsilon_0 r \times \exp\left[-r/\lambda_D\right]$, where $\lambda_D = \sqrt{\epsilon_0 k_B T/ne^2}$ is the Debye-length, T is the plasma temperature and n is the particle density. This is due to the Coulomb interactions between constituent particles within the plasma medium; an ion attracts electrons while it repels other ions. This response of the plasma medium acts to 'screen' the ion potential, resulting in the exponential cutoff.

Conventional kinetic theories assume that the number of particles within one 'Debye sphere',:

$$\Lambda = \frac{4\pi}{3} n \lambda_D^3 = \frac{4\pi}{3} n \left(\frac{k_B T \epsilon_0}{ne^2}\right)^{3/2} = \frac{1}{(3\Gamma)^{3/2}} \gg 1, \tag{1.2}$$

In this limit, collisional transport is dominated by weak, long-range interactions between the (many) particles within a Debye sphere. As Λ approaches unity, this picture breaks down; isolated collisions between close pairs of ions determine collisional transport. Furthermore, short-range spatial correlations between ions develop[41, 42], similar to those observed in liquid systems[43]. These effects are not accounted for in conventional kinetic theory[44, 45], leading to wild divergences in predictions of transport quantities such as self-diffusion, viscosity, and thermal conductivity for plasmas with $\Gamma \geq 1$[40, 39].

Extending kinetic theory to the SCP regime is an ongoing goal for plasma theorists [46, 47]. However, tests of these theories are difficult to perform in dense laboratory SCPs, due to fast ion dynamics. This motivates the study of other, less dense, SCP systems, such as dusty plasmas[48], trapped non-neutral plasmas[49, 50, 51, 38], and UNPs. In dusty plasmas, 'dust' particles (for example, $7\,\mu$m melamine/ formaldehyde spheres [52]) inserted into an rf discharge plasma containing Ar^+ and e^- acquire a very large ($Q \sim -10000e$) charge due to electron adhesion. These large charges lead to strong Coulomb interactions between dust particles, and thus large values of Γ (for species with charge $q = Ze$, Γ is multiplied by an additional factor of Z^2). However, interactions between the dust and the surrounding cloud of Ar, Ar^+, and e^- affect the dynamics of these systems. The non uniformity of the dust charges also plays a role, as does the fact that, in many cases, these systems are limited to 2D planes. In contrast, systems of $\sim 10^6$ laser-cooled ions trapped in a Penning trap [49], are very clean realizations of strongly coupled plasmas; the low temperatures ($T \sim 10\,\mathrm{mK}$) achievable in these systems have allowed researchers to reach $\Gamma > 172$, at which point a first-order solidification phase transition is realized [53] (See Figure. 1.2). However, these systems are by their nature non-neutral (electrons are anti-trapped) and exist only in the presence of external fields, neither of which is true for many SCPs of interest, such as ICF plasmas.

UNPs, however, do not have these limitations: they are able to exist without ex-

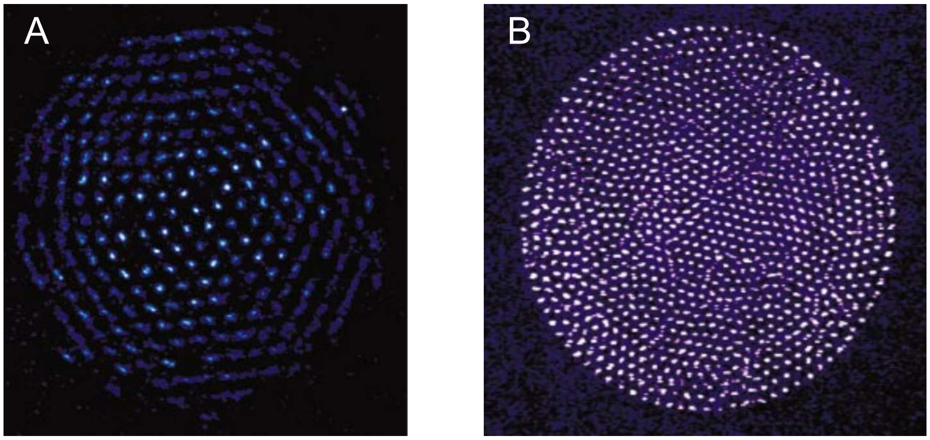

Figure 1.2 : (**A**): A trapped plasma of Be$^+$ ions. (**B**): A dusty plasma. Both of these systems clearly exhibit long range crystalline order, a characteristic of SCPs with $\Gamma > 172$. Figures adapted from[9].

ternal fields, are free from interactions with background particles, have known values for the charge number Z (typically $Z = 1$), and have easily resolvable dynamical timescales. However, unlike dusty plasmas and non-neutral plasmas, both of which can easily achieve $\Gamma \geq 172$, UNPs have historically been limited to $\Gamma \sim 3$ by an ion equilibration process known as disorder induced heating. We note here that Γ is referring to the ions, the electrons are typically weakly coupled in UNPs, with $\Gamma_e \leq 0.1$; the ion and electron temperatures can be treated as distinct because the ion-electron thermalization timescale ($\sim 1\,\text{ms}$) is very slow compared to ω_{pi}^{-1}.

Increasing Γ beyond this limit has long been a goal of the UNP field, as we discuss in section 1.3; the main focus of this thesis is on the successful use of laser-cooling to achieve this goal. After laser-cooling, we are able to achieve $\boldsymbol{\Gamma = 11}$, the highest recorded in a UNP system.

1.3 Disorder Induced Heating: The Limit on UNP Coupling Strength

Under the assumption that the ions retain the initial density and temperature of the MOT, we find $\Gamma > 1000$, which would easily be high enough to observe Coulomb crystallization and a host of other SCP phenomena of interest. However, it turns out that this assumption is incorrect. The atoms in the MOT lack spatial correlations due to the lack of strong atomic interactions while an equilibrated plasma of $\Gamma > 1000$ would have strong spatial correlations between ions[53]. Thus, we see that the plasma that is created by photoionization is very far out of equilibrium. During the subsequent equilibration process, short range correlations develop between ions, as expected in a SCP system. The development of correlations lowers the total interaction energy; this energy is converted to thermal energy of the ions. Another way to think about this is that, after photoionization, almost all of the energy of the system is 'stored' in the ion-ion interactions (typical interaction energy scale of $T_c = E_c/k_B = e^2/4\pi\epsilon_0 a k_B \sim 1\,\mathrm{K}$, which is quite large compared to the initial temperature $T \sim 1\,\mathrm{mK}$). This is entropically unfavorable, thus, the system equilibrates by equipartitioning these energies, heating up the ions to $T \sim 1\,\mathrm{K}$ (see Fig. 1.3), resulting in $\Gamma \sim 3$. This phenomena is referred to as disorder induced heating (DIH)[54].

DIH has drawn intense interest[1, 2, 34, 55, 36] (see also Section 2.2.2 of this thesis), as it is a good example of equilibration after a rapid interaction quench in a strongly coupled system. Unfortunately, it has also historically limited the level of coupling achievable in UNP systems to $\Gamma \leq 4$; strong enough to modify transport[40, 39, 32, 56, 57, 58], modify collective mode dispersion relations[59, 60], and result in development of short range correlations, but too weak to observe other

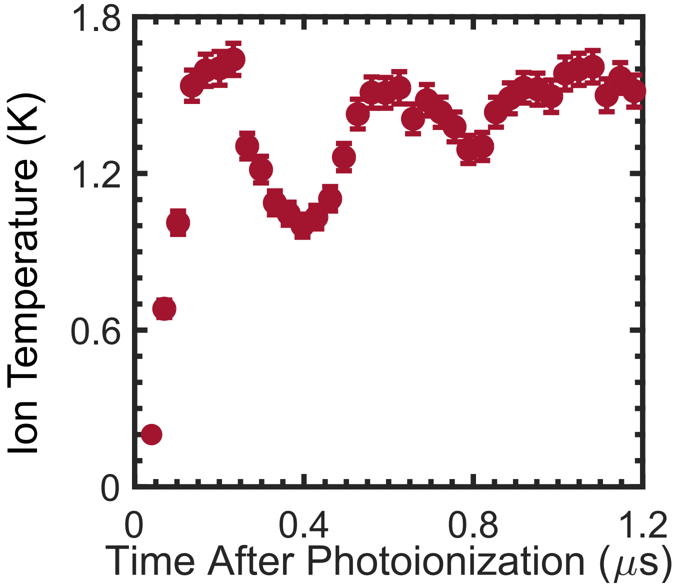

Figure 1.3 : Disorder Induced Heating after photoionization. On the timescale of $\omega_{pi}^{-1} \sim 500\,\mathrm{ns}$, the plasma heats up to around 1 K; this is the result of an equipartioning of the coulomb energy introduced during the rapid quench in the interactions between the Sr ions. The oscillations observed here, which have a frequency proportional to ω_{pi} are a characteristic of strongly coupled systems: for more details, see Section 2.2.2.

interesting effects such as long range correlations [61, 49, 50], the onset of a viscosity minimum ($\Gamma = 20$)[57], the Yukawa liquid ($30 \leq \Gamma \leq 172$) regime[47], and transport inhibition through particle caging [62]. This also has limited the use of UNPs as a testing ground for new kinetic theories that extend into the deeply coupled regimes relevant to astrophysical systems ($\Gamma > 10$)[47, 46]. Furthermore, even without these fascinating plasma specific applications, strengthening the coupling in UNPs would allow for comparisons to other strongly coupled systems where interactions dominate over kinetic energy scales; examples include quantum gases in the unitary regime[63, 64, 65], quark-gluon plasmas[66], and superconducting strongly correlated electron systems[67]. Thus, moving beyond the limits on Γ set by DIH has been long been a goal for the UNP community. There are many proposals for how to do this, and they can generally be broken down into two groups.

1.3.1 Proposals for Overcoming Disorder Induced Heating

The first group focuses on mitigating DIH by precorrelating the gas before ionization; examples of pre-correlated gases include atoms cooled to a Mott insulating state in a 3D optical lattice[68, 54], degenerate Fermi gases[69, 70], and rydberg blockaded gases[54, 18]. The first two techniques are well established, however, there are a number of issues with creating UNPs from these cold quantum gases. First, these systems tend to be very small (system sizes of 100μm or less) and, as we shall see in Sec. 2.3, UNPs have a lifetime that scales with system size. For cloud sizes of only 100μm, typical lifetimes become on the order of 1 μs, comparable to the timescales of the ion dynamics that we wish to study. Second, these systems are typically comprised of fewer than 10^6 particles; the level of non-neutrality scales *inversely* with both system size and ion number (Sec. 2.1), and would become quite significant for plasmas ionized from a quantum gas[3]. In principle, rydberg blockaded gases do not have these issues, however, they can spontaneously auto-ionize[15] in a way that destroys the correlations. In order for the correlations to remain, the rydberg blockaded system must be created and then ionized rapidly; ionization can take no longer than ω_{pi}^{-1}[18]. To date, this technique has not been implemented.

The second group of ideas for pushing UNPs to higher Γ focuses on increasing Γ after DIH. One technique is to sequentially excite the ions to higher ionization states. If this excitation is timed correctly, this can in principle increase Γ to 6.8; thus far, the highest Γ achieved with this method is 3.6[71]. However, this eliminates the ability to use laser transitions in the ion species as a diagnostic tool, as it removes the valence electron responsible for optically accessible internal state transitions in alkaline earth ions.

The approach implemented in this thesis is to lower the ion temperature after DIH by laser-cooling the ions[61, 72, 73, 74]. The next section will briefly summarize the history of laser-cooling & give a summary of optical molasses, the technique that we have chosen to use for laser-cooling of a UNP.

1.4 Laser Cooling: Driving Advances in Physics Research Since 1978

The seemingly counterintuitive idea that irradiating particles with lasers can actually remove energy was proposed in 1975[75, 76] and first implemented in 1978 in a system of trapped Mg^+ ions[77]. The first applications in neutral atoms were demonstrated in 1981 and 1982 in Na [78, 79]. More recently, these techniques have been applied to molecules[80, 81], solids[82, 83], and mesoscopic quantum objects[84]. Over the last few decades, laser-cooling has played a critical role in many ground-breaking advances in physics, a few of the most well known examples include the achievement of quantum degenerate gases[85, 86, 87, 70], the cold non-neutral plasmas discussed earlier[49, 50], and quantum computation in cold ion systems[88, 89]. It is our hope that the successful application of this technique in neutral plasma systems results in similarly ground-breaking advances.

There are actually a variety of ways to use lasers to remove energy from a system, but the most common method, and the one we use, is called ‘optical molasses’[90]. The exact details of how this works in a UNP of Sr^+ are left for Chapter 4, however, I will briefly summarize the technique here.

In Figure 1.4 we consider an two-level atom in the presence of counter-propagating lasers of wavelength λ that are each red-detuned from the transition between the levels (labeled $|g\rangle$ and $|e\rangle$). If the atom is not moving (Figure 1.4A), it is equally likely to absorb photons from each laser, thus there is no net force on the atom. If the atom is moving to the right (Figure 1.4B), the left-ward propagating laser (in green) is blue-shifted towards resonance by an amount equal to the doppler shift $\delta_{dopp} = kv = 2\pi v/\lambda$ and the right-ward propagating laser (in purple) is red-shifted even further from resonance by that same amount. Vice versa for an atom moving to the left. The resulting net force is illustrated in Figure 1.4C. In the region $|v| < v_c$ the force is linear in velocity and can be written as $\vec{F} = -(m\beta/2)\vec{v}$, where β is a damping coefficient that depends on the photon scattering rate and m is the mass of the particle. Assuming that all particles of interest have $v < v_c$, this cools the system according to $\dot{T} = -\beta T$.

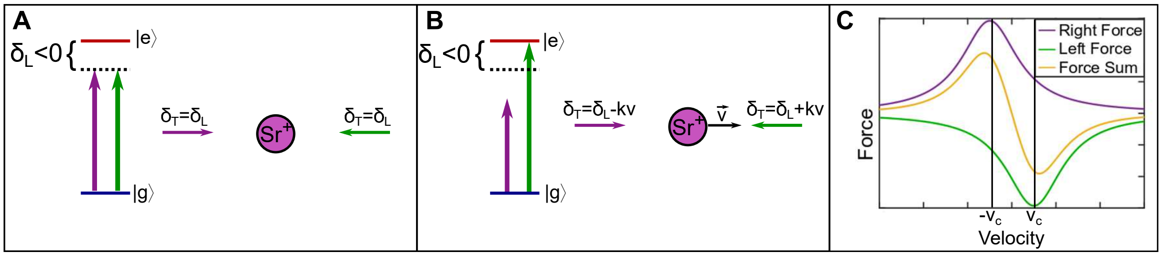

Figure 1.4 : Schematic demonstrating how optical molasses works in a two level system. In panel A, the ion is stationary and equally likely to absorb from each red-detuned ($\delta_L < 0$) laser, providing zero net force. In panel B, the ion is moving to the right, which blue shifts the leftward pointing laser (green) onto resonance through the Doppler shift $\delta_{Dopp} = kv$ while the rightward pointing laser is redshifted further away from resonance. Panel C shows the force from each laser as a function of the ion velocity along with the sum of the two forces; we see that in the region $|v| < v_c$, the particle experiences a linear damping force in velocity ($F = -\beta v$).

For typical optical molasses applications, $v_c \approx \gamma/k$, where γ is the natural linewidth of the transition. Typically, $\lambda \sim 500\,\mathrm{nm}$ and $\gamma \sim 10^8\,\mathrm{s}^{-1}$, and thus $v_c \sim 10\,\mathrm{m/s}$. For reference, in order for the thermal velocity v_T of a cloud of Sr^+ ions to be below 10 m/s, the temperature must be below 1 K. This is the main reason why laser-cooling was never attempted in neutral plasma systems before the advent of UNPs; the coldest 'conventional' neutral plasmas are at room temperature or higher, much too hot to be laser-cooled effectively. UNPs present their own challenges that make laser-cooling difficult, such as rapid hydrodynamic expansion into surrounding vacuum[21, 1, 2, 22] and high ion-ion collision rates[39, 40], which create an environment that differs significantly from other systems that have been laser cooled. These challenges are discussed in detail in Chapter 4.

1.5 Roadmap

In Chapter 2, we will briefly summarize the evoluton of a UNP after its creation, with a specific focus on our studies of DIH in a UNP, in which we demonstrate that DIH will inevitably lead to plasmas with $\Gamma \sim 3$, *regardless* of the plasma density and electron temperature[36]. Chapter 3 will focus on our apparatus for producing, diagnosing, and cooling Sr^+ UNPs.

Chapter 4 will focus on a combined Quantum Trajectories (QT) and Molecular Dynamics (MD) simulation, which we call a 'MDQT' code. This is a new tool that we developed in order to test the feasibility of cooling a rapidly expanding and highly collisional UNP system. In Chapter 5, we discuss the results of our implementation of laser-cooling and the achievement of $\Gamma \geq 10$. We will also show the impact of the collisionality and hydrodynamic expansion on laser-cooling before concluding with a discussion of what impact this achievement should have on the field of SCP research, with emphasis on how new and established techniques can be used to measure the effect of this increased coupling on transport. In Chapter 6, we propose techniques designed to improve upon the laser-cooling results presented in Chapter 5.

In Chapter 7, we discuss how the MDQT code can be used to study how correlations between spin and velocity are induced by optical pumping. It can also be used to study the subsequent relaxation of the correlations after the pumping lasers are turned off. We use the code to verify how, under certain conditions, the relaxation of the nth moment of the velocity distribution of a given spin state (e.g. $\langle v^n \rangle_\uparrow(t)$) can be directly related to the velocity autocorrelation function for that moment $\langle v^n(t)v^n(0)\rangle$. Autocorrelation functions can be used to measure transport coefficients through Green-Kubo formulas [91, 92, 43]. Measurements of transport quantities in the SCP regime are very important for the reasons discussed in Sec. 1.2, so techniques that can be used to measure them with reasonable accuracy are highly sought after. This also motivates Chapter 8, where we discuss ways to use optical forces to *directly* measure four transport coefficients: the self-diffusion coefficient, the shear viscosity, the thermal conductivity, and the temperature anisotropy relaxation rate.

Chapter 2

From Birth to Death in 100μs: The Life of an Ultracold Neutral Plasma

In this chapter, we discuss the evolution of a UNP after its creation. Section 2.1 focuses on the fast ($\sim 1\,$ns) electron equilibration processes, with a specific focus on the development of an ionic space charge that traps the electrons after a small portion ($\lesssim 1\%$ typically) escape the plasma, leading to an effectively neutral plasma[3]. Section 2.2 focuses on DIH; this is discussed in more detail in[93]. Here, I briefly review those results and show that, no matter what values of n and T_e are chosen, $\Gamma \sim 3$ after $\omega_{pi}^{-1} \sim 1\mu$s due to DIH [36]. Section 2.2 also introduces the Yukawa One-Component Plasma model (YOCP), an important model for describing the physics of strongly coupled plasmas. Section 2.3 discusses the long-term ($\sim 5 - 100\mu$s) electron thermal pressure driven expansion of the plasma into vacuum[21, 22], which effectively sets the plasma 'lifetime', and thus the amount of time available for laser-cooling. The well-separated time-scales of these processes (see Fig. 2.1) allow them to be considered independently. Finally, in section 2.4, we discuss the process of three-body recombination (TBR), in which two electrons and an ion collide to create a Rydberg atom, with the remaining electron acquiring the Rydberg binding energy. We will see that, due to the strong dependence of the TBR rate on electron temperature ($R_{TBR} \propto T_e^{-9/2}$), this ultimately limits the electron coupling parameter Γ_e to 0.1 or less.

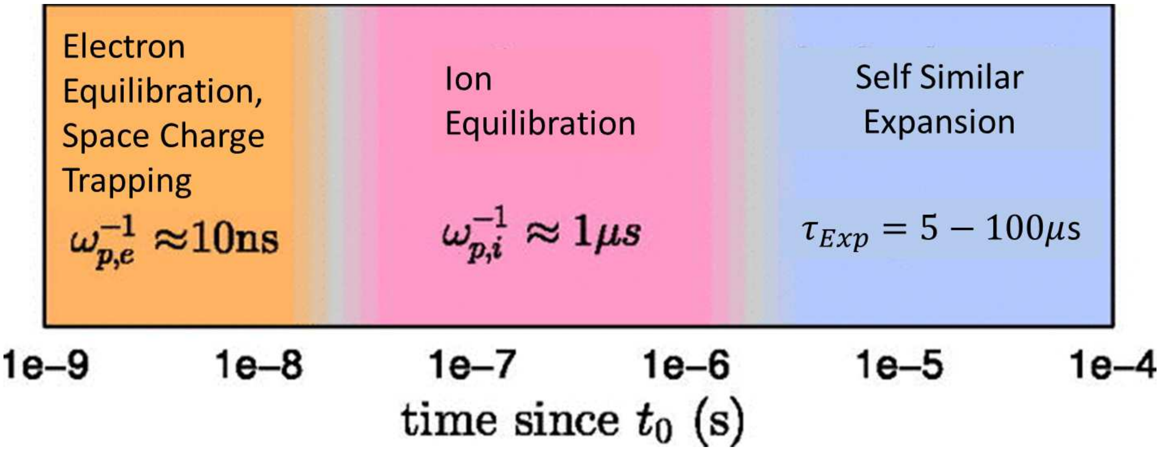

Figure 2.1 : The UNP lifecycle broken up into three stages. First, electron equilibration and development of an ion space charge (Section 2.1), followed by ion equilibration (DIH, section 2.2), and eventually a 'self-similar' expansion in which the cloud retains a gaussian shape throughout (Section 2.3).

2.1 Electron Equilibration & Trapping by Ion Space Charge

The excess energy above the ionization threshold is $\Delta E = \hbar\omega - E_{threshold}$ where ω is the frequency of the photoionizing photon and $E_{threshold}$ is the energy required to free an electron. The fraction of this energy that is transferred to the ion is given by $m_e/m_i = 6 \times 10^{-6}$. This is low enough that we use the approximation that *all* of ΔE goes into electron kinetic energy. Initially, all electrons will have velocity $v = \sqrt{2\Delta E/m_e}$, however, they quickly ($\sim 100\,\text{ns}$[94], see Fig. 2.2) thermalize with $T_e = 2\Delta E/3k_B$.

However, as this is happening, electrons are also escaping from the plasma. After photoionization, the plasma is neutral everywhere, thus, initially there is no potential keeping the quickly moving electrons from simply escaping from the plasma. As electrons escape, an overall positive charge builds up in the plasma. In order for any electrons to be trapped at all, the depth of the potential created by all of the ions in the cloud in absence of any electrons ($U(N_i)$, where N_i is the total number of ions)

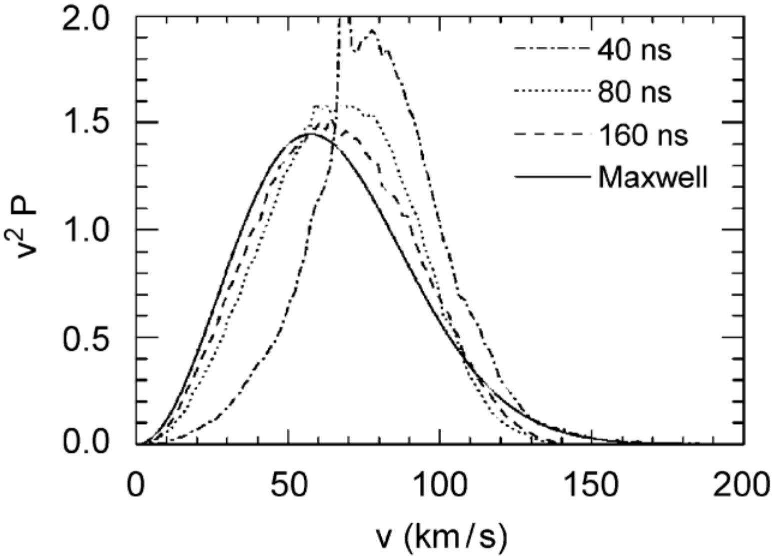

Figure 2.2 : Electron thermalization process for $n = 10^{15}\,\mathrm{m}^{-3}$ and $T_e = 100\,\mathrm{K}$. Over a few 100 ns the electron velocity distribution moves towards a maxwellian. These results are from particle in cell simulations with Monte-Carlo collisions [94].

must exceed ΔE. Assuming a gaussian cloud,

$$U(N_i) = -4\pi \frac{N_i}{(2\pi\sigma^2)^{3/2}} \int_0^\infty dr \frac{e^2}{4\pi\epsilon_0} r \exp\left[-\frac{r^2}{2\sigma^2}\right] = -\frac{N_i e^2}{4\pi\epsilon_0\sigma}\sqrt{\frac{2}{\pi}} \tag{2.1}$$

and thus, the threshold number for ion trapping is [1, 3]

$$N^* = \frac{3}{2}\sqrt{\frac{\pi}{2}}\frac{4\pi\epsilon_0\sigma}{e^2}k_B T_e \tag{2.2}$$

In most UNP experiments, this threshold is easily exceeded. The parameter of concern is actually the level of non-neutrality caused by the necessary excess in the ion component; the fraction of trapped electrons is phenomenologically given by [95]

$$\frac{N_e}{N_i} = \frac{\sqrt{N_i/N^*} - 1}{\sqrt{N_i/N^*}} \tag{2.3}$$

This behavior has been demonstrated in experiment [3] (see Fig. 2.3). For most data presented in this thesis, $\sigma \sim 3\,\mathrm{mm}$, $T_e \sim 15\,\mathrm{K}$, and $N_i \sim 5 \times 10^7$, giving $N^* \sim 5000$ and $N_e/N_i \sim 0.99$, justifying our assumption of an effectively neutral plasma.

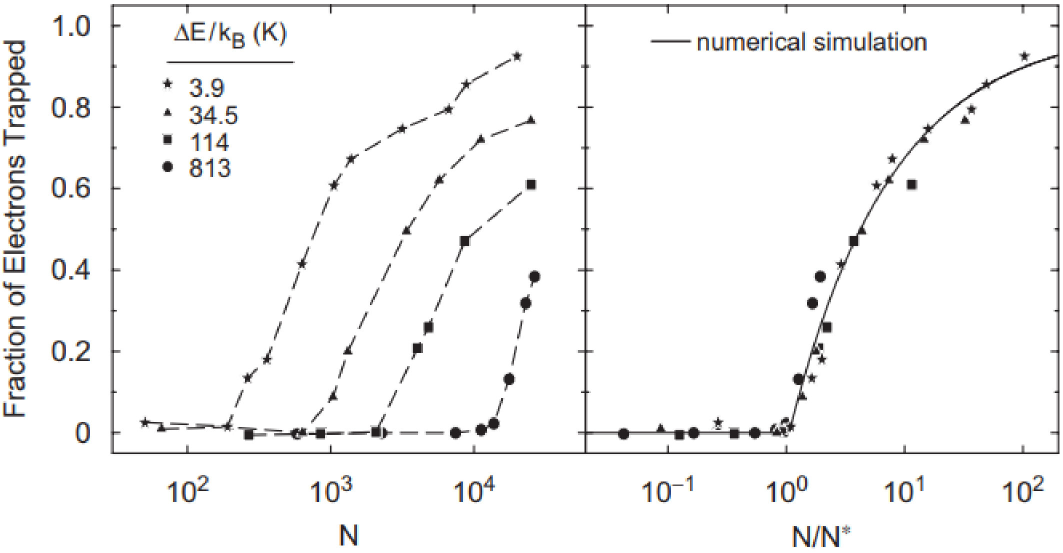

Figure 2.3 : Left: N_e/N_i vs N_i for varying electron temperatures. Right: Same data with number of ions scaled by N^*. Here we clearly see that the N_e/N_i depends solely on N_i/N^*. The line is a numerical simulation. Both the data and the simulation exhibit good agreement with Eq. 2.3 [95]. Adapted from[3].

To summarize, within 1-100 ns the electrons thermalize and a non-neutrality of $\sim 1\%$ is established, trapping the electrons in the plasma.

2.2 Ion Equilibration: Disorder Induced Heating

Due to their heavier mass, the ions remain largely stationary as the electrons thermalize and the $\sim$1% non-neutrality is established. However, the ions eventually undergo their own equilibration process. Immediately after photoionization the ion kinetic energy is characterized by the temperature of the cold gas ($T_g \sim 1\,\mathrm{mK}$), while the potential energy per ion is proportional to $E_c = e^2/4\pi\epsilon_0 a$. For typical UNP densities, $E_c/k_B \sim 1\,\mathrm{K} \gg T_g$. Intuitively, this suggests that the plasma is initialized in a very *entropically unfavorable* state and, therefore, the energy should equipartition to a more 'equitable' distribution between potential and kinetic energy. This is what happens during the DIH process introduced earlier (Fig. 1.3). In this section, I will only present a brief overview of the relevant physics needed to understand this process, for more detail, see [93, 36].

2.2.1 The Yukawa One Component Plasma Model

As discussed above, the heating observed during DIH makes sense from the perspective of equipartitioning between the potential and kinetic degrees of freedom. However, the oscillations observed during DIH (Fig. 1.3) do not have such a simple explanation. These oscillations are not present in any kinetic theory calculations of similar equilibration phenomena [96, 97]; thus, DIH is one process where we can see the failure of standard kinetic theory to capture the totality of the relevant physics of SCPs.

To explain the oscillations, we turn to the underlying Hamiltonian governing the dynamics:

$$H = \sum_{j,k} \frac{p_j^2}{2m_i} + \frac{p_k^2}{2m_e} + \sum_{j \neq l, k \neq n} \frac{1}{2} \frac{e^2}{4\pi\epsilon_0} \left(\frac{1}{r_{jl}} + \frac{1}{r_{kn}} - \frac{1}{r_{jk}} - \frac{1}{r_{ln}} \right) \tag{2.4}$$

where j and l refer to ions and k and n refer to electrons. However, the electrons in our system are weakly coupled $\Gamma_e \leq 0.1$, and we are generally not interested in their dynamics. Thus, we simply treat the electrons as a neutralizing, *screening* fluid background for a cloud of N ions (see Fig. 2.4), allowing us to rewrite the Hamiltonian as

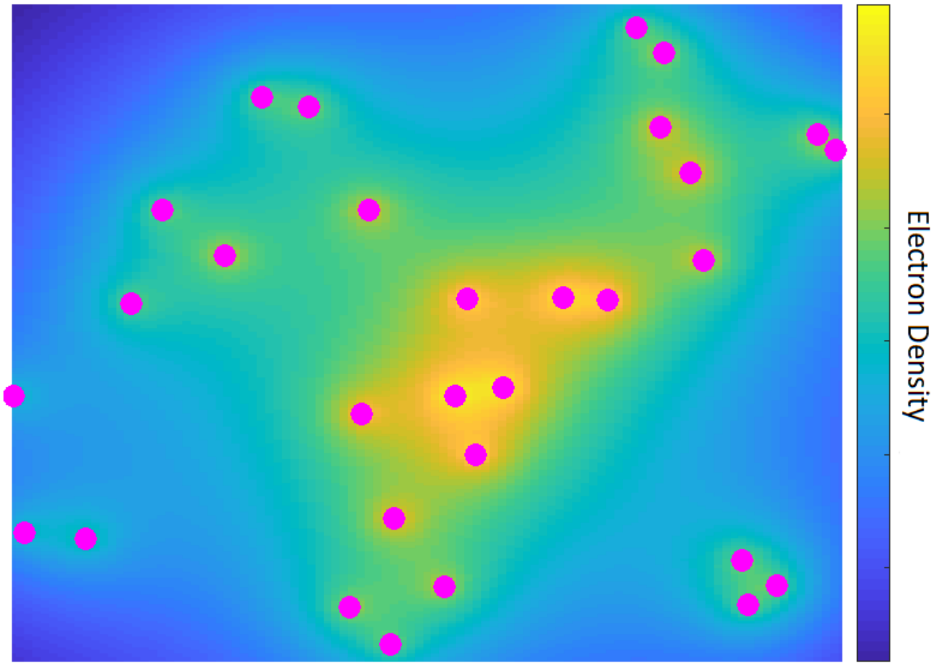

Figure 2.4 : Mockup of the Yukawa OCP picture. In this picture, the plasma is treated as a system of N ions (pink circles) surrounded by a neutralizing, screening, electron fluid. The electron fluid congregates around ions, resulting in Debye screening.

$$H = \sum_j \frac{p_j^2}{2m_i} + \sum_{j \neq l} \frac{1}{2} \frac{e^2}{4\pi\epsilon_0 r_{jl}} \exp\left[-r_{jl}/\lambda_D\right] \tag{2.5}$$

where $\lambda_D = \sqrt{\epsilon_0 k_B T_e / n e^2}$.

By considering the 'natural units' of the plasma (natural energy scale E_c, natural timescale ω_{pi}^{-1} and natural length a), Eq. 2.5 can be recast in unitless form:

$$\tilde{H} = \frac{1}{2}\left(\sum_j 3\tilde{p}_j^2 + \sum_{j \neq l} \frac{\exp\left[-\kappa \tilde{r}_{jl}\right]}{\tilde{r}_{jl}}\right) \tag{2.6}$$

where $\kappa = a/\lambda_D$ is called the 'screening parameter' and the tildes imply dimensionless units (e.g. $\tilde{H} = H/E_c$). Eq. 2.6 is known as the **Yukawa One Component Plasma** model (YOCP).

The YOCP model is very important in the field of SCP physics and has been studied extensively, primarily through molecular dynamics (MD) simulations which numerically propagate Hamilton's equations of motion. These simulations have been used to map the YOCP phase diagram [98, 99, 53], including the $\kappa = 0$ case (commonly referred to as the one component plasma (OCP) model) [8]. In lieu of accurate kinetic theories for $\Gamma > 1$, important features like transport coefficients and collective mode dispersion relations in warm dense matter and ICF plasmas are determined from state of the art simulations of the YOCP[57, 56, 58, 59] or similar models[100].

However, there are very few experimental demonstrations of the validity of this model. After the first experiments on UNPs were performed, it was realized that they should be well described by the YOCP model, motivating simulations [72, 101]. The diagnostic capabilities and resolvable timescales inherent to alkaline earth UNPs provide a means to check those simulations. DIH has been very extensively studied using MD simulations [97, 34, 35] and, in the next section, I will review experiments which demonstrate agreement between experimentally measured DIH curves and MD data [34, 36]. The agreement implies that the YOCP model is valid for describing UNPs and, conversely, that UNPs are ideal experimental realizations of this important model.

2.2.2 Universality in a Diabatic Interaction Quench of the YOCP model

One key feature of the YOCP model is that explicit dependences on density and temperature have been removed. Indeed, the only free parameter, other than the initial conditions, is κ. Thus, any pair of plasmas with the same initial conditions and κ will evolve exactly the same in the dimensionless units of the YOCP even if their densities and temperatures differ dramatically. In this picture, photoionization can be thought of as a *rapid interaction quench* from $\kappa = \infty$ (the situation before photoionization) to $\kappa = \kappa_F(n, T_e) = a(n)/\lambda_D(n, T_e)$ in a system with initial conditions $\{p_j\} = 0$ and random $\{r_j\}$.

In Fig 2.5A and Fig 2.5B we show that, although the DIH curves of two plasmas with densities differing by a factor of 30 vary dramatically in 'real' units, in scaled units the two curves fall on top of each other, a striking demonstration of this concept of *universality* [36]. In principle, universality should extend to higher densities, such as those relevant for strongly coupled astrophysical plasmas and ICF plasmas. Therefore, we can generalize results from UNP experiments to dense plasmas, making UNPs a powerful tool for increasing our understanding of these important systems.

We also performed MD simulations to obtain DIH curves corresponding to the YOCP model, with κ as an input parameter for the simulation. These simulations are discussed in more detail in Sec. 4.3, results are shown as solid curves in Fig. 2.5B and Fig. 2.5D.

In Fig. 2.5D we show that experimental data for plasmas of different κ agree with the expected MD results with good enough measurement resolution to distinguish between curves of different κ. From these results, we conclude that our systems are very well described by the YOCP model and, therefore, any results obtained from studies of UNPs are generalizable to all other systems that are described by this model.

Eventually, the DIH oscillations damp out, leaving an equilibrated plasma with $\Gamma \sim 3$. The exact value of Γ depends on κ, and it can be calculated through conservation of energy by equating the difference in ion potential energy between an equilibrated plasma and a plasma with randomly distributed ion positions, $\Delta\tilde{U}(\Gamma, \kappa)$, which depends on the equilibrium value of Γ, to the ion kinetic energy after equili-

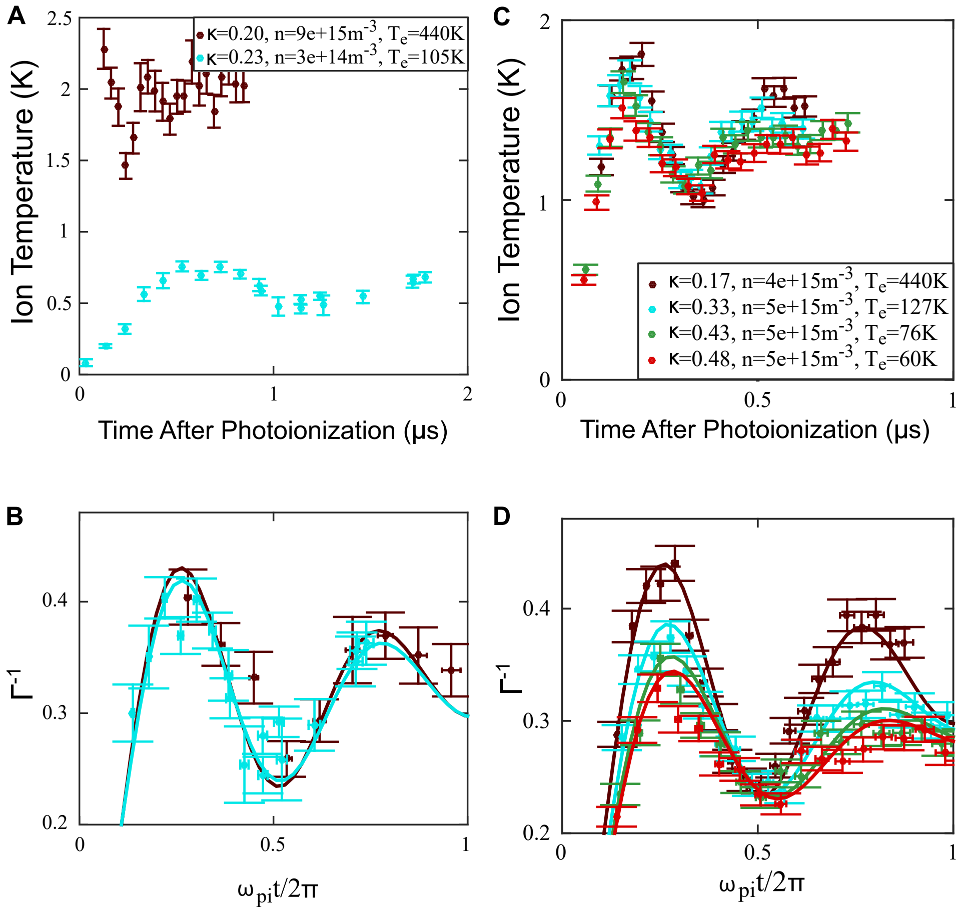

Figure 2.5 : (**A**): DIH curves for plasmas of similar κ differing by a factor of 30 in density and a factor of 4 in electron temperature. The denser cloud reaches a higher temperature ($T_{DIH} \propto E_c \propto n^{1/3}$) and oscillates at a faster rate ($\omega_{pi} \propto n^{1/2}$), as expected from energy and time scaling. (**B**): When DIH curves from **A** are plotted in scaled units $k_B T_i/E_c = \Gamma^{-1}$ and $\omega_{pi}t/2\pi$, the data all collapse onto the same universal curve. The lines are results from a MD simulation of the Yukawa OCP. (**C**): DIH curves for plasmas of different κ and similar n. (**D**): After scaling, the experimental data from **C** clearly match the MD curve for the appropriate κ, with enough resolution to distinguish between curves. Adapted from [36]

bration (this assumes that the initial kinetic energy is zero, a good approximation for UNPs). In scaled units, this can be written as:

$$\Gamma^{-1} = -\Delta\tilde{U}(\Gamma, \kappa). \tag{2.7}$$

Numerical evaluations of $\Delta\tilde{U}(\Gamma, \kappa)$ from MD simulations [98, 99, 53] can be used to solve 2.7 [35, 36], see Fig. 2.6.

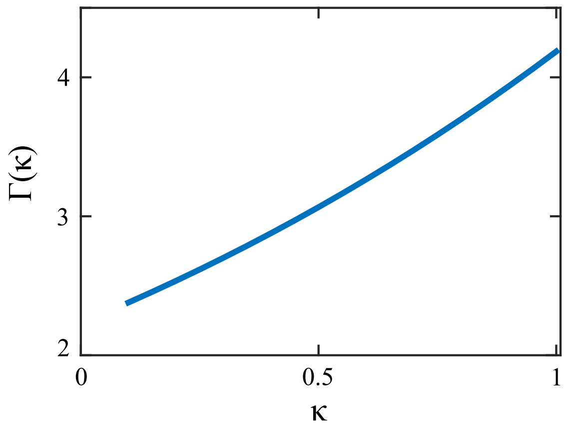

Figure 2.6 : Plot of numerical solutions of Eq. 2.7 using MD data [53]. Adapted from [36]

2.2.3 Development of Short Range Spatial Correlations

As the plasma equilibrates, it develops short range spatial correlations. This can be most easily understood by considering the pair correlation function $g(r)$ which describes the local density surrounding a particle at $r = 0$ by $n_{local}(r) = g(r)n$. Although this cannot be directly measured experimentally, we can still examine this behavior in the MD results, shown in Fig. 2.7. Immediately after photoionization, $g(r) = 1$ everywhere, reflecting the lack of correlations in the neutral gas. During equilibration, correlations begin to build, manifesting in the ‘Coulomb Hole’ depletion at low r. Intuitively, this comes from the Coulomb repulsion; it is energetically unfavorable for ions to be close together. As the hole develops, the potential energy decreases; in other words the kinetic energy ultimately results from the initial lack of correlations, hence the name *disorder induced* heating. The correlations eventually reach an equilibrium value $g(r, \Gamma_f, \kappa)$ where Γ_f indicates the value of Γ after DIH concludes.

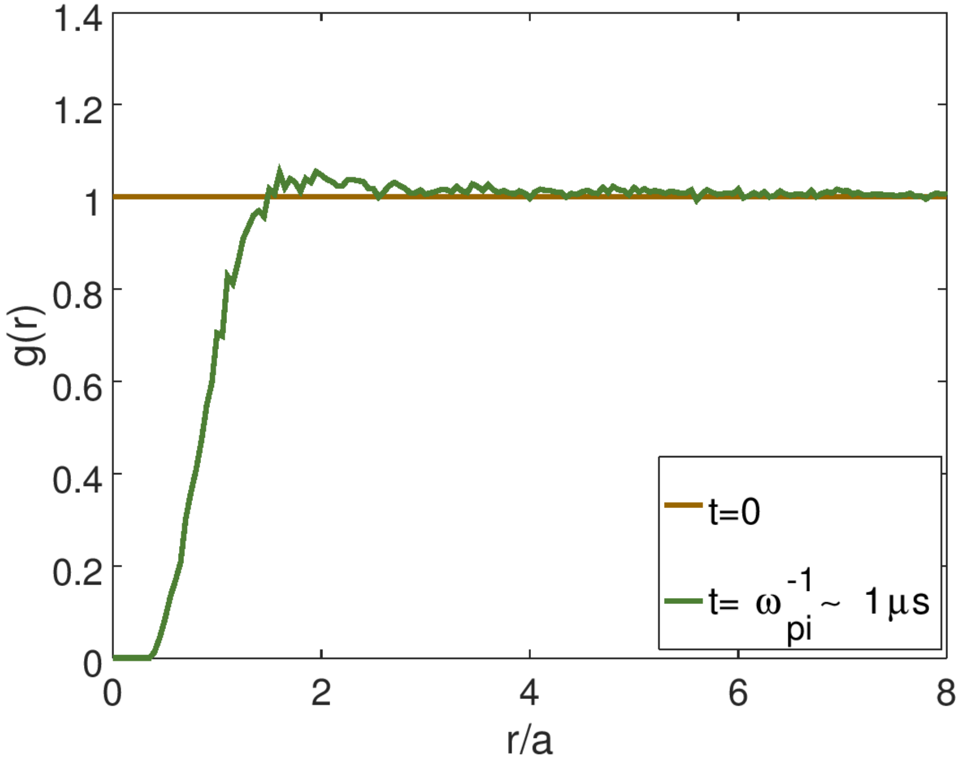

Figure 2.7 : Pair correlations from MD simulations of DIH at $t = 0$ (the uncorrelated initial gas) and $t = \omega_{pi}^{-1}$ (after DIH has occurred). We clearly see here the relation between DIH and the development of spatial correlations; specifically, the 'Coulomb hole' at $r < a$. The development of correlations lowers the potential energy of the ions, which is converted to ion thermal energy.

We can turn this picture around; even though we cannot measure $g(r)$, the fact that we see heating in UNPs is itself *evidence of spatial ordering.* As we stated in Sec. 1.2, this ordering is one reason why kinetic theory fails to describe the physics of SCP systems, including oscillations during DIH[96, 97].

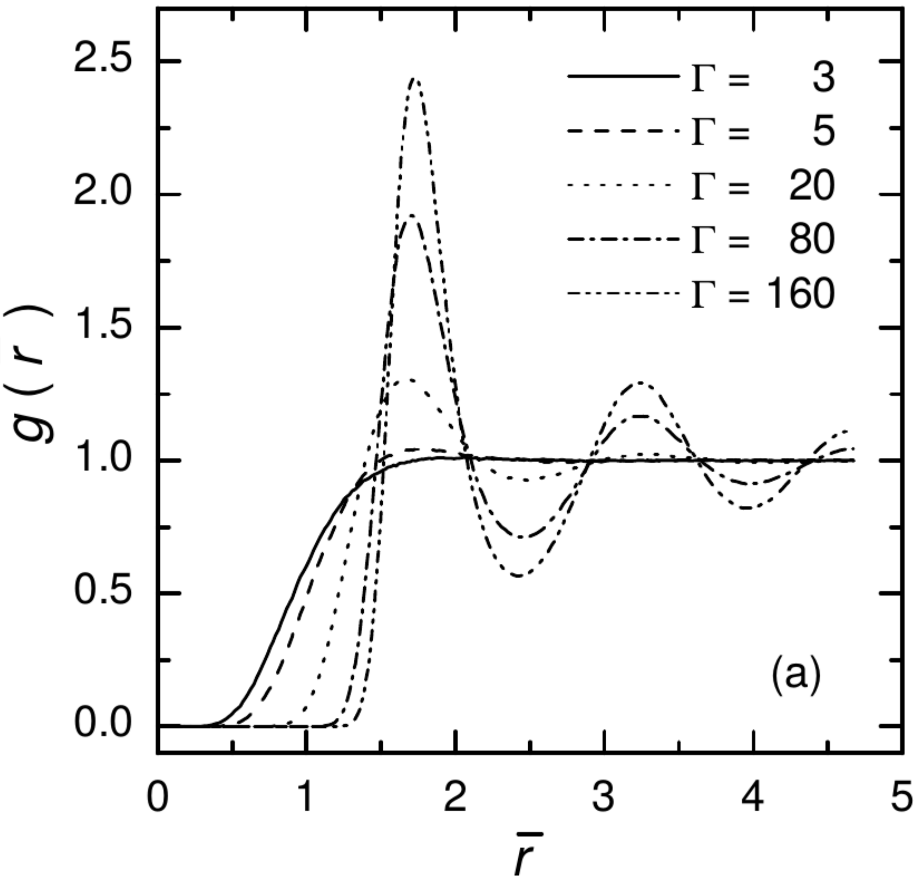

Figure 2.8 : Pair correlations from equilibrium MD simulations [102] for $\kappa = 0$. As Γ increases, we see the development of long-range structure.

For plasmas of higher Γ, one would in principle observe even stronger short-range spatial correlations and eventually the development of long-range correlations. This behavior is reflected in equilibrium MD simulations (see Fig. 2.8 [102]). In principle, DIH can be eliminated if correlations similar to those of $g(r, \Gamma_f, \kappa)$ for high Γ_f are induced in the neutral gas before photoionization, since no kinetic energy will be introduced by 'reordering'. This idea undergirds proposals for ionizing pre-correlated gases such as Rydberg blockaded atoms[18], though there is as of yet no experimental implementation of such a proposal.

2.2.4 Summary of Ion Equilibration in a UNP

Ions equilibrate to $\Gamma \sim 3$ on a timescale $t \sim \omega_{pi}^{-1}$ by DIH (Fig. 2.5). After equilibration, the initially disordered ions have developed short-range spatial correlations, a hallmark of strongly coupled systems (Fig. 2.7). The exact shape of the DIH curve clearly depends on κ (Fig. 2.5D); the fact that our experimental data match an ideal MD simulation of the YOCP model for each value of κ demonstrates the validity of the model for describing UNPs. In addition, the shape of the DIH curve in scaled units was shown to be universal over a factor of 30 in density for plasmas of similar κ; a striking demonstration of the *universality* inherent in the YOCP model. These two observations, universality and good agreement, imply that we can generalize results from UNP experiments to *any* plasma that can be described by the YOCP model, including very interesting, yet hard to probe, systems like white dwarf stars and ICF plasmas

The plasma reaches equilibrium in $t \sim \omega_{pi}^{-1} \lesssim 1\mu\text{s}$ for typical UNP densities (Fig. 2.5). This is much faster than the timescale of the subsequent hydrodynamic expansion of the plasma ($\tau_{Exp} \sim 5 - 100\mu\text{s}$), which is the subject of the next section, justifying our treatment of DIH as a process independent from any expansion dynamics.

2.3 Hydrodynamic Expansion

The equations governing the hydrodynamic expansion of the cloud can be derived directly from the kinetic equations for the ion and electron distributions [103], and are shown in Eqs 2.22- 2.26 below. Rather than reproducing that derivation here, we instead derive the equations using a complementary intuitive approach.

First, consider the two-fluid momentum equations for the ions and electrons [11]:

$$\begin{aligned} n_e m_e \dot{\vec{v}}_e + e n_e \vec{E} &= -\nabla P_e \\ n_i m_i \dot{\vec{v}}_i - e n_i \vec{E} &= -\nabla P_i. \end{aligned} \tag{2.8}$$

Due to quasi-neutrality, we can set $n_i = n_e = n(r)$ and, therefore, $v_e = v_i = v_{Exp}$ and sum the equations to obtain

$$n(r)(m_e + m_i)\dot{\vec{v}}_{exp} = -\nabla(P_e + P_i) \tag{2.9}$$

Since $m_e \ll m_i$, we can set $m_e = 0$. The electron component is weakly coupled ($\Lambda \gg 1$); in this limit, the electron thermal pressure matches that of an ideal gas $P = nk_BT_e$ [104]. Expressing the ion pressure in a similar way would require some correction terms, since the ions are strongly coupled. Even still, the ion pressure will be on the order of nk_BT_i and, since $T_e \gg T_i$, we can neglect it. Making these approximations, we find

$$m_i n(r)\dot{\vec{v}}_{exp} = -k_B T_e \nabla n(r) \tag{2.10}$$

UNPs are typically created from a cloud with a gaussian density profile ($n(r) = n_0 \exp[-r^2/2\sigma_0^2]$). Therefore, at $t = 0$, Eq. 2.10 becomes

$$\dot{\vec{v}}_{exp}(t = 0) = \frac{k_B T_{e0}}{m_i \sigma_0^2}\vec{r}. \tag{2.11}$$

One may intuitively expect that the linear dependence of the force profile on r will result in a 'self-similar' expansion in which, at subsequent times, the plasma is still a gaussian with a re-scaled size σ [21, 105, 106]. Indeed, it can be rigorously shown using the kinetic equations that this is the case and that, furthermore, the resulting expansion velocity is also linear in r and takes the form $\vec{v}_{exp} = \gamma(t)\vec{r}$ [105, 106, 103]. Thus, the expansion force at *all* times can be written as

$$\dot{\vec{v}}_{exp}(t) = \frac{k_B T_e(t)}{m_i \sigma(t)^2}\vec{r}. \tag{2.12}$$

where the time evolution of $\sigma(t)$ is described by

$$\frac{\partial \sigma^2}{\partial t} = 2\gamma\sigma^2. \tag{2.13}$$

From these equations, it is also clear that the timescale of the hydrodynamic expansion is

$$\tau_{Exp} = \sqrt{\frac{m_i \sigma_0^2}{k_B T_{e0}}}. \tag{2.14}$$

As the cloud undergoes adiabatic expansion, the plasma must also cool. We can clearly see that, in time dt a chunk of volume ΔV within the plasma expands by $dV = 3\gamma dt \Delta V$. By conservation of energy, the work done during adiabatic expansion must cause a loss in thermal energy: $-P[dV/dt] = -3\gamma n k_B T_e \Delta V = [(3/2)n\Delta V k_B] dT_e/dt$, where the $n\Delta V$ term on the right reflects the number of electrons within ΔV. Rearranging, it is clear that

$$\frac{\partial T_e}{\partial t} = -2\gamma T_e \tag{2.15}$$

and, assuming no collisions between ions and electrons and that ion correlations have no effect, a similar equation is developed for the ion component

$$\frac{\partial T_i}{\partial t} = -2\gamma T_i. \tag{2.16}$$

Eqs 2.13- 2.16 imply that $\sigma^2 T_{e,i}$ =const, meaning that as the cloud expands both components cool.

To close these equations, we need to determine an expression for $\partial\gamma/\partial t$. One way of achieving this is by considering conservation of energy: the total energy of the plasma (ignoring ionic correlations) E will be a sum of the kinetic energy ($(3/2)k_B T_e$) and the expansion energy ($(3/2)m_i\gamma^2\sigma^2$), where we've again neglected terms depending on m_e and T_i. Thus

$$\frac{\partial E}{\partial t} = \frac{3}{2}k_B\frac{\partial T_e}{\partial t} + \frac{3}{2}m_i\left[2\gamma\sigma^2\frac{\partial\gamma}{\partial t} + 2\gamma^2\sigma\frac{\partial\sigma}{\partial t}\right] = 0. \tag{2.17}$$

Substituting in Eqs. 2.13 and 2.15 and rearranging gives

$$\frac{\partial\gamma}{\partial t} = \frac{k_B T_e}{m_i\sigma^2} - \gamma^2 \tag{2.18}$$

Eqs. 2.13- 2.16 and 2.18 form a complete set of equations for the hydrodynamic evolution of an expanding plasma, for which exact solutions can be obtained [105, 106]; a rarity for plasma systems! The solutions are:

$$\sigma(t)^2 = \sigma(0)^2\left(1 + t^2/\tau_{Exp}^2\right) \tag{2.19}$$

$$T_{i,e}(t) = T_{i,e}(0)\left(1 + t^2/\tau_{Exp}^2\right)^{-1} \tag{2.20}$$

$$\vec{v}_{Exp}(r,t) = \frac{t}{t^2 + \tau_{Exp}^2}\vec{r} \tag{2.21}$$

The validity of these solutions was demonstrated in [21] (see Fig. 2.9 and Fig. 2.10). Here we pause to note that the expansion velocities observed in Fig. 2.10 ($v_{Exp} \gtrsim 50\,\mathrm{m/s}$) are much higher than the capture velocity for laser-cooling ($v_c \sim 10\,\mathrm{m/s}$)

defined in Sec. 1.4; this has major implications for the effectiveness of laser-cooling, which are discussed in detail in Sec. 5.1.

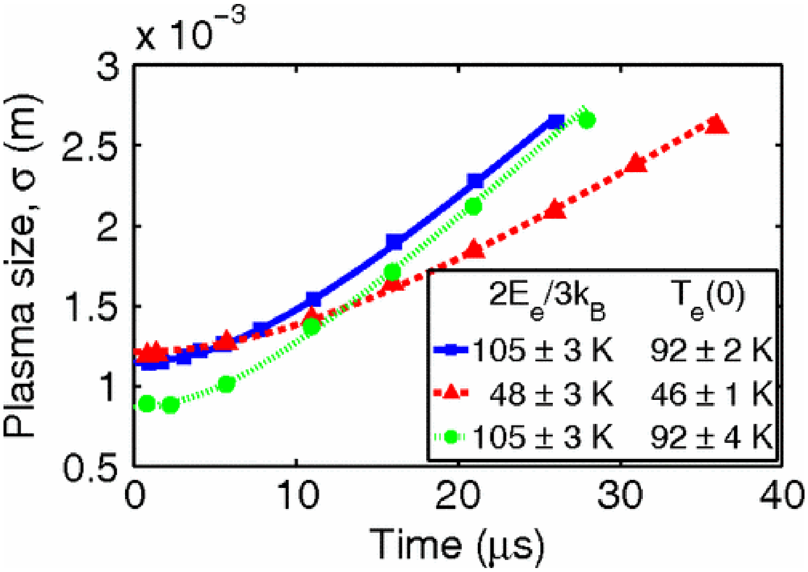

Figure 2.9 : Evolution of σ in a UNP. Fitting the data to Eq. 2.19 with $T_e(0)$ as a free parameter yields results that largely agree with the temperature expected from the excess photon energy above threshold (E_e), which is $2E_e/3k_B$. Adapted from [21].

2.3.1 Impact of Electron-Ion Collisions and Ion Correlations

In the development of the solutions above, we ignored the impact of electron-ion collisions and of ion-ion correlations. However, it turns out that these have a significant effect on the evolution of T_i. The rate of temperature exchange between ions and electrons is given by $\gamma_{ei}(T_e - T_i)$, where $\gamma_{ei} = 2\sqrt{2/3\pi}\Gamma_e^{3/2}\omega_{pe}(m_e/m_i)\ln[\Lambda]$ [45, 22], and $\Lambda = \left[1 + 0.4\Gamma_e^{-3/2}\right]$ is the 'electron Coulomb Logarithm' (we note that this differs from the so-called 'Spitzer estimate' ($\Lambda = \sqrt{3}\Gamma_e^{-3/2}$); here we are using a result derived from a phenomenological fit to direct MD simulation in [107]).

The ion-ion correlation energy is given by the $\Delta\tilde{U}(\Gamma, \kappa)$ term introduced in Sec. 2.2.2, and is generally negative, as it reflects the difference between the in-

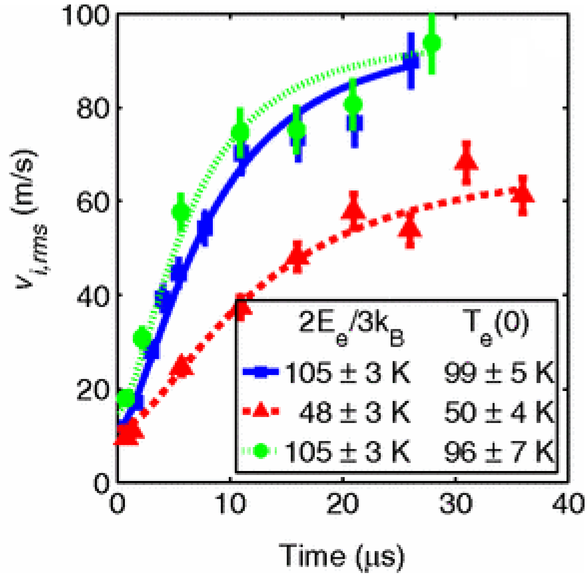

Figure 2.10 : Plot of $v_{Exp}(r,t)$ evaluated at $\sigma(t)$ along with fits to the hydrodynamic expansion solutions, as in Fig. 2.9. Adapted from [21].

teraction energy of ions with the equilibrium value of $g(r)$ and the interaction energy of uncorrelated ions [53, 103]; the latter is generally higher than the former. The correlation energy affects the evolution in two ways. First, it adds an additional term to the total energy E, affecting the equation for γ. Second, it adds an additional term to the ion temperature evolution equation because any energy change in $\Delta\tilde{U}(\Gamma,\kappa)$ due to increased ion-ion correlations will lead to ion heating.

We define the 'correlation temperature' $(3/2)k_BT_{corr} = \Delta\tilde{U}(\Gamma,\kappa) \times E_c(n)$, where the $E_c(n)$ term reflects that $\Delta\tilde{U}(\Gamma,\kappa)$ is a scaled energy (see Eq. 2.7). The equilibrium correlation temperature $T_{corr,Eq}(n,T_i)$ can be calculated from MD simulations [53]. Assuming that differences between T_{corr} and $T_{corr,Eq}$ are resolved on a timescale ω_{pi}^{-1}, we can obtain the following set of equations to describe the plasma expansion[103]

$$\frac{\partial\sigma^2}{\partial t} = 2\gamma\sigma^2 \tag{2.22}$$

$$\frac{\partial \gamma}{\partial t} = \frac{k_B\left(T_e + T_i + \frac{T_{corr}}{2}\right)}{m_i \sigma^2} - \gamma^2 \tag{2.23}$$

$$\frac{\partial T_e}{\partial t} = -2\gamma T_e - \gamma_{ei}(T_e - T_i) \tag{2.24}$$

$$\frac{\partial T_i}{\partial t} = -2\gamma T_i + \gamma_{ei}(T_e - T_i) - \gamma T_{corr} - \frac{\partial T_{corr}}{\partial t} \tag{2.25}$$

$$\frac{\partial T_{corr}}{\partial t} = \omega_{pi}\left[T_{corr,Eq}(n_i, T_i) - T_{corr}\right]. \tag{2.26}$$

This set of eqs can be solved numerically for the initial conditions of the plasma ($\sigma(0) = \sigma_0$, $T_e(0) = 2\Delta E/3k_B$, and $\gamma(0) = T_i(0) = T_{corr}(0) = 0$). Though the solutions do not capture the oscillations observed in DIH, they do capture the ion heating through the last term in Eq. 2.25.

The main effect of the added terms on the long-term evolution of the cloud comes from the electron-ion heating, as demonstrated in Fig. 2.11 [22]. Electron-ion collisions heat the ions considerably, nearly doubling T_i for $t = 2\tau_{Exp}$ for the conditions in Fig. 2.11. This heating limits the levels of Γ we would expect to achieve through adiabatic cooling (Fig. 2.12). We observe that $\Gamma \sim 2 - 3$ throughout $t = 3\tau_{Exp}$ of expansion time, after which Γ starts to slowly increase. However, at this point, the plasma is very dilute, inhibiting our ability to do studies at $\Gamma \sim 5$, achieved after $t = 4\tau_{Exp}$.

2.3.2 Summary of Hydrodynamic Expansion of a UNP

If electron-ion heating and ion correlations are ignored, the expansion of an initially gaussian UNP represents a rare example of an exactly solvable hydrodynamic expansion problem. The evolution of the size of the cloud follows the exact solutions (Fig. 2.9 and Fig. 2.10) very closely. The expanding cloud develops a significant characteristic expansion velocity $\langle v_{Exp}\rangle \gg v_c$, which has major implications for laser cooling which we will address in Sec. 5.1. The timescale for the expansion is set by

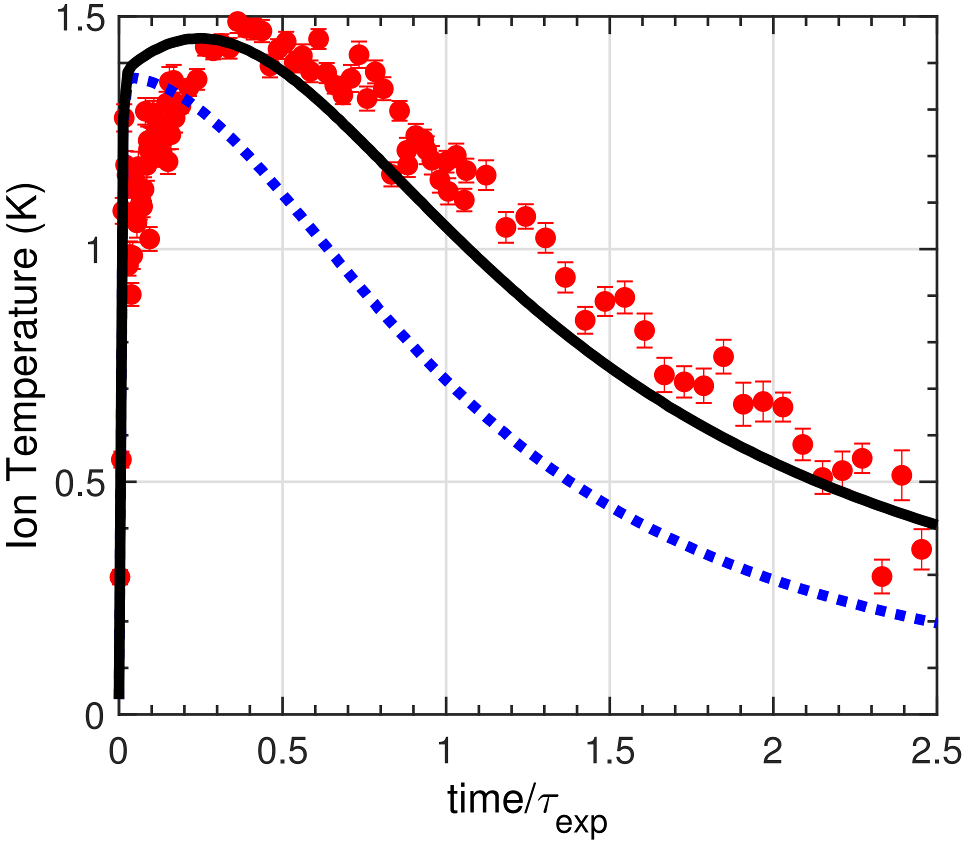

Figure 2.11 : Evolution of $T_i(t)$. The solid black curve represents the solutions to Eqs 2.22- 2.26 for the same initial conditions as the data, while the dashed blue curve is calculated from Eq. 2.20. The data clearly show evidence of electron-ion thermalization. Data adapted from [22].

τ_{Exp}, defined in Eq. 2.14. This limits the time available for laser cooling. For typical UNP sizes and T_e, $\tau_{Exp} \leq 100\mu$s, thus, this is a pretty onerous time restriction!

Additionally, the ion temperature evolution clearly shows that electron-ion thermalization is significant. The net effect of this additional heating term, along with some unexplained extra heating that likely stems from density waves created by an imperfect ionization laser, is to keep $\Gamma \sim 2-3$ throughout the most of the evolution. In absence of these effects, Γ would increase to 5 within $t = 2\tau_{Exp}$ (Fig. 2.12). Therefore, the additional cooling from a laser-cooling scheme must be strong enough

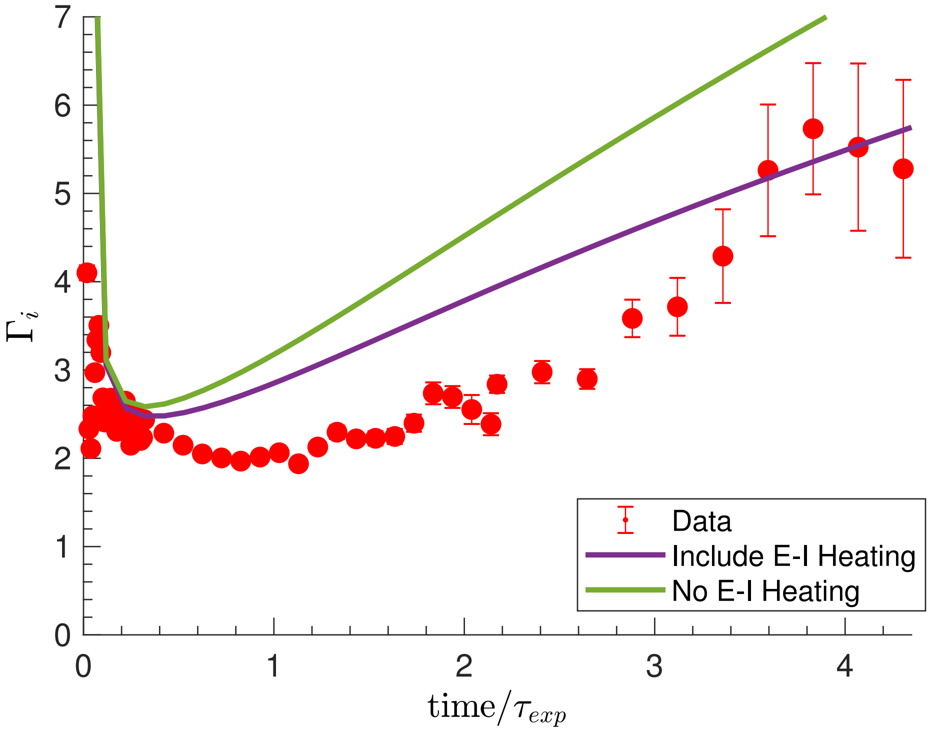

Figure 2.12 : Evolution of $\Gamma_i(t)$ for $T_e(0) = 430\,\mathrm{K}$, $n_0 = 4 \times 10^{15}\mathrm{m}^{-3}$ and $\sigma_0 = 1\,\mathrm{mm}$. In addition to the electron ion heating, there appears to be an additional source of heating, perhaps from density waves induced by imperfections in the ionization beam. We observe $\Gamma \sim 2-3$ throughout most of the 'useful' portion of the evolution, only increasing when the plasma has become very dilute due to expansion.

to overcome the electron-ion heating in order to have a significant effect on Γ. We discuss this in more detail in Sec. 6.2.2.

2.4 Three Body Recombination

During the UNP evolution, three-body recombination (TBR) events can occur, in which two electrons and an ion collide inelastically, resulting in a rydberg atom and a 'hot' electron that carries away the Rydberg binding energy. The rate at which these collisions occur was first calculated by Mansbach and Keck [108]. More recent theory [109] and measurements [25] resulted in a slight modification to the Mansbach and Keck theory, giving a three-body recombination rate of:

$$R_{TBR} = C_{rec} T_e^{-9/2} n^2 \tag{2.27}$$

where $C_{rec} = 2.77 \times 10^{-21}\,\mathrm{K}^{9/2}\,\mathrm{m}^6\,\mathrm{s}^{-1}$ (the Mansbach and Keck coefficient was $C_{rec} = 3.9 \times 10^{-21}\,\mathrm{K}^{9/2}\,\mathrm{m}^6\,\mathrm{s}^{-1}$). If we substitute in $n^{1/3}/T_e = [4\pi k_B \epsilon_0/e^2]\,(3/4\pi)^{1/3}\,\Gamma_e$ and $\sqrt{n} = \sqrt{\epsilon_0 m_i}\omega_{pi}/e$, we find:

$$\frac{R_{TBR}}{\omega_{pi}} = C_{rec}\frac{\sqrt{m_i\epsilon_0}}{e}\left[\frac{4\pi k_B\epsilon_0}{e^2}\left(\frac{3}{4\pi}\right)^{1/3}\right]^{9/2}\Gamma_e^{9/2} = 7.28\Gamma_e^{9/2} \tag{2.28}$$

We see that, for small Γ_e ($\ll 0.1$), TBR is effectively negligible due to the dependence on $\Gamma_e^{9/2}$. For $\Gamma_e \gtrsim 0.1$, TBR is expected to cause significant deviations in the plasma evolution from what one would expect by solving Eqs. 2.22-2.26 given some set of initial conditions. This is because TBR results in electron heating. The changes in electron temperature then increase the hydrodynamic expansion force, leading to a faster expansion then that expected from the initial conditions [110].

There is a feedback between Γ_e and TBR: high Γ_e means that R_{TBR} is high, which results in electron heating. The electron heating, in turn, reduces Γ_e, leading to fewer TBR events and thus a reduction in the electron heating rate. This effectively 'thermostats' Γ_e to ~ 0.1 (the exact value will depend on the balance between electron heating resulting from R_{TBR} and the electron cooling resulting from adiabatic expansion).

For the experiments presented in this thesis, we want to avoid TBR, as it will result in unobservable (we do not have a way of directly measuring T_e) changes in the screening parameter κ, knowledge of which is necessary in order to compare measurements made in our system to other YOCPs. It would also result in 'anomalous' plasma density depletion, as ions and electrons are converted to rydberg atoms. Thus, for a given initial density n_0, we generally choose T_{e0} such that $\Gamma_e < 0.1$, in which case TBR is expected to be a negligible effect [110].

Chapter 3

Experimental Techniques

This chapter describes the experimental techniques for UNP generation, diagnostics, and laser-cooling. In sections 3.1 and 3.2, I will describe in detail how we create UNPs from an ultracold gas of Sr atoms. We choose Sr because, as an alkaline earth atom, it contains two valence electrons. Thus, after photoionization, the Sr^+ ion has an 'alkali-like' electronic energy level diagram with accessible optical transitions. The 'D1' line corresponds to 422 nm light while the 'D2' line corresponds to 408 nm light. In section 3.3 I discuss how we use the 'D1' transition for our laser-induced fluorescence (LIF) diagnostic[111] used to measure the ion quantities of interest, such as density, temperature, and hydrodynamic velocities, all of which can be measured to a spatial resolution of $13\,\mu$m. Finally, in section 3.4 I discuss our setup for laser-cooling the plasma using the 'D2' line.

3.1 Atom Trapping

We start by loading a magneto-optical trap of ^{88}Sr atoms; this trap operates on the dipole allowed $^1\mathrm{S}_0 \rightarrow ^1\mathrm{P}_1$ transition at 461 nm. A steady state number of $\sim$200 million atoms can be trapped at a detuning $\Delta_{MOT} = -50\,\mathrm{MHz}$. The cooling transition has a small leak into the $^3\mathrm{P}_1$ and $^3\mathrm{P}_2$ states; see Fig. 3.1. Atoms in the $^3\mathrm{P}_1$ state decay back down to $^1\mathrm{S}_0$ relatively quickly (the $^3\mathrm{P}_1$ lifetime is 7.5μs) and can be recycled into the MOT, however, atoms in $^3\mathrm{P}_2$ are long lived ($\sim 100\,$s). Atoms that decay to low field seeking Zeeman sublevels of ^{3}P$_2$ (m_j = +2,+1) remain in the trap, as they are magnetically trapped by the quadrupole field used in the MOT[112]. So, while the MOT is in its steady state, a magnetically trapped ^{3}P$_2$ population builds up, saturating at $\sim 10^9$ atoms after ~ 1 s.

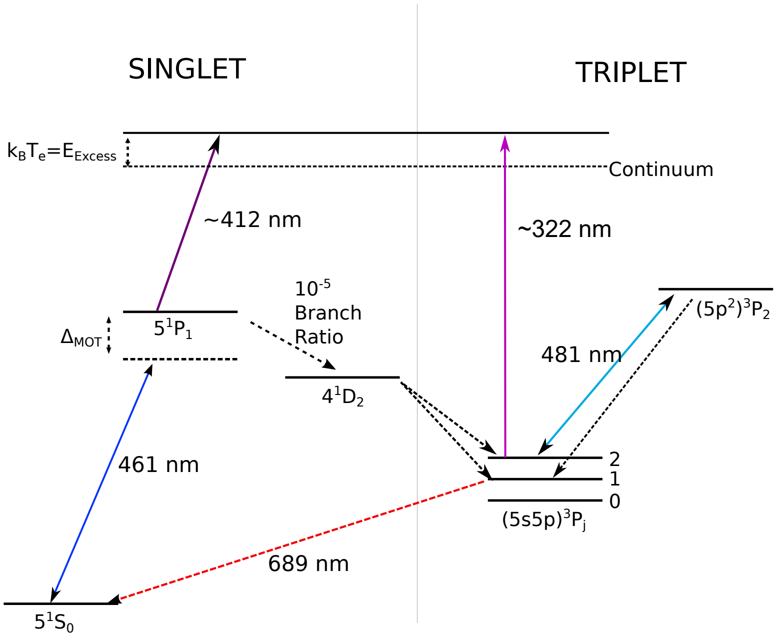

Figure 3.1 : Sr atom level diagram. The MOT works off of the dipole allowed ^{1}S$_0$ $\rightarrow$^{1}P$_1$ transition (30.5 MHz [113]). In steady-state MOT operation, atoms continually accrue in the magnetically trapped weak-field seeking zeeman substates of the ^{3}P$_2$ state, as this state is long-lived ($\sim$100 s lifetime). We ionize from either the ^{1}S$_0$ state or the $^3P_2$ state. The former requires a pulse-amplified 461 nm beam in combination with a pulsed dye laser tuned to 412 nm, while the latter requires a 322 nm pulse, which can be generated by doubling the output frequency of a pulsed dye laser tuned to 644 nm.

We can choose to ionize from either the magnetically trapped ^{3}P$_2$ state, in which case we use one photon at 322 nm, or the ^{1}S$_0$ state, in which case we use two photons at 461 nm and 413 nm (see Fig. 3.1), depending on whether total ion number or repetition rate is more important. For the results presented in Chapter 5, we ionize from ^{3}P$_2$.

It turns out that the MOT atoms and the magnetically trapped atoms have different spatial profiles, which can affect the subsequent plasma dynamics. To determine the spatial profile of the MOT, we must first consider the MOT force. The force in the $+x$ direction is given by [114]

$$F(x) = \frac{\hbar k \gamma_{MOT} s_0}{2}\left[\frac{1}{1+s_0+4\frac{(\Delta+\mu_B m_J g_J b x)^2}{\gamma_{MOT}^2}} - \frac{1}{1+s_0+4\frac{(\Delta-\mu_B m_J g_J b x)^2}{\gamma_{MOT}^2}}\right] \tag{3.1}$$

where $\gamma_{MOT}/2\pi = 30.5\,\mathrm{MHz}$ is the natural linewidth of the ${}^1\mathrm{S}_0 \rightarrow {}^1\mathrm{P}_1$ transition, $s_0 = I/I_{sat}$ is the 'saturation parameter', where I is the laser intensity and $I_{sat} = 2\pi^2\hbar c\gamma_{MOT}/3\lambda^3$ [114], $m_J = 1$ is the magnetic quantum number of the ${}^1\mathrm{P}_1$ state driven during the MOT transition, $g_j = 4/3$ is the Lande g-factor for the ${}^1\mathrm{P}_1$ level, and b is the magnetic gradient (typically 71.9 G/cm along the strong axis and 35.9 G/cm along the weak axes)[112]. In the limits of $s_0 \ll 1$ and $\mu_B m_J g_J b x \ll \Delta$, which are typically valid in a MOT, this force simplifies to:

$$F(x) = \left[\frac{32 k s_0 \mu_B b \Delta}{3\gamma_{MOT}}\left(1+\frac{4\Delta^2}{\gamma_{MOT}^2}\right)^{-2}\right] x = \alpha x, \tag{3.2}$$

where $\alpha < 0$ if $\Delta < 0$. Thus, for red detuning, the atom experiences a spring-like restoring force with an associated potential $U = (\alpha/2)x^2$. The density is therefore

$$n(x) = n_0 \exp\left[\frac{\alpha x^2}{2k_B T}\right] \tag{3.3}$$

and, generalizing to 3D, we have

$$n_{MOT}(r) = n_0 \exp\left[\frac{\alpha r^2}{2k_B T}\right], \tag{3.4}$$

where here we've assumed that the potential is equal along all three dimensions (this can be done by making the saturation parameter for the beam propagating along the strong axis half of that along the weak axis). After the release of the trap, the atoms ballistically expand, modifying the density profile:

$$\begin{aligned} n_{MOT,Released}(r,t) &= \frac{1}{\sqrt{2\pi t^2 v_T^2}} \int_{-\infty}^{\infty} n_{MOT}(r') \exp\left[-\frac{(r-r')^2}{2t^2 v_T^2}\right] d^3r' \\ &= n_0 \left(\frac{\sigma_0^2}{\sigma_0^2 + v_T^2 t^2}\right)^{3/2} \exp\left[-\frac{r^2}{2\left(\sigma_0^2 + v_T^2 t^2\right)}\right] \end{aligned} \tag{3.5}$$

where $\sigma_0 = \sqrt{k_B T/\alpha}$. As we can see, they are released from the MOT, the atoms retain their gaussian profile with a width given by $\sigma(t) = \sqrt{\sigma_0^2 + v_T^2 t^2}$.

In contrast, the magnetic trapping potential for the $^3\mathrm{P}_2$ atoms results from the Zeeman shift. In order to understand this trap, one assumes that the magnetic moment follows the magnetic field adiabatically as it moves around the trap, which is a good approximation except at a negligibly small region near $r = 0$, which can be neglected for our experimental conditions [112]. Thus, the magnetic moment m_j is the projection along the local magnetic field, *not* a projection along a fixed axis. In 1D, the shift then becomes

$$U_{3P2}(x) = \mu_B m_J g_b b|x| = \frac{8}{3}\mu_B b|x| \tag{3.6}$$

where I've assumed the atoms are in the $m_J = 2$ state and, therefore, the profile is

$$n(x) = n_0 \exp\left[-\frac{8\mu_B b|x|}{3k_B T}\right] = n_0 \exp[-a|x|] \tag{3.7}$$

where $a = 8\mu_B b/3k_B T$. Generalizing to 3D, we get

$$n_{MagTrap}(x,y,z) = n_0 \exp\left[-a\sqrt{x^2 + y^2/4 + z^2/4}\right] \tag{3.8}$$

where the factors of 1/4 reflect the fact that the gradient is twice as strong along x

than along y and z due to the nature of the quadrupole field. Upon release from the trap at time $t = 0$, the profile becomes

$$n_{MagTrap,Released}(x, y, z, t) = n_0 \int_{-\infty}^{\infty} dx' \int_{-\infty}^{\infty} dy' \int_{-\infty}^{\infty} dz' \exp\left[-a\sqrt{x'^2 + y'^2/4 + z'^2/4}\right] \times \exp\left[-\frac{(x-x')^2 + (y-y')^2 + (z-z')^2}{2t^2 v_T^2}\right] \tag{3.9}$$

Unfortunately, this integral cannot be evaluated analytically. However, the 1D version does have an analytic solution

$$\begin{aligned} n(x,t) &= \frac{n_0}{\sqrt{2\pi v_T^2 t^2}} \int_{-\infty}^{\infty} dx' \exp[-a|x'|] \exp\left[-\frac{(x-x')^2}{2v_T^2 t^2}\right] \\ &= \frac{n_0}{2} \exp\left[a^2 v_T^2 t^2/2 - ax\right] \times \\ &\left[\operatorname{erfc}\left(\frac{1}{\sqrt{2} a v_T t}(a^2 v_T^2 t^2 - ax)\right) + \exp[2ax] \operatorname{erfc}\left(\frac{1}{\sqrt{2} a v_T t}(a^2 v_T^2 t^2 + ax)\right)\right] \end{aligned} \tag{3.10}$$

where $\operatorname{erfc}(z) \equiv 1 - \operatorname{erf}(z)$ is the 'complementary error function'. It is clear from this expression that there is a natural timescale $\tau = 1/av_T$ and a natural length-scale $1/a$. Letting $\tilde{t} = t/\tau$ and $\tilde{x} = ax$, we see:

$$n(x,t) = \frac{n_0}{2} \exp\left[\tilde{t}^2/2 - \tilde{x}\right] \left[\operatorname{erfc}\left(\frac{\tilde{t}^2 - \tilde{x}}{\sqrt{2}\tilde{t}}\right) + \exp[2\tilde{x}] \operatorname{erfc}\left(\frac{\tilde{t}^2 + \tilde{x}}{\sqrt{2}\tilde{t}}\right)\right]. \tag{3.11}$$

The temperature can be determined through ballistic expansion measurements; for our typical measured temperature of $T = 1 - 2\,\text{mK}$, we find characteristic size $a^{-1} = 0.8 - 1.6\,\text{mm}$ and characteristic expansion time $1/av_T = 2.5 - 3.5\,\text{ms}$.

By numerically solving Eq. 3.9, we can obtain the spatial profile at any time during the expansion. In particular, it is instructive to look at 'transects' of the cloud along the strong axis and along one of the weak axes (e.g., $n(x,0,0)$ and $n(0,y,0)$). These are shown in Fig. 3.2A and Fig. 3.2B, respectively. Fig. 3.2C, meanwhile, shows the residuals of a gaussian and of an exponential fit to $n_{MagTrap,Released}(x,y,z,t)$ at different normalized times $\tilde{t}$. Figure 3.2 illustrates that, after they are released, the magnetically trapped atoms evolve from a 'cuspy' exponential profile towards a gaussian profile over a timescale of a few τ.

3.2 Photoionization

No matter what ionization scheme we use, Eqs 3.5 and 3.9 tell us that the initial size of the plasma can be controlled by varying how long we wait after the cloud is released from the trap before photoionizing. In addition, when ionizing from the magnetic trap, the 'wait time' also affects the spatial profile of the resulting plasma whereas the density profile for atoms released from the MOT remains gaussian throughout. The ionization beam is typically much larger than the spatial extent of the atom cloud, thus, either Eq. 3.5 or Eq. 3.9 reflects the initial plasma density profile, depending on which state we photoionize from.

The amount of atoms that will be ionized depends on the photoionization cross section σ_{pi}, which is typically given in units of 'Megabarns' ($1\,\mathrm{Mb}=10^{-22}\,\mathrm{m}^2$). Knowledge of the photoionization cross section can also be used to calculate the oscillator strengths of rydberg transitions [115]. However, there appears to be only one measurement of the cross section for photoionization from the ^{3}P state [116]. We decided to complement that previous work by doing our own measurement of the photoionization cross section using UNPs. This work was performed in a collaboration with Ilian Plompen from Eindhoven University of Technology.

For a cloud of atoms irradiated by a laser pulse with photon energy tuned above

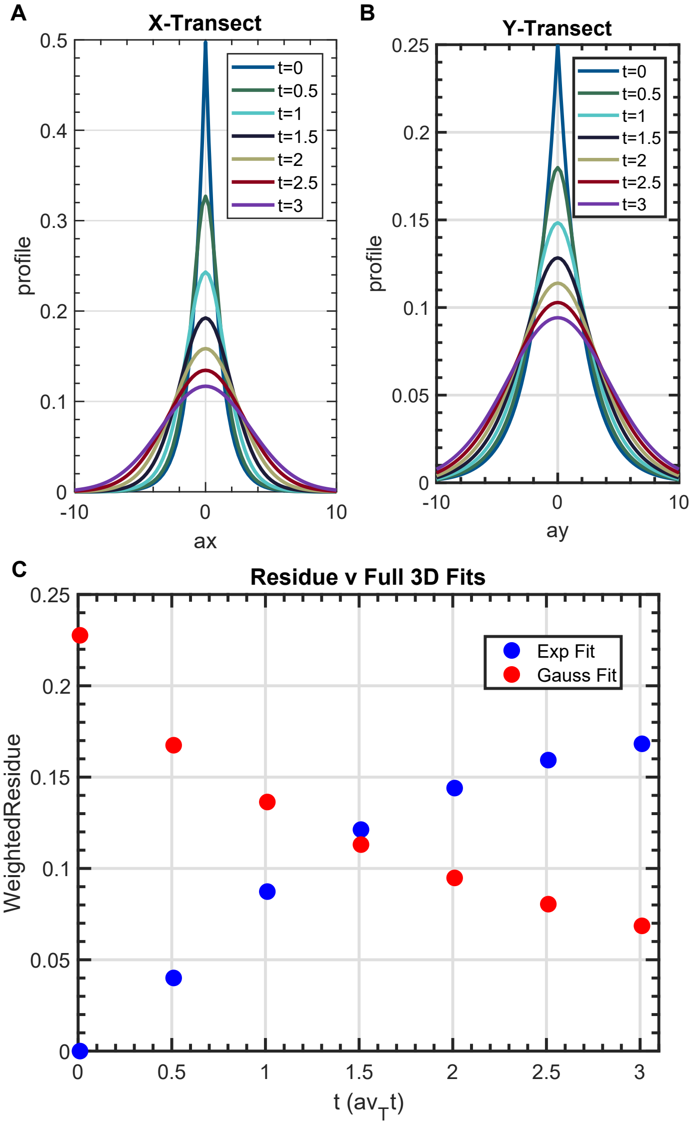

Figure 3.2 : (**A**): Plot of $n_{MagTrap,Released}(\tilde{x}, 0, 0, \tilde{t})$ at various time $\tilde{t}$. (**B**): Plot of $n_{MagTrap,Released}(0, \tilde{y}, 0, \tilde{t})$ at various time $\tilde{t}$. We can clearly see that both axes are evolving from a 'cuspy' exponential profile to a smoother gaussian profile. (**C**): Residuals of 3D fit to a numerical evaluation of $n_{MagTrap,Released}(x, y, z, t)$ vs time. We clearly see that the cloud evolves from being best described by a 3D exponential profile (at $t = 0$) to being better described by a 3D gaussian at later times.

threshold, propagating along the y axis, the probability that a given atom at location (x, z) will be ionized is given by:

$$p(x,z) = 1 - \exp\left(-\frac{\epsilon(x,z)\sigma_{PI}}{hf}\right) \tag{3.12}$$

where $\epsilon(x,z)$ is the areal energy density of the pulse and f is the photon frequency. To measure the energy density, we need to profile the beam. We use the knife-edge profiling technique to obtain the horizontal and vertical profiles and found that they could both be described by a bimodal gaussian distribution:

$$P_{1D}(x, x_{coeffs}) = \frac{1}{\sqrt{2\pi}\,(\sigma_1 + A\sigma_2)}\left(\exp\left[-\frac{(x-d_{x1})^2}{2\sigma_1^2}\right] + A\exp\left[-\frac{(x-d_{x2})^2}{2\sigma_2^2}\right]\right) \tag{3.13}$$

where x_{coeffs} include A, d_{x1}, d_{x2}, σ_1, and σ_2. After fitting both the x and z profiles to P_{1D}, we then set the origin at (d_{x1},d_{z1}) and assumed that the total beam profile $P_{2D} = P_{1D}(x, x_{coeffs})P_{1D}(z, z_{coeffs})$ such that

$$\begin{aligned} P_{2D}(x, x_{coeffs}, z, z_{coeffs}) = & \frac{\left(\exp\left[-\frac{x^2}{2\sigma_{1x}^2}\right] + A_x\exp\left[-\frac{(x-d_x)^2}{2\sigma_{2x}^2}\right]\right)}{\sqrt{2\pi}\,(\sigma_{1x} + A_x\sigma_{2x})} \times \\ & \frac{\left(\exp\left[-\frac{z^2}{2\sigma_{1z}^2}\right] + A_z\exp\left[-\frac{(z-d_z)^2}{2\sigma_{2z}^2}\right]\right)}{\sqrt{2\pi}\,(\sigma_{1z} + A_z\sigma_{2z})} \end{aligned} \tag{3.14}$$

where $d_x = d_{x2} - d_{x1}$ and $d_z = d_{z2} - d_{z1}$.

We also tested this by taking a knife-edge profile at a 45° degree angle. Good agreement was observed between the 45° data and the expected profile based on Eq. 3.14. These results, including the fitted values of x_{coeffs} and z_{coeffs}, are summarized in Fig. 3.3.

The total energy density $\epsilon(x,z)$ is simply $EP_{2D}(x,z)$, where E is the total pulse energy. With knowledge of the pulse repetition rate, E can easily be measured using a simple power meter. We measure the ion density in the region corresponding to the

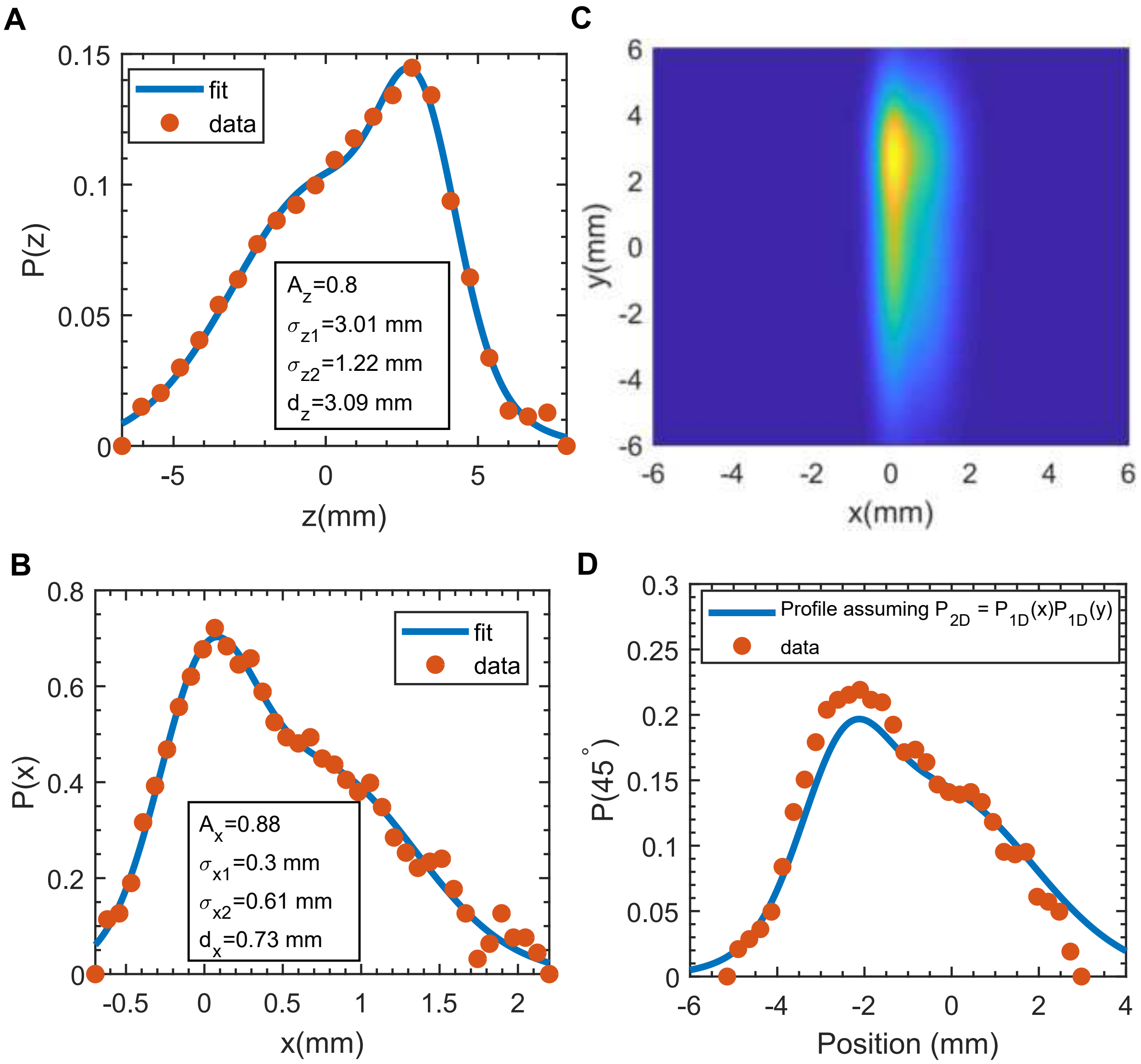

Figure 3.3 : (**A**): $P_{1D}(z)$, the vertical profile of the UV beam. The fitted values for z_{coeffs} are displayed as text in the figure. (**B**): $P_{1D}(x)$, the horizontal profile of the UV beam. The fitted values for x_{coeffs} are displayed as text in the figure. (**C**): Image of P_{2D} assuming that the profile is simply a product of the two 1D profiles $P_{2D}(x, z) = P_{1D}(x)P_{1D}(z)$. (**D**): 45° knife edge profile data plotted alongside the 'expected' profile derived numerically from P_{2D}. The relatively good match between the two indicates that the assumption that the 2D profile can be decomposed as a product of 1D profiles along x and z is reasonable.

maximum of $P_{2D}(x, z)$ using laser-induced fluorescence (LIF, see Sec. 3.3). For the values of x_{coeffs} and z_{coeffs} shown in Fig. 3.3, this corresponds to $x_c = 0.08\,\text{mm}$ and

$z_c = 2.702\,\text{mm}$. Due to the nature of the LIF technique & to obtain better signal to noise, we collect data that measures the number of ions in the region $x = x_c \pm s_x/2$ and $z = z_c \pm s_z/2$, where s_z=1 mm and $s_x = 0.26\,\text{mm}$. The average beam intensity in this region is given by

$$\langle\epsilon\rangle = \frac{E}{s_z s_x}\int_{z_c-s_z/2}^{z_c+s_z/2}\int_{x_c-s_x/2}^{x_c+s_x/2} P_{2D}(x, x_{coeffs}, z, z_{coeffs})dxdz \tag{3.15}$$

Inserting the measured values of x_{coeffs} and z_{coeffs} and plugging in the values for s_x and s_y, we calculate $\langle\epsilon\rangle = 0.0925E$, where ϵ is measured in J/mm^2. Using Eq. 3.12, we see that the measured number of ions within the region

$$N = C\left[1 - \exp\left(-\frac{\langle\epsilon\rangle\sigma_{PI}}{hf}\right)\right] \tag{3.16}$$

We can measure σ_{PI} by obtaining N as a function of E and fitting to Eq. 3.16 with σ_{PI} and C as the only free parameters. This is called the ‘saturation’ method [116, 115]. The energy is varied by simply lowering the pumping energy in the pulsed dye laser system. The results are shown in Fig. 3.4.

3.3 Laser Induced Fluorescence

The main advantage of using an alkaline earth atom like Sr (as opposed to an alkali atom like Rb) in a UNP experiment is that the ion has an alkali-like level structure (e.g., ‘D1’ and ‘D2’ lines that are optically accessible). In this section, I will show how we use the ‘D1’ line at 422 nm (see Fig. 3.5) as a diagnostic tool for the measurement of:

- local density in the $z = 0$ plane $n(x, y, z = 0)$
- local temperature $T(x, y, z = 0)$

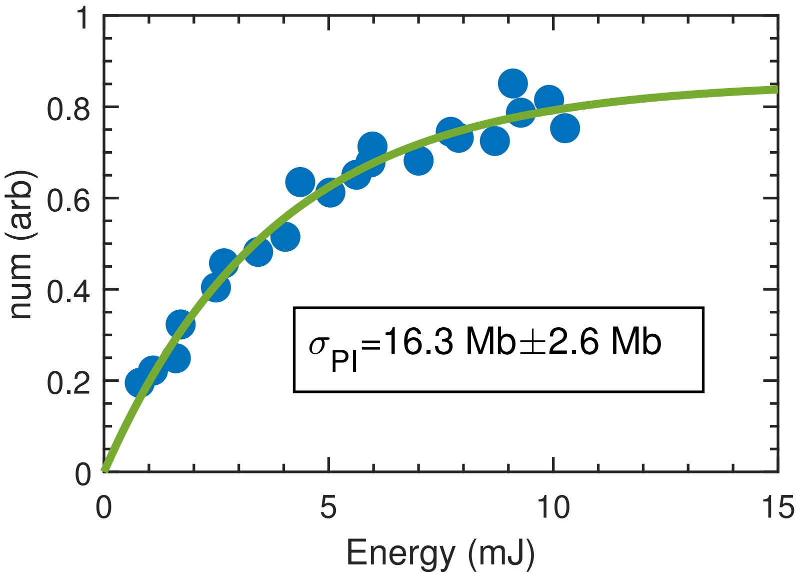

Figure 3.4 : Measurement of the photoionization cross section. The LIF signal we record is directly proportional to the number of ions within the region defined by s_x and s_z. We record this signal as a function of UV beam energy and fit the data to Eq. 3.16 to obtain σ_{PI}. For comparison, σ_{PI} was measured to be 10.7±1.7 Mb in [116].

- the mean local expansion velocity along the x-axis $v_{Exp,x}(x) = \vec{v}_{Exp} \cdot \hat{x}$.

In the next section I will show our setup for using the 'D2' line at 408 nm for laser cooling.

The LIF setup has been described in detail in papers[111] and in previous theses[93, 117, 118, 119]; here we briefly summarize this diagnostic tool.

In LIF imaging, a gaussian beam of 422 nm light ($1/e^2$ radii $w_y = 8.05$ mm and $w_z = 6.7$ mm) linearly polarized along y, detuned from the D1 resonance by δ, where δ is in rad/s, and propagating along the x axis (see Fig. 3.5) passes through a slit of width ℓ along the z axis before illuminating the central portion of the plasma (e.g., the ions with $-\ell/2 < z < \ell/2$). For most data in this thesis, ℓ is 2 mm while the gaussian width of the cloud along the z axis is $\sigma_z \sim 3$ mm. Thus, the maximum

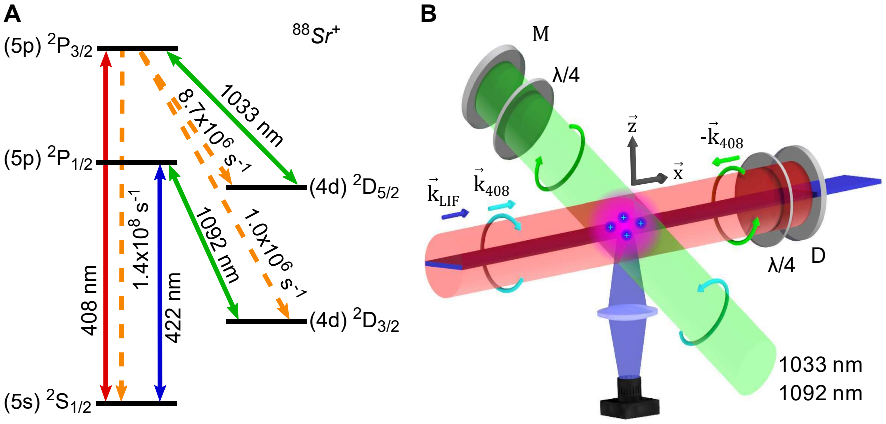

Figure 3.5 : (**A**): Level diagram for Sr$^+$ including all levels & transitions relevant for LIF and laser-cooling (solid lines) along with all relevant decay rates for laser cooling transitions (dashed orange lines). The D1 line at 422 nm is used for LIF while the D2 line at 408 nm is used for laser-cooling. The two D states are both long lived metastable states, hence the need for repump lasers (green). (**B**): Illustration of implementation of LIF and laser-cooling in our experiment. The LIF beam illuminates a slice of the plasma centered at $z = 0$; photons are then collected onto the camera below using a 1:1 relay system. The laser cooling beam is retro-reflected by a dichroic, which ensures the LIF beam is *not* retroreflected, and its polarization is switched from σ^+ (cyan arrow) to σ^- (green arrow) by a $\lambda/4$ waveplate. The two IR repump lasers at 1033 nm and 1092 nm are combined with an additional dichroic (not pictured); they are also set up in a cross-polarized counter-propagating configuration.

density variation along the z axis for the illuminated portion is $1 - e^{-(\ell/2)^2/(2\sigma_z^2)} = 5\%$. Having a low density variation along the unresolved axis is critical, as the ion temperature and the timescale for ion dynamics both depend on n ($T \propto n^{1/3}$ and $\omega_{pi}^{-1} \propto n^{-1/2}$), meaning that unresolved density variations could blur out ion dynamics. The maximum intensity variation along the z axis, meanwhile, is $1 - e^{-2(\ell/2)^2/w_z^2} = 4\%$.

The camera records the scattered photon pattern in a 1024 X 1024 pixel grid (pixel width d is 13μm). For an image with CCD gating time dt, the signal in an individual pixel at x, y is given by:

$$S(x,y,\delta) = Cl\gamma_0 n(x,y,0) d^2 f_{exc}(\delta,x,y) dt \tag{3.17}$$

where we are ignoring the variations of density and beam intensity along the z axis, $\gamma_0/2\pi = 20.3\,\text{MHz}$, and $C = f_{capt} C_{P\rightarrow S}$ where f_{capt} is the fraction of emitted photons that reach the camera and $C_{P\rightarrow S}$ is the photon to signal conversion factor (in practice, C is measured through an external density calibration, either to an absorption image[119] or to a DIH scan [93, 36]). The fraction of ions in the $^2\text{P}_{1/2}$ state $f_{exc}(\delta,x,y)$ stabilizes after a few $\gamma_0^{-1} = 7\,\text{ns}$; since we typically measure for $dt \geq 500\,\text{ns}$, we assume that $f_{exc}(\delta,x,y)$ is in its 'steady state' throughout imaging. For a laser linewidth of $\gamma_L/2\pi = 5\,\text{MHz}$ (which we measure by doing spectroscopy on the $5s$ to $6p$ ($J = 1/2$) Rb transition[120]) and a plasma temperature $T(x,y)$ we find

$$f_{exc}(\delta,x,y) = \left(\frac{\gamma_0 \pi s(y)}{4\sqrt{1+s(y)}}\right)\left[\frac{\gamma_{eff}/2\pi}{\gamma_{eff}^2/4+\delta^2} \circ \frac{\gamma_L/2\pi}{\gamma_L^2/4+\delta^2} \circ \frac{1}{\sqrt{2\pi}\sigma_f}\exp\left(-\frac{(\delta-\delta_c(x))^2}{2\sigma_f^2}\right)\right] \tag{3.18}$$

where $\gamma_{eff} = \gamma_0\sqrt{1+s(y)}$, $s(y) = I(y)/I_{sat}$ where $I(y)$ is the y dependent intensity of the x-propagating LIF laser, $\sigma_f = k\sigma_v = k\sqrt{k_B T(x,y)/m}$ is the doppler broadened linewidth, $\delta_c(x) = k v_{Exp,x}(x)$ is the additional doppler shift resulting from expansion along the laser axis ($v_{Exp,x} = \vec{v}_{Exp}\cdot\hat{x}$, see Eq. 2.21), and $\circ$ indicates a convolution[93].

To get the density of the cloud, we integrate S over δ; the term in the square brackets of Eq. 3.18 integrates to 1, as its just a convolution of normalized distribution functions, thus, after integration and rearranging of Eq. 3.17, we find;

$$n(x,y,0) = \frac{\int S(x,y,\delta)d\delta}{Cl\gamma_0 d^2\left(\frac{\gamma_0\pi s(y)}{4\sqrt{1+s(y)}}\right)} \tag{3.19}$$

Meanwhile, $T(x,y)$ and $v_{Exp,x}$ are obtained by examining the dependence of S on δ. We can see that

$$S(x,y,\delta) \propto \frac{\gamma_T/2\pi}{\gamma_T^2/4+\delta^2} \circ \frac{1}{\sqrt{2\pi}\sigma_f} \exp\left(-\frac{(\delta-\delta_c(x))^2}{2\sigma_f^2}\right) \tag{3.20}$$

where $\gamma_T = \gamma_{eff} + \gamma_L$ (the convolution of two lorentzians of width γ_a and γ_b is itself a lorentzian with width $\gamma_c = \gamma_a + \gamma_b$). This is an example of a 'Voigt profile', or a convolution of a gaussian and lorentzian. We can then fit $S(x,y,\delta)$ with $\sigma_f(x,y)$ and $\delta_c(x)$ as free parameters, giving measurements of $T(x,y)$ and $v_{Exp,x}$ respectively.

In practice, the signal within just one pixel is much too noisy to obtain an accurate fit; instead, we typically sum the signal over a rectangle of pixels with corners defined by $(x-w/2, y-h/2)$ and $(x+w/2, y+h/2)$ to get a measure of $T(x,y)$. However, there are limits to how large h and w can be; h must be small enough that the density does not vary too much over the analysis region, or else density dependent variations in T will be obscured, while w must be small enough for variations in δ_c to not affect the temperature measurement. For a region of width w, we find:

$$\langle v^2 \rangle = \int_{-\infty}^{\infty} dv \int_{-w/2}^{w/2} dx \frac{1}{\sqrt{2\pi}\sigma_f}\frac{1}{w} \exp\left[-\frac{(v-cx)^2}{2\sigma_v^2}\right] = \sigma_v^2 + \frac{c^2w^2}{12}. \tag{3.21}$$

where $c = t/(t^2+\tau_{Exp}^2)$ (Eq. 2.21). When fitting, we assume that $\langle v^2 \rangle = \sigma_v^2 = k_B T_i/m_i$, so any non-zero w results in an overestimation of the temperature $T_{meas}(x,y)$. We must choose w small enough for this error to be small; for the maximum value of $c = 1/2\tau_{Exp}$, we obtain

$$\epsilon = \frac{T_{meas}-T_{real}}{T_{meas}} = \frac{1}{12}\frac{c^2w^2}{\sigma_v^2} = \frac{1}{48}\frac{\left(\frac{k_BT_{e0}}{m_i\sigma_0^2}\right)w^2}{\left(\frac{k_BT_i}{m_i}\right)} = \frac{1}{48}\frac{T_{e0}}{T_i}\frac{w^2}{\sigma_0^2} \tag{3.22}$$

where we use Eq. 2.14. For the data presented in chapter 5, $T_{e0} = 15\,\mathrm{K}$, $\sigma_{0x} = 2.4\,\mathrm{mm}$, and $w = 260\mu\mathrm{m}$, giving an expected error of at most 7% for the lowest measured value of T_i of $50\,\mathrm{mK}$ (this actually overestimates the error, since the expansion of the cloud is itself slowed during laser cooling, see Sec. 5.4). This effect is also illustrated in Fig. 3.6.

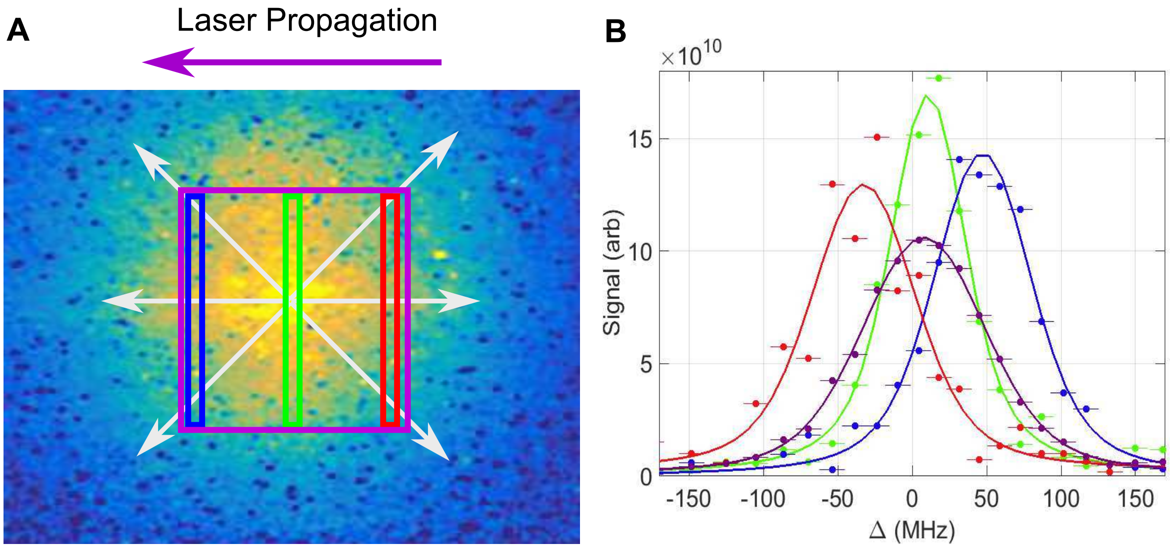

Figure 3.6 : Illustration of ‘expansion broadening’. (**A**): Plasma image $n(x, y, 0)$ with various color-coded regions for subsequent calculation of $v_{Exp,x}(x)$ and $T(x, y)$. The white arrows represent radially directed expansion velocity v_{Exp}. (**B**): Spectra from each region. Clearly the wide region (purple) appears to be much hotter (broader) than the narrower regions; this is due to ‘expansion broadening’ (Eq. 3.22). The ‘skinnier’ regions, in contrast, more accurately reflect the local temperature $T(x, y)$. The centers of these regions correspond to $v_{Exp,x}(x)/\lambda$. Adapted from[93]

3.4 Laser Cooling Setup

In alkali-atoms, cross-polarized counter-propagating lasers tuned to the ‘D2’ line are commonly used for laser-cooling [90], since the $J = 1/2 \rightarrow J' = 3/2$ level structure results in scattering more photons from the preferred laser (see Fig. 3.7). We follow this approach for our Sr$^+$ cooling scheme.

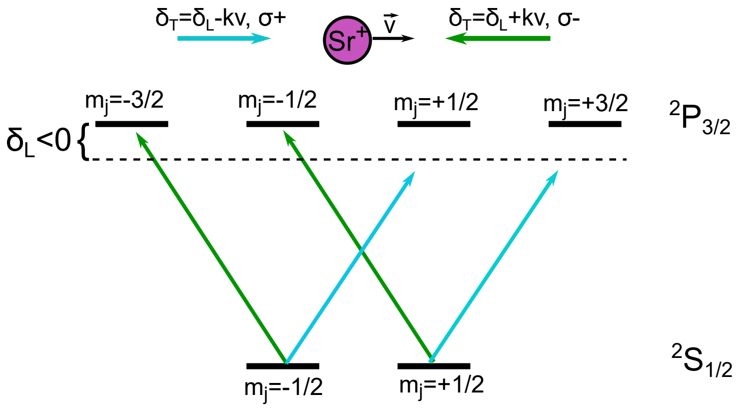

Figure 3.7 : Cycling Transition Schematic. An atom moving rightward with $m_j = -1/2$ is more likely to scatter photons from the σ^- laser, operating on the $m_j = -1/2 \rightarrow m_{j'} = -3/2$ transition, than the σ^+ laser, operating on the transition $m_j = -1/2 \rightarrow m_{j'} = +1/2$ transition, due to the fact that the σ^- laser is Doppler shifted closer to resonance while the σ^+ laser is Doppler shifted away from resonance. This is similar to the situation in 2-level laser cooling. However, the Clebsch-Gordon coefficient for $m_j = -1/2 \rightarrow m_{j'} = +1/2$ transitions is $1/\sqrt{3}$ while for $m_j = -1/2 \rightarrow m_{j'} = -3/2$ transitions it is 1, further inhibiting scattering from the 'incorrect' laser and making it even more likely that the ion remains in the 'cycling' transition. This enhancement makes the D2 line preferable for laser cooling in alkali-like systems.

However, as we can see from Fig. 3.5A, there are two additional states that an ion in the ^{2}P$_{3/2}$ level can decay to: 1 in 17 scattering events will leave the ion in the ^{2}D$_{5/2}$ state, while 1 in 150 events will leave the ion in the ^{2}D$_{3/2}$ state, both of which are long-lived ($\gtrsim$ 100 ms) metastable states. In order to change an ion's velocity by $v \sim 7\,\mathrm{m/s}$ (equivalent to v_T for $T = 500\,\mathrm{mK}$), an ion must scatter at least 600 photons in a timeframe $t \sim \tau_{exp} \lesssim 100\mu$s (see Sec. 2.3), therefore, we need to repump out of both of these states. In order to ensure that we address all Zeeman sublevels of the D states, we also set up these lasers in a counter-propagating cross-polarized configuration.

In addition, it is clear that there is a Λ configuration between the ^{2}S$_{1/2}$, ^{2}P$_{3/2}$, and

$^2\mathrm{D}_{5/2}$ states, which could in principle lead to electro-magnetic induced transparencies due to the existence of a 'dark state' $|\psi\rangle = a|^2\mathrm{S}_{1/2}\rangle + b\exp[-i\theta]|\mathrm{D}_{5/2}\rangle$ that is an eigenstate of the combined atom-light Hamiltonian; ions that wind up in this state will no longer scatter photons. We find that this has a very small effect on the effectiveness of laser-cooling in our system for two reasons: First, dark states only exist for a very narrow-band of velocities and, second, the ions are highly collisional, meaning that ions do not remain within that narrow band for long enough to be driven into the dark state. This is discussed in more detail in Chapter 4.

For laser-cooling to be effective, the intensity of the 408 nm light must be on the order of $I_{sat} = 2\pi^2\hbar c\gamma_{SP}/3\lambda^3 = 43.1\,\mathrm{mW/cm^2}$ throughout the plasma ($\gamma_{SP} = 1.41 \times 10^8\,\mathrm{s^{-1}}$). We expand a 1 W beam produced by a Toptica TA-SHG pro laser to a $1/e^2$ radius of 9 mm, giving an intensity of $785.9\,\mathrm{mW/cm^2}$, more than enough to saturate the transition, even if we split the power into three beams to cool in all dimensions (though, as we will see in Chapter 4, this is not necessary for cooling all degrees of freedom). In practice, we typically attenuate the beam using an AOM with a voltage controlled attenuator to $I = 100\,\mathrm{mW/cm^2}$ and thus $s_0 = 2.3$.

The repump lasers must be broad enough to repump all of the ions; for the 1033 nm transition, the Doppler-broadened linewidth for a plasma with $v_T \sim 7\,\mathrm{m/s}$ is $\sigma_f/2\pi = 6.3\,\mathrm{MHz}$ while the natural linewidth $\gamma_{1033}/2\pi$ is only 1.4 MHz, thus, we must broaden the effective linewidth. The most straightforward way of doing this is through power-broadening, setting $\gamma_{tot} = \sqrt{1+s_{0,1033}}\gamma_{1033} = 2f_{dopp}$ gives $s_{0,1033} = 80$. For this transition, $I_{sat} = 0.164\,\mathrm{mW/cm^2}$, meaning we need a 1033 nm intensity of $80I_{sat}$=$13.12\,\mathrm{mW/cm^2}$. We obtain 100 mW of 1033 nm power from a Toptica DL Pro laser, which, for a width of 9 mm gives $I = 78\,\mathrm{mW/cm^2}$, which is enough to broaden the linewidth to 30 MHz; easily enough to repump all of the ions. Similar calculations can be made for the 1092 nm transition; the 100 mW that we obtain from a taper-amplifier seeded by a Sacher-Diode laser is also enough to broaden that transition sufficiently.

3.4.1 Transfer Locking

We need to control the frequency of the laser-cooling and repump lasers. To do this, we employ the technique of transfer locking [121] illustrated in Fig. 3.8. In this technique, the stability of one laser (in this case, the pre-doubled 922 nm laser that is stabilized by the Sr atom lock for 461 nm) is used to stabilize the length of a Fabry-Perot cavity through an offset voltage that is summed with a triangle wave ramp; by changing this offset to ensure that the 922 nm transmission peak remains at the same location in the cavity ramp, the mean length of the cavity is stabilized. Other lasers that are co-propagating with the stable laser into the cavity can then be stabilized by locking the location of their peaks in the stabilized cavity length-ramp; this is accomplished through feedback to frequency controlling PZTs within these lasers (in this case, the repump lasers and the pre-doubled 816 nm light from the TA-SHG pro cooling laser).

One unique aspect of our transfer lock scheme is that it is all done digitally using a labVIEW program. Using an NI-DAQ card, the program reads the ramp voltage and the transmission signals from each laser's photodiode and then determines the location of each laser's transmission peak using a peak detection algorithm. These peak locations are compared to user-controlled setpoints, and a PID locking algorithm sends out PZT voltages, via the same NI-DAQ card, to the ramp and the laser-cooling and repump lasers in order to minimize the difference.

In order to lock the lasers where we want, we need to determine what setpoint

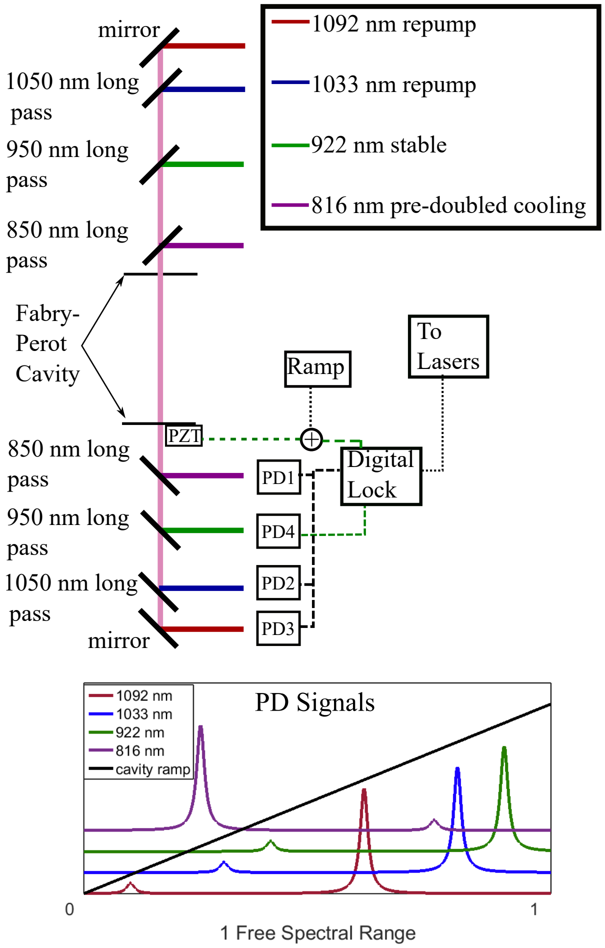

Figure 3.8 : Transfer cavity “Superlock” schematic. The three ‘unstable’ cooling & repump beams are coaligned with a stable 922 nm beam and aligned into a Fabry-Perot Cavity, whose length is scanned by a linear ramp applied to a PZT. The mean length throughout the ramp is stabilized by the stable laser through a feedback voltage which keeps the 922 nm transmission peak at the same point in the ramp; this voltage is summed to the ramp voltage. The previously ‘unstable’ lasers are stabilized through feedback to frequency controlling PZTs within the lasers; the feedback keeps the transmission peaks at the same point in the, now stable, ramp of the Fabry-Perot cavity length. The feedback voltages are all determined by a ‘Digital Lock’ (aka a LabVIEW program) that runs a PID locking algorithm with calculates the locations of the transmission peaks for each laser and compares them to ‘setpoint’ locations for each laser; the digital PID lock minimizes the differences between these quantities.

for each laser corresponds to ‘on-resonance’ for the given transition. The cavity free spectral range is 1.5 GHz; using this along with measuring the voltage difference between successive peaks, we can detune the laser with $\sim 1\,\mathrm{MHz}$ accuracy. Finding the resonance can most easily be done using the UNP itself. To find the 408 nm resonance, we can do the following

- Choose a 408 nm setpoint
- Block the repump lasers
- Create a UNP
- Turn on the 408 nm laser for $\sim 1\mu$s, long enough for ions to decay into D states if the 408 nm is near resonance
- Image the UNP with on resonance 422 nm light; the signal will be *minimized* if the 408 nm light is on resonance, as this is when the D states are most efficiently populated.
- Change the 408 nm setpoint and repeat

An example of such a scan is shown in Fig. 3.9. Once the 408 nm resonance is found, the repumper resonances can also be found by doing the following (see Fig. 3.10)

- Lock the 408 nm to resonance
- Choose a repump setpoint
- Create a UNP
- Turn on the 408 nm laser for a few μs; long enough for ions to decay into the D states if the repumpers are not on resonance.

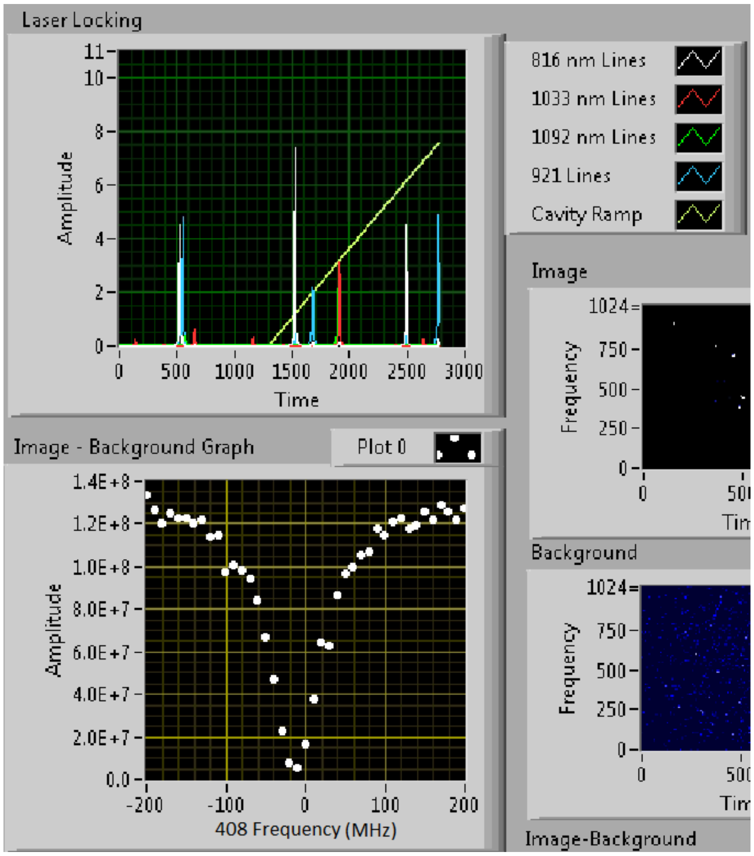

Figure 3.9 : Screenshot of superlock control software during a scan over the 408 nm laser frequency for finding the resonance. The signal in 'image-background graph' is proportional to the total 422 nm photons scattered after the 408 nm laser is on for $\sim 1\mu$s; the signal is minimized when the 408 nm is on resonance since this leads to the most ions being transferred to unobserved D states. The 408 nm is scanned by moving the setpoint for the 408 nm transmission peak (the larger of the white peaks in the 'Laser Locking' plot above). Based on this data, we can clearly see that, in this instance, our assumption of 'zero' detuning (where the minimum occurs) was off by about +20 MHz; this tells us how much we need to move the 'on-resonance' set point. This knowledge of the on-resonance setpoint, along with the conversion between frequency and 'time' which we can get from our knowledge of the Free-Spectral range of the cavity (1.5 GHz), allows us to detune the 408 nm with 1 MHz resolution.

- Image the UNP with on resonance 422 nm light; the signal will be *maximized* if the repumper light is on resonance, as this is when ions that decay to D states

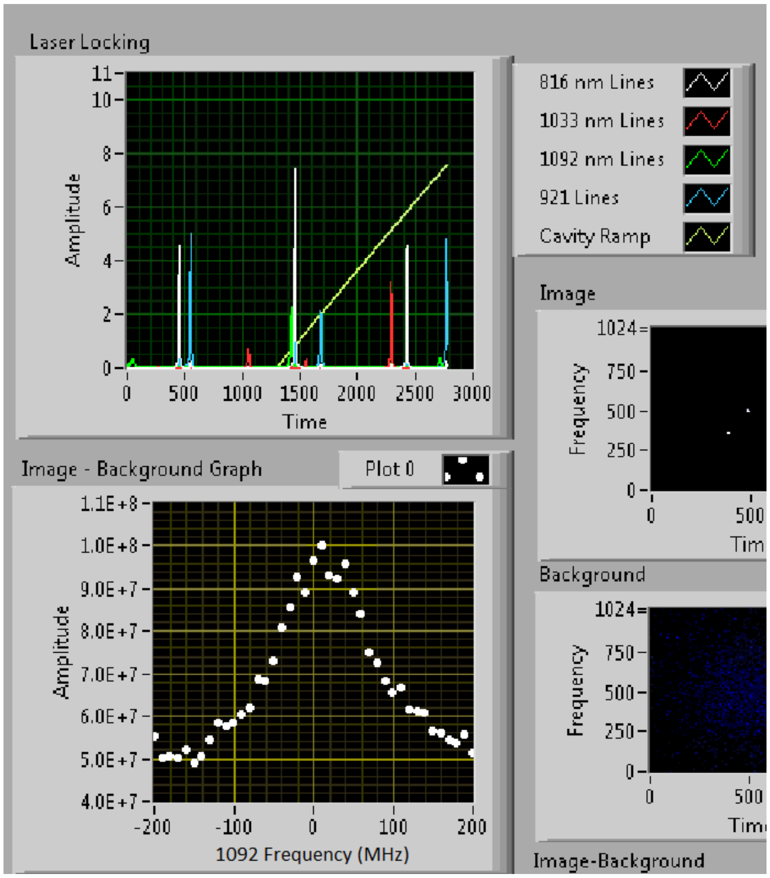

Figure 3.10 : Screenshot of superlock control software during a scan over the 1092 nm laser-frequency. Signal is now maximized on resonance, as this is when the most ions are repumped out of the D state, which is ‘dark’ to the LIF light. The 1092 nm laser is scanned by moving the setpoint of its transmission peak (the largest ‘green’ peak in the plot above). From here, we see that our assumption of ‘zero’ detuning was off by about -10 MHz. This allows us to find the 1092 nm ‘on resonance’ setpoint and detune with high resolution in the same way as we do for the 408 nm (see Fig. 3.9 caption).

are most effectively repumped to the imageable S state

- Change the repump setpoint and repeat

This procedure reproducibly measures the setpoints of the superlock that correspond to the Sr^+ resonances.

3.5 Summary

Using well established techniques of atom trapping and photoionization, we can make UNPs consisting of $\sim 10^8$ Sr^+ ions. In addition, trapping in the magnetic trap allows us the ability to easily create plasmas with an initially non-gaussian density profile (see Eq. 3.9), should that be desired. However, for the data presented in this thesis, we typically allow the atoms to expand to the point where the profile is well described by a gaussian.

We choose to make UNPs of alkaline earth ions primarily because of their alkali-like level structure, which provides optically accessible transitions allowing for the application of standard atomic physics tools like spectroscopy and laser-cooling. Using LIF on the D1 line at 422 nm, we are able to obtain the density profile $n(x, y, z = 0)$, temperature profile $T_i(x, y, z = 0)$, and the x-component of the expansion velocity $v_{Exp,x}(x, y, z = 0)$ in a central sheet of the plasma.

In this thesis, we report on the use of the D2 line at 408 nm for laser-cooling of the ions. The cooling laser, along with two necessary repump lasers, are locked digitally to a transfer-lock stabilized by the principal Sr atom transition. One of the repumper lasers forms a Λ transition which couples the $\mathrm{S}_{1/2}$ and $\mathrm{D}_{5/2}$ states together directly which may, in principle, inhibit laser-cooling through population of a 'dark state'. However, there is reason to believe that the collisionality of the plasma may prevent population of the dark state. The rapid collisions and hydrodynamic expansion may also have other, less predictable, impacts on laser-cooling. In order to learn more about these impacts, we wrote a computer code to simulate laser-cooling in an expanding plasma; this code is the subject of the next chapter.

Chapter 4

A Combined Quantum Trajectories and Molecular Dynamics Code for Simulation of Laser-Coupled Collisional Systems

In this chapter, we introduce a code that implements a quantum trajectories (QT) approach within a molecular dynamics (MD) simulation. The aim is to simulate the wavefunction evolution and the effect of optical forces that result from the introduction of lasers coupling internal states of particles in a collisional system. In contrast to collisionless systems, in which the quantum dynamics of multi-level laser-driven particles with spontaneous emission are determined by solving the optical Bloch equations (OBEs), in sufficiently collisional systems the velocities of the particles change on timescales comparable to those of the laser-induced wavefunction evolution. These transient velocity changes can cause the time-averaged velocity dependence of the quantum state to differ from that expected from the steady-state OBE solution. Using MD, the velocity changes due to collisions can be accurately tracked while the wavefunction evolution and the optical forces are determined using QT.

We apply this simulation to the problem of laser-cooling in a UNP. Features that we investigate here include rapid thermalization between cooled and un-cooled dimensions for anisotropic laser cooling and the suppression of electromagnetically induced transparencies through rapid velocity-changing collisions. We also demonstrate how this code can be used to simulate cooling in an *expanding* ultracold neutral plasma system.

More generally, this code can be used for any study in which laser manipulation of the quantum state of a particle in a collisional system is relevant. For example, the code can be used to study how spin becomes correlated with velocity when ions in the $J = 1/2$ ground state are coupled to a $J' = 1/2$ excited state through red-detuned counter-propagating cross-polarized lasers. The utility of this aspect of the code will be discussed in greater detail in Chapter 7.

4.1 Motivation: Coupling of Motion and Internal States Through Atom-Laser Interactions

Over the past half-century, the field of atomic physics has benefited greatly from the development of lasers for manipulating the internal quantum states of the constituent particles of gaseous systems. Using lasers to couple the external momentum and the internal state of a particle is what gives rise to laser-cooling and forms the basis for most atom interferometry techniques. In UNPs, this coupling is used for spectroscopic thermometry (see Sec. 3.3), to develop spin-velocity correlations for use in measuring velocity relaxation rates[40, 39] (Ch. 7), and for the laser-cooling described in this thesis.

The evolution of the quantum state, along with the induced optical forces, in these experiments is typically described by the steady-state solution of the optical Bloch equations (OBEs) resulting from the master equation, which describes the evolution of quantum systems with both coupling and dissipation (in this case, spontaneous emission)[122]. For example, when the ground and excited states of a system are coupled by red detuned light in an optical-molasses scheme, the resultant velocity-dependent steady-state OBE solutions can be used to obtain the velocity dependent force profile $F(v)$. The time it takes for the OBEs to converge to a steady state solution, t_{conv}, will depend on the natural decay rates and Rabi frequencies of the laser-coupled system. If the system is collisionless and we are concerned with timescales longer than t_{conv}, the steady state OBE solutions will work for describing the behavior of the system.

However, this is not the case in a collisional system. Consider a feature like electromagnetically induced transparency (EIT) [123], which can take a long time (t_{EIT}) to develop (Sec. 4.4.5) and manifests as a 'hole' of width δv in $P_e(v)$, the probability of being in an 'excited' state. If collisions are rapid and strong enough such that they induce velocity changes $> \delta v$ on a timescale $< t_{EIT}$, then this feature is 'washed out' due to collisions. A quantum trajectories (QT) approach [124, 125], which correctly treats the short-time wave-function dynamics, combined with a technique for tracking collisionally induced changes in velocity, is a good approach for collisional systems.

In systems with long range interactions, such as plasmas, the dynamics of a single particle is coupled to that of all nearby particles, and therefore trajectories of external states of the constituent particles must be tracked *simultaneously*. Moreover, if interactions are strong enough to result in *correlations* between position and velocities of nearby particles, as is the case for strongly coupled plasmas, a standard Boltzmann type operator for describing collisions will not suffice. Molecular dynamics (MD) simulations are typically used in this case, thus motivating the approach outlined in this chapter for dealing with the problem of laser-coupling in a collisional system, which is to implement a QT approach within a MD simulation, which we call a 'MDQT' code.

One particular system that is of interest as a candidate for laser-cooling, and is also highly collisional, is a UNP[61, 72, 73]. Thus, here we focus primarily on the application of this code to the problem of 1D laser-cooling in a UNP.

The rest of this chapter is structured as follows. First, in section 4.2, we give a brief overview of the description of laser-forces in a collisionless system and then an example of how collisions can obscure the effect of laser-cooling. Next, in Secs. 4.3 and 4.4 we describe the methods of molecular dynamics and quantum trajectories simulation, before discussing our MDQT code that combines the two in Sec. 4.4.6. In Sec. 4.5, we use our MDQT code to demonstrate collisional suppression of dark state formation. Then, in Sec. 4.6 we show the results from an MDQT simulation of laser-cooling of a UNP of Sr$^+$ ions interacting via screened Coulomb interactions, and observe collisional redistribution between cooled and uncooled axes. In Sec. 4.6.2 we discuss simulations of UNP laser-cooling in an accelerating frame designed to mimic expansion. Finally, in Sec. 4.7 we conclude with a discussion about potential applications of this simulation as a component of an accurate multi-scale model of an expanding laser-cooled UNP.

4.2 Laser Cooling in a Collisionless Gas

To make the impact of collisions on laser-cooling a bit clearer, let's first consider how cooling works in a collisionless system. The velocity-dependent force profile can be determined by solving the Optical Bloch Equations (OBEs) with the velocity dependent Doppler-shift as an additional 'detuning' term, yielding a velocity-dependent density matrix $\hat{\rho}(v)$. From there, the force profile,

$$\langle F(v)\rangle = \mathrm{Tr}\left(\hat{\rho}(v)\frac{dp}{dt}\right) = \mathrm{Tr}\left(-\hat{\rho}(v)\left[\hat{\nabla},\hat{H}\right]\right), \tag{4.1}$$

can be calculated.

4.2.1 Example: Optical-Molasses in a 2 Level System

We consider a two level system (ground state $|1\rangle$ and excited state $|2\rangle$) illuminated by a monochromatic electromagnetic field of form $\vec{E}(z) = \mathcal{E}e^{i(\nu t-kz)} + \mathcal{E}e^{-i(\nu t-kz)}$ (we are assuming that the beam size $w \gg L$ where L is the system size, typical for molasses cooling). The field interacts with the electric dipole moment of the atom, given by operator $\hat{d} = e\hat{r}$, which for a two level system is simply $\hat{d} = |1\rangle\langle 2|\mu + |1\rangle\langle 2|\mu^*$ where $\mu = \langle 1|e\hat{r}|2\rangle$, through the electric dipole energy term $\vec{d}\cdot\vec{E}$. The full Hamiltonian is therefore

$$\hat{H} = \hbar\omega|2\rangle\langle 2| - (|1\rangle\langle 2|\mu + |2\rangle\langle 1|\mu^*) \cdot \left(\mathcal{E}e^{i(\nu t-kz)} + \mathcal{E}e^{-i(\nu t-kz)}\right) \tag{4.2}$$

where $\hbar\omega$ is the energy difference between $|1\rangle$ and $|2\rangle$.

If we use a unitary transformation of form $\hat{U} = \exp\left[-i\nu|2\rangle\langle 2|\right]$, apply the rotating wave approximation (where time varying terms of order ν are ignored), and define $\Omega = 2\mathcal{E}\mu/\hbar$, we recover the well known atom-light coupling hamiltonian $H = -\hbar\delta|2\rangle\langle 2| - \frac{\hbar\Omega e^{ikz}}{2}|2\rangle\langle 1| + \frac{\hbar\Omega e^{-ikz}}{2}|1\rangle\langle 2|$, where $\delta = \nu - \omega$ is the detuning of the laser frequency from the resonance of the transition. For this Hamiltonian, Eq. 4.1 becomes

$$\langle\vec{F}(\vec{v},\vec{k})\rangle = \frac{\hbar\vec{k}}{2}|\Omega|^2\,\mathrm{Im}\left(\frac{\rho_{21}(v)}{\Omega/2}\right) \approx \frac{\hbar\vec{k}}{2}\frac{\gamma|\Omega|^2}{\gamma^2+(\delta-kv)^2} \approx \frac{\hbar\vec{k}}{2}\frac{\gamma|\Omega|^2}{\gamma^2+\delta^2}\left(1+\frac{2\delta\vec{k}\cdot\vec{v}}{\gamma^2+\delta^2}\right) \tag{4.3}$$

where γ is the natural linewidth of the transition and in the last two steps we assume that the saturation parameter $s_0 \ll 1$[90], which leads to the solution $\mathrm{Im}\left(\rho_{21}(v)/(\Omega/2)\right) = \gamma/\left(\gamma^2+(\delta-kv)^2\right)$, and that $v < \gamma/k$. Summing the forces from two counter-propagating beams of equal detuning gives

$$\langle \vec{F}_{OM}(\vec{v}) \rangle = \langle \vec{F}(\vec{v},\vec{k}) \rangle + \langle \vec{F}(\vec{v},-\vec{k}) \rangle \approx \frac{2\hbar\gamma|\Omega|^2\delta}{\left(\gamma^2+\delta^2\right)^2}|\vec{v}\cdot\vec{k}|\vec{k}. \tag{4.4}$$

For velocity along the beam axis x, the force is of the form $F_x = -\beta v_x$ when $\delta < 0$, as expected for optical-molasses given the approximations we've made. For finite velocity and for multi-level atoms, the force profile is a little more complicated (see Fig. 4.1), but it can still be derived by solving the OBEs for $\hat{\rho}$ and using Eq. 4.1.

4.2.2 Evolving the Distribution Function Given a Force Profile

In a collisionless system, once the force profile is calculated, the velocity distribution function $f(v_x,t)$ can also be obtained by solving $\dot{v}(t) = F_x(v_x)/m$. Using this solution, one can find the mapping $v_f = g(v_i,t)$, where g is defined such that a particle with velocity v_i at $t = 0$ will have velocity v_f at time t. The value of $f(v_f,t)$ is thus proportional to $f(v_i,0) = f(g^{-1}(v_f,t),0)$:

$$f(v,t) = \frac{f(g^{-1}(v,t),0)}{\int dv f(g^{-1}(v,t),0)} \tag{4.5}$$

where the term in the denominator ensures that the distribution function remains normalized.

For example, take the optical molasses solution $F = -\beta v$. In this case, the differential equation for v can easily be solved for $v_f(t) = g(v_i,t) = v_i \exp\left[-\beta t/m\right]$. If the distribution is initially gaussian ($f(v,0) = \exp\left[-v^2/(2\sigma_0^2)\right]/\sqrt{2\pi\sigma_0^2}$), we have

$$f(v,t) = \frac{f(ve^{\beta t/m},0)}{\int dv f(ve^{\beta t/m},0)} = \sqrt{\frac{e^{2\beta t/m}}{2\pi\sigma_0^2}}\exp\left[\frac{-v^2e^{2\beta t/m}}{2\sigma_0^2}\right] = \frac{\exp[-v^2/2\sigma(t)^2]}{\sqrt{2\pi\sigma(t)^2}} \tag{4.6}$$

where $\sigma(t) = \sigma_0/\sqrt{e^{2\beta t/m}}$. Setting $\sigma(t) = \sqrt{k_BT(t)/m}$, we find $T(t) = T_0\exp[-2\beta t/m]$. This is the expected result for cooling using a damping force.

4.2.3 Impact of Collisional Thermalization on Observation of Laser-Cooling

Numerical differential-equation solvers are typically employed to obtain $g(v,t)$ for a more complicated force profile. We illustrate this for the 'full' laser cooling force (e.g. where we do not make the $v \ll \gamma/k$ approximation) shown in Fig. 4.1A for a 2-level system corresponding to the Sr$^+$ D2 line ($\gamma/2\pi = 22\,\mathrm{MHz}$, λ=408 nm) with $\delta = 2\gamma/3$ and $s_0 = 0.7$. In Fig. 4.1B, we plot $f(v,0)$, the initial velocity distribution for $T = 750\,\mathrm{mK}$ in blue, along with $f(v,5\mu s)$ in red, which is calculated from Eq. 4.5 and a numerical solution for $g(v,t)$. Comparing these two curves, the impact of the laser-cooling is obvious, and would be relatively easy to see with either spectroscopic or time of flight techniques. Observing a distribution like this is typically how laser-cooling of new systems is first demonstrated, such as in the first direct laser-cooling of molecules shown in Fig. 4.1C [80].

However, let's consider what happens after this system thermalizes. After thermalization, energy conservation requires that the distribution relaxes to a gaussian with a width defined by $\sigma^2 = \int dvv^2 f(v,t = 5\mu s)$. This is plotted in yellow in Fig. 4.1. Now, the difference between the cooled and un-cooled distributions is much less obvious; if the technique employed to measure $f(v)$ does not have very good resolution, the two curves will be basically indistinguishable, making this standard 'first' measurement of laser-cooling much more difficult [126].

Of course, in a collisional system, thermalization happens throughout the cooling process. To first order (ignoring any effect that the collisionality has on the rate of removal of energy during the 5μs laser cooling process) we can state that $f(v,t = 5\mu s)$ after cooling in a *rapidly* collisional system (one where the thermalization timescale is much faster than the cooling timescale) will match the yellow curve in Fig. 4.1, thus

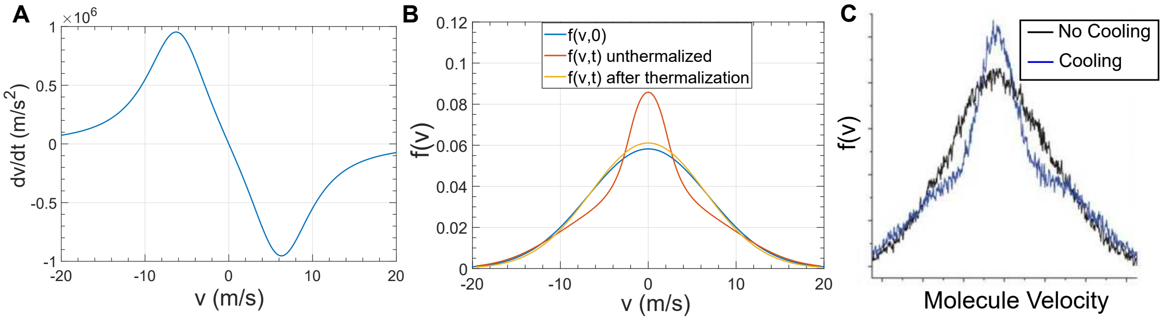

Figure 4.1 : (**A**): Force profile $F(v)/m$ from optical molasses in a two level system with γ and k corresponding to the D2 line of the Sr^+ ion with $\delta = -2\gamma/3$ and $s_0 = 0.7$. (**B**): Distributions before and after the application of $F(v)$ for $5\,\mu$s. While the difference between the distributions are clear without thermalization, if the system is allowed to collisionally thermalize, the distinctions become much less clear. (**C**): First observation of direct laser cooling of a diatomic molecule [80]. The profile is similar to the 'unthermalized' cooled cloud in **B**, providing clear evidence of laser-cooling. If, instead, the molecules collisionally thermalized, either throughout the cooling process or else sometime before the measurement, the distribution would be similar to the yellow curve in **B**, and deviations due to laser cooling would be much more difficult to measure. UNPs are highly collisional, so this avenue to proving the effect of laser-cooling of a UNP by observing a non-thermalized distribution will not be available.

making observation of the effect of the cooling force much more challenging in systems like UNPs. We are also assuming a 1D system here; for a collisional 3D system with two uncooled axes, the blue and yellow curves would be even more similar as heat flows from the uncooled axes into the cooled dimension.

The uncertainty of collisional redistribution rates in strongly coupled plasma systems [60, 46, 40], along with uncertainties in how the collisions affect $\langle F(v) \rangle$ itself, motivated our development of the MDQT code for simulating laser-cooling in a collisional system.

4.3 Molecular Dynamics Simulation

In molecular dynamics (MD) simulations, one solves the equations of motion of an N body system with an interaction potential typically given by $V(\boldsymbol{r}_1, \boldsymbol{r}_2) = V(|\boldsymbol{r}_1 - \boldsymbol{r}_2|) = V(\boldsymbol{r}_{12})$. This is done by propagating Hamilton's equations of motion:

$$H = \sum_i \frac{p_i^2}{2m} + \frac{1}{2} \sum_{i \neq j} V(\boldsymbol{r}_{ij}) \tag{4.7}$$

$$\dot{p_i} = -\partial_{r_i} H \tag{4.8}$$

$$\dot{r_i} = \partial_{p_i} H = p_i/m \tag{4.9}$$

throughout time.

These techniques [127] were first applied to hard-spheres[128] and liquids interacting through the standard Lennard-Jones potential [129, 130], before being applied in plasmas [131]. Plasmas are a very simple system to simulate in MD, as the mean interparticle spacing a is the only relevant length scale, whereas some other systems (e.g. Lennard-Jones liquids) present additional length-scales. This is what allows the Hamiltonian for a plasma system to be easily written in scaled units, as in the YOCP model described in Eq. 2.6, which is what we use in our MD code.

Periodic boundary conditions (PBC) are implemented to deal with particles that 'escape' from the box. For example, if, during a timestep, the x coordinate of a particle becomes $x > L$, where $L = (4\pi N/3)^{1/3}$ is the length of the box, its position is adjusted to become $x' = x - L$.

MD simulations are designed to deal with N-particle subsets of a much larger system, so the simulation must somehow take the existence of the 'surrounding' particles into account. One way to do this is through the 'minimum image convention' (MIC). Consider the interaction between particles i and j at locations (dx,y,z) and

$(L-dx,\, y,\, z)$, respectively, where $dx \ll L$. In MIC, the force from j on i is calculated as if the location of j were $(-dx,y,z)$, and the force from i on j is calculated as if the location of i were $(L+dx,y,z)$. These 'new' locations are actually the locations of the nearest 'image' of j and i, respectively, where the 'images' come from transpositions of the original simulation box by $\pm L$ in any dimension. In general, the effective interaction potential between particles j and i is $V_{ij}(|r_i - r'_j|)$ where r'_j is $(x_j + L\times\text{round}(\frac{x_i-x_j}{L}),y_j + L\times\text{round}(\frac{y_i-y_j}{L}),z_j + L\times\text{round}(\frac{z_i-z_j}{L}))$. This is illustrated in Fig. 4.2.

When using MIC, it is important that the system size be large enough such that the force on a charge due to charges other than the nearest image charge is negligible. For a YOCP system, this depends strongly on κ due to the $\exp[-\kappa r]$ term. In general, the condition for MIC validity can be written as $L\kappa \gg 1$. In [132], convergence in the observed melting point of a Yukawa solid was demonstrated for a number of particles $N_{conv} \approx 435/\kappa^3$.

We have written an MD code that implements PBC and MIC using a timestep $dt = 0.0035\omega_{pi}^{-1}$ with initial conditions $\{p_i\} = 0$ and random $\{r_i\}$, characteristic of a UNP immediately after photoionization. This is what we used to obtain the MD curves of DIH shown in Fig. 2.5. We want to adapt this code to simulate laser-cooling of the gas during and after the DIH process. To laser cool effectively, τ_{Exp} (see Eq. 2.14) must be maximized. Therefore, we will choose the highest possible κ allowed under the restriction that we want three-body recombination to be negligible. Using $\kappa = \sqrt{3\Gamma_e}$ and the TBR limit of $\Gamma_e \leq 0.1$ (Sec. 2.4), this gives $\kappa \leq 0.55$. To give a little bit of 'headroom', we perform the simulations for $\kappa \approx 0.5$ and thus $N_{conv} \approx 3500$ [110].

Our approach for adding laser-cooling to the simulation uses a technique called

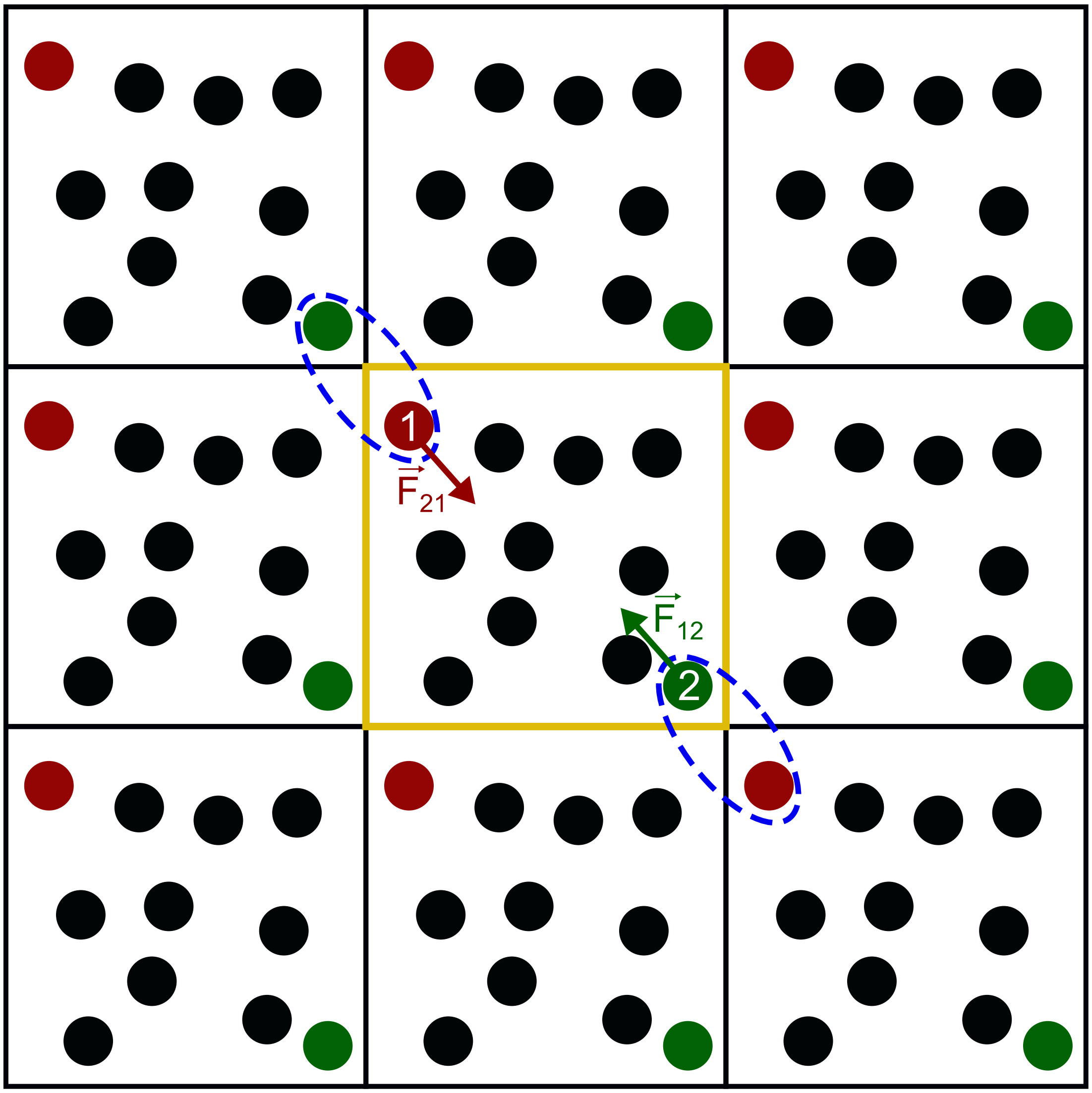

Figure 4.2 : Illustration of minimum image convention in 2D. The 'actual' simulation region is the yellow square in the center, while the 'image' charges are in the surrounding squares. In the *full* image convention, to calculate the force of charge 2 (green) on charge 1(red), one would sum the forces from *all* green charges in the figure. In the *minimum* image convention, which we use for our MD simulations, only the force of the closest green charge (which could be either the actual charge or one of the images) on the red charge is calculated. The closest pairs for this particular example are indicated in a blue ellipse, and both $\vec{F}_{21}$ and $\vec{F}_{12}$ are shown.

quantum trajectories (QT). It is also possible to simulate atom-laser coupling by keeping track of a density matrix for each particle and solving the full OBEs [133], however, the QT approach only requires the storage of a particle's wavefunction, taking up less memory than the density matrix.

4.4 Quantum Trajectories

4.4.1 Introduction

The method of quantum trajectories was developed by the group of Dalibard, Castin, and Molmer [124] and, simultaneously, by H. J. Carmichael [125], and is discussed in detail in Chapter 6 of [122], which we will follow closely here. The basic approach is to identify an equivalence between the master equation, which describes the time evolution of a density matrix ρ_s in an open quantum system, and the evolution of a wavefunction $|\psi\rangle$ under a *non-Hermitian* Hamiltonian which can also, during any timestep, 'jump' via spontaneous emission to 'ground states' $|g\rangle$ with a probability determined by the current expectation value for the 'excited state' population $|\langle e|\psi\rangle|^2$.

The master equation for the evolution of a pure quantum state, in its most general form, can be written

$$\frac{d\rho_s}{dt} = \frac{1}{i\hbar}\left[H_s, \rho_s\right] - \sum_k \frac{\gamma_k}{2}\left(c_k^\dagger c_k \rho_s + \rho_s c_k^\dagger c_k - 2 c_k \rho_s c_k^\dagger\right) \tag{4.10}$$

where c_k are "decay jump" operators with associated rate γ_k (e.g. $c_1 = |1\rangle\langle 2|$ implies that atoms in state $|2\rangle$ decay to $|1\rangle$ at a rate γ_1), and H_s is the "system Hamiltonian", which is independent of coupling to the reservoir/vacuum. The second term on the RHS of Eq. 4.10 is often referred to as the 'Liouvillian' operator. By simple grouping of terms, Eq. 4.10 can be rewritten as

$$\begin{aligned}\frac{d\rho_s}{dt} &= \frac{1}{i\hbar}\left(H_{eff}|\psi\rangle\langle\psi| - |\psi\rangle\langle\psi|H_{eff}^\dagger\right) + \sum_k \gamma_k c_k|\psi\rangle\langle\psi|c_k^\dagger \\ &= \frac{1}{i\hbar}\left[H_{eff}, \rho_s\right] + \sum_k \gamma_k c_k|\psi\rangle\langle\psi|c_k^\dagger\end{aligned} \tag{4.11}$$

where $|\psi\rangle\langle\psi| = \rho_s$ and $H_{eff} = H_s - i\hbar\sum_k \frac{\gamma_k}{2}c_k^\dagger c_k$.

The first term on the RHS corresponds to the evolution of a pure state $|\psi\rangle$ under the *non-Hermitian* Hamiltonian H_{eff}, i.e.

$$i\hbar\frac{d}{dt}|\psi\rangle = H_{eff}|\psi\rangle. \tag{4.12}$$

According to this Hamiltonian, if we start with a wavefunction $|\psi(t)\rangle$ at time t, then at time $t + dt$ the wavefunction is written as

$$|\psi(t+dt)\rangle_{wrong} = \left(1 + \frac{H_{eff}\delta t}{i\hbar}\right)|\psi(t)\rangle \tag{4.13}$$

The reason I added the "wrong" subscript is because it turns out that this wavefunction is *not normalized* due to the non-Hermitian nature of H_{eff}. Assuming that $|\psi(t)\rangle$ is normalized, it turns out that ${}_{wrong}\langle\psi(t+dt)|\psi(t+dt)\rangle_{wrong} = 1 - dt\sum_k \gamma_k\langle\psi(t)|c_k^\dagger c_k|\psi(t)\rangle = 1 - dp$, where we've defined

$$dp = dt\sum_k \gamma_k\langle\psi(t)|c_k^\dagger c_k|\psi(t)\rangle = \sum_k dp_k \tag{4.14}$$

where, as we'll see later, dp is the probability that the wavefunction has "jumped". So, to get the normalization right, we define:

$$|\psi(t+dt)\rangle_{correct} = \frac{1 + H_{eff}dt/i\hbar}{\sqrt{1-dp}}|\psi(t)\rangle \tag{4.15}$$

where, in the rest of this chapter, I'll drop the "correct" subscript.

The second term on the RHS of Eq. 4.11 handles quantum jumps that change $|\psi\rangle$ into another state $|\phi_k\rangle = c_k|\psi\rangle$, which are caused by the coupling to the external environment that results in, for example, spontaneous emission. However, we can see that these states are also unnormalized, since $\langle\phi_{k,wrong}|\phi_{k,wrong}\rangle = \langle\psi|c_k^\dagger c_k|\psi\rangle = dp_k/(\gamma_k dt)$. Thus, we can define the proper normalized state $|\phi\rangle_{k,correct} = \sqrt{\gamma_k dt/dp_k}|\phi_{k,wrong}\rangle$. In the rest of the chapter, I'll drop the "correct" subscript

The master equation in Eq. 4.11 can be propagated for discrete time dt, yielding

$$\begin{aligned}\rho_s(t+dt) &= |\psi(t+dt)\rangle_{wrong\ \ wrong}\langle\psi(t+dt)| + dt\sum_k \gamma_k|\phi_k\rangle_{wrong\ \ wrong}\langle\phi_k| \\ &= (1-dp)|\psi(t+dt)\rangle\langle\psi(t+dt)| + \sum_k dp_k|\phi_k\rangle\langle\phi_k|.\end{aligned} \tag{4.16}$$

This equation can be interpreted in the following way: given a wavefunction $|\psi(t)\rangle$, in a timestep dt the wavefunction will either evolve to $|\psi(t+dt)\rangle$ according to Eq. 4.15 with probability 1-dp or, with probability dp_k, the wavefunction will jump into one of the $|\phi\rangle_k$ states. This is relatively straightforward to implement in a computer simulation through the following algorithm:

- Pick initial state $|\psi(0)\rangle$
- Pick random number r
- Calculate dp over some interval dt. If $dp < r$, $|\psi\rangle$ evolves according to Eq. 4.15. If $dp > r$, jump to $|\phi\rangle_k$ with probability determined by dp_k/dp (this will involve 'rolling' another random number)
- Repeat steps (2) and (3) over as many particles as you want for as many timesteps as you want.

In the next section, I will describe how we apply this algorithm to the specific case of a system of Sr$^+$ ions with laser-induced coupling via the D2 line and an additional repump laser coupling $^2D_{5/2}$ and $^2P_{3/2}$.

4.4.2 Applying Quantum Trajectories to the Laser Cooling of a ^{88}Sr Ion

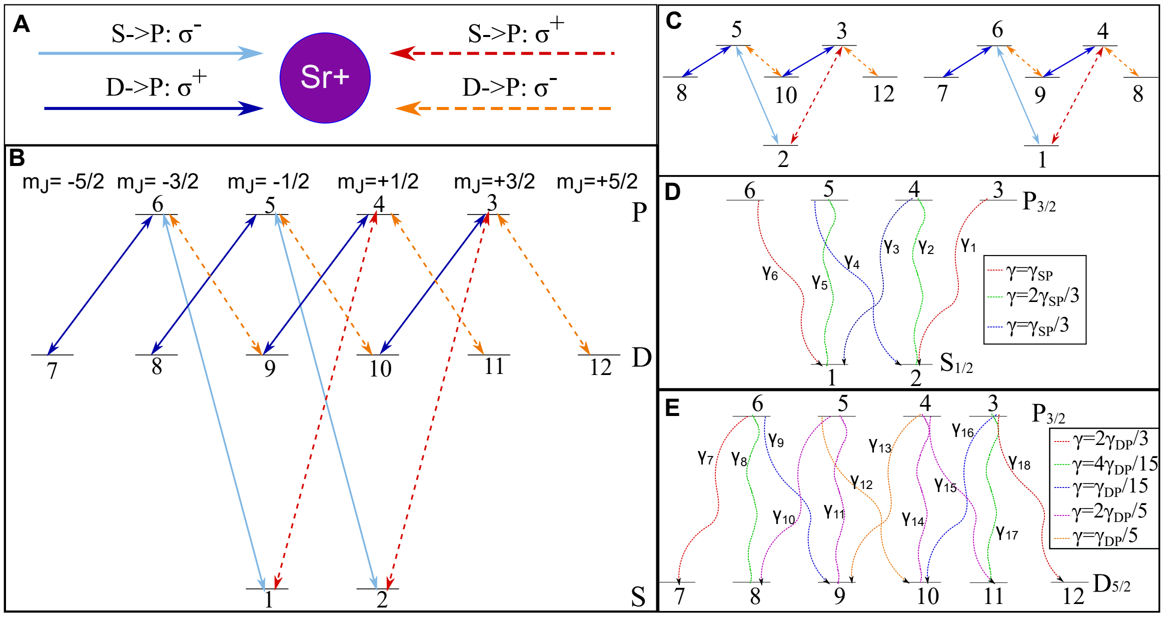

Figure 4.3 : (**A**): Counter-propagating cross-polarized laser configuration considered in our Quantum Trajectories simulation. Dashes indicate leftward propagating lasers, which are doppler-shifted by $+kv_x$. (**B**): Corresponding level diagram with laser-couplings indicated and including full Zeeman substructure. (**C**): If the states are coupled only by circularly polarized light, the 12 state system can be broken up into two 6 state subsystems, making it easier to recognize dark states induced by near resonant two photon coupling between combinations of S and D sublevels (see Sec. 4.4.5). (**D**): Decay channels from P to S, with decay rates indicated. $\gamma_{SP} = 1.41 \times 10^8\,\mathrm{s}^{-1}$. (**E**): Decay channels from P to D, with decay rates indicated. $\gamma_{DP} = 8.7 \times 10^6\,\mathrm{s}^{-1}$.

In Fig. 4.3B, we show the full Sr$^+$ level diagram with all relevant levels, including Zeeman substructure, included. We ignore decay into the $D_{3/2}$ state and the corresponding repump laser. This is justified due to the small branching ratio (1:150) into this state (compare to 1:15 for the $D_{5/2}$ state) and because ions that fall into this state are repumped via the $P_{1/2}$ level, not the $P_{3/2}$ level, and therefore this repump laser does not directly couple together the $D_{3/2}$ state to any of the states used in the cycling transition.

The effective Hamiltonian for this system is

$$
\begin{aligned}
H_{eff} &= \hbar\omega(|3\rangle\langle 3| + |4\rangle\langle 4| + |5\rangle\langle 5| + |6\rangle\langle 6|) \\
&+ \hbar\omega_D(|7\rangle\langle 7| + |8\rangle\langle 8| + |9\rangle\langle 9| + |10\rangle\langle 10| + |11\rangle\langle 11| + |12\rangle\langle 12|) \\
&- \frac{\hbar}{2}\left(|2\rangle\langle 3| + \frac{|1\rangle\langle 4|}{\sqrt{3}} + h.c.\right)(\Omega_{SP}\exp\left[-i(\nu_{SP}+kv)t\right] + \Omega_{SP}^{*}\exp\left[i(\nu_{SP}+kv)t\right]) \\
&- \frac{\hbar}{2}\left(\frac{|2\rangle\langle 5|}{\sqrt{3}} + |1\rangle\langle 6| + h.c.\right)(\Omega_{SP}\exp\left[-i(\nu_{SP}-kv)t\right] + \Omega_{SP}^{*}\exp\left[i(\nu_{SP}-kv)t\right]) \\
&- \frac{\hbar}{2}\left(\frac{|10\rangle\langle 3|}{\sqrt{15}} + \frac{|9\rangle\langle 4|}{\sqrt{5}} + \frac{\sqrt{2}|8\rangle\langle 5|}{\sqrt{5}} + \frac{\sqrt{2}|7\rangle\langle 6|}{\sqrt{3}} + h.c.\right) \times \\
&(\Omega_{DP}\exp\left[-i(\nu_{DP}-k_D v)t\right] + \Omega_{DP}^{*}\exp\left[i(\nu_{DP}-k_D v)t\right]) \\
&- \frac{\hbar}{2}\left(\frac{|9\rangle\langle 6|}{\sqrt{15}} + \frac{|10\rangle\langle 5|}{\sqrt{5}} + \frac{\sqrt{2}|11\rangle\langle 4|}{\sqrt{5}} + \frac{\sqrt{2}|12\rangle\langle 3|}{\sqrt{3}} + h.c.\right) \times \\
&(\Omega_{DP}\exp\left[-i(\nu_{DP}+k_D v)t\right] + \Omega_{DP}^{*}\exp\left[i(\nu_{DP}+k_D v)t\right]) \\
&- i\sum_{k=1}^{18}\frac{\gamma_k}{2}c_k^{\dagger}c_k
\end{aligned}
\tag{4.17}
$$

where $\hbar\omega$ is the energy of the P state, $\hbar\omega_D$ is the energy of the D state, Ω_{SP} is the laser-induced Rabi frequency between states S and P for a hypothetical transition with Clebsch-Gordon (C-G) coefficient of 1, Ω_{DP} is the same but for coupling between D and P, ν_{SP} and ν_{DP} refer to the frequency of the coupling lasers, γ_k and c_k refer to the 18 decay paths indicated in Fig. 4.3D and Fig. 4.3E, and we have factored in the relevant C-G coefficients and Doppler shifts of magnitude kv and $k_D v$ where k

is the wavenumber for the S→P transition and k_D is the wavenumber for the D→P transition.

To eliminate the time dependence, it is customary to transform to a basis set where wavefunctions are rotating with the light field (including the doppler shift) and eliminate resulting terms of the form $\exp[2i\nu]$, since we are not interested in dynamics on the timescale ν^{-1}. However, in this case we cannot completely eliminate the time dependence. This is because the $m_j \pm 1/2$ states in the D manifold are coupled to the $m_j \pm 1/2$ states in the S manifold through two different P states. For example, states $|1\rangle$ and $|9\rangle$ are coupled through both $|6\rangle$ and $|4\rangle$, meaning that there is some ambiguity regarding which rotating field to use for the transformation of these states. In this case, we choose to transfer $|9\rangle$ and $|10\rangle$ to the frame rotating with the σ^+ D→P laser. The resulting Hamiltonian after the unitary transform to the rotating frame then becomes

$$\begin{aligned}\frac{H_{eff}}{\hbar} &= (-\delta - vk)(|3\rangle\langle 3| + |4\rangle\langle 4|) + (-\delta + vk)(|5\rangle\langle 5| + |6\rangle\langle 6|)\\ &+ (-\delta + \delta_D + (k - k_D)v)(|7\rangle\langle 7| + |8\rangle\langle 8|)\\ &+ (-\delta + \delta_D + (-k + k_D)v)(|11\rangle\langle 11| + |12\rangle\langle 12|)\\ &+ (-\delta + \delta_D + (-k - k_D)v)(|9\rangle\langle 9| + |10\rangle\langle 10|)\\ &+ \left(\frac{\Omega^*_{SP}}{2}|2\rangle\langle 3| + \frac{\Omega^*_{SP}}{2\sqrt{3}}|1\rangle\langle 4| + \frac{\Omega^*_{SP}}{2}|1\rangle\langle 6| + \frac{\Omega^*_{SP}}{2\sqrt{3}}|2\rangle\langle 5| + h.c\right)\\ &+ \left(\frac{\sqrt{2}\Omega^*_{DP}}{2\sqrt{3}}|7\rangle\langle 6| + \frac{\sqrt{2}\Omega^*_{DP}}{2\sqrt{5}}|8\rangle\langle 5| + \frac{\Omega^*_{DP}}{2\sqrt{5}}|9\rangle\langle 4| + \frac{\Omega^*_{DP}}{2\sqrt{15}}|10\rangle\langle 3| + h.c\right)\\ &+ \left[\exp\left[2i(k + k_D)vt\right]\left(\frac{\Omega^*_{DP}}{2\sqrt{15}}|9\rangle\langle 6| + \frac{\Omega^*_{DP}}{2\sqrt{5}}|10\rangle\langle 5|\right) + h.c\right]\\ &+ \left(\frac{\sqrt{2}\Omega^*_{DP}}{2\sqrt{5}}|11\rangle\langle 4| + \frac{\sqrt{2}\Omega^*_{DP}}{2\sqrt{3}}|12\rangle\langle 3| + h.c\right)\\ &- i\sum_{k=1}^{18}\frac{\gamma_k}{2}c^\dagger_k c_k\end{aligned} \tag{4.18}$$

where the remaining time dependence results from the difference in frequency between the chosen rotating frame and the frame rotating with the ‘alternate’ paths coupling the S and D states.

When implementing a QT simulation, it is helpful to consider some ‘natural’ units, similar to when performing an MD simulation. In this case, we choose to normalize our timesteps by γ_{SP}^{-1}. Eq. 4.15 then becomes

$$|\psi(t + \delta t)\rangle = \frac{1 + H_{eff}dt_{code}/i\hbar}{\gamma_{SP}\sqrt{1 - dp}}|\psi(t)\rangle \tag{4.19}$$

where $dt_{code} = dt_{real}\gamma_{SP}$. The natural energy scale then becomes $\hbar\gamma_{SP}$ and thus we define $H_{code} = H_{eff}/\hbar\gamma_{SP}$. Then we have

$$|\psi(t + \delta t)\rangle = \frac{1 - iH_{code}dt_{code}}{\sqrt{1 - dp}}|\psi(t)\rangle \tag{4.20}$$

where

$$dp = dt_{code} \sum_{k=1}^{18} \frac{\gamma_k}{\gamma_{SP}} \langle \psi(t) | c_k^\dagger c_k | \psi(t) \rangle. \tag{4.21}$$

This handles the propagation of the wavefunction according to H_{code}. Next, we need to determine the force at each timestep. Since we are implementing 1D cooling, all forces and velocities are assumed to be along the x-axis unless otherwise indicated. For simplicity, let's just consider the application of Eq. 4.1 to the $|2\rangle\langle 3|$ term of H_{eff}, in which case we obtain

$$\langle F \rangle = -\langle [\nabla, H] \rangle = \langle \psi | \nabla \left(\frac{\hbar\Omega^*}{2} |2\rangle\langle 3| + \frac{\hbar\Omega}{2} |3\rangle\langle 2| \right) |\psi\rangle - \langle \psi | \left(\frac{\hbar\Omega^*}{2} |2\rangle\langle 3| + \frac{\hbar\Omega}{2} |3\rangle\langle 2| \right) \nabla |\psi\rangle \tag{4.22}$$

The 2nd term on the RHS is zero, as $|\psi\rangle$ has no spatial dependence. Inserting $\Omega = \Omega_{SP} \exp[-ikx]$ (the minus sign is due to the fact that the σ^+ wave for the S→P transition is propagating to the left) and $\Omega^* = \Omega_{SP} \exp[ikx]$, we get:

$$\langle F \rangle = \frac{ik\hbar\Omega_{SP}}{2} \left(\langle \psi | 2 \rangle \langle 3 | \psi \rangle - \langle \psi | 3 \rangle \langle 2 | \psi \rangle \right) = \frac{ik\hbar\Omega_{SP}}{2} \left(\rho_{32} - \rho_{32}^* \right) = -k\hbar\Omega_{SP} Im[\rho_{32}] \tag{4.23}$$

After considering all such terms in the Hamiltonian, the total force is written as

$$\begin{aligned} \langle F \rangle = {} & k\hbar\Omega_{SP} \left(-Im[\rho_{32}] + Im[\rho_{61}] \right) + \frac{k\hbar\Omega_{SP}}{\sqrt{3}} \left(-Im[\rho_{41}] + Im[\rho_{52}] \right) \\ & + \frac{\sqrt{2} k_D \hbar\Omega_{DP}}{\sqrt{3}} \left(Im[\rho_{67}] - Im[\rho_{3\,12}] \right) + \frac{\sqrt{2} k_D \hbar\Omega_{DP}}{\sqrt{5}} \left(Im[\rho_{58}] - Im[\rho_{4\,11}] \right) \\ & + \frac{k_D \hbar\Omega_{DP}}{\sqrt{5}} \left(Im[\rho_{49}] - Im[\rho_{5\,10}] \right) + \frac{k_D \hbar\Omega_{DP}}{\sqrt{15}} \left(Im[\rho_{3\,10}] - Im[\rho_{69}] \right) \end{aligned} \tag{4.24}$$

Therefore, in a timestep dt during which a quantum jump has *not* occurred, the velocity changes by

$$
\begin{aligned}
d\tilde{v} = {} & \frac{\hbar k\tilde{\Omega}_{SP}}{m\gamma_{SP}/k}\left(-Im[\rho_{32}] - \frac{Im[\rho_{41}]}{\sqrt{3}} + Im[\rho_{61}] + \frac{Im[\rho_{52}]}{\sqrt{3}}\right) d\tilde{t} \\
& + \frac{\hbar k\tilde{\Omega}_{DP}}{m\gamma_{SP}/k}\sqrt{\frac{2}{3}}\frac{k_D}{k}\left(Im[\rho_{67}] - Im[\rho_{3\,12}]\right) d\tilde{t} \\
& + \frac{\hbar k\tilde{\Omega}_{DP}}{m\gamma_{SP}/k}\sqrt{\frac{2}{5}}\frac{k_D}{k}\left(Im[\rho_{58}] - Im[\rho_{4\,11}]\right) d\tilde{t} \\
& + \frac{\hbar k\tilde{\Omega}_{DP}}{m\gamma_{SP}/k}\sqrt{\frac{1}{5}}\frac{k_D}{k}\left(Im[\rho_{49}] - Im[\rho_{5\,10}]\right) d\tilde{t} \\
& + \frac{\hbar k\tilde{\Omega}_{DP}}{m\gamma_{SP}/k}\sqrt{\frac{1}{15}}\frac{k_D}{k}\left(Im[\rho_{3\,10}] - Im[\rho_{69}]\right) d\tilde{t}
\end{aligned}
\tag{4.25}
$$

where $\tilde{}$ implies normalized units (frequencies normalized by γ_{SP}, velocity by γ_{SP}/k, and time by γ_{SP}^{-1}). If a quantum jump occurs, the velocity receives a random kick either of magnitude $\tilde{v}_{kick} = \hbar k/(m\gamma_{SP}k)$ or $\hbar k_D/(m\gamma_{SP}k)$ depending on whether the jump was to an S state or a D state.

Finally, we can describe an algorithm for evolving both the velocities and the wavefunction. Given a wavefunction $|\psi(t)\rangle$ and velocity $\tilde{v}(t)$ we obtain $|\psi(t+dt)\rangle$ and $\tilde{v}(t+dt)$ in the following way:

- (1) Pick a random number r between 0 and 1.
- (2) Calculate dp using Eq. 4.14. If $dp < r$, there is no jump, move to Step (3a). If not, then there is a jump, move to Step (3b).
- (3a) Calculate $d\tilde{v}$ using Eq. 4.25 (note, to get density matrix ρ, just calculate $\rho = |\psi(t_0)\rangle\langle\psi(t_0)|$). Set $\tilde{v} \rightarrow \tilde{v}(t) + d\tilde{v}$
- (4a) Using the new $\tilde{v}$ and $\psi(t_0)$, calculate $H_{code} = H_{eff}/\hbar\gamma_{SP}$ using Eq. 4.18.
- (5a) Plug this into Eq. 4.20 to determine $|\psi(t+\delta t)\rangle$.
- (6a) Go back to Step 1

- (3b) Pick a random number r_2. If $dp_{k=1} < r_2$, the $k = 1$ transition indicated in Fig. 4.3D occurs and the particle state jumps to $|2\rangle$. Else If $dp_{k=2} + dp_{k=1} < r_2$, the $k = 2$ transition occurs, and so on. For example, if the $k = 10$ jump is selected, that puts it in the $|8\rangle$ state.

- (4b) Randomly decide the direction of the kick.

- (5b) If the state jumped to is either $|2\rangle$ or $|1\rangle$, then set $\tilde{v}(t) \rightarrow \tilde{v}(t) + \tilde{v}_{kick}$. Else, set $\tilde{v}(t) \rightarrow \tilde{v}(t) + \tilde{v}_{kick}k_D/k$

- (6b) Go back to Step 1.

Before combining this with a MD code, we first will test how it performs on a cloud of Sr^+ ions with interactions *neglected.* In this case, the initial velocity distribution will, in most cases, be set by an initial temperature:

$$\frac{1}{2}m\sigma_v^2 = \frac{1}{2}k_BT \tag{4.26}$$

in real units. Thus, in normalized units:

$$\sigma_{\tilde{v}}^2 = \frac{k_BT}{m\gamma_{SP}^2/k^2} \tag{4.27}$$

where $\sigma_{\tilde{v}}^2$ sets the standard deviation of a normal distribution from which we randomly select velocities for however many particles we have in our system. So, basically the code will evolve a system of Sr ions with a set of inputs:

- 1: normalized detunings $\tilde{\delta}$ and $\tilde{\delta}_D$.

- 2: normalized Rabi Frequencies $\tilde{\Omega}_{SP}$ and $\tilde{\Omega}_{DP}$.

- 3: initial temperature

The code is implemented in C++, which is necessary for the future step of integrating it with the MD simulation. The code uses the “Armadillo” (http://arma.sourceforge.net/) library for matrix manipulation in C++ (basically, it allows for “mat” and “cx_mat” objects; matrices and complex matrices, respectively, and can handle things like multiplication, transposes and adjoints, inverses, etc. which are necessary for our simulation). In the next subsection, we will discuss how we verify that the code reproduces analytic solutions in simpler coupling schemes in order to give confidence that the code will work for our somewhat more complex 12-level system.

Before doing that, I'll list some numerical values that are important for the Sr^+ laser-coupling scheme:

- $\lambda = 407.8865\,\mathrm{nm}$
- $k = 1.54 \times 10^5 \mathrm{cm}^{-1}$
- $\lambda_d = 1033.0139\,\mathrm{nm}$
- $k_d = 6.0825 \times 10^4 \mathrm{cm}^{-1}$
- $\gamma_{SP} = 1.41 \times 10^8 \mathrm{s}^{-1}$
- $\gamma_{DP} = 8.7 \times 10^6 \mathrm{s}^{-1}$
- $\gamma_{DP}/\gamma = 0.0617$
- $\gamma_{SP}^{-1} = 7.09\,\mathrm{ns}$
- $v_{norm} = \gamma_{SP}/k = 9.1559$ m/s
- $\tilde{v}_{kick} = \frac{\hbar k}{m\gamma_{SP}/k} = 0.001208$

- $\sigma_{\tilde{v}}(\mathrm{m/s}) = \sqrt{\frac{k_B}{m\gamma_{SP}^2/k^2}}\sqrt{T} = 1.0588\sqrt{T(\mathrm{K})}$

- $I_{sat} = \frac{2\pi^2\hbar c\gamma_{SP}}{3\lambda^3} = 43.1\,\mathrm{mW/cm}^2$. This is the saturation intensity for the $|2\rangle \rightarrow |3\rangle$ and $|1\rangle \rightarrow |6\rangle$ transitions.

- $I_{satD} = \frac{2\pi^2\hbar c\gamma_{DP}}{3\lambda_D^3} = 0.164\,\mathrm{mW/cm}^2$. This is the saturation intensity for the $D \rightarrow P$ transition assuming a C-G coefficient of 1 (i.e., the intensity required for $\Omega_{DP} = \gamma_{SP}/\sqrt{2}$. Divide by the square of the appropriate C-G coefficient to get I_{satD} for a specific $D \rightarrow P$ transition.)

4.4.3 Testing a Quantum Trajectories Code for Simple Level Diagrams

NOTE: Unless I specify otherwise, all units here are normalized and I'll be dropping the tildes. The laser is also always red-detuned unless otherwise specified.

Test 1: Reproduce Rabi Oscillations and Steady State Population in a 2 Level System

The first test for the code is to see if an implementation using just two states of a motionless ion, $|1\rangle$ and $|2\rangle$, coupled by a laser would produce the damped Rabi oscillations in the populations within each state that are observed in the solutions to the two state OBEs. One can also check if the steady state solution follows Fermi's golden rule (i.e. if the excited state population for a given Ω as a function of δ matches the expected power-broadened lorentzian). To that end, the evolution of $|\psi(t)\rangle$ is simulated using the hamiltonian

$$H_{code} = -\delta|2\rangle\langle 2| + \frac{\Omega}{2}\left(|1\rangle\langle 2| + |2\rangle\langle 1|\right) - \frac{i}{2}|2\rangle\langle 1|1\rangle\langle 2| \tag{4.28}$$

for 3000 particles starting in the ground state.

The results are compared to the solution of the two state OBEs:

$$\begin{aligned}\frac{d\rho_{22}}{dt} &= -\frac{i\Omega}{2}\rho_{21}^{*} + \frac{i\Omega}{2}\rho_{21} - \rho_{22}, \\ \frac{d\rho_{21}}{dt} &= -i\delta\rho_{21} - \frac{\rho_{21}}{2} + \frac{i\Omega}{2}(2\rho_{22} - 1)\end{aligned} \tag{4.29}$$

Specifically, two comparisons were made between the QT simulation and the OBE results. First, the time dependent value of $\langle\rho_{22}\rangle$ from the QT simulation, where the brackets in this case refer to an ensemble average over the 3000 particles, was compared to the OBE solution for $\rho_{22}(t)$. In addition, the "steady state" simulation result for $\langle\rho_{22}\rangle$ for different Ω and δ is compared to the expected power broadened Lorentzian:

$$\rho_{ee} = \frac{s_0/2}{1 + s_0 + 4\delta^2} \tag{4.30}$$

where $s_0 = 2\Omega^2$.

In the first iteration of the code, $|\psi(t)\rangle$ was propagated using the Eulerian method with a timestep $dt = 0.005$. This worked well for low Rabi frequencies like $\Omega = 0.2$, however, at higher frequencies like $\Omega = 5$ the code began to fail. Lower timesteps were observed to improve the simulation, however, the issues never really went away. This motivated moving to a 4th order Runge-Kutta propagator, which worked much better. These results are summarized in Fig. 4.4. All other QT data presented in this thesis is obtained using the 4th order Runge-Kutta propagator.

Test 2: Reproduce Laser Cooling in a Three Level System

In a three-level optical molasses system, such as one formed by the application of counter-propagating σ^+ and σ^- lasers operating on a $J = 0 \rightarrow J' = 1$ transition, the cooling rate can be derived analytically for $v_T \ll k/\gamma_{SP}$ [134]:

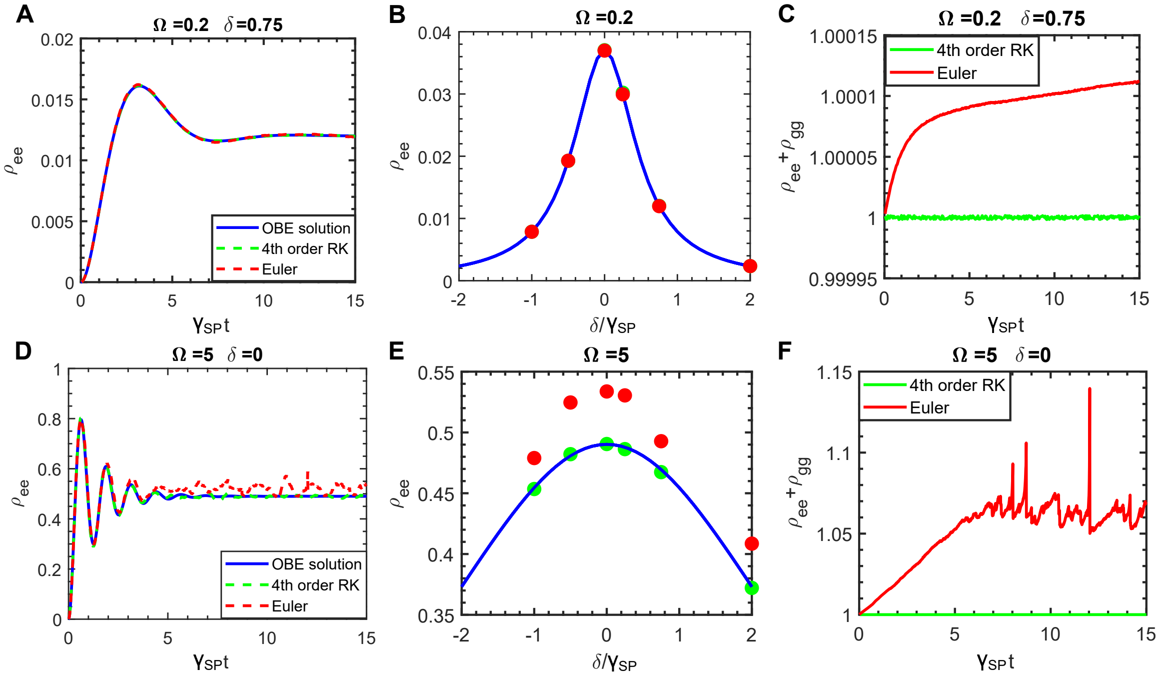

Figure 4.4 : (**A**): Damped Rabi Oscillation in ρ_{ee}. We see that both the Eulerian and Runge-Kutta (RK) propagators replicate the OBE solution. (**B**): Steady state ($\gamma_{SP}t \gg 1$) solution for $\rho_{ee}(\delta)$. We also observe agreement here between the QT simulations and the OBE solutions. (**C**): Total population in QT simulation. The Eulerian solution is behaving somewhat nonphysically by adding population. (**D-F**): Same curves for $\Omega = 5$. We clearly see here that, while the Eulerian propagator does not replicate the OBE results and also acquires significant errors in the total population, the RK propagator replicates the OBE solutions.

$$\frac{dT}{dt} = -\beta T, \tag{4.31}$$

where

$$\beta = -\frac{\hbar k^2}{m}\frac{4s}{1+2s}\frac{2(2\delta)}{(2\delta)^2 + \left\{1 + \frac{s}{2}\left[(2\delta)^2+1\right]\right\}^2}, \tag{4.32}$$

and

$$s = \frac{2\Omega^2}{1+(2\delta)^2}. \tag{4.33}$$

A simulation of laser-cooling in a 3 state system of $N = 3000$ particles where the velocity of each ion at $t = 0$ is drawn randomly using a gaussian distribution corresponding to $T = 2.5\,\mathrm{mK}$, after which the temperature is recorded at each timestep, was performed in order to test if the QT code can replicate these results. For a transition with k and γ of the Sr$^+$ D2 line, $T = 2.5\,\mathrm{mK}$ gives $kv_T = 3.6 \times 10^6\,\mathrm{s}^{-1} \ll \gamma_{SP} = 1.41 \times 10^8\,\mathrm{s}^{-1}$, so we are well within the approximation for which Eq. 4.32 is valid. The application of the 'kick' whenever a spontaneous emission occurs was removed for this test, as this adds a heating term that would affect the results (we discuss this in the next section). The three level Hamiltonian that we use to evolve each wavefunction is

$$\begin{aligned} H_{code} =& (-\delta - kv)|2\rangle\langle 2| + (-\delta + kv)|3\rangle\langle 3| + \frac{\Omega}{2}\left(|1\rangle\langle 2| + |2\rangle\langle 1| + |3\rangle\langle 1| + |3\rangle\langle 1|\right) \\ & - \frac{i}{2}\left(|2\rangle\langle 2| + |3\rangle\langle 3|\right) \end{aligned} \tag{4.34}$$

and the velocity step for a particle with a wavefunction $|\psi(t)\rangle$ is, using the 'three-level' version of Eq. 4.25

$$dv = v_{kick}\Omega\left(-Im[\rho_{21}] + Im[\rho_{31}]\right) dt \tag{4.35}$$

where $\rho_{ij} = \langle i|\psi\rangle\langle\psi|j\rangle$.

This test was performed at various δ and Ω. $T(t)$ can be measured directly through calculating $\langle v^2\rangle$, where the average is over all of the particles, or by fitting the distribution $P(v)$ to a gaussian. These two methods yield similar results (Fig. 4.5C). The resulting $T(t)$ curves were fit to an exponential decay to obtain β. The simulation reliably reproduced the expected decay rates from Eq. 4.32, as expected. These results are summarized in Fig. 4.5.

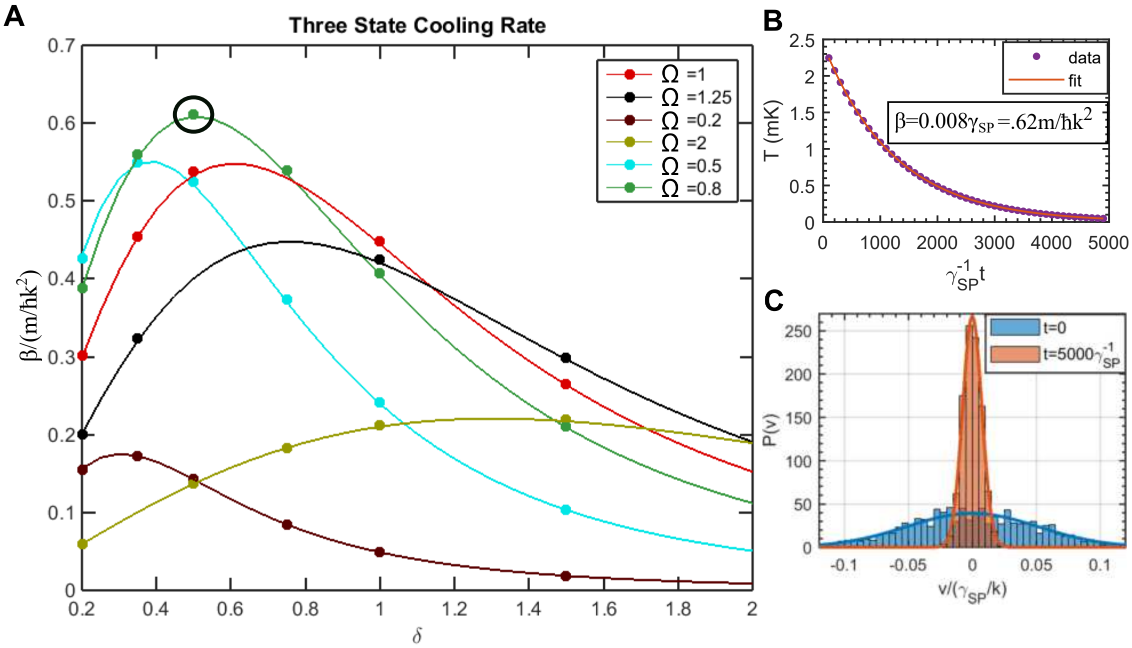

Figure 4.5 : (**A**): Comparison of QT measurements (points) of cooling rate normalized by $m/\hbar k^2$ with analytical formula (lines, Eq. 4.32). The good agreement indicates that the QT code implements the laser-forces correctly. (**B**): Measurement of $T(t)$ for the QT simulation circled in **A**. The curve matches an exponential decay, as expected. (**C**): Plots of the velocity distribution at the beginning and the end of that same simulation. The distributions (shaded rectangles) clearly match gaussians (solid lines). The widths are determined by the temperature.

Test 3: Observation of the Doppler Limit

In 1D, when N random momentum kicks of magnitude $\hbar k$ are applied to a particle that is initially at rest, the mean square momentum $\langle p^2 \rangle$ becomes:

$$\langle p^2 \rangle = N \hbar^2 k^2 \tag{4.36}$$

This will also result in heating, since $T = \langle p \rangle^2 / m k_B$. During optical molasses, *two* random momentum 'kicks' are delivered to the atom for each absorption/emission event (this is only true for temperatures such that $v_T \ll k/\delta$, in which case the particles are equally likely to absorb from either beam). Thus, for a given scattering rate R_s, the 'random walk' heating term becomes:

$$(\partial_t T)_{RW} = \frac{1}{mk_B}\partial_t(\langle p^2\rangle) = 2R_s\frac{\hbar^2k^2}{mk_B} \tag{4.37}$$

During optical molasses, if there are no other heating terms, the final temperature is determined by equating this heating rate to the molasses cooling rate. For a two-level system, if one assumes $|kv| \ll \gamma$ and $s_0 \ll 1$ one can show [134]

$$(\partial_t T)_{RW} = \frac{2\hbar^2k^2}{mk_B}\gamma\frac{s_0}{1+(2\delta/\gamma)^2} \tag{4.38}$$

and

$$(\partial_t T)_{Cool} = -\frac{8\hbar k^2}{m}s_0\frac{(2\delta/\gamma)}{\left[1+(2\delta/\gamma)^2\right]^2}T \tag{4.39}$$

Setting $(\partial_t T)_{RW} = -(\partial_t T)_{Cool}$ and solving for T, one can show that the minimum temperature is achieved for $\delta = -\gamma/2$ and that $T_{min} = \hbar\gamma/2k_B$. This is what is commonly cited as the 'Doppler limit'. In general, the minimum temperature achievable through laser-cooling will depend on the values of δ and Ω that are chosen.

To test if the QT code could replicate this feature, we apply the 'three-level' QT code introduced in the previous test to atoms with initial temperature $T = 10\,\mathrm{mK}$ for $t = 4500/\gamma$. The resulting $T(t)$ curves are fit to an exponential decay to determine the equilibrium temperature T_{eq} as a function of δ and Ω. We then compare the results to the values that are expected from the analytical formulas for the cooling rate (Eq. 4.32) and the random walk heating term, which, for a three level system, is [135]

$$(\partial_t T)_{RW} = \frac{\hbar^2 k^2}{m k_B} \gamma \frac{s}{1+2s} \tag{4.40}$$

where s is given by Eq. 4.33. Equating the magnitudes of the heating and cooling terms, one finds:

$$T_{eq} = \frac{\hbar\gamma}{4k_B}\left[\frac{4\delta^2 + \left\{1 + \frac{1}{2}s(\delta,\Omega)\left(4\delta^2+1\right)\right\}^2}{4\delta}\right] \tag{4.41}$$

In Fig. 4.6, we plot T_{eq} determined from the QT code (**NOTE: Do I need to include a figure for this? It's just the "offset" value from an exponential fit**) along with Eq. 4.41 for $\Omega = \{0.5, 1, 2\}$ and various δ. We clearly see good agreement between the simulation results and the expected values, indicating that the simulation accurately incorporates this additional heating effect.

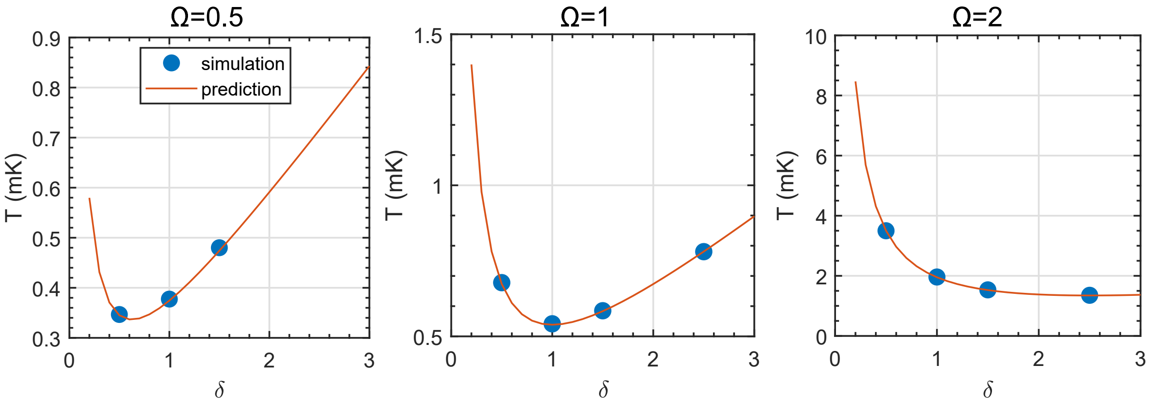

Figure 4.6 : Comparison of the equilibrium temperature resulting from competition between random-walk heating and laser-cooling determined from the QT code and the expected equilibrium temperature (Eq. 4.41) for various Ω and δ. We observe very good agreement between the simulation results and the theoretical prediction.

4.4.4 Testing Quantum Trajectories Code For Sr^+ level diagram

After verifying that the code replicates known analytical results for cooling in a three-level system, the next step is to test how effective cooling can be in an Sr^+ ion given its level structure (Fig. 4.3). For an initial test, the D state decay is turned off and Ω_{DP} is set to zero in order to obtain an upper limit on the cooling rate. We found that the cooling rate for a set of Ω_{SP} and δ is strongly dependent on the temperature (see Fig. 4.7). At high T, cooling effectiveness is maximized for higher Ω and δ than for low T. This is primarily due to the fact that the doppler width of the velocity distribution becomes on the order of, or greater than, γ_{SP} at $T \gtrsim 250\,\mathrm{mK}$; and therefore the lasers must be further detuned in order for cooling to be effective throughout the velocity distribution.

The code was then ran with the D state decay and coupling terms included. The simulation contained 1000 particles at $T_0 = 500\,\mathrm{mK}$ with $\Omega_{SP} = 1$, $\delta = -1$, $\delta_{DP} = +1$, and $\Omega_{DP} = 1$. Including the effect of D state decay and coupling increases the cooling timescale from 12.5μs to 17.6μs, see Fig. 4.8. This is good news, as this timescale is still shorter than the limiting timescale of $\tau_{Exp} \sim 80\mu$s (Eq. 2.14).

4.4.5 Examining the OBE solutions for the Sr^+ Level Diagram

Although collisionally induced rapid velocity changes may change the ultimate form of the time averaged force profile $F(v)$ with respect to the force profile derived from solving the OBEs ($F_{OBE}(v)$), it is still worth obtaining $F_{OBE}(v)$ to gain some intuition. In particular, the OBE solutions illustrate the effect of ‘dark states’, which are eigenstates of the atom-light coupled Hamiltonian (basically, H_{eff} without the decay terms) comprised of superpositions of only S and D states[123, 124]. If an ion winds up in a dark state, then it will no longer scatter light.

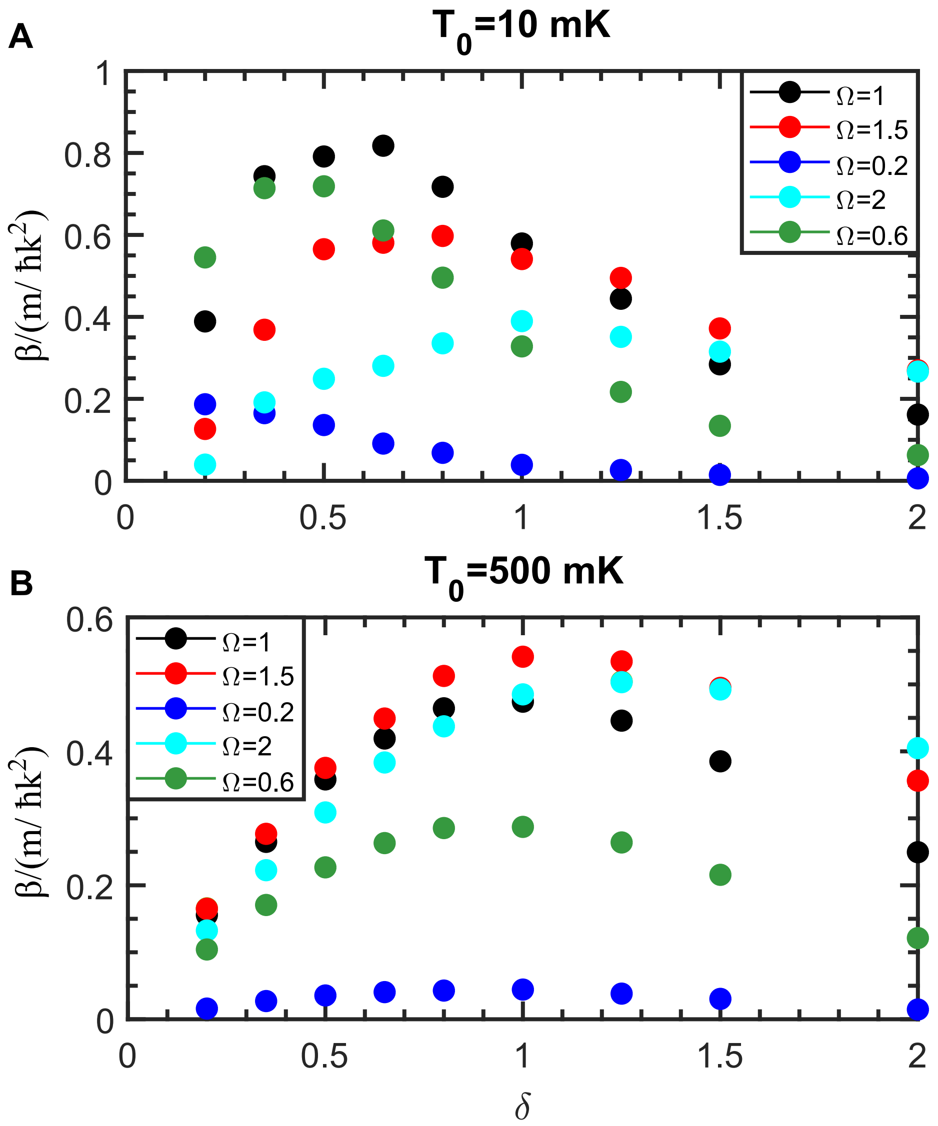

Figure 4.7 : (**A**): Cooling rate at various Ω and δ measured by QT simulations of Sr$^+$ level diagram *without* decay into the D state for an initial temperature $T = 10\,\text{mK}$. (**B**): Same, but with an initial temperature of 500 mK. Clearly the optimal values of both Ω and δ increase with T. This is primarily due to the increase in the Doppler linewidth σ_v at higher T: as σ_v approaches γ_{SP}, δ must increase in order for the full velocity distribution to experience the cooling force.

Upon close examination, we see that for the case where both S→P and D→P levels are coupled by σ^+ and σ^- lasers, the 12 level Sr$^+$ diagram can be broken into two

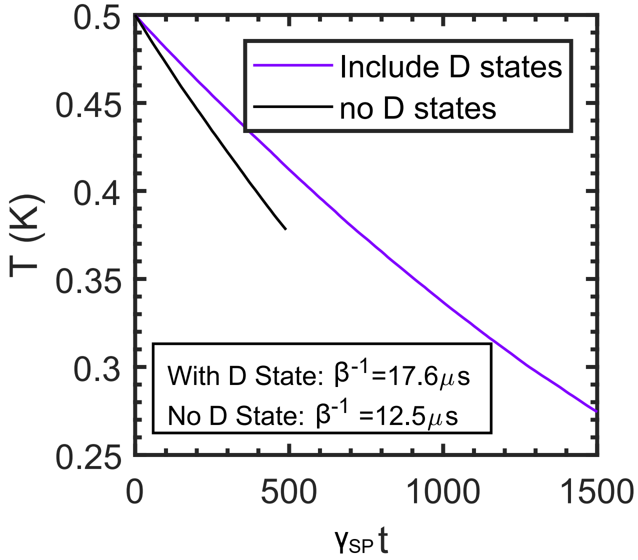

Figure 4.8 : Cooling curves with and without decay into the D state ($\Omega_{SP} = \Omega_{DP} = 1$, $\delta = -1$, $\delta_{DP} = +1$). The D state decay noticeably reduces the cooling efficiency, however, the cooling timescale β^{-1} is still less than typical $\tau_{Exp} \sim 80\mu$s, making UNP laser-cooling feasible.

subsystems of 6 levels each (See Fig. 4.3C). The eigensolutions of the corresponding 6 state matrices are too complicated to include here. Nevertheless, some intuition can be gained by examining the subsystems. Dark states typically exist when two states are coupled by a resonant two photon transition. For example, we may expect a dark state when the detunings of the photons coupling states $|2\rangle$ and $|3\rangle$ and states $|12\rangle$ and $|3\rangle$ cancel each other out, which will occur when $\delta - vk = \delta_D - vk_D$. Similarly, the condition for the two photon coupling from $|2\rangle$ to $|8\rangle$ to be resonant is $\delta + vk = \delta_D + vk_D$. There can also be dark states comprised solely of D states; the D states are all resonantly coupled for $v = 0$. We arrive at the conclusion that we expect dark states at:

- $v = 0$ (one comprised of $|8\rangle$, $|10\rangle$ and $|12\rangle$ and another comprised of $|7\rangle$, $|9\rangle$ and $|11\rangle$)

- $v = \pm(\delta - \delta_D)/(k - k_D)$
  - + one comprised of $|2\rangle$ and $|12\rangle$ and another comprised of $|1\rangle$ and $|8\rangle$
  - - one comprised of $|2\rangle$ and $|8\rangle$ and another comprised of $|1\rangle$ and $|7\rangle$
- $v = \pm(\delta - \delta_D)/(k + k_D)$ (each correspond to couplings between $|2\rangle$ and $|10\rangle$ and between $|1\rangle$ and $|9\rangle$ from opposite photon pairs).

We can observe these dark states in the steady state OBE solution for the full Sr$^+$ level diagram. Specifically, the dark states will correspond to minima in $P_p(v)$, the steady-state population in the P level. We observe that the locations depend on δ_D (Fig. 4.9). Identifying the dark state location with the minima in $P_p(v)$, we see good agreement with the predicted locations (Fig. 4.9B). From the steady state OBE solutions we can directly calculate $a(v) = F_{OBE}(v)/m$, the laser-force induced acceleration profile, which we plot in Fig. 4.9C for $\delta = -1$, $\delta_D = +1$, $\Omega_{SP} = \Omega_{DP} = 1$. We see that, in the region defined by $|v| \leq 9\,\mathrm{m/s}$, we find $a \propto -v$.

It is also worth considering how $P_p(v)$ depends on time. In Fig. 4.10A we plot $P_p(v)$ after the propagation of the OBEs for various lengths of time. We see that the different dark states develop at different rates, with the $v = 0$ one taking the longest to develop. Plotting $P_p(v = 0)$ vs time and fitting to an exponential decay curve, we see that the timescale for population of this dark state is $370\gamma_{SP}^{-1} = 2.6\mu$s (Fig. 4.10B). This is on the order of the timescale for collisionally induced velocity relaxation ($t_{relax} \sim 4\omega_{pi}^{-1} = 3\mu$s for $n = 10^{14}\,\mathrm{m}^{-3}$)[40]. As we will see in Sec. 4.5, this leads to collisional suppression of dark state population, as ions are collisionally pushed out of $v = 0$ before they are optically pumped into the dark state.

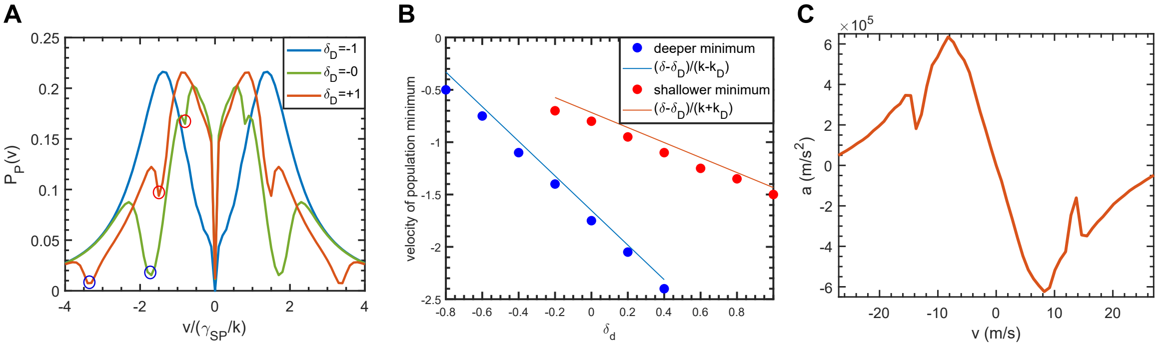

Figure 4.9 : (**A**): P state population as a function of ion velocity v from steady state OBE solutions for various δ_D ($\delta = -1$, $\Omega_{SP} = 1$, and $\Omega_{DP} = 1$ for all plots). We clearly see evidence of velocity dependent dark states, associated with minima in the P state populations, with locations circled in red and blue (we only circle the $v < 0$ states since $P(v)$ is symmetric about v). (**B**): Location of local minima in P state populations vs δ_D. There is good agreement with the locations expected from considering when the two photon transitions between S and D states are resonant. (**C**): Acceleration profile $a(v) = F_{OBE}(v)/m$ obtained from steady-state OBE solution for $\delta = -1$, $\delta_D = +1$, $\Omega_{SP} = \Omega_{DP} = 1$. Within the range defined by the capture velocity, $|v_c| = \delta/k = 9\,\mathrm{m/s}$, $a \propto -v$.

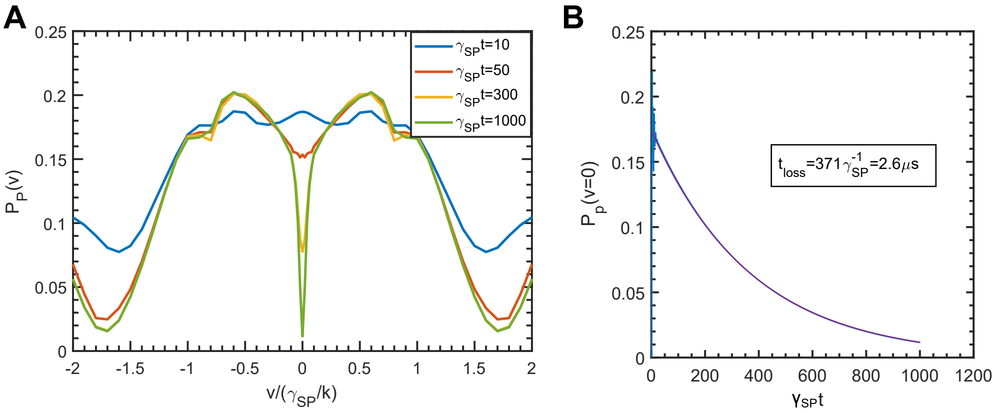

Figure 4.10 : (**A**): Time dependence of OBE solutions for $\delta_D = 0$, $\delta = -1$, $\Omega_{SP} = 1$, and $\Omega_{DP} = 1$. The $v = 0$ state associated with the dark state comprised solely of D state sublevels develops quite slowly. (**B**): P state population at $v = 0$ vs time. The timescale for the development of this dark state is shown to be $\sim 2.6\mu$s, on the order of the timescale for velocity changing collisions $\sim 4\omega_{pi}^{-1}$, and thus we may expect this state to be collisionally suppressed.

4.4.6 Combining Quantum Trajectories and Molecular Dynamics

To observe collisional suppression, along with the effects of collisional rethermalization and equipartioning between cooled and uncooled axes, we implement QT within an MD simulation. When combining two simulations, care must be taken to ensure that the units are consistent. Thus, we convert the ‘quantum units’ to ‘plasma units’. Below, I list a few of the important conversion factors:

- $\frac{\gamma_{SP}}{\omega_{pi}} = \frac{301}{\sqrt{n}}$
- $\frac{dt_p}{dt_q} = \frac{0.0035\omega_{pi}}{0.01\gamma_{SP}} = \frac{34.81}{\sqrt{n}}$
- $\frac{v_q}{v_p} = \frac{\gamma_{SP}/k}{a\omega_{pi}} = 2.05n^{1/6}$

where n is in units of $10^{14}\,\mathrm{m}^{-3}$. We see that, for all reasonable densities ($n < 10^{17}\,\mathrm{m}^{-3}$), the quantum trajectories timestep dt_q is the smaller timestep. Thus, the code is written such that dt_q defines the timestep. The quantum trajectories are propagated in each timestep. Every dt_p/dt_qth timestep (rounded to the nearest integer) the ion-ion interaction force calculation is performed in addition to propagating the quantum trajectories. For $n = 2 \times 10^{14}\mathrm{m}^{-3}$, this winds up being every 25th timestep.

To confirm that the QT code was integrated into the MD code successfully, the code was tested with the inter-particle forces turned off and the system initialized with $T_x = 450\,\mathrm{mK}$ and $n = 2 \times 10^{14}\,\mathrm{m}^{-3}$. The simulation returned a plot of temperature vs time in plasma units $\Gamma^{-1}(\omega_{pi}t)$. These results were converted to SI units and compared to the results from the previous simulations, which propagated the QT code in the quantum units, see Fig. 4.11. The good agreement implies that no errors were made in converting the QT code to plasma units.

Now, with the confidence that the difference in timescales has being handled properly, the MDQT code can be used to simulate laser cooling of a UNP.

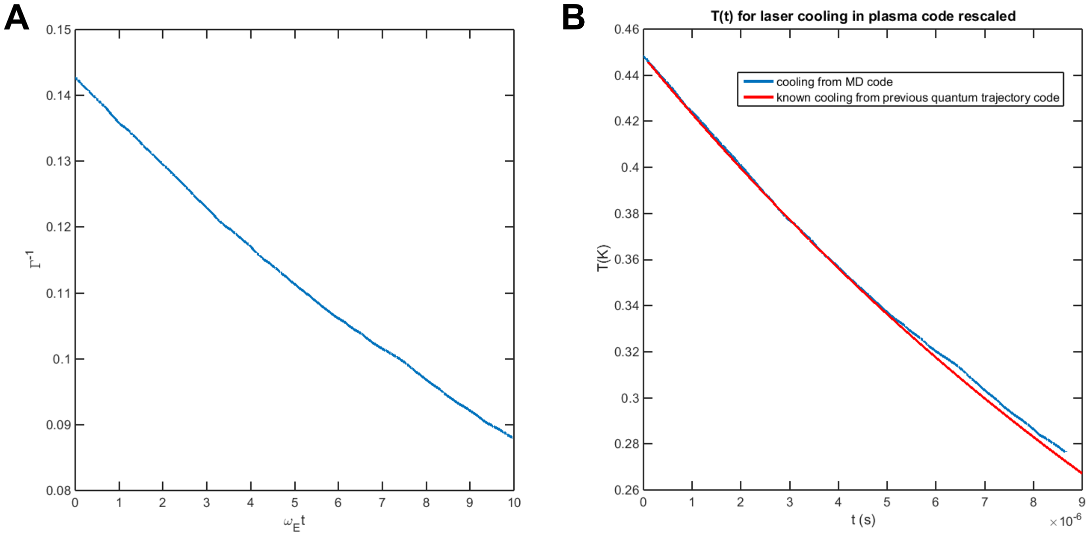

Figure 4.11 : (**A**): Γ_x^{-1} vs $\omega_E t$, where $\omega_E = \omega_{pi}/\sqrt{3}$ from the MDQT simulation with interactions off. (**B**): Same graph, but now plotted in units T (K) vs $t(\mu$s) and compared with the QT only simulation; the agreement indicates that the unit conversions were done properly in the implementation of QT within the MD simulation.

4.5 Observation of Collisional Suppression of Dark States

As we discussed in Secs. 4.1 and 4.4.5, collisions can inhibit the development of velocity dependent dark states. The dark state at $v = 0$ in Fig. 4.10 is particularly slow to develop, with $t_{EIT} \sim 2.6\mu$s, and also very narrow, with a velocity 'full-width half-max' (FWHM) of $\delta v = 0.6\,\mathrm{m/s}$. Meanwhile, we expect the velocity change due to collisions to be given by $dv \sim \omega_{coll} v_T dt$, where ω_{coll} is the 'velocity changing collision' (VCC) rate and is proportional to ω_{pi}. In [40] ω_{coll} was measured to be $\sim 0.2\omega_{pi}$ for $\Gamma \sim 3$. Per the discussion in Sec. 4.1, we expect this feature in $P_P(v)$ to be suppressed if $\omega_{coll} t_{EIT} v_T > \delta v$. Substituting in $0.2\omega_{pi}$ for ω_{coll} and assuming $\Gamma = 3$, we find that this is the case for $n \geq 10^{11}\,\mathrm{m}^{-3}$.

In order to test this, MDQT simulations were conducted for 7μs ($\sim 1000\gamma_{SP}^{-1}$) at a number of densities near this threshold with $\delta = -1$, $\delta_{DP} = 0$, $\Omega_{SP} = 1$, and $\Omega_{DP} = 1$.

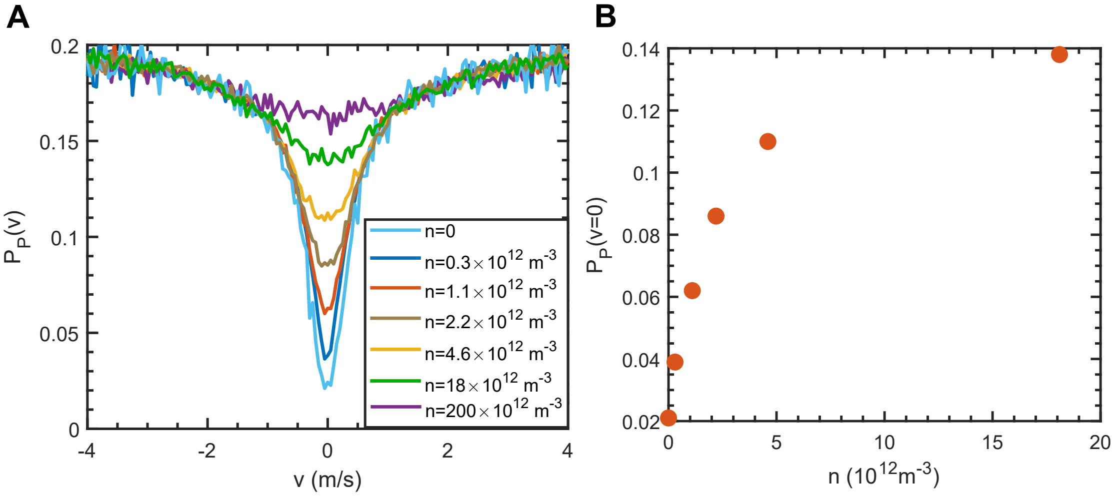

Figure 4.12 : (**A**): $P_p(v)$ vs v, where we've zoomed into the $v = 0$ dark state location, after 7μs of evolution performed by the MDQT code. We show data for a few different plasma densities. We observe that, as the density increases beyond $10^{11}\,\mathrm{m}^{-3}$, the state becomes suppressed due to velocity changing collisions, which ensure that the time for which the x component of a given ion's velocity (v_x) remains within the FWHM of the dark state is less than the dark state coupling timescale. (**B**): Population in the P state at $v = 0$ after 7μs of evolution as a function of n. The population saturates for $n \gtrsim 10^{13}\,\mathrm{m}^{-3}$, indicating full collisionally induced suppression of the dark state.

The resulting $P_P(v)$ curves are shown in Fig. 4.12A. We clearly see some suppression of this feature for $n \gtrsim 3 \times 10^{11}\,\mathrm{m}^{-3}$, which is around the density that we expected suppression to occur. In Fig. 4.12B, we plot the value of $P_P(v = 0)$ as a function of n. This is an indicator of how effectively the feature is suppressed. We observe that the suppression saturates for $n \gtrsim 10^{13}\,\mathrm{m}^{-3}$. This is lower than typical UNP densities ($10^{13}\,\mathrm{m}^{-3}$ or greater), and therefore the existence of this state should not affect the laser-cooling experiments described in Chapter 5, as it should be entirely collisionally suppressed.

On the other hand, the large dark state at $v \sim \pm 1.8\gamma_{SP}/k$ for $\delta_{DP} = 0$ observed in Fig. 4.10 develops on a timescale of $t \sim 10\gamma_{SP}^{-1} = 70\,\mathrm{ns}$ and has a width $\delta v \sim 3\,\mathrm{m/s}$. Estimating the suppression density in the same way we did for the $v = 0$ dark state gives $n \geq 2 \times 10^{16}\,\mathrm{m}^{-3}$. To test suppression of this state, MDQT simulations were performed for a range of densities between $5 \times 10^{14}\,\mathrm{m}^{-3}$ and $5 \times 10^{16}\,\mathrm{m}^{-3}$ for the same values of δ, δ_{DP}, Ω_{SP}, and Ω_{DP} for 500 ns of plasma evolution. The resulting $P_p(v)$ curves are shown in Fig. 4.13A. The feature is centered at $v = \pm 16\,\mathrm{m/s}$. Plotting $P_p(v = \pm 16\,\mathrm{m/s})$ vs n we see that as n increases this feature becomes increasingly suppressed as well, becoming fully suppressed for $n \gtrsim 2.5 \times 10^{16}\,\mathrm{m}^{-3}$ (Fig. 4.13B).

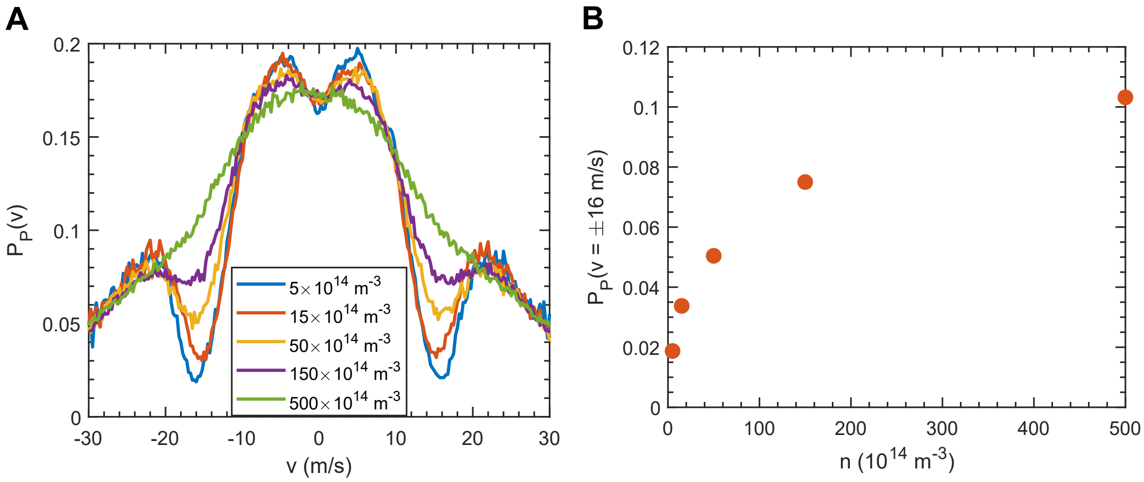

Figure 4.13 : (**A**): $P_p(v)$ vs v for a few densities after 500 ns of evolution performed by the MDQT code. We observe that, as the density increases beyond $10^{14}\,\mathrm{m}^{-3}$, the dark state becomes increasingly collisionally suppressed. (**B**): Population in the P state at $v = \pm 16\,\mathrm{m/s}$ after 500 ns of evolution as a function of n. The population saturates for $n \gtrsim 2.5 \times 10^{16}\,\mathrm{m}^{-3}$, indicating full collisionally induced suppression of the dark state.

4.6 Simulating Laser Cooling in a UNP

Based on the results in Section 4.4.4, we choose to run our simulation for $\Omega_{SP} = 1$, $\Omega_{DP} = 1$, $\delta_D = +1$, and $\delta = -1$. To reflect the initial conditions of our experiment, we choose a density $n = 2 \times 10^{14}\,\mathrm{m}^{-3}$, a screening parameter $\kappa = 0.5$, and for the cooling lasers to propagate along the x-axis.

4.6.1 Cooling in a Uniform, Non-Expanding Plasma

The first simulation that we consider here reproduces cooling conditions in the center of the cloud, where there is no expansion velocity. The simulation also ignores the effects of adiabatic cooling and electron-ion heating; we will discuss some ideas for how to incorporate these effects in Sec. 4.7.

Every $0.14\omega_{pi}t$, the following quantities are recorded:

- The kinetic energy along each axis $\langle v_{x,y,z}^2 \rangle$
- The total interaction energy.
- The velocity distribution along each axis $f(v_x, v_y, v_z)$, with a bin spacing of $0.0043a\omega_{pi}$.
- The x velocity of each particle, along with its probability of being measured in the P state (This is to record $P_P(v)$).

In Figure 4.14, we plot the kinetic energy along each axis vs time, expressed in plasma units (Fig. 4.14A) and SI units (Fig. 4.14B). At very short times DIH and kinetic energy oscillations are evident, after which the plasma approaches local thermal equilibrium at a scaled temperature value of $\Gamma^{-1} \sim 0.33$ in a few ω_{pi}^{-1}. Without laser cooling, this temperature eventually stabilizes. With laser cooling, we see a clear reduction in temperature throughout time. Moreover, there is clear evidence of cross-axis thermalization, as the energies along the uncooled axes start to decrease at a rate comparable to the cooled axis. All three axes lose energy at a rate comparable to 1/3 of the rate expected from the QT simulation of laser cooling (Compare Fig. 4.8 to Fig. 4.14B), consistent with what one might expect in a system that is laser cooled along 1D and exhibits rapid collisionally induced temperature redistribution between axes.

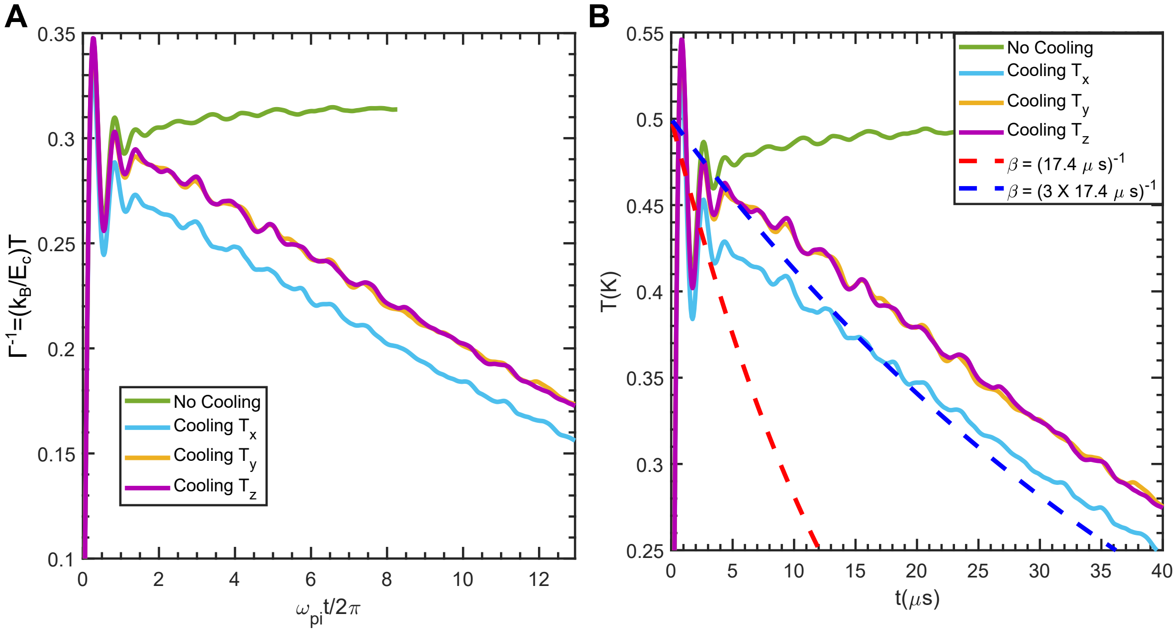

Figure 4.14 : (**A**): Γ^{-1} vs $\omega_{pi}t/2\pi$ for $n = 2 \times 10^{14}\,\mathrm{m}^{-3}$, $\kappa = 0.5$, $\delta = -1$, $\delta_D = 1$, $\Omega_{SP} = 1$, and $\Omega_{DP} = 1$. It's clear that, even though the cooling force is only applied along x, all three axes experience cooling due to collisional energy redistribution (e.g., heat flowing out of uncooled axes into the cooled axis). For the conditions used in the simulation, $\omega_{pi} = 2 \times 10^6\,\mathrm{s}^{-1}$ and $E_c/k_B = e^2/4\pi\epsilon_0 a_{ws} k_B = 1.57\,\mathrm{K}$. (**B**): Same plot but in SI units. Here we see that the cooling rate for each axis is approximately 1/3 of the cooling rate derived from a collisionless QT simulation $\beta = (17.4\mu\mathrm{s})^{-1}$, see Fig. 4.8. We see that we are able to reduce the temperature by a factor of ~ 2 in 40μs, which should be easily observable with LIF.

The collisional temperature redistribution makes it more difficult to observe the effect of laser cooling, as it reduces the amount by which the velocity distribution, which is what we actually measure, along the cooled axis is narrowed; in a collisional system, one must cool for $3t_{cool}$ to achieve a narrowing equivalent to what would be achieved in t_{cool} in a collisionless system. Nevertheless, the factor of 2 reduction in temperature observed after 40μs of cooling is large enough to observe using LIF, and occurs quickly enough to be observed *before* the plasma expands significantly ($\tau_{Exp} \sim 80\mu$s).

Measuring Thermalization Rates Through Laser Cooling

The fact that we do see the temperatures along the cooled and uncooled axes separate before the temperature difference stabilizes indicates that we could potentially use laser-cooling as a tool for measurement of the cross-axis thermalization rate (we discuss this in more detail in Sec. 8.1). Assuming a cooling rate β and a cross-axis thermalization rate ν, we would naively assume that the differential equations for the temperatures along ($\|$) and perpendicular ($\perp$) to the cooling axis are:

$$\begin{aligned}\frac{\partial T_{\|}}{\partial t} &= -\beta T_{\|} + 2\nu(T_{\perp} - T_{\|}) \\ \frac{\partial T_{\perp}}{\partial t} &= -\nu(T_{\perp} - T_{\|})\end{aligned} \tag{4.42}$$

However, there is another energy sink in the plasma: the correlation energy. As the plasma cools, the plasma becomes more spatially correlated, lowering the potential energy and thus reheating the plasma (see Sec. 2.2). We can determine the magnitude of this effect by calculating the difference between the potential energy at time t and the initial potential energy (where there are no spatial correlations). We plot this difference in Fig. 4.15. It is clear from the figure that cooling causes a subsequent lowering of the potential energy. Thus, we need to add terms to compensate for that in our equation for solving $T_{\|}$ and $T_{\perp}$:

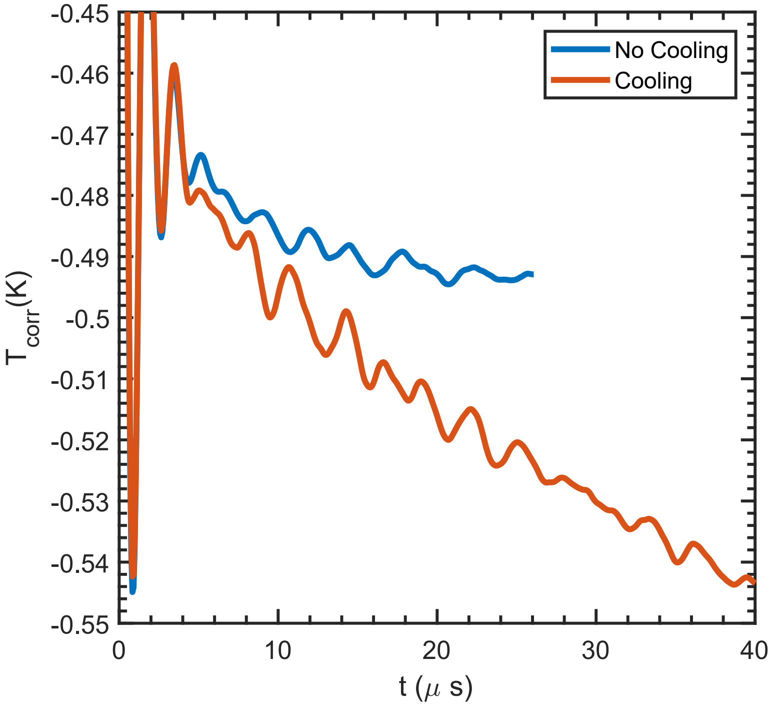

Figure 4.15 : Correlation Temperature with and without laser cooling. The more negative correlation temperature recorded when laser cooling reflects the fact that the ions become more spatially correlated as they are cooled, lowering the total potential energy. Due to energy conservation, this adds an additional heating term to the differential equations determining the temperature evolution in a laser-cooled plasma, see Eq. 4.43

$$\begin{aligned}\frac{\partial T_{\|}}{\partial t} &= -\beta T_x - \frac{\partial T_{corr}}{\partial t} + 2\nu(T_{\perp} - T_{\|})\\ \frac{\partial T_{\perp}}{\partial t} &= -\nu(T_{\perp} - T_{\|}) - \frac{\partial T_{corr}}{\partial t}\\ \frac{\partial T_{corr}}{\partial t} &= -\mu\left(T_{corr} - T_{corr,Eq}\left(\frac{T_{\|} + 2T_{\perp}}{3}, \kappa\right)\right)\end{aligned} \tag{4.43}$$

where T_{corr} and $T_{corr,Eq}$ are the same quantities defined in Sec. 2.3.1. These equations do not factor in any of the oscillatory behavior in DIH, thus, we choose to fit the simulation data for $t > 4.5\mu$s, the results are shown in Fig. 4.16. We measure the following values:

- $\beta = (6.2 \pm 0.1) \times 10^4 \mathrm{s}^{-1}$
- $\nu = (0.117 \pm 0.005)\omega_{pi}$
- $\mu = (0.089 \pm 0.005)\omega_{pi}$

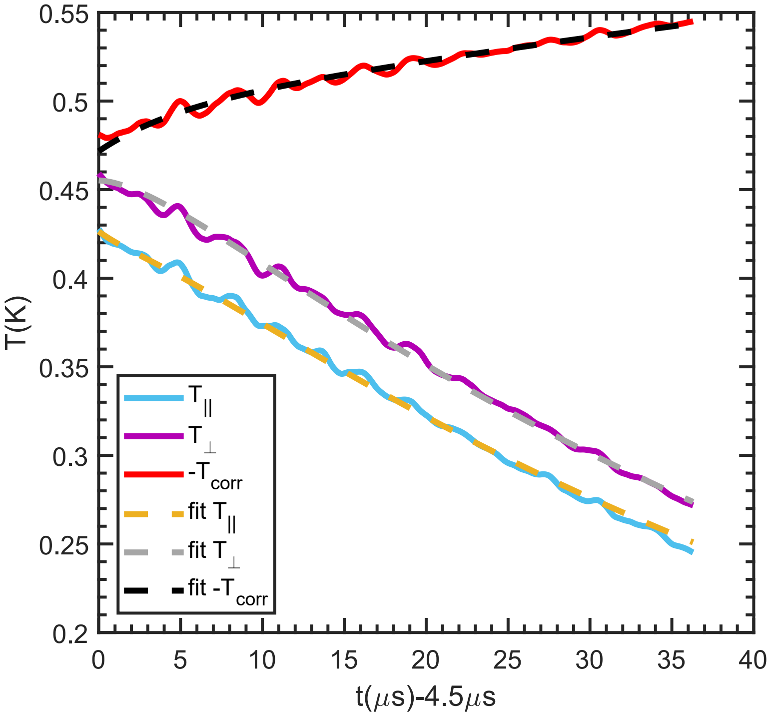

Figure 4.16 : Results of fitting MDQT data to Eq. 4.43 with β, ν, and μ as free parameters.

This fitted value of β is within 10% of the value expected from the collisionless quantum trajectories simulation (from Fig. 4.8: $\beta^{-1} = 17.6\mu\mathrm{s} \rightarrow \beta = 5.7 \times 10^4\,\mathrm{s}^{-1}$). The value for ν agrees with direct MD simulations (see Sec. 8.1).

4.6.2 Laser Cooling in an Accelerating Frame

As the plasma expands into vacuum, we expect the cooling efficiency to drop off in regions away from the center. This is due to the development of expansion velocities

$v_{Exp} > v_c$, where $v_c \sim \gamma_{SP}/k \sim 9\,\mathrm{m/s}$ and v_{Exp} is given by Eq. 2.21. For example, at $r = 2.5\,\mathrm{mm}$ in a plasma with $\sigma_0 = 2.5\,\mathrm{mm}$ and $T_e = 15\,\mathrm{K}$, $v_{Exp} = 19\,\mathrm{m/s}$ after $70\mu\mathrm{s}$ of expansion. That group of ions is shifted far enough off-resonance by the expansion that the ions do not scatter photons from either laser, even the one opposing their motion. Another way to think about this is that, for $v_{Exp} > v_c$, the slope of dv/dt is no longer negative and thus the force is no longer a damping force. This effect is illustrated in Fig. 4.17.

We can estimate the expected magnitude of this effect by calculating the rate of change of the thermal energy per particle $\langle \partial_t E_T \rangle$, where the brackets indicate an ensemble average over the velocity distribution function $f(v, v_{Exp})$ and $E_T = m\left(v - v_{Exp}\right)^2/2$. Given a force profile $F(v)$ and a thermalized velocity distribution $f(v, v_{Exp}) = 1/\sqrt{2\pi\sigma_v}\exp\left[-(v - v_{Exp})^2/2\sigma_v^2\right]$, where $\sigma_v = \sqrt{k_B T/m_i}$, we can write $\langle \partial_t E_T \rangle = \int_{-\infty}^{\infty} f(v, v_{Exp}) F(v)(v - v_{exp}) dv$. Assuming that the thermalization timescale is faster than the cooling timescale, this rate of energy change can be related to a rate of temperature change $\beta = -\langle \partial_t E_T \rangle / k_B T$. Deriving the expected force profile $F(v)$ directly from the OBE solution allows us to numerically calculate β as a function of v_{Exp}, see Fig. 4.17C.

From the plot of $\beta(v_{Exp})$, it's clear that the cooling efficiency drops drastically for non-zero v_{Exp}, and eventually becomes completely ineffective for $v_{Exp} \sim 10\,\mathrm{m/s}$. Since this velocity is eventually achieved by all ions except those within the central region (defined as $|x| < x_c \lesssim 1\,\mathrm{mm}$, see Fig. 4.17A), we expect that cooling will only be effective throughout the plasma expansion for these central ions. Moreover, even for $5\,\mathrm{m/s} < v_{Exp} < 10\,\mathrm{m/s}$, the cooling efficiency still drops pretty severely, so the ions towards the outer edge of x_c will also be cooled less effectively.

Although we cannot simulate the full hydrodynamic expansion & adiabatic cooling

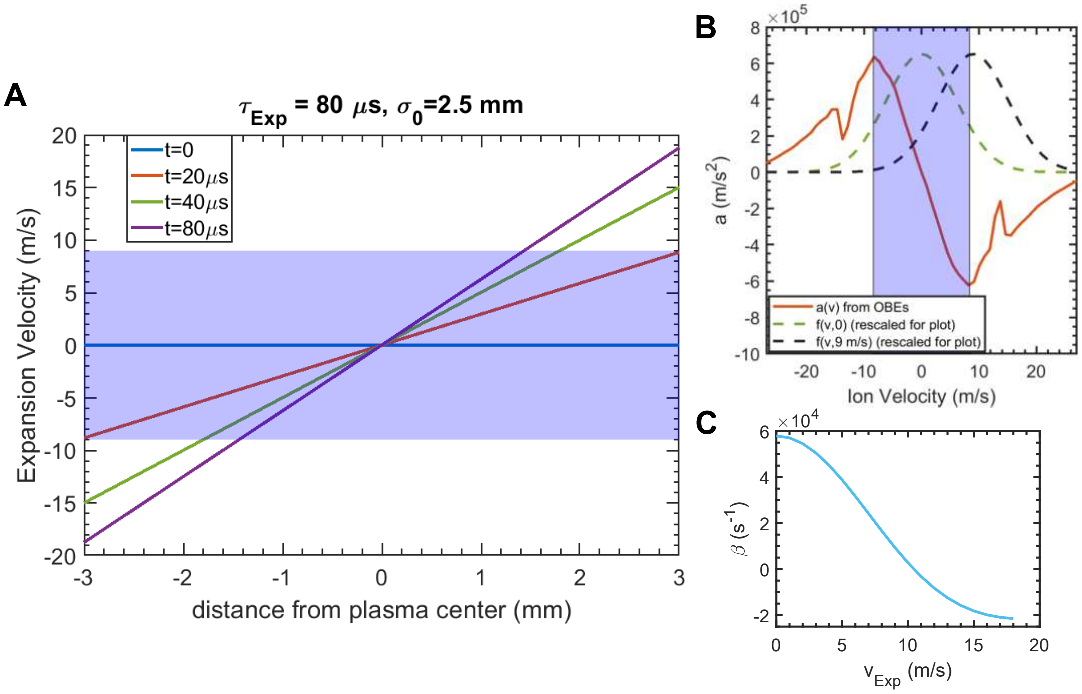

Figure 4.17 : (**A**): Expansion velocity vs distance from plasma center at various time t after photoionization for $\sigma_0 = 2.5\,\mathrm{mm}$ and $T_e = 15\,\mathrm{K}$. The capture region bounded by $\pm v_c$ is indicated in blue. As time and distance from plasma center increase, $|v_{Exp}|$ begins to exceed $|v_c|$. (**B**): Plot of a direct calculation of the force from the OBE solutions for $\delta = -1$, $\delta_D = +1$, $\Omega_{SP} = 1$, and $\Omega_{DP} = 1$, (see Fig. 4.9C) where the shaded capture velocity region corresponds to where the force is linear. We also plot the velocity distribution functions (arbitrarily normalized) for $T = 400\,\mathrm{mK}$ with $v_{exp} = 0$ and $v_{Exp} = 9\,\mathrm{m/s}$ as green and black dashed lines, respectively. We see that for $v_{Exp} = 9\,\mathrm{m/s}$, half of the ions are outside of the capture range, and thus we expect poor cooling efficiency. (**C**): Numerically calculated cooling rate as a function of expansion velocity for $T = 400\,\mathrm{mK}$. Here we see that the cooling rate reaches zero for $v_{Exp} \sim 9\,\mathrm{m/s}$, as expected.

of the plasma, we can still use the simulation to test how cooling is affected by plasma expansion. Our approach is to follow the frame of an element of the plasma as a function of time after photoionization. This results in a time dependent Doppler-shift of magnitude $kv_{frame}(t)$ to each laser, where v_{frame} is the velocity of the plasma element. For an element of plasma initially located at $x = c\sigma_0$, where c is a constant indicating the ion position as a fraction of σ_0, we can use Eq. 2.19 to determine:

$$v_{frame}(t) = \frac{d\left(c\sigma(t)\right)}{dt} = \frac{c\sigma_0}{\tau_{exp}^2}\frac{t}{\sqrt{1+t^2/\tau_{Exp}^2}} \tag{4.44}$$

We set $c > 0$, such that the frame is moving towards $+x$ and therefore the added shift is negative for the right-ward pointing lasers and positive for the left-ward pointing lasers in Fig. 4.3A.

We perform simulations for $c = 0.5$ and $c = 1$ in a plasma with $n = 2 \times 10^{14}\,\mathrm{m}^{-3}$, $T_e = 19\,\mathrm{K}$, and $\sigma_0 = 4\,\mathrm{mm}$, comparable to the values that we will ultimately use when performing laser-cooling in the experiment. We continue to use the values for detunings and Rabi frequencies described in the previous section.

In Fig. 4.18A, we plot the resulting $T(t)$ curves from the simulations. At early times, we observe that the cooling efficiency is largely unaffected by the motion of the frame, which makes sense since v_{frame} is small for early times. As v_{frame} increases, however, the cooling efficiency clearly drops in both expanding cases, and it drops more rapidly for $c = 1$, as expected. What this implies is that, as the plasma expands, eventually we will develop a spatial gradient in T, as cooling becomes less effective far away from the center. Indeed, we do see this behavior in our experiment, see Sec. 5.1.

We can also observe an additional effect, namely, the slowing of the expansion itself. We track the mean velocity in the x direction ($\langle v_{Sim} \rangle$) during the simulation and we observe that it becomes negative throughout the cooling process, meaning that the ions are *receding* from the expanding frame. This makes sense, since a velocity damping force should also inhibit the development of expansion velocity in addition to reducing the thermal velocities. In the laboratory frame, the expansion velocity is then given by $v_{Exp} = v_{frame} - \langle v_{Sim} \rangle$. The results are shown in Fig. 4.18B and C. We observe a clear reduction in velocity for both $c = 1$ and $c = 0.5$.

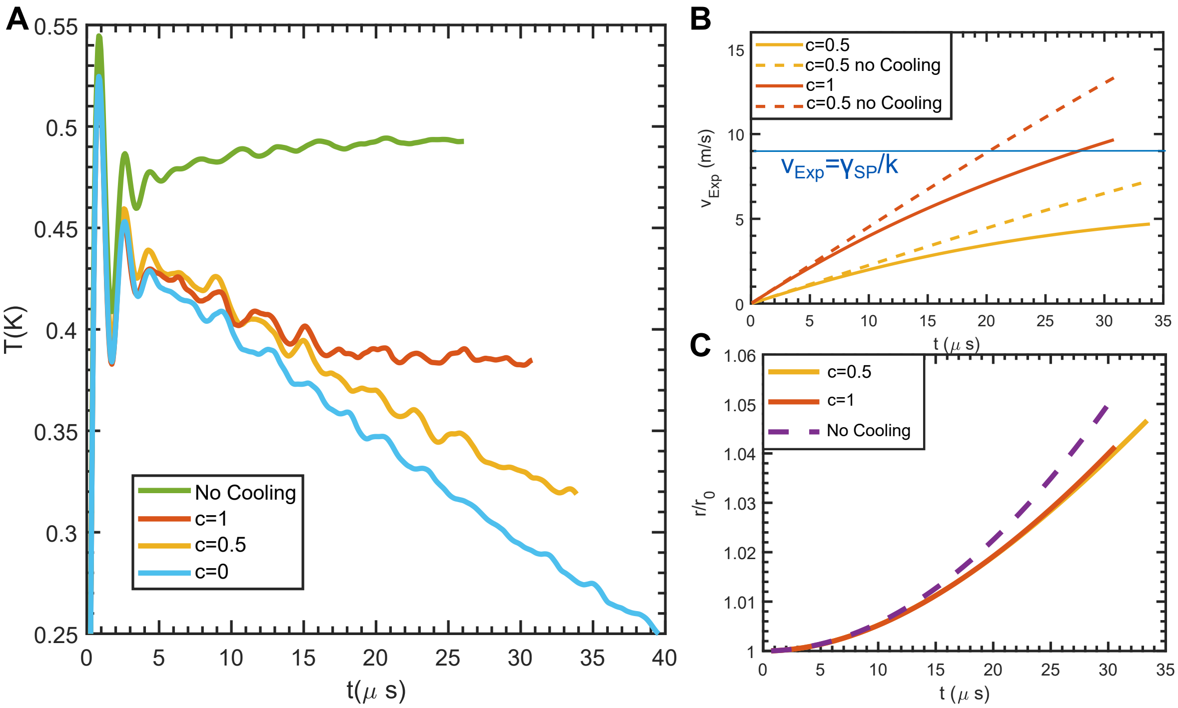

Figure 4.18 : (**A**): Results of MDQT simulations of laser-cooling in an accelerating frame corresponding to a group of ions with initial starting location at $c\sigma_0$ where $\sigma_0 = 4\,\mathrm{mm}$, $T_e = 19\,\mathrm{K}$, and $n = 2 \times 10^{14}\,\mathrm{m}^{-3}$. For finite c, the cooling eventually 'turns off'. (**B**): Expansion velocity in the laboratory frame. The laser-cooling clearly inhibits the development of expansion velocity. We also indicate when the expansion velocity becomes greater than v_c, which seems to correspond to when the cooling for $c = 1$ turns completely off (although the cooling rate becomes negligible even before that point, see Fig. 4.17C). (**C**): Corresponding value of r/r_0 for each 'chunk' with and without laser cooling, derived by numerical integration of v_{Exp} over time. After $t \sim 25\mu$s we begin to see the effect of differential retardation; as the $c = 1$ ions develop enough expansion velocity, the lasers become less effective at retarding expansion. This will eventually lead to the development of non-Gaussian spatial profiles, see Sec. 5.4.

Eventually, however, the expansion velocity in the outer regions becomes so large that the lasers are also no longer effective at retarding the expansion. We see some evidence of this in Fig. 4.18C, as the position shift of the $c = 1$ group with respect to its traveling frame becomes less than that of the $c = 0.5$ group at later times. This will eventually result in the plasma developing a *non-gaussian* spatial distribution along the cooled axis, which invalidates the assumptions used to derive Eq. 2.19 and, therefore, Eq. 4.44 would become invalid as well. We observe this behavior in our experiment, see Sec. 5.4. As it stands now, the MD simulation has no way of taking this 'differential retardation' into account. We include a discussion of how to incorporate this effect in Sec. 4.7.

4.7 Future Work

The combined MDQT code for simulating laser-couplings in a collisional system is clearly a powerful tool. In this chapter, we have applied this code to the laser-cooling of a UNP, while in Chapter 7 we will demonstrate its utility for testing how optical pumping techniques can be used to induce spin-velocity correlations, and how the relaxation of those correlations after the pumping lasers are turned off can be related to transport quantities like viscosity.

The laser-cooling simulations have demonstrated that collisions will isotropize energy across all degrees of freedom on a timescale faster than that for which energy is removed, and thus cooling along one dimension effectively cools all degrees of freedom in the plasma. This will make it extremely difficult to observe the effect of laser-cooling through a modification of the velocity distribution of low v particles, as is typically done in a 'first' laser-cooling demonstration of a new substance (as in Fig. 4.1C for diatomic molecules [80]). Nevertheless, with the right parameters, an optical molasses laser-cooling scheme can remove enough energy from the plasma to reduce the temperature (along all axes) by about a factor of 2 in 40μs (Fig. 4.14), which is less than the expansion timescale, τ_{Exp}, achievable in large UNP systems ($\sim 80\mu$s). This is easily observable using spectroscopic thermometry (Sec. 3.3). We also observed that collisions suppress the development of dark states (Fig. 4.12), which would otherwise inhibit laser-cooling.

Finally, we demonstrated that laser-cooling can, for a time, be effective at both cooling and slowing expansion of ions that are away from the center of the cloud. However, the cooling efficiency drops dramatically as v_{Exp} approaches $v_c \sim \gamma_{SP}/k \sim 9\,\mathrm{m/s}$. This may ultimately result in a thermal gradient where ions near $x = 0$ become very cold while the rest of the cloud is cooled much less effectively.

However, although this simulation is a powerful tool for the reasons described above, it is in some sense incomplete, as it does not fully account for the expansion of the plasma. For example, the effects of adiabatic cooling and of the density reduction are noticeably absent. The effect of non-gaussian spatial distributions resulting from stronger retardation of ion expansion in the center of the plasma (see Fig. 4.18C) is also neglected. A full treatment of the problem of laser cooling a UNP would by necessity involve a multiscale approach in which the MDQT simulation acts at the lowest level while either a hydrodynamic or kinetic code handles the macroscopic expansion.

Nevertheless, the results presented in this chapter give us confidence that a UNP can be effectively laser-cooled. The next chapter discusses our successful experimental implementation of laser cooling in a UNP!

Chapter 5

Laser Cooling Results

In Chapter 3, we introduced the lasers and frequency stabilization techniques needed for laser-cooling Sr^+ ions in a UNP, while in Chapter 4 we used our MDQT code to demonstrate the feasibility of laser-cooling in UNPs. In this chapter, we introduce results from the first ever successful implementation of laser-cooling in a neutral plasma, resulting in $T = 50\,\mathrm{mK}$ and $\Gamma = 11$ after 135μs of cooling. We observe many of the features indicated in the simulation data from Chapter 4, such as expansion slowing, non-gaussian spatial profiles induced by differential expansion retardation, the development of spatial thermal gradients due to the 'turn off' of cooling efficiency in expanding regions of the plasma, and cross-axis thermalization.

If we only consider the temperature in the center of the cloud, where cooling is effective throughout the plasma evolution, the laser-cooling results are well described by augmenting the hydrodynamic model discussed in Eqs. 2.22-Eqs. 2.26 with additional terms determined by the cooling rate β introduced in the previous chapter. We determine a value for β from a measurement of the scattering rate, which we discuss in Sec. 5.1.1. The measured value agrees with the cooling rate observed in the QT simulation within 10%. Further, with this β value as input, the hydrodynamic model matches the laser-cooling results quite nicely. These results are introduced in Section 5.2 while the model is discussed in Section 5.5.

We will also discuss how expansion retardation and cooling effectiveness depend on the laser detuning (Sec. 5.6). In particular, we emphasize that the hydrodynamic expansion forces us into a choice between cooling most effectively, but only in the center, which occurs for relatively low detuning, or cooling somewhat less effectively, but cooling a larger region of the plasma, which is the case for far detuned light. This results from the fact that further detuning of the laser increases the capture velocity v_c, thus increasing the portion of the plasma that has expansion velocity $v_{Exp} < v_c$, while at the same time lowering the overall cooling rate (for far detuning, $\beta \propto \delta^{-1}$). We also show data indicating that blue detuning the 408 nm beams results in heating the plasma ($\Gamma = 0.8$ after 135μs of heating) and enhances the plasma expansion.

We conclude with a discussion about the broader impact of the main result, which is the ability to tune Γ by using lasers to cool or heat the plasma. In particular, the ability to reach $\Gamma > 10$ places UNPs in a regime similar to some regions of white dwarf stars, which are interesting but yet under-diagnosed strongly coupled plasma systems. More generally, tuning Γ further into the strong coupling regime will allow for a number of interesting studies of transport, equilibration, and equilibrium properties of strongly coupled plasmas, which are ill described by conventional plasma kinetic theory. Such measurements should aid ongoing efforts from the plasma community for extending kinetic theory into the strongly coupled regime by providing accurate tests of the theory.

We note here that for all data in this chapter, excluding the results presented in Figs 5.9 and 5.10, the initial conditions of the plasma after photoionization are $n = 1.3 \times 10^{14}\,\mathrm{m}^{-3}$, $T_e = 15.5(3)\,\mathrm{K}$, $\sigma_x = 2.4(1)\,\mathrm{mm}$, $\sigma_{y,z} = 3.1(1)\,\mathrm{mm}$, and $\kappa = 0.51$, leading to a post DIH temperature of $T_{DIH} = 0.41(0.03)\,\mathrm{K}$ and an expansion time $\tau_{Exp} = 75\mu$s.

5.1 First Tests of Laser Cooling

Immediately after photoionization, we turn on counter-propagating σ^+ and σ^- beams tuned near the D2 Sr^+ transition at 408 nm, which propagate along the x-axis, along with the associated repump beams (see Fig. 3.5) at 1033 nm and 1092 nm. These lasers remain on for a time t_{cool}. The detunings, δ, δ_{DP}, and δ_{D3P1} (the latter is the detuning of the 1092 nm laser from the $\mathrm{D}_{3/2}$ to $\mathrm{S}_{1/2}$ transition, which we always set to 0), are set by the transfer lock technique described in Sec. 3.4.1. The power of the 408 nm laser, and therefore its Rabi frequency ($\Omega_{SP} = \sqrt{s_0/2}\gamma_{SP} = \sqrt{I/2I_{Sat}}\gamma_{SP}$, where $I_{sat} = 43.1\,\mathrm{mW/cm^2}$), is controlled by an acousto-optic modulator (AOM) with a voltage controlled attenuator. The AOM is also used to shutter the beam. After cooling, we use LIF (Sec. 3.3) to measure the velocity distribution along the LIF beam axis, which is set to either $\hat{x}$ (e.g. along the cooling lasers) or $\hat{y}$ (perpendicular to the cooling lasers). From these distributions we can determine spatially resolved temperature profiles $T_x(x, y)$ and $T_y(x, y)$.

For the first attempt at laser cooling, we chose parameters that closely reflect the optimal conditions discussed in Chapter 4: $\delta/2\pi = 0.9\gamma_{SP}/2\pi = -20\,\mathrm{MHz}$, $\delta_{DP}/2\pi = +15\,\mathrm{MHz}$, and $s_{0,SP} = 2.3$ which gives $\Omega_{SP}/2\pi = 1.07\gamma_{SP}/2\pi \sim 24\,\mathrm{MHz}$. For comparison purposes, we also took data with $\delta/2\pi = +20\,\mathrm{MHz}$ and with no cooling lasers.

In Fig. 5.1 we plot T_x as a function of x for these three conditions. For $\delta/2\pi = -20\,\mathrm{MHz}$, after 60μs we see a factor of 2 reduction in the temperature in the center of the cloud ($|x| \leq 1.5\,\mathrm{mm}$) with respect to the temperature for the case where no lasers are applied, while the temperature outside of this region is unaffected by the lasers. This is the **first** successful application of laser-cooling in a neutral plasma!

The cooling in the center continues throughout the plasma evolution, eventually

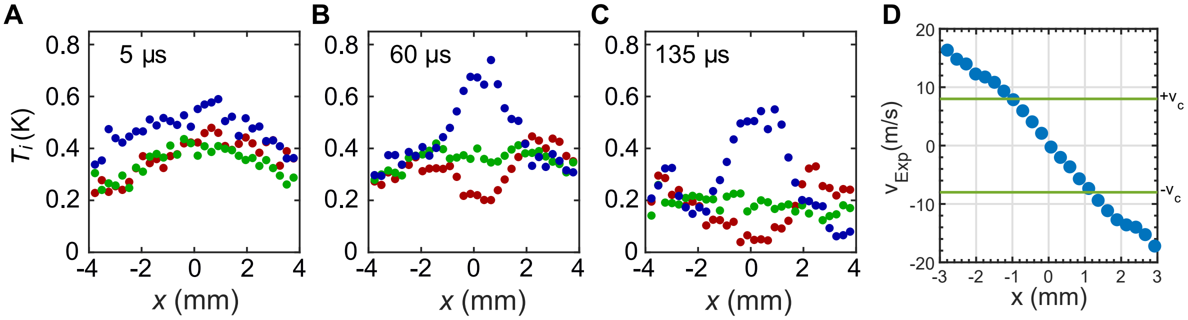

Figure 5.1 : (**A-C**): Spatially resolved measurements of ion temperature at various times after photoionization for laser detuning $\delta/2\pi = -20\,\mathrm{MHz}$ (red, cooling), $\delta/2\pi = +20\,\mathrm{MHz}$ (blue, heating), and no 408 nm laser (green). Each measurement corresponds to a region with $\Delta x = 260\mu\mathrm{s}$ and $\Delta y = 4.5\,\mathrm{mm}$ centered at $y = 0$. (**A**): Shortly after photoionization, we observe that the lasers have had little effect on the temperature. The observed spatial dependence here reflects the density profile of the plasma ($T_{DIH} \propto n^{1/3}$). (**B**): After 60μs, we observe that the temperature within a central region of the cloud $|x| \leq 1\,\mathrm{mm}$ is strongly affected by the 408 nm laser. For red detuning we observe a factor of 2 reduction in ion temperature compared to the case where no laser is applied. (**C**): After 135μs we observe a factor of 4 reduction in temperature when cooling. (**D**): LIF measurement of expansion velocity 30μs after photoionization, with the capture range defined by $|v| < v_c$ indicated by green lines. We see that even after only 30μs of evolution, all regions of the cloud with $|x| \geq 1\,\mathrm{mm}$ have $v_{Exp} > v_c$, for which the cooling (or heating) is ineffective. This is responsible for the spatial temperature dependence at subsequent times in **B** and **C**.

leading to a factor of 4 reduction in temperature after 135μs of cooling. Blue detuned light heats the plasma, as expected, and the heating is also only effective in the center.

The spatial gradient in temperature ultimately results from regions away from the center of the cloud achieving expansion velocity $|v_{Exp}| > v_c$, where the capture velocity $v_c = |\delta/k| \sim 8\,\mathrm{m/s}$ (see Fig. 5.1D). We observed this behavior in the MDQT simulation as well (see Figs 4.17 and 4.18).

As a side note, throughout our analysis we ignore the effect of thermal conductivity which should, in principle, eventually reduce the spatial temperature gradient. We justify this by approximating the effect of thermal conductivity. The 1D heat equation [136],

$$\frac{\partial T}{\partial t} = \frac{K}{c_p \rho}\frac{\partial^2 T}{\partial x^2} \approx \frac{2K}{5nk_B}\frac{\partial^2 T}{\partial x^2}, \tag{5.1}$$

where K is the thermal conductivity, ρ is the mass density, and c_p is specific heat capacity at constant pressure, determines the rate of temperature change resulting from spatial variations in temperature. In the last step we assumed that c_p is equal to the ideal gas value of $5nk_B/2\rho$ (in principal, there should be some strong coupling corrections, however they should not change c_p by more than an order of magnitude). For SCPs, the thermal conductivity $K \sim nk_B\omega_{pi}a^2$ [58], and therefore $\partial_t T = 2\omega_{pi}a^2\partial_x^2 T/5$. Fitting the red-detuned $T(x)$ data for $|x| < 0.5\,\mathrm{mm}$ in Fig. 5.1B to a quadratic, we find $\partial_x^2 T = 0.075\,\mathrm{K/mm}^2$. For $n \sim 10^{14}\,\mathrm{m}^{-3}$, this gives $\partial_t T \approx 7\mu\mathrm{K}/\mu\mathrm{s}$, resulting in a negligible effect throughout the $\sim 100\mu$s evolution considered here.

5.1.1 Spatially Resolved Measurement of Photon Scattering Rate

To further explore how expansion affects laser cooling, we developed a tool for measuring the scattering rate $R_s(x, y, t_{cool})$ as a function of ion location, where the origin is defined by the plasma center, throughout the plasma evolution:

- The cooling and repump beams are applied for a time t_{cool}
- For a time t_{loss}, the 1092 nm repump laser is turned off while the 408 nm and 1033 nm lasers remain on. During this time, ions will fall into the unobserved $\mathrm{D}_{3/2}$ at a rate equal to the branching ratio for this state (1/150, see Fig. 3.5) multiplied by the scattering rate $R_s(x, y, t_{cool})$.
- The 408 nm laser is turned off after t_{loss}.

- We wait $\sim 1\mu$s for the 1033 nm laser to repump all ions in the $\mathrm{D}_{5/2}$ state back into $\mathrm{S}_{1/2}$.

- We use LIF to measure the density of ions in the S state, $n_S(x, y)$, as a function of t_{decay}. By fitting this density within regions of width $dx = 650\mu$m and $dy = 650\mu$m to an exponential decay curve, we obtain the spatially-dependent leak rate into the $\mathrm{D}_{3/2}$ state ($R_{leak}(x, y, t_{cool})$). Multiplying R_{leak} by 150 gives $R_s(x, y, t_{cool})$.

This procedure is summarized in Fig. 5.2A, and is similar to a procedure described in[81] for measuring the scattering rate for lasers interacting with a triatomic molecule. We will always plot R_s/γ_{SP}.

In Fig. 5.2A and Fig. 5.2B we show 'false color maps' of $R_s(x, y, t_{cool})$ at $t_{cool} = 5\mu$s and $t_{cool} = 60\mu$s, respectively, for $\delta/2\pi = -20$ MHz. Here we clearly observe the effect of expansion: for $t_{cool} = 60\mu$s only the region $|x| \leq 1.5$ mm seems to scatter effectively, as the outer regions have $v_{Exp} > v_c$. This is further illustrated in Fig. 5.2C, in which we plot R_s averaged over the y axis $R_{x,s}(x) = \frac{1}{w_y}\int_{-w_y/2}^{w_y/2} R_s(x, y)dy$, where w_y is the size of the y dimension of the false-color maps.

We can also use this technique to study how the scattering rate in different regions changes with δ. In Fig. 5.3A-C we show false-color maps at $t_{cool} = 60\mu$s for $\delta/2\pi = -20$ MHz, $\delta/2\pi = -40$ MHz and $\delta/2\pi = -60$ MHz. As the cooling laser becomes further detuned, we see the false-color map bifurcate in x. The peaks in the false-color maps correspond to regions where the magnitude of the doppler shift due to the x component of expansion velocity, $|kv_{x,Exp}|$, matches $|\delta|$ (see Fig. 5.3E). In Fig. 5.3D we plot $R_{s,x}(x)$ for this data, here it is clear that the splitting of the peaks increases with δ, as expected. The asymmetry in the peaks is caused by a power imbalance

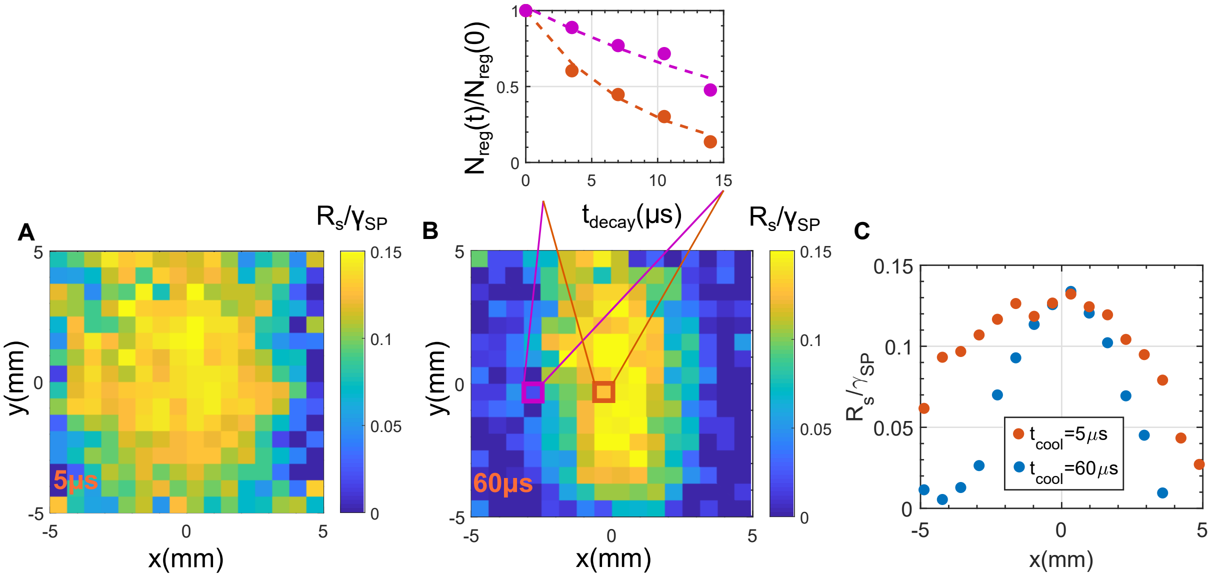

Figure 5.2 : (**A**): 'False-color map' of $R_s(x,y)/\gamma_{SP}$ for t_{cool}=5μs. The region of plasma for which the ions strongly scatter light from the cooling laser is much larger after 5μs of expansion than it is after 60μs of expansion (**B**). The shrinking of this region along the x axis, which is the axis along which the lasers propagate, at later times is caused by the increasing expansion velocity v_{Exp} with both t and x (Eq. 2.21). Inset of (**B**): Plot of N_{reg}/N_0 vs. t_{decay} for two highlighted regions in **B** along with associated fits to exponential decay curves. These fits are what we use to derive the R_s displayed in the false-color maps. (**C**): Average value of R_s integrated along the y axis. The size of the region over which the cooling lasers induce photon scattering is clearly seen to shrink in size as the plasma expands, while the scattering rate in the center of the cloud where $v_{exp} = 0$ remains constant throughout time.

between the two counter-propagating 408 nm beams caused by losses from optical elements along the beam path.

If we assume that the cooling is optimized when R_s is maximized, then we can also use this tool to determine the optimal parameters for the 1033 nm laser. We simply vary the detuning and power in order to maximize R_s. In Fig. 5.4A we plot R_s, averaged over the central 1 mm×1 mm region of the cloud, vs. $\delta_{DP}/2\pi$ and see that it is peaked at $\sim$ +15 MHz. We suspect that the non-zero optimal detuning results from the influence of dark states (Sec. 4.4.5 and 4.5). In Fig. 5.4B we plot R_s,

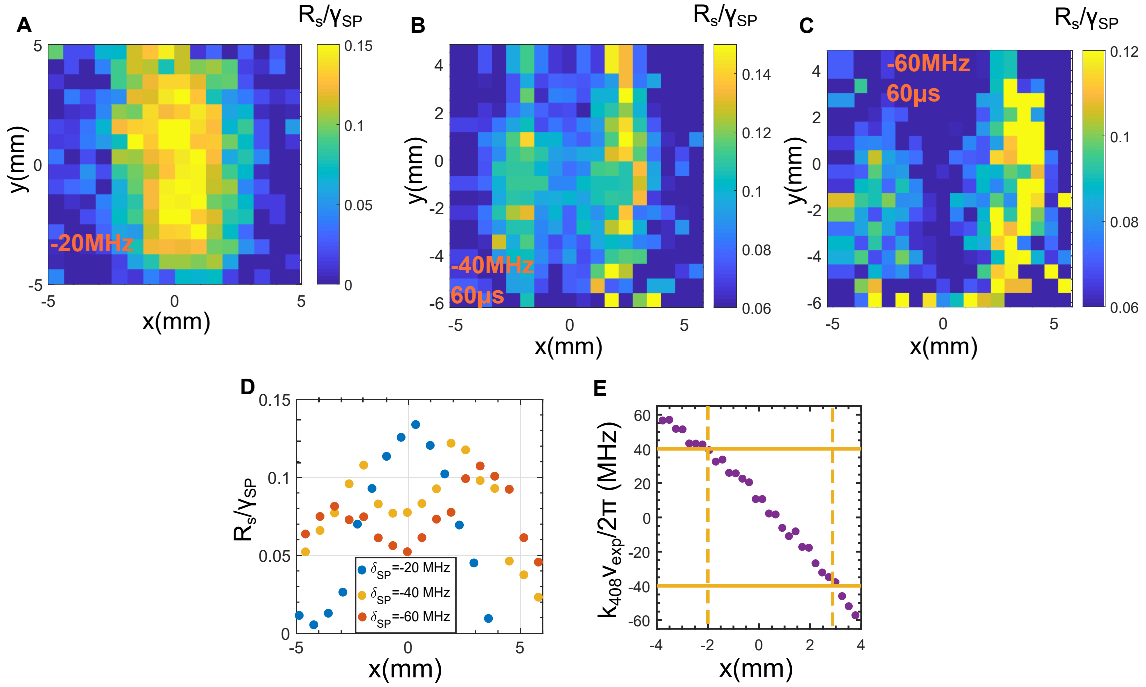

Figure 5.3 : (**A-C**): False-color maps of R_s for $\delta/2\pi = -20\,\mathrm{MHz}$, $\delta/2\pi = -40\,\mathrm{MHz}$, and $\delta/2\pi = -60\,\mathrm{MHz}$ for $t_{cool} = 60\mu\mathrm{s}$. We see that, as the laser is detuned further from resonance, the scattering false-color map bifurcates into two regions of high scattering. (**D**): Average value of R_s integrated along the y axis. The peaks clearly move apart as δ is increased. We associate the peak locations with the position for which $kv_{exp}(x) = \delta$. The asymmetry in the peaks is caused by a power imbalance between the two counter-propagating 408 nm beams caused by losses from optical elements along the beam path. (**E**): Plot of $kv_{exp}(x)$. We have marked $kv_{exp}(x)/2\pi = \pm 40\,\mathrm{MHz}$ with solid yellow lines, and have drawn dashed yellow lines to indicate where the $kv_{exp}(x)/2\pi$ data intersect with 40 MHz. Comparing **D** and **E**, we indeed observe that the peaks in R_s are located within $\sim 0.5\,\mathrm{mm}$ of the points in space where $kv_{exp}(x)/2\pi = \pm 40\,\mathrm{MHz}$.

averaged over the same region, versus the 1033 nm laser intensity and show that we are well within the saturation regime. Therefore, we can conclude that the 1033 nm laser power is not limiting the cooling efficiency.

Finally, we can also use these measurements to obtain an estimate of the cooling rate. We make two assumptions. First, we assume that the force is linear and of

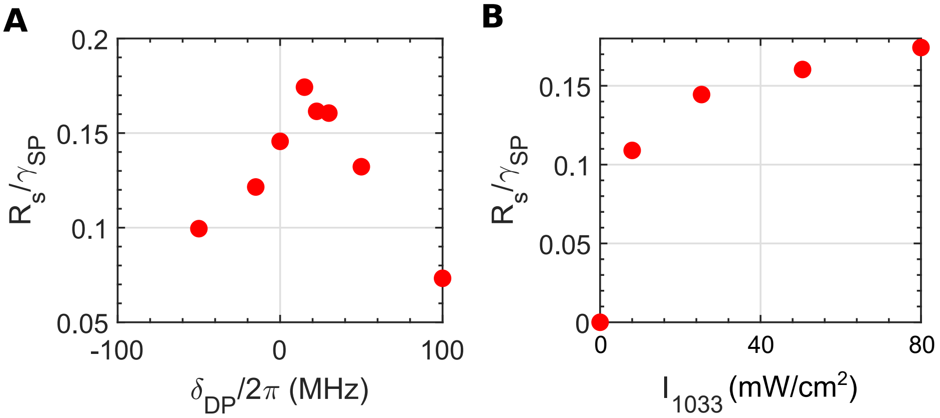

Figure 5.4 : (**A**): R_s/γ_{SP} vs $\delta_{DP}/2\pi$. The scattering rate is peaked around $\delta_{DP}/2\pi \approx$ 15 MHz, and thus we use this detuning for the remainder of the data presented in this chapter. (**B**): Scattering rate vs 1033 nm intensity. We see that 80 mW/cm^2 (the maximum available given the 1033 mm laser power and the need for the beam size w to be $\gtrsim$ 5 mm in order to illuminate the whole plasma) is sufficiently high to place the system in the saturation regime, where R_s no longer depends linearly on intensity.

form $F = -\beta v/2m$, where β is the cooling rate introduced in chapter 4 (a force of this form leads to $\partial_t T = -\beta T$), for $|v| < |\delta/k|$, which is justified by examining the force profile determined in Fig. 4.17B. Second, we assume that for $v = |\delta/k|$ the scattering is entirely from the laser propagating opposite to the velocity projection along $\hat{x}$, which is a reasonable assumption for $|\delta| \gtrsim \gamma_{SP}$. Thus, the laser-cooling force for this specific velocity is $\vec{F}(v = \pm\delta/k) = \mp R_s \hbar k \hat{x}$ and, using the linear force assumption, we find $\beta = 2R_s\hbar k^2/\delta m_i$. The -20 MHz data in Fig. 5.3 corresponds to the parameters used in the laser cooling data in Fig. 5.1. For the peak value of $R_s \sim 0.14\gamma_{SP} = (19 \pm 1) \times 10^6\,\mathrm{s}^{-1}$, we find $\beta_R = (52 \pm 2) \times 10^3\,\mathrm{s}^{-1}$. This is within 10% of the result from the QT simulation, $\beta_{QT} = 57 \times 10^3\,\mathrm{s}^{-1}$ (see Fig. 4.8).

5.2 Cooling in the Central Region of the Plasma: Achievement of $\Gamma > 10$

In this section, we will consider only the 'central' region defined by $|x| \leq 0.5\,\mathrm{mm}$, where the cooling is most effective. In Fig. 5.5A, we plot the temperature in this region vs time, while in Fig. 5.5B we plot the corresponding value of Γ. For the data taken without the cooling lasers, we see the features of electron-ion heating and adiabatic cooling discussed in Sec. 2.3, which ultimately leads to $\Gamma \sim 2.5$ throughout the evolution.

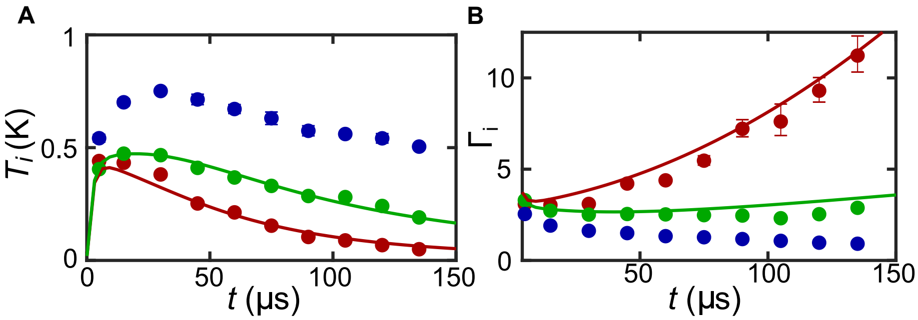

Figure 5.5 : (**A**): Temperature in the central region ($|x| < 0.5\,\mathrm{mm}$) vs. time after photoionization for laser detuning $\delta/2\pi = -20\,\mathrm{MHz}$ (red), $\delta/2\pi = +20\,\mathrm{MHz}$ (blue), and no 408 nm laser (green). (**B**): Γ vs time after photoionization. We achieve $\Gamma = 11(1)$ after laser cooling, and $\Gamma = 0.8(1)$ after laser-heating, for 135μs. By only cooling or heating for part of the plasma evolution, we can tune Γ between these parameters. Thus, the introduction of optical forces provided by the 408 nm laser allows for tunability of Γ over an order of magnitude. Studying plasma transport quantities and thermodynamic properties over this order of magnitude in phase space will help elucidate the ways in which strong coupling affects plasma behavior. Solid lines come from the model described in Sec. 5.5.

With the addition of the cooling (or heating) lasers, we can see from Fig. 5.5 that Γ can be tuned between 0.8 and 11 after applying the lasers for 135μs. Thus, UNP experiments are now capable of exploring a full order of magnitude in Γ, which should prove very useful for studying how strong coupling modifies plasma behavior.

The solid lines in Fig. 5.5 derive from a hydrodynamic model similar to that presented in Sec. 2.3, which we discuss in greater detail in Sec. 5.5. Based off of the good agreement to the model, it seems likely that cooling continues to increase Γ even after 135μs. However, below $50\,$mK the LIF based temperature measurements become difficult. This is because the doppler linewidth ($\sigma_f/2\pi \leq 5\,$MHz for $T \leq 50\,$mK) has become much smaller than the natural linewidth of the D1 line used for LIF spectroscopy ($\gamma_{D1}/2\pi = 21\,$MHz). Increasing the temperature resolution by, for example, using a narrow two-photon transition to one of the metastable D states would be needed to demonstrate further enhancement of Γ after the point at which $T_i < 50\,$mK.

5.3 Observation of Cross-Axis Thermalization

The plasma must be in local thermal equilibrium in order for Γ to be well-defined and useful for describing thermodynamic properties. This cannot necessarily be assumed in this case because the cooling is applied only along one dimension. However, as we discussed in Sec. 4.6.1, cross-axis thermalization should be rapid enough for the temperature to stay nearly isotropic throughout the plasma evolution process, with all three axes cooling at roughly the same rate. This is because local thermal equilibrium is established on the timescale of a few times the inverse ion plasma frequency [137]. We observe that ω_{pi}^{-1} ranges from $0.7\,\mu$s to 2μs throughout the plasma evolution, and thus the equilibration timescale is much faster than the 1D cooling timescale of $\beta^{-1} \sim 20\mu$s.

We can verify this in our plasma by measuring T_y, the temperature along an axis perpendicular to the cooling axis x. We do this by propagating the LIF laser along the $\hat{y}$ instead of $\hat{x}$; the doppler broadened data will then reflect the velocity distribution along that axis (Sec. 3.3).

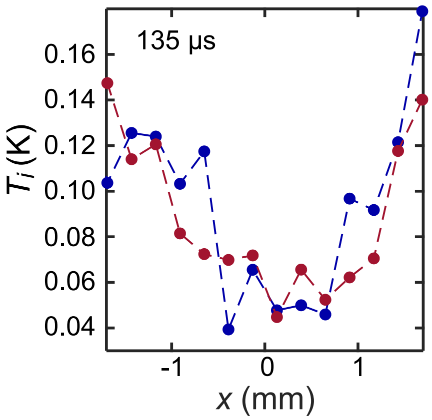

Figure 5.6 : Temperature parallel (T_x,blue) and perpendicular (T_y, red) to the laser-cooling axis as a function of the displacement along the cooling axis 135μs after photoionization. T_y data come from spectral distribution measurements taken by propagating the LIF beam along $\hat{y}$. The temperatures along both axes match, both in the center of the plasma where cooling is most effective, and away from the center as cooling efficiency diminishes. This indicates that the cross-axis thermalization rate is indeed higher than the cooling rate, and thus that all degrees of freedom are cooled by 1D optical molasses and that the plasma is truly at local thermal equilibrium with $\Gamma = 11$ (Fig. 5.5) in the center after laser-cooling.

In Fig. 5.6 we plot both T_x and T_y vs x after cooling for 135μs. If the plasma is in local thermal equilibrium, then the pattern exhibited in the T_x data, with cold temperatures in the center and warmer temperatures away from the center (see also Fig. 5.1), should also be reflected for T_y and, further, T_y should be as cold as T_x in the center. This is indeed what we observe in Fig. 5.6, and therefore we conclude that local thermal equilibrium is achieved throughout the plasma and thus the thermodynamic properties in the center of the cloud after laser-cooling should be reflective of $\Gamma \geq 10$.

5.4 Retardation of Hydrodynamic Expansion

In addition to reducing the temperature of the plasma, a velocity-damping force of the form $F \propto -v$ should also inhibit the development of expansion velocity. We observed this in the MDQT simulations in Sec. 4.6.2. In Fig. 5.7A we show the evolution of the plasma density for the same data shown in Figs. 5.1 and 5.5. From the figure, it is clear that the expansion is indeed slowed along the cooling axis x for red detuning. This is further demonstrated in Fig. 5.7B, which shows σ_x derived from fitting the density profile integrated along y, $n_x = \frac{1}{w_y}\int_{-w_y/2}^{w_y/2} dy\, n(x,y)$, where w_y is the size of the image along the y axis, to a gaussian. In 5.7C we plot $v_{Exp}(x)$ at 60μs for each configuration; clearly the velocity is enhanced for blue detuning and retarded for red detuning.

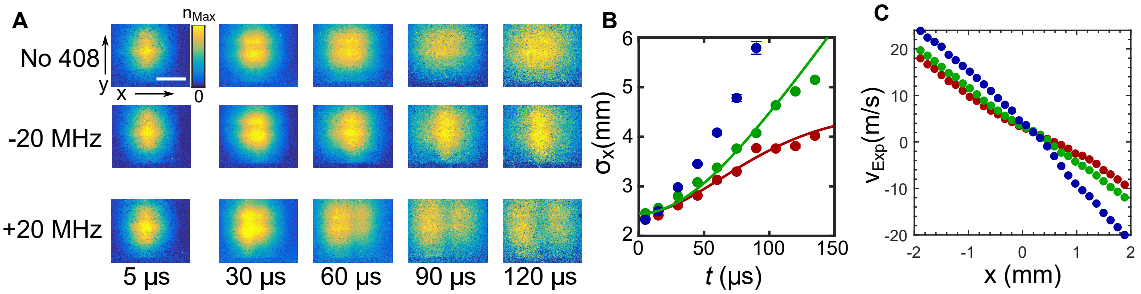

Figure 5.7 : (**A**) Evolution of plasma density distribution. Red-detuned optical molasses along $\hat{x}$ retards expansion, while blue-detuned light accelerates it, eventually leading to bifurcation. The scale bar is 5 mm. The color bar is rescaled for each time to $n_{max} = (13, 8.5, 4.2, 2.2, 1.3) \times 10^7\,\mathrm{cm}^{-3}$ for $t = (5, 30, 60, 90, 120)\,\mu$s. (**B**) RMS radius $\sigma_x(t)$ from gaussian fit to experimental data for $\delta/2\pi = -20\,\mathrm{MHz}$ (red), $\delta/2\pi = +20\,\mathrm{MHz}$ (blue), and no 408 nm laser (green). Solid lines come from the model described in Sec. 5.5. (**C**): $v_{Exp,x}(x)$ at $t = 60\mu$s for same parameters. Here we clearly observe an enhancement in expansion velocities for blue detuned light and a reduction in expansion velocity for red detuned light.

The solid lines in Fig. 5.7B are generated from the same hydrodynamic model used to generate the solid lines in Fig. 5.5, which is discussed in detail in Sec. 5.5.

One of the assumptions inherent in that model is that the spatial profile of the plasma remains gaussian throughout. This is clearly not the case for the blue-detuned data in Fig. 5.7B, for which the plasma bifurcates along the heating axis, which is why we *do not* include any model results for the blue-detuned data. The plasma bifurcates in this case because ions are accelerated away from the center by the 408 nm laser until they develop $v_{Exp} > v_c$, at which point the force diminishes. The diminishing of the force outside of the center causes ions to pile up around locations in x where $|v_{Exp}| = v_c$.

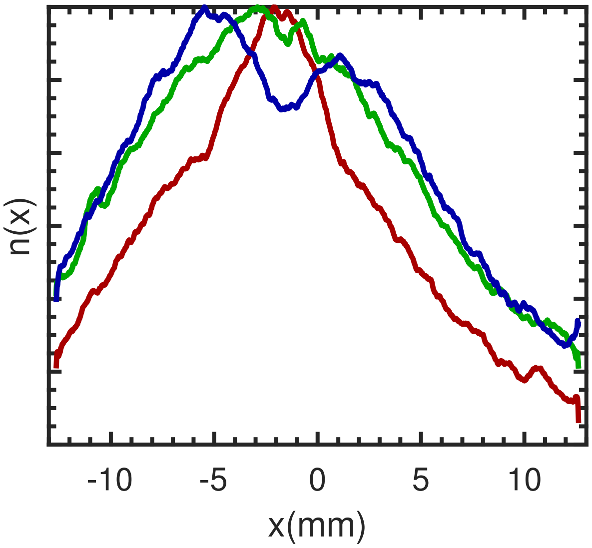

Figure 5.8 : Plot of the density profile after integrating along the y axis after 135μs of expansion with and without the 408 nm laser (colors correspond to the same conditions here as they do in Fig. 5.1). The profiles are normalized such that the peak values are equivalent. We see that, for blue detuning, the plasma bifurcates. This is also observed in Fig. 5.7A. The spatial profile also differs from a gaussian when the laser is red detuned, as we clearly see a sharp peaking of the density in the center of the profile (compare to the profile in absence of light, which does reflect a gaussian spatial profile). This results from differential retardation in the presence of red-detuned light; the expansion is inhibited more strongly in the center of the plasma than it is along the wings.

The spatial profile of the plasma is also modified by the red-detuned beam, albeit less severely. In Fig. 5.8 we plot $n_x(x)$ after 135μs for all three conditions. It is clear that the profile from the red-detuned case is also not quite a gaussian, but instead is more sharply peaked towards the center of the cloud as compared to the profile of the plasma taken without any 408 nm laser, which is gaussian. This results from the concept of differential retardation, which was introduced in Sec. 4.6.2, in which the expansion of ions that start near the center of the plasma is more strongly inhibited than that of ions further away from the center. Intuitively, this should result in a sharper peaking of the ion profile around the center of the plasma, as observed. Despite the non-gaussian profile, we still use the hydrodynamic model for fitting this data; a full description would likely involve a multiscale simulation with laser-cooling at the lowest level feeding into a hydrodynamic or kinetic model on a higher level, as alluded to in Sec. 4.7.

The effect of the expansion retardation can be further magnified by starting with a larger plasma, as this decreases the radial expansion force (Eq. 2.11) and increases τ_{Exp}. In Fig. 5.9, we show data for a plasma of initial size $\sigma_x = 3.2\,\mathrm{mm}$ and $\sigma_{y,z} = 4.5\,\mathrm{mm}$ with an initial density $n_0 = 4.4 \times 10^{13}\,\mathrm{m}^{-3}$ and electron temperature of $T_{e0} = 15.5(3)\,\mathrm{K}$. For this data, we also increased the saturation parameter s_0 up to 7 and further detuned the lasers to ±50 MHz. Once again, we clearly see a slowing of the expansion, however, the effect is much stronger than in the previous dataset. An enhancement of the central density for the red-detuned case can also be observed (this was true of the data in Fig. 5.7 as well, however it is much less evident in that dataset). The effectiveness of the optical forces observed in this case raises the possibility of confinement of the plasma, perhaps in combination with magnetic fields in a hybrid MOT [114] and magnetic bottle [138] configuration; we discuss this possibility in greater detail in Sec. 6.1.

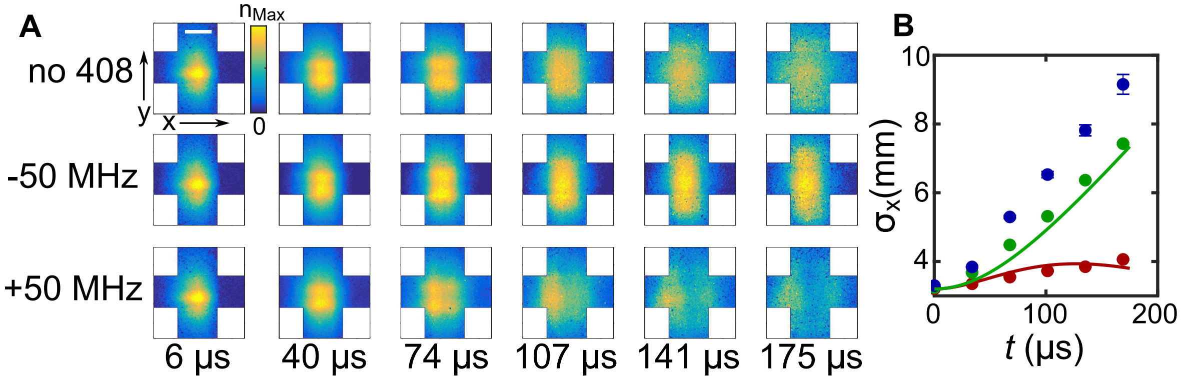

Figure 5.9 : (**A**) Evolution of the density distribution for larger initial size ($\sigma_x = 3.2\,\text{mm}$, $\sigma_{y,z} = 4.5\,\text{mm}$), detuning ($\delta/2\pi = \pm 50\,\text{MHz}$), and laser intensity ($s_0 = 7$). The 408 nm laser configuration is indicated beside each row of images, and the laser-cooling time is below. The scale bar is 5 mm. The color bar is rescaled for each time to $n_{max} = (4.4, 2.7, 1.6, 1.0, 0.7, 0.5) \times 10^7\,\text{cm}^{-3}$ for $t = (6, 40, 74, 107, 141, 175)\,\mu\text{s}$. The effects of laser forces on the expansion appear to be stronger in this configuration than in the smaller plasmas discussed in Fig. 5.7. The images are a composite of data for LIF laser propagation along the $\hat{x}$ direction and $\hat{y}$ direction, which extends the spatial range of usable data but leads to the cross-pattern of each image. (**B**) RMS radius $\sigma_x(t)$ from gaussian fit to experimental data. Red, Green, and Blue correspond to $\delta/2\pi = -50$ MHz, no 408 nm laser, and $\delta/2\pi = +50$ MHz, respectively. Solid lines come from the model described in Sec. 5.5.

For this dataset we consider the evolution of σ_y as well, see Fig. 5.10A. We observe nearly no effect resulting from the presence of the 408 nm laser. At very long times, we may expect that slowing expansion along the x axis should actually *increase* the rate of expansion along other axes. This is because inhibiting the adiabatic expansion should decrease the rate at which electron temperature T_e decreases, and we would then expect the higher value of T_e to result in an enhancement of the expansion rate along the other axes (Eq. 2.11). We do see some evidence of this when plotting $\vec{v}_{Exp} \cdot \hat{y}$, see Fig. 5.10B, however it appears the velocity is not enhanced enough for the difference to be reflected in the spatial profile.

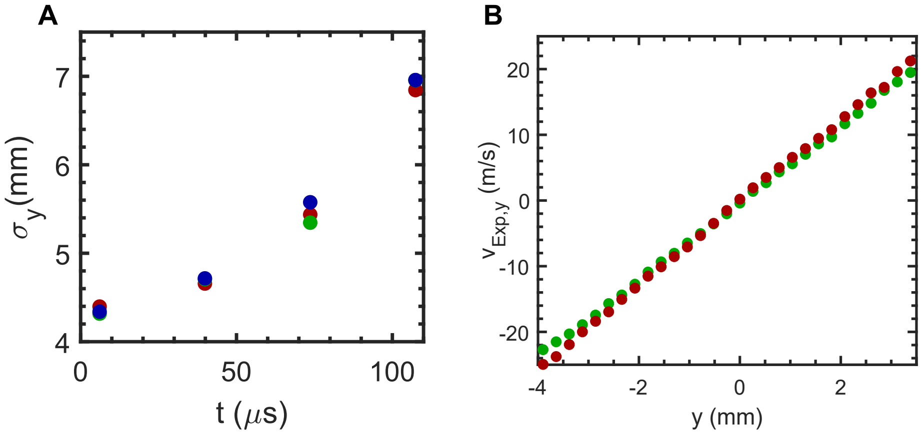

Figure 5.10 : (**A**) Evolution of $\sigma_y(t)$ for the same parameters considered in Fig. 5.9. Red, Green, and Blue correspond to $\delta/2\pi = -50\,\mathrm{MHz}$, no 408 nm laser, and $\delta/2\pi = +50\,\mathrm{MHz}$, respectively. We see no evidence that the application of the 408 nm laser along the x axis affects the evolution of the size of the cloud in the y dimension. (**B**) $v_{exp,y}(y)$ for red detuning and without 408 nm laser. We see some evidence that slowing along the x axis may lead to enhancement in the expansion velocity along y here, but this difference is apparently not large enough to be resolved in the measurements of the size of the plasma shown in **A**. In any case, the effect of the laser on the expansion along perpendicular axes is clearly negligible compared to the effect along the laser axis (compare **B** to Fig. 5.7C)

5.5 Adding Laser Cooling to the Hydrodynamic Equations for Plasma Evolution (Eqs. 2.22- 2.26)

The solid lines in Figs. 5.5, 5.7, and 5.9 all come from fits using a model describing the hydrodynamic evolution of the plasma in the presence of Doppler-cooling beams. This derivation largely follows the one presented in [61], which was one of the earliest papers (along with [72] and [73]) to discuss laser-cooling of a UNP. In that model, however, it was assumed that optical molasses was applied in 3D and, further, that the induced damping force was effective for all velocities, not just for velocity $|v| < v_c$ as is the case in our system. As a result, we will need to make some modifications to the equations presented in that paper.

The introduction of the cooling lasers means that we must modify the hydrodynamic description given in Eqs. 2.22- 2.26. First, we must add an additional term $-\beta T_i/3$ to the differential equation for the time evolution of the ion temperature. This assumes that the effective 3D cooling rate is 1/3 of the 1D doppler cooling rate β and that we can describe the plasma as having an equal temperature along all three axes due to rapid relaxation of temperature anisotropy. The simulation results shown in Sec. 4.6.2 and the experimental data shown in Sec. 5.3 justify these assumptions. Second, we must add an additional term $c\beta/6$ to the differential equation for the time evolution of the hydrodynamic expansion parameter γ, where the coefficient c is a fit parameter that takes into account the fact that not all of the plasma is slowed by the cooling beam (see Fig. 5.8).

Finally, we must take into account the anisotropy that develops in σ due to the expansion being slowed only along the x axis, in addition to the fact that the plasma begins in an anisotropic state with $\sigma_x < \sigma_{y,z}$. We make two assumptions here. First, we interpret the size parameter in the hydrodynamic equations to be the geometric mean of the rms radii $\sigma_{GM} \equiv \left(\sigma_x \sigma_{y,z}^2\right)^{1/3}$. Second, we assume that cooling the plasma does not affect the evolution of the plasma size along uncooled axes (see Fig. 5.10A) and that this evolution is simply determined by Eqs. 2.22- 2.26 with σ_0 set to be the initial size along that axis; we denote these solutions $\sigma_{x,y,z|NC}$.

For the data taken without 408 nm light *all* axes are uncooled axes. Applying the assumptions above to that data, the model temperature curve in Fig. 5.5 results from the solution of Eqs. 2.22- 2.26 with $\sigma_0 = \sigma_{GM0}$ while the model curves for σ_x in Figs. 5.7 and 5.9 are solutions to Eqs. 2.22- 2.26 with $\sigma_0 = \sigma_{x0}$.

After incorporating all of the assumptions above, the equations describing the hydrodynamic evolution of a plasma irradiated by 1D cooling lasers are:

$$\frac{\partial \sigma_{GM}^2}{\partial t} = 2\gamma \sigma_{GM}^2 \tag{5.2}$$

$$\frac{\partial \gamma}{\partial t} = \frac{k_B\left(T_e + T_i + \frac{T_{corr}}{2}\right)}{m_i \sigma_{GM}^2} - \gamma\left(\gamma + \boldsymbol{c}\frac{\boldsymbol{\beta}}{\mathbf{6}}\right) \tag{5.3}$$

$$\frac{\partial T_e}{\partial t} = -2\gamma T_e - \gamma_{ei}(T_e - T_i) \tag{5.4}$$

$$\frac{\partial T_i}{\partial t} = -2\gamma T_i + \gamma_{ei}(T_e - T_i) - \gamma T_{corr} - \frac{\partial T_{corr}}{\partial t} \boldsymbol{-} \frac{\boldsymbol{\beta}}{\mathbf{3}}\boldsymbol{T_i} \tag{5.5}$$

$$\frac{\partial T_{corr}}{\partial t} = \omega_{pi}\left[T_{corr,Eq}(n_i, T_i) - T_{corr}\right]. \tag{5.6}$$

$$\sigma_x(t) = \sigma_{GM}^3(t)/\sigma_{y,z|NC}^2(t) \tag{5.7}$$

where $\sigma_{y,z|NC}$ are the solutions to the above equations for $\beta = 0$ (which are simply identical to Eqs. 2.22- 2.26) for $\sigma_0 = \sigma_{y,z}(t = 0)$ and we have bolded the terms we've added to account for laser-cooling forces.

For the model lines describing the cooling data, we have used the value of β determined by the peak value of the R_s measurements described in Sec. 5.1 ($52(2) \times 10^3\,\mathrm{s}^{-1}$ for the data in Figs. 5.5 and 5.7 and $20(2) \times 10^3\,\mathrm{s}^{-1}$ for the data in Fig. 5.9), while c is a fit parameter. We find that $c = 0.6(1)$ for the data in Figs. 5.5 and 5.7 and $c = 2.9(5)$ for the data in Fig. 5.9.

The model appears to qualitatively describe the data quite well, despite its limitations. However, we expected to measure $c < 1$ in all cases, since this parameter is designed to take into account *inefficiencies* resulting from expansion velocity shifting ions with $v_{Exp} > v_c$ out of resonance with the cooling lasers. We attribute the fitted value of $c > 1$ for the expansion data in Fig. 5.9 to the greater asymmetry of the expansion for these conditions; we believe that this model will begin to fail when the plasma becomes sufficiently asymmetric.

5.6 Impact of Varying δ on the Efficiency of Laser-Cooling and of Expansion Retardation

Thus far, we have only looked at temperature data with $\delta/2\pi = \pm 20\,\mathrm{MHz}$. However, the $R_s(x,y)$ data in Sec. 5.1 demonstrate why looking at how both laser-cooling and expansion slowing depend on δ can be of interest. Fig. 5.3 indicates that, as the laser becomes further detuned, the region of plasma that scatters photons broadens. This suggests that a larger portion of the cloud may be cooled for $\delta/2\pi < -20\,\mathrm{MHz}$, as opposed to just the region where $|x| < 0.5\,\mathrm{mm}$ indicated in Fig. 5.1 for $\delta/2\pi = -20\,\mathrm{MHz}$. However, the way in which we derived β in Sec. 5.1 makes it clear that $\beta \propto |\delta|^{-1}$ (this is only true for $|\delta| \gtrsim \gamma_{SP}$, since for δ nearer to resonance an ion moving with velocity $v = \delta/k$ will still have a significant probability of scattering light from the 'wrong' laser, violating one of the assumptions made in that derivation), and thus as a trade-off, we should expect lower cooling efficiency at far detuning.

In Fig. 5.11A, we plot the temperature in the center of the plasma after 135μs of cooling vs δ. Indeed, for $|\delta| \gtrsim \gamma_{SP}$ the effectiveness of the laser-cooling and laser-heating appears to have an inverse relation to $|\delta|$. The peak cooling and heating efficiencies occur for $\delta/2\pi = \pm 20\,\mathrm{MHz}$. In Fig. 5.11B we plot T vs x for $\delta/2\pi = -10\,\mathrm{MHz}$ and -30 MHz. We can clearly see that the region of plasma that is effectively cooled is much broader when $\delta = -30\,\mathrm{MHz}$, coming at the cost of lower cooling efficiency in the center of the cloud.

We also examined how changes in δ affect how the expansion is modified by the 408 nm laser, see Fig. 5.11C. What we observe is that the values of δ for which expansion is most effectively slowed (or enhanced, for $\delta > 0$) are further from resonance than $\pm 20\,\mathrm{MHz}$. This makes sense, since in order for the laser to affect the plasma

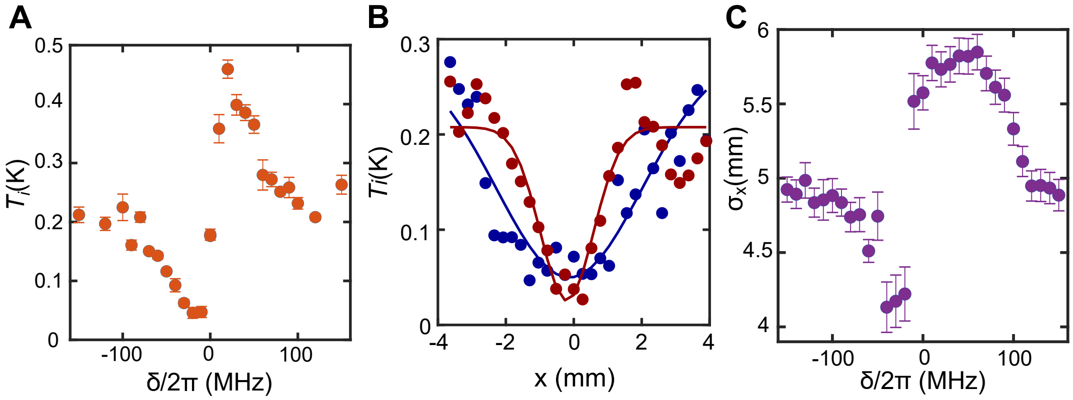

Figure 5.11 : (**A**) Temperature at $x = 0$ vs detuning for 135μs of plasma evolution. The lowest temperature is achieved for $\delta/2\pi = -20\,$MHz while the highest is achieved for $\delta/2\pi = +20\,$MHz. These values are reasonable, since peak cooling and heating efficiencies are expected to occur for $\delta \sim \gamma_{SP}$, where $\gamma_{SP}/2\pi$=23 MHz. For $|\delta| > \gamma_{SP}$, we see that the effectiveness of cooling & heating appear to depend inversely on δ, reflective of the dependence on β on δ ($\beta \propto \delta^{-1}$) discussed in Sec. 5.1. (**B**) Temperature vs ion position for $\delta/2\pi = -10\,$MHz (red) and $\delta/2\pi = -30\,$MHz (blue). Since $v_c \propto |\delta|$, we expect that a larger portion of the cloud will be cooled when the laser is further detuned, which is indeed what we see here. However, the cooling efficiency in the center of the cloud is clearly reduced compared to the nearer-detuned case, as expected. The lines are gaussian fits to the spatial temperature profile. (**C**): Plasma size σ_x vs detuning after 135μs of evolution. We see that the greatest efficiencies in expansion slowing and enhancement are achieved for further detuning than that which led to the greatest efficiencies in cooling and heating. This is because expansion will be most affected when the laser is interacting with the whole cloud, not just the central region.

expansion, it should be far enough detuned such that it interacts with the majority of the plasma, not just the central portion.

5.7 A Broader View: Impact of Laser-Cooling a UNP

In this chapter we have demonstrated the ability to cool a significant fraction of a UNP to $T_i < 50\,$mK with a corresponding $\Gamma > 10$, with all degrees of freedom successfully cooled by a 1D optical molasses configuration. By performing spatially resolved measurements within this region, one could study the thermodynamic and transport properties in this coupling regime, which is relevant for certain white dwarf stars [8] and laser-produced plasmas important for warm dense matter studies [10, 9]. Measurements in this regime can also serve as benchmarks for predictions made by new theories intended to describe plasmas in the strongly coupled regime [46, 47, 60]. In Chapters 7 and 8 we introduce pre-existing techniques and future proposals for the measurement of transport quantities, such as the self-diffusion coefficient and the shear viscosity, that can be applied to laser-cooled UNPs.

Improving upon the coupling achieved here would open the door to even more interesting SCP physics. For example, the region $\Gamma = 20 - 30$ is expected to contain a minimum in the viscosity[57, 47] and is also associated with the onset of the 'Yukawa liquid' regime [47], in which effects such as particle-caging [62] are expected to become relevant. Attempts to extend kinetic theory into the SCP regime through modifications of Boltzmann collision operators begin to diverge dramatically from MD results in this regime. Experimental measurements would be a valuable tool for diagnosing the physics that limits these approaches. In the next chapter, we will discuss a few ideas for how we can improve upon the results discussed in this chapter.

Chapter 6

Approaches to Improving Laser-Cooling in a UNP

In the previous chapter we showed that $\Gamma > 10$ can be achieved in a central 'slice' of width x_{cool} $\sim$1 mm along the laser-cooling axis in a UNP after 135μs. In this chapter, we consider a number of ways to improve upon this result, both in terms of the fraction of the UNP that experiences effective cooling and in how effectively the UNP is cooled within x_{cool}.

In Sec. 6.1 we discuss how magnetic fields can be used to improve cooling in a variety of ways. In one configuration, known as the anti-MOT, it is possible to cancel out the spatially-dependent expansion-induced Doppler shift, potentially allowing for cooling to be effective throughout the plasma. We discuss this configuration in Sec. 6.1.1. It is also potentially possible to use MOT forces, similar to those used in atom trapping, to prevent expansion of the plasma in the first place. In addition, the magnetic field on its own can also help to confine the plasma by a technique known as 'magnetic bottling'. These spatial confinement techniques are discussed in Sec. 6.1.2 and Sec. 6.1.3.

Then, in Sec. 6.2, we discuss ways in which cooling can be improved by simply increasing the expansion timescale τ_{Exp}. It seems intuitive that allowing for more time to cool should improve upon the results in the previous chapter, however, the improvements that can be achieved are limited by electron-ion heating, as we discuss in Sec. 6.2.2.

6.1 Magnetic and Mangeto-optical forces

Magnetic fields are turned off in most UNP experiments. This is because they can affect the dynamics of the plasma in complicated ways that can obscure the SCP dynamics that UNP experiments are typically employed to study. However, for laser-cooling experiments there are a number of advantages to keeping fields on. In particular, as we discuss in this section, the same quadrupole fields that are used in the Sr MOT can also be used in a number of ways to improve laser cooling of the UNP.

6.1.1 Mitigating Expansion-Induced Doppler Shifts through an 'anti-MOT' configuration

Laser-cooling for ions with $|x| > x_c \sim 1\,\mathrm{mm}$ is limited due to expansion-induced doppler shifts $|kv_{Exp}| > kv_c$, where $v_c = |\delta/k|$. Consider the expansion-induced Doppler shift for the leftward propagating laser in the optical-molasses configuration. At a given time t, this is given by

$$k\vec{v}_{Exp} \cdot \hat{x} = \frac{kt}{t^2 + \tau_{Exp}^2} x = \alpha_{Exp}(t)x \tag{6.1}$$

where $\vec{v}_{Exp}$ is given by Eq. 2.21. Thus, for $\delta < 0$, as x increases the ion is increasingly likely to scatter photons from this laser up until $x_c = -\delta/\alpha_{Exp}$. This is simply an alternate picture for explaining why the molasses force also retards the expansion of the cloud.

For circularly polarized light in a field of form $B_x = -bx$, which can be provided by a quadrupole field, the Zeeman shift of the transition is $V = -\mu_B b \left[(m_J g_J)_e - (m_J g_J)_g\right] x$, where the subscript refers to the internal state $|g\rangle$ and $|e\rangle$, is also linearly dependent on x. For the Sr$^+$ D2 transition operating on the σ^+ cycling transition $|\frac{1}{2}, \frac{1}{2}\rangle \rightarrow |\frac{3}{2}, \frac{3}{2}\rangle$ this becomes $V = -\mu_B bx = -\hbar\alpha_M x$ where

$\alpha_M = \mu_B b/\hbar$. The resonant energy for the transition is now $E_T = \hbar\omega + \hbar\delta_Z(x)$, where $\delta_Z(x) = V(x)/\hbar$ and $\hbar\omega$ is the energy difference between $|g\rangle$ and $|e\rangle$ in absence of magnetic fields. If the leftward propagating laser considered in the previous paragraph is σ^+ polarized, then for an ion moving with velocity $v = v_{Exp} + w$ where w is the 'thermal' velocity of the ion, the resonance condition $E_T = \hbar\nu + \hbar k v$, where ν is the laser frequency, for the transition becomes:

$$\hbar\omega + \hbar\delta_Z(x) = \hbar\nu + \hbar k v_{Exp} + \hbar k w \rightarrow \delta_{Tot}(w, x) = \delta + (\alpha_{Exp}(t) + \alpha_M)\, x + kw \tag{6.2}$$

where $\delta = \nu - \omega$ is the laser detuning, and we've defined an effective detuning δ_{Tot} that depends on x and w and for which resonance occurs at $\delta_{Tot} = 0$. The force due to this laser is directed towards negative x and is equal to

$$\vec{F}_{left}(x, w) = -\frac{\hbar k \Gamma s_0}{2}\left[1 + s_0 + 4\frac{(\delta + (\alpha_{Exp}(t) + \alpha_M)\, x + kw)^2}{\gamma^2}\right]^{-1}\hat{x} \tag{6.3}$$

If we ignore the velocity dependent terms (e.g. α_{Exp} and w set to zero), it is clear that for red-detuning, the magnitude of this force increases with x up until $\alpha_M x = -\delta$, e.g. as x increases the atom experiences an increasing force in the negative direction. This is what occurs in a MOT (Sec. 3.1), and thus we define this configuration as the **MOT** configuration (in contrast to the antiMOT configuration discussed in the next paragraph). If the oppositely propagating optical molasses laser is σ^- polarized, then the force due to that laser is

$$\vec{F}_{right}(x, w) = \frac{\hbar k \Gamma s_0}{2}\left[1 + s_0 + 4\frac{(\delta - (\alpha_{Exp}(t) + \alpha_M)\, x - kw)^2}{\gamma^2}\right]^{-1}\hat{x} \tag{6.4}$$

and the total optical molasses force on an ion in the MOT configuration is

$$\begin{aligned}\vec{F}_{MOT}(x,w) = \frac{\hbar k \Gamma s_0}{2} \Bigg(&\left[1 + s_0 + 4\frac{\left(\delta - \left(\alpha_{Exp}(t) + \alpha_M\right)x - kw\right)^2}{\gamma^2} \right]^{-1} \\ &- \left[1 + s_0 + 4\frac{\left(\delta + \left(\alpha_{Exp}(t) + \alpha_M\right)x + kw\right)^2}{\gamma^2} \right]^{-1} \Bigg) \hat{x}\end{aligned} \tag{6.5}$$

If either the sign of b is reversed *or* the laser polarizations are reversed, then the sign of α_M reverses as well. Ignoring velocity terms, this would provide an anti-confining force, and hence we refer to this configuration as the **antiMOT** configuration. The force in this case is

$$\begin{aligned}\vec{F}_{antiMOT}(x,w) = \frac{\hbar k \Gamma s_0}{2} \Bigg(&\left[1 + s_0 + 4\frac{\left(\delta - \left(\alpha_{Exp}(t) - \alpha_M\right)x - kw\right)^2}{\gamma^2} \right]^{-1} \\ &- \left[1 + s_0 + 4\frac{\left(\delta + \left(\alpha_{Exp}(t) - \alpha_M\right)x + kw\right)^2}{\gamma^2} \right]^{-1} \Bigg) \hat{x}\end{aligned} \tag{6.6}$$

At first glance, the antiMOT configuration seems to lack utility. After all, why would one want to use an ‘anti-confining’ force? However, upon an examination of Eqs. 6.5 and 6.6 the utility becomes clear; in the antiMOT, $\alpha_M x$ can cancel out the expansion induced Doppler-shifts $\alpha_{Exp} x$ which, in the previous chapter, were shown to inhibit cooling outside of the central region of the plasma. In contrast, the MOT just makes the problem worse.

Ideal Case

For the ideal case in which $|\alpha_M| = \alpha_{Exp}$, this behavior is demonstrated in Fig. 6.1, in which we show color plots of $F(x,w)$ in absence of magnetic field ($\alpha_M = 0$, Fig. 6.1A), $F_{MOT}(x,w)$ (Fig. 6.1B), and $F_{antiMOT}(x,w)$ (Fig. 6.1C), for $\delta/2\pi = -20\,\mathrm{MHz}$, $t = 40\mu\mathrm{s}$, $\tau_{Exp} = 80\mu\mathrm{s}$, and $b = 98\,\mathrm{G/cm}$ (these are conditions for which $|\alpha_M| = \alpha_{Exp}$).

We also demonstrate a procedure for how these color plots can be used to estimate $|x_c|$, the 'capture region' outside of which the optical force no longer cools the ions. Per the discussion in Sec. 4.6.2, the optical force only cools when $\langle dF/dw \rangle_w < 0$ (note the w in the derivative) where the $\langle \rangle_w$ indicates a weighted average over the distribution function $f(w) = e^{-w^2/(2v_T^2)}/\sqrt{2\pi v_T^2}$ where $v_T = \sqrt{k_B T/m}$. By definition $\frac{dF}{dw}\Big|_x$ switches signs at the peaks in $F(x, w)$. Thus, at the value of x for which $F(x, w)$ peaks at $w = 0$, half of the ions experience $\frac{dF}{dw} < 0$ and the other half experience $\frac{dF}{dw} > 0$. We estimate that x_c is given by this value of x. The black lines in Fig. 6.1A and Fig. 6.1B illustrate this procedure, and demonstrate that the MOT configuration decreases $|x_c|$, the opposite of what we want!

In Figs. 6.1D-F, we plot $F(v, x = 0)$ and $F(v, x = 1.5\,\text{mm})$ corresponding to the $F(x, w)$ plots in the above panels. Let's consider $F(w)$ for $x = 1.5\,\text{mm}$ for each configuration. Without any fields, $F(w)$ acts as a damping force ($\frac{dF}{dw} < 0$) for w between -14 m/s and 2 m/s, and has $\frac{dF}{dw} > 0$ outside of this region. For typical ion temperatures of $\sim 400\,\text{mK}$ (see black dashed curve in Fig. 6.1G) a substantial fraction of the ions have $w > 2\,\text{m/s}$, and thus the thermally averaged cooling force will be significantly weaker at $x = 1.5\,\text{mm}$ than at $x = 0$, where nearly all ions experience a damping force. In the MOT configuration (Fig. 6.1E), the damped velocity range is now between -22 m/s and -7 m/s. Therefore, most of the ions actually experience an anti-damping force $\frac{dF}{dw} > 0$, and thus ions at this position will be heated ($\beta < 0$, see Fig. 6.1H). Finally, in the anti-MOT configuration (Fig. 6.1F), we see that the damping region remains centered at $w = 0$ for $x = 1.5\,\text{mm}$ (and for all x) and therefore nearly all ions in the thermal distribution experience damping ($\frac{dF}{dw} < 0$). We plot $\frac{df}{dw}$ vs w for $x = 1.5\,\text{mm}$ in Fig. 6.1G, along with $f(w)$, to help visualize this analysis.

The critical figure is Fig. 6.1H. In this figure, we plot the cooling rate, $\beta(x) =$

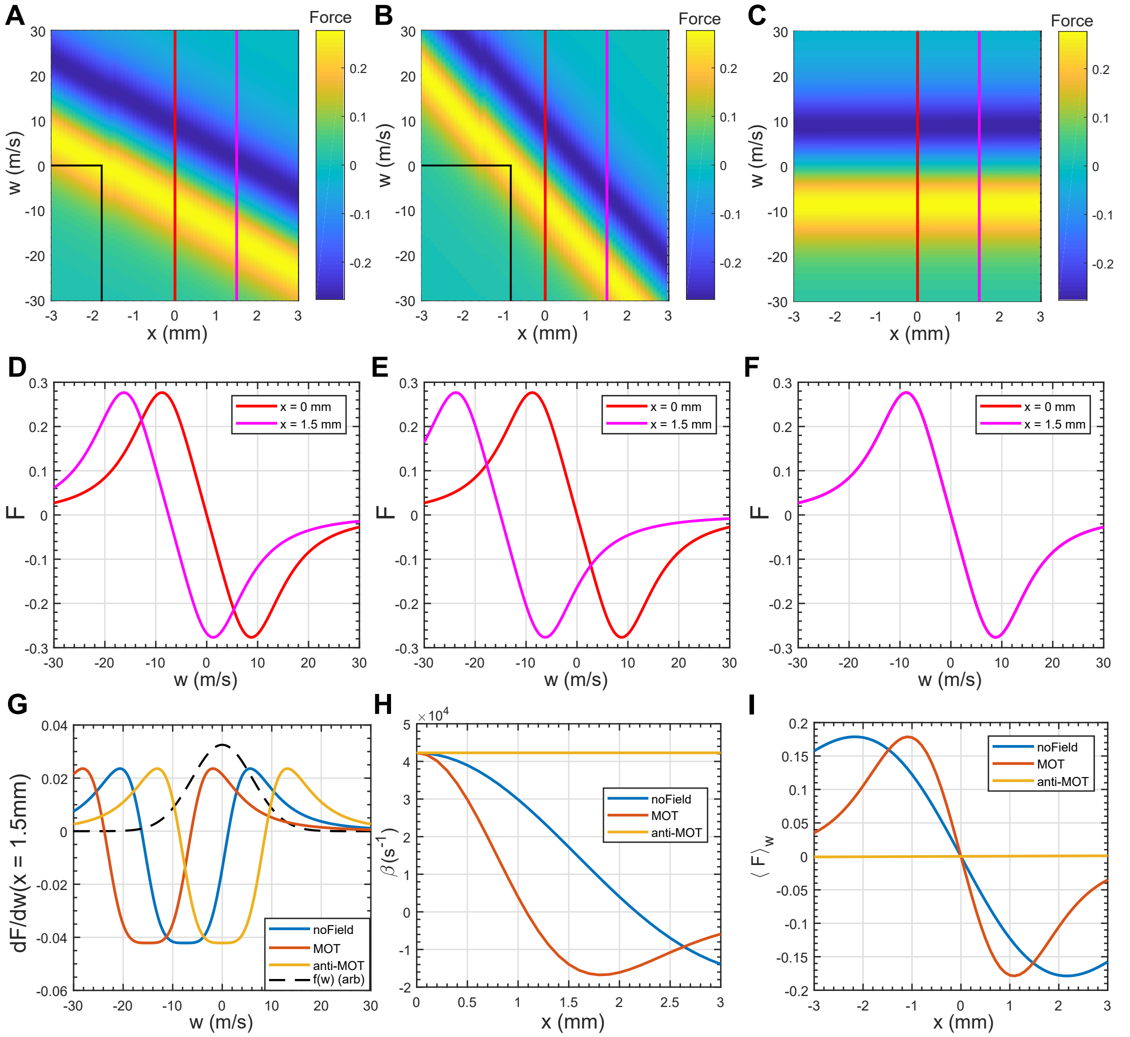

Figure 6.1 : For all panels, $\delta/2\pi = -20\,\mathrm{MHz}$, $b = 98\,\mathrm{G/cm}$, $\tau_{Exp} = 80\mu\mathrm{s}$, and we are calculating the forces $40\mu\mathrm{s}$ into the plasma evolution. (**A-C**): Color plot of $F(w, x)$ for the field-less configuration (**A**), the MOT configuration (**B**), and the antiMOT configuration (**C**). The red and magenta lines indicate $x = 0$ and $x = 1.5\,\mathrm{mm}$, for which we plot $F(w)$ in **D-F**. The black lines in **A** and **B** illustrate how we estimate x_c (see text). The line extends rightward from $w = 0$ until F reaches its maximum value, and then drops down to define $-x_c$. (**G**): Plot of $\frac{dF}{dw}$ for $x = 1.5\,\mathrm{mm}$ in the three configurations alongside $f(w)$, the thermal distribution. (**H**): Cooling rate $\beta(x)$ averaged over w for the three configurations. In the anti-MOT configuration, β remains at its maximum value throughout the plasma. (**I**): Total force at x averaged over the thermal distribution, $\langle F \rangle_w$, for the three configurations. In the anti-MOT, the cooling-lasers no longer provide any confinement.

$-\langle \partial_t E_T \rangle_w(x)/k_B T$, where $\langle \partial_t E_T \rangle_w(x) = \int_{-\infty}^{\infty} dw f(w) F(x,w) w$, which is defined such that $\partial_t T = -\beta(x) T$ (see discussion in Sec. 4.6.2). In the MOT configuration, the cooling rate is observed to rapidly diminish with increasing x, turning off completely at $x = 1.1\,\mathrm{mm}$, which is fairly close to the value predicted by the estimation technique ($x_{est} = 0.9\,\mathrm{mm}$) discussed earlier (Fig. 6.1B). Without the field, the cooling rate diminishes a bit more slowly with increasing x, turning off completely at $x = 2.15\,\mathrm{mm}$, again reasonably close to the estimated value of 1.8 mm (Fig. 6.1A). In the anti-MOT configuration, however, the cooling rate remains the same throughout the plasma due to the complete cancellation of α_{Exp} by α_M.

However, this comes at a cost: for this example, in which $|\alpha_M| = \alpha_{Exp}$, the force averaged over all of the ions at a given position $\langle F \rangle_w$ no longer depends on x at all in the anti-MOT configuration. Thus, the optical forces will not inhibit the expansion of the cloud in this case. For the MOT configuration, the confining force is strengthened with respect to the field-less case, however it ‘rolls over’ at a lower value of $|x|$ (1.05 mm compared to 2.1 mm).

Non Ideal Cases

The above analysis was for an ideal case, with parameters set such that α_{Exp} was exactly canceled out by α_M in the antiMOT configuration. In principle, then, if the field gradient b can be adjusted on a μs timescale such that α_M cancels α_{Exp} for all times, cooling can be achieved throughout the plasma over its entire evolution. However, we can not verify this in our experiment for a few reasons. First, we do not currently have the ability to change b on a μs timescale. Second, the presence of the magnetic field affects the LIF measurement technique by adding a spatially dependent Zeeman shift, which broadens the spectrum from the macroscopically sized analysis regions used to measure $T(x,y)$. We have not yet determined a procedure for deconvolving this field-induced broadening, and as a result we cannot obtain temperature measurements while the magnetic field is on.

However, even with the added Zeeman shifts, the procedure for obtaining $n(x,y)$ by integrating over the spectrum is still valid (Sec. 3.3). In this section we consider the differences between the MOT and antiMOT configuration in the evolution of $n(x,y)$ in the regime where $\alpha_{Exp} > \alpha_M$ for the majority of the plasma evolution. For this experiment, we ionize directly from the magnetic trap (i.e., we do not let the atoms expand before ionization). In this case, the plasma length scale is quite small ($\leq 1\,\mathrm{mm}$, compare to $\sim$3 mm in previous chapter), reducing τ_{Exp} to $\sim 30\mu$s (T_e is still 15.5 K) and increasing typical values of $\alpha_{Exp}(t)$ considerably. Because the resulting expansion velocities are quite large, we choose to work with relatively far detuned 408 nm light of $\delta/2\pi = -40\,\mathrm{MHz}$ and a relatively high intensity $s_0 = 7$. The field gradient is set to $b = 115\,\mathrm{G/cm}$, the maximum achievable in our apparatus. Even so, it only takes 6μs of expansion time for α_{Exp} to exceed α_M, after which α_{Exp} remains the larger of the two throughout the remainder of the relevant portion of the plasma lifetime. Thus, for the majority of the plasma evolution, the anti-MOT configuration will not act to *cancel* the spatially-dependent expansion-induced Doppler shift, but rather it will simply *mitigate* the effect.

This is illustrated in Fig. 6.2A and B, in which we show plots of β and $\langle F\rangle_w$ vs x for these conditions at $t = 30\mu$s into the evolution. These quantities are calculated in the same way as in the previous section. These figures make it clear that, for these realistic experimental conditions, the antiMOT configuration simply mitigates the effect of the expansion-induced Doppler shift. We also show the excited state population $\langle P_P(x)\rangle_w(x)$ for both the MOT and anti-MOT configurations (Fig. 6.2C).

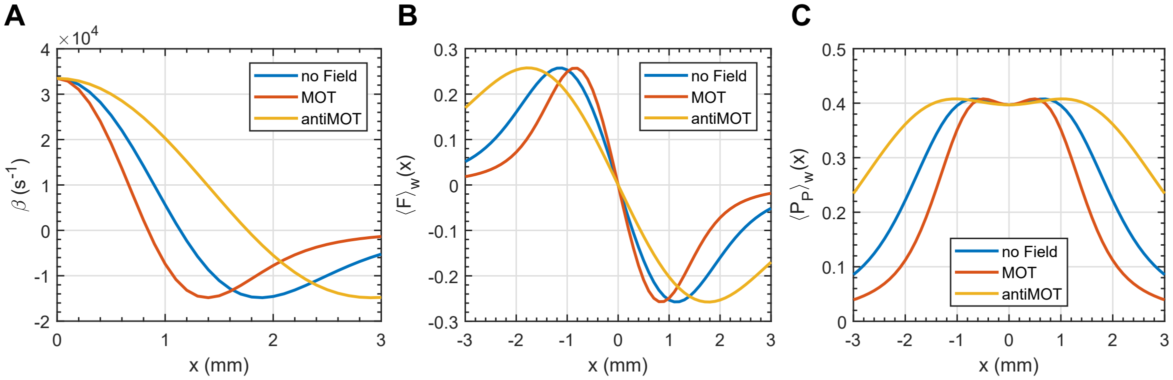

Figure 6.2 : For all panels, $\delta/2\pi = -40\,\mathrm{MHz}$, s_0=7, $b = 115\,\mathrm{G/cm}$, $\tau_{Exp} = 30\mu$s, and $t = 30\mu$s. (**A**): Cooling rate $\beta(x)$ averaged over w for the three configurations. Unlike in Fig. 6.1H, we see here that the anti-MOT configuration merely slows down the rate at which β falls with increasing x. This is because $\alpha_{Exp}(30\mu\mathrm{s}) > |\alpha_M|$ for these parameters. (**B**): Total force at x averaged over the thermal distribution, $\langle F\rangle_w$, for the three configurations. In the MOT case, the confinement force is only effective for a very small region of the plasma $|x| < 0.8\,\mathrm{mm}$ (compare to $\sigma(30\mu\mathrm{s}) \sim 2.2\,\mathrm{mm}$, see Fig. 6.4). The anti-MOT configuration greatly extends the fraction of the plasma that experiences an effective confinement force. (**C**): $\langle P_P(x)\rangle_w(x)$ for the configurations. Here we observe that, in the MOT configuration, the expected fraction of ions in the excited state falls off rapidly with x. This is because the combined Zeeman and expansion shifts with x have become so large as to put ions out of resonance with both lasers. In contrast, in the antiMOT configuration the range over which ions are successfully excited increases as the Zeeman shift helps cancel the expansion shift.

The excited state population $\langle P_P(x)\rangle_w(x)$, plotted in Fig. 6.2C, is directly proportional to the scattering rate $R_{x,s}$, which we are able to measure using the technique outlined in Sec. 5.1. We performed these measurements in plasmas ionized directly from the magnetic trap with parameters equivalent to the ones used to derive the 'model' data in Fig. 6.2, the results are shown in Fig. 6.3 for $t_{cool} = 30\mu$s. We clearly see that, indeed, the region of plasma over which the cooling lasers are active is enhanced in the anti-MOT configuration.

The net effect should be that, counter-intuitively, cooling lasers in an anti-MOT configuration should provide better confinement than in the MOT, since it is more

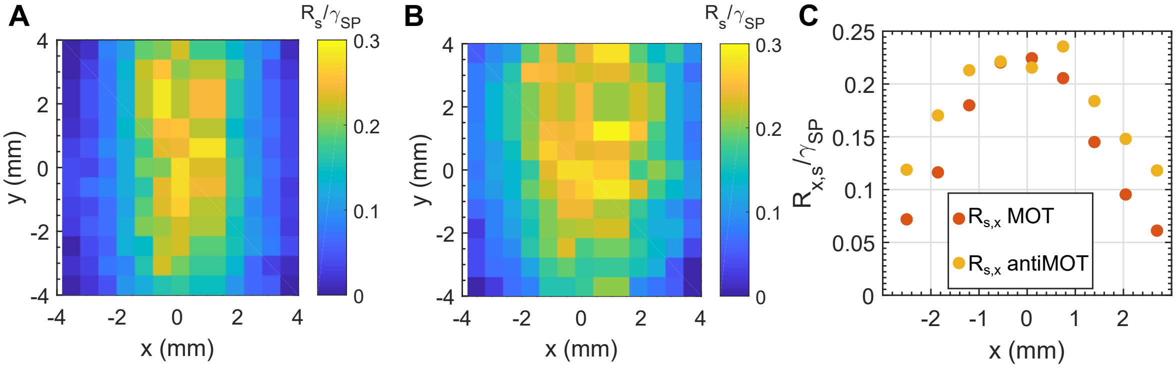

Figure 6.3 : (**A-B**): Scattering heat maps $R_s(x, y)$ for the MOT (**A**) and antiMOT (**B**) configurations. It is clear that the region over which the cooling lasers interact with the plasma is larger in the antiMOT configuration. (**C**): The y integrated value of the scattering map $R_{x,s}(x)$ vs x for the two configurations. The MOT clearly falls off faster than the antiMOT, as expected from Fig. 6.2C. However, the scattering rate observed here is about a factor of 2 lower than expected from Fig. 6.2C. This is likely because, in the model, we do not factor in D state decay, which inhibits scattering rates in the experiment.

effective over a wider region of the plasma. Indeed, this is what we observe in our experiment. In Fig. 6.4A we plot the density profile of the plasma integrated along the y axis ($n(x)$) after 33μs of cooling for both configurations; the antiMOT is seen to clearly do a better job confining the plasma. This is made even clearer in Fig. 6.4B, in which we plot σ_x from gaussian fits of y-integrated density profiles vs time in the two configurations.

Summary

We motivated this section by discussing an ideal situation in which the antiMOT can be used to cancel out the effect of the x-dependent doppler shift caused by the hydrodynamic expansion (Fig. 6.1H), which has been shown to limit the effectiveness of the cooling lasers outside of the central region of the plasma (Sec. 4.6.2 and 5.1). However, we are currently unable to test this exact behavior experimentally for

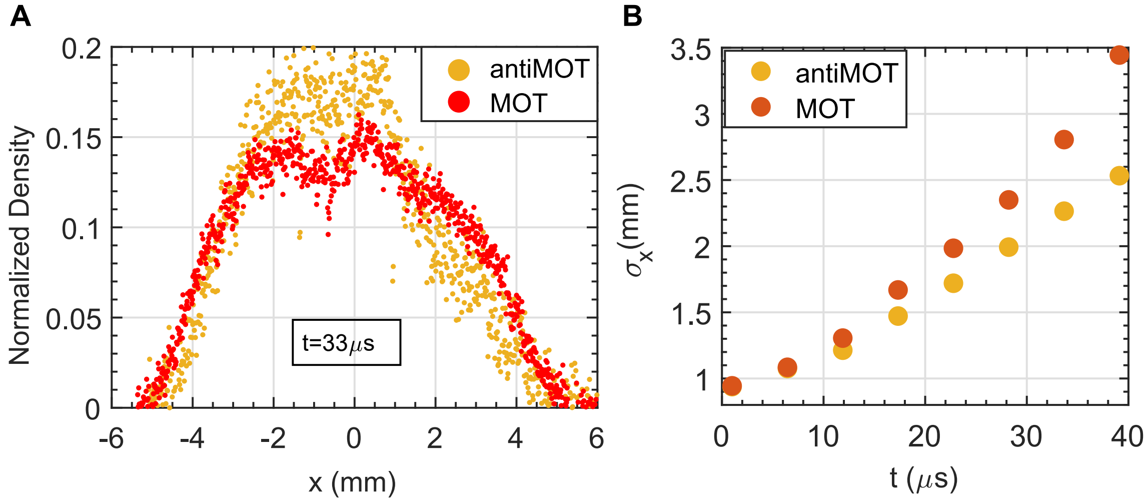

Figure 6.4 : (**A**): y integrated density profile for both the MOT and antiMOT configuration after $t_{cool} = 33\mu$s. We observe that the confinement is stronger in the antiMOT, which we attribute to the confinement force being effective over a larger fraction of the plasma (Fig. 6.2B). (**B**): σ_x from gaussian fits to the y-integrated profile vs t in the two configurations. Again, we see that the antiMOT more effectively confines the plasma.

two reasons. First, the presence of the magnetic field affects the LIF measurement technique by adding a spatially dependent Zeeman shift. We have not determined a procedure for deconvolving these shifts, and as a result we cannot obtain temperature measurements while the magnetic field is on. Second, we do not have the ability to adjust b on a μs timescale, which is needed in order to vary α_M such that it cancels out the time-dependent α_{Exp}.

Therefore, we demonstrated the principal undergirding the antiMOT's effectiveness in a different way. Specifically, we work in a regime where, for most of the plasma evolution, $\alpha_{Exp} > \alpha_M$. In this regime, the antiMOT configuration was shown to enhance the region over which the confinement force is effective (Fig. 6.2B). We verified this experimentally in two ways. First, we determined that the range of the plasma over which the ions interact with the cooling lasers is larger in the antiMOT than in the MOT (Fig. 6.3). Second, we showed that the antiMOT configuration more effectively inhibited the expansion of the plasma. We verified this by measuring the plasma size along the laser axis (σ_x) as a function of evolution time in each configuration (Fig. 6.4).

This demonstration of the antiMOT's effectiveness motivates looking into ways to make the improvements to thermometry and field control that are needed in order to test the 'ideal' situation, as the ability to cool the whole plasma would indeed be a significant improvement even if it comes at the cost of a loss in expansion retarding capabilities (Fig. 6.1I).

6.1.2 Magneto-Optical Trapping of a UNP

The effectiveness of expansion slowing observed in larger plasmas (Fig. 5.9) demonstrates the potential of using optical-forces as a tool for plasma confinement. Fully confining the plasma would be helpful for a number of reasons. First, if we are able to prevent expansion from occurring in the first place, we do not need to worry about expansion velocity induced doppler shifts limiting the region of the plasma for which laser-cooling is effective. Second, it will allow for laser-cooling to be performed over arbitrarily long times. Finally, development of plasma confinement techniques is a very important topic in general, such as for fusion applications [139] or creation of trapped antihydrogen [140], and demonstration of a new confinement technique would be a significant development. In this section, we will discuss how the MOT configuration can potentially be used for this purpose.

In Chapter 3 we demonstrated that, for $|x| < x_c = |\delta/\alpha_M| = |\hbar\delta/\mu_B b|$, the MOT force (in 1D) is given by Eq. 3.2, which we reproduce here (the coefficient differs slightly because we are exciting a $J = 1/2 \rightarrow J = 3/2$ transition, whereas in Ch. 3

we considered a $J = 0$ to $J = 1$ transition):

$$\vec{F}(x) = \left[\frac{8ks_0\mu_B b\delta}{\gamma}\left(1+\frac{4\delta^2}{\gamma^2}\right)^{-2}\right]\vec{x} \tag{6.7}$$

However, this equation was derived assuming that the MOT is operating under ideal conditions, specifically, it assumes that there is no 'loss' from the excited state. For the Sr^+ transition, there is a significant (1:17 branching ratio) loss to the $\mathrm{D}_{5/2}$ state; needing to repump from this state limits the scattering rate. In our experiment, $R_{s,Max} = \gamma_{SP}/4$ is the highest scattering rate that we have measured. To estimate the 'effective' MOT force under these limitations, we will consider an analysis similar to the one employed in Sec. 5.1 to determine the cooling rate (β) from the R_s measurement. First, we assume that for $x = x_c$ the ion only scatters from the laser propagating opposite to the displacement along x (e.g., for $x = x_c$ the ion scatters only from the leftward propagating beam, and vice versa for $x = -x_c$). Therefore, the force for this displacement is $\vec{F}(x = \pm x_c) = \mp\frac{\gamma}{4}\hbar k\hat{x}$. We also assume that the force is linear within the region $|x| < x_c$. Thus, the force becomes:

$$\vec{F}_{MOT}(x) = -\hbar k\frac{\gamma}{4}\frac{\vec{x}}{x_c} = k\mu_B b\frac{\gamma/4}{\delta}\vec{x} \tag{6.8}$$

In chapter 2 we demonstrated that the plasma expansion force along the x dimension at $t = 0$ after photoionization is given by Eq. 2.11, which we reproduce here:

$$\vec{F}_{Exp}(x) = \frac{k_B T_{e0}}{\sigma_0^2}\vec{x}. \tag{6.9}$$

For judicious choices of T_{e0}, σ_0, δ, and b, the MOT force can cancel the expansion force. However, one constraint on the allowable values of δ, b, and σ_0 is set by the need to make the MOT force applicable over a region $x_c > \sigma_0$, such that the expansion is halted throughout the plasma. We choose the limitation $x_c = |\hbar\delta/\mu_B b| = 2\sigma_0$. Thus, the condition for force cancellation becomes:

$$\frac{\gamma\hbar k}{8\sigma_0} = \frac{k_B T_e}{\sigma_0^2}. \tag{6.10}$$

and therefore

$$T_e(\mathrm{K}) = \frac{\gamma\hbar k\sigma_0}{8k_B} = 2.06\sigma_0(\mathrm{mm}) \tag{6.11}$$

As discussed in Sec. 2.4, three body recombination limits how low the electron temperature can be for a given density by the condition $\kappa \leq 0.55 \rightarrow \Gamma_e \leq 0.1$ [110]. We assume here that we will not want to work with densities below $10^{13}\,\mathrm{m}^{-3}$, which limits **T_e to 5.5 K or greater**. By Eq. 6.11, this sets **$\sigma_0 \geq 2.7\,\mathrm{mm}$**. A plasma of this density and size contains only 3M ions; easily achievable in our apparatus.

Next we must determine reasonable values for δ and b under the constraint $x_c = 2\sigma_0$ and the constraint that the force must be linear in the region $x < |x_c|$, which is approximately the case as long as $|\delta| < \sqrt{1+s_0}\gamma_{SP}/2$, where $s_0 = I/I_{sat}$ and $I_{sat} = 43.1\,\mathrm{mW/cm^2}$ (Ch. 3) ($\sqrt{1+s_0}\gamma_{SP}$ is known as the "power broadened linewidth" of the transition). We assume that we will want the 408 nm laser to have a $1/e^2$ radius (w) equal to $4\sigma_0$, such that there is little to no variation in beam power throughout the plasma. Thus, $w \sim 1\,\mathrm{cm}$. The maximum power of the 408 nm laser is 1 W, however, we assume that we will want to reserve the ability to try a 3D MOT, so we will restrict the power for this analysis to 300 mW. Therefore, $I = 2P/\pi w^2 = 190\,\mathrm{mW/cm^2}$ and $s_0 \approx 4.5$. This gives $\sqrt{1+s_0}\gamma_{SP}/2/2\pi = 27\,\mathrm{MHz}$, and thus we will choose **$\delta/2\pi = 27\,\mathrm{MHz}$**. Finally, plugging the selected values of δ and $x_c = 2\sigma_0 = 5.4\,\mathrm{mm}$ into the expression for $|b| = |\hbar\delta/\mu_B x_c|$ gives **$b = 35\,\mathrm{G/cm}$**, which is well within the range of gradients achievable in our apparatus.

To summarize: for realistic conditions of $n_0 = 10^{13}\,\mathrm{m}^{-3}$, $\sigma_0 = 2.7\,\mathrm{mm}$, $T_e = 5.5\,\mathrm{K}$, $s_0 = 4.5$, $\delta/2\pi = 27\,\mathrm{MHz}$, and $b = 35\,\mathrm{G/cm}$, it should be possible for a MOT force to cancel the expansion force for $|x| < x_c = 2\sigma_0 = 5.4\,\mathrm{mm}$.

We plot F_{MOT}, F_{Exp} and $F_{MOT} + F_{Exp}$ in Fig. 6.5A and observe *almost* perfect cancellation between -5 mm and +5 mm, as expected, where we have used the expression in Eq. 3.1, with an additional factor of 1/2 on the overall force to account for the observation that the maximum scattering rate in our system, $\gamma_{SP}/4$, is 1/2 the maximum scattering rate in a two level system, to determine F_{MOT}. The imperfection becomes clearer when we look at $(F_{MOT} + F_{Exp})/F_{Exp}$ (Fig. 6.5B); we see that for the chosen conditions F_{MOT} is around 80% of F_{Exp} under these assumptions. For perfect cancellation, the electron temperature must be lowered to $\sim 4.5\,\mathrm{K}$.

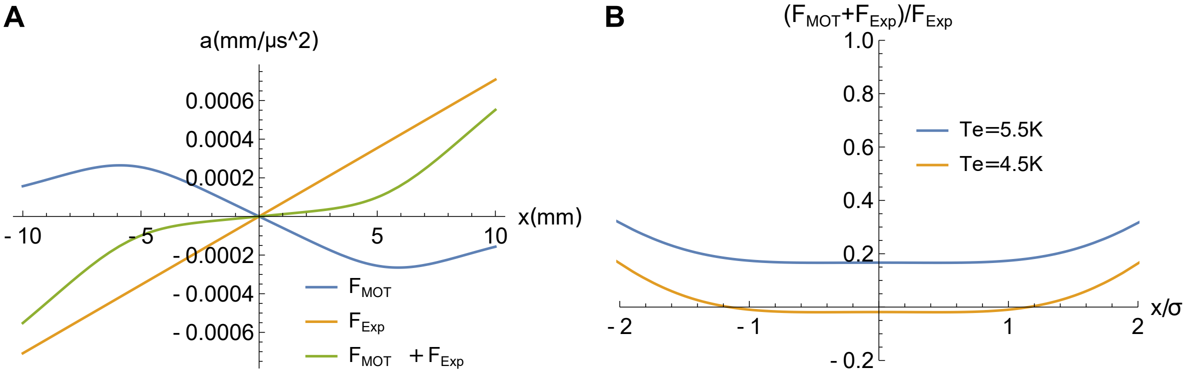

Figure 6.5 : (**A**): Plots of F_{MOT}, F_{Exp} and $F_{MOT} + F_{Exp}$ in units $a = F/m_i$ (mm/μs^2) vs x for the conditions described in the text. We observe good cancellation in the region between $-2\sigma_0$ and $2\sigma_0$ ($\sigma_0 = 2.7\,\mathrm{mm}$). (**B**): Total force with the MOT added ($F_{MOT} + F_{Exp}$) divided by the force without the MOT (F_{Exp}). We observe $\sim 80\%$ cancellation throughout the region between $-2\sigma_0$ and $2\sigma_0$. If the electron temperature is reduced to 4.5 K, the MOT force can completely cancel the expansion force.

We have not yet attempted to magneto-optically trap a plasma in our apparatus. However, the idea appears to have promise, and we hope the discussion of it here prompts future attempts to confine plasmas using MOT forces.

6.1.3 Magnetic Bottling

Thus far, we have only considered the effect that magnetic fields can have *in combination with* optical forces. However, magnetic fields can also be employed in plasma confinement schemes where the confinement comes *solely* from the magnetic fields. The most basic example of this is called 'magnetic mirroring' [11]. The concept is straightforward: absent a magnetic field zero, the magnetic moment of a particle, $\mu = mv_{\perp}^2/2B$, is an adiabatic invariant, where $v_{\perp}$ is the velocity perpendicular to the field axis. Critically, this is true of both ions and electrons. If the electric potential does not change much as the particle moves (largely true for small movements within a neutral plasma), then the kinetic energy is also invariant: $\epsilon = \frac{1}{2}mv_{\|}^2 + \frac{1}{2}mv_{\perp}^2$.

Consider the situation shown in Fig. 6.6, in which the magnitude of the field increases as a particle travels in either direction along the field axis, with respect to the field at the 'trap center'. This device is referred to as a 'magnetic mirror'. As the field strengthens, the velocity perpendicular to the field must increase as well for μ to remain constant. However, it can only increase up to the point where $\epsilon = \frac{1}{2}mv_{\perp}^2$ (e.g., no velocity parallel to the field) due to conservation of energy. The particle cannot penetrate any deeper into the region of high magnetic field, and is forced to turn around ('mirroring').

For example, consider the situation where a plasma is created at the center of the mirror machine, where the field is B_{center} and the particle velocity is initially thermal (e.g. $\langle\epsilon\rangle = \frac{3}{2}mv_T^2$). As particles move towards the center of the small coils (where the field is B_{edge}), the perpendicular velocity of the particles increases to maintain their magnetic moment. If a particle makes it to the center of the small coil, $v_{\perp}^2 = \frac{B_{edge}}{B_{center}}v_T^2$.

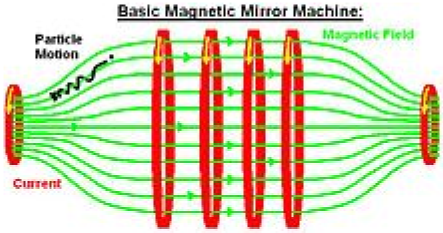

Figure 6.6 : Basic Magnetic mirror machine [11]. From $x = 0$ (the center of the machine), the field increases along x in either direction. Particles with $|v| \leq v_T$ can move within the region of the mirror trap where magnetic fields are small enough such that $B < 3B_{center}$. If the field at the edge of the trap (the smaller coils on either side) is larger than this value, then these particles are trapped. In general, its desirable to trap as many particles as possible, even those on the high energy tail of the thermal distribution, and thus one would choose $B_{edge} \gg B_{center}$.

However, for a particle with exactly the thermal velocity, by conservation of energy, $v_\perp^2$ can be no greater than $3v_T^2$, thus, if $B_{edge} > 3B_{center}$, all such particles are trapped. In practice, one would want to make $B_{edge} \gg B_{center}$ such that even particles in the high energy tail of the thermal distribution are trapped.

The mirror configuration obviously differs from a quadrupole field. However, it turns out that a quadrupole field should still act as a magnetic mirroring based trap, as the field increases in all directions moving away from its center (which is co-located with the plasma center). Thus, theoretically, this field should trap the plasma along all dimensions. This method has been studied in the past, and has been called a 'biconic cusp' trap[138] (see Fig. 6.7).

However, unlike the mirror machine, this configuration has a null point in the field, causing particles that pass through that point to 'lose' their magnetic moment (μ goes to ∞). Particles with trajectories that pass near this point are considered 'erratic' and it is possible for them to escape from the trap. So, there is a question of whether or not the majority of particles in plasmas that we generate in the presence

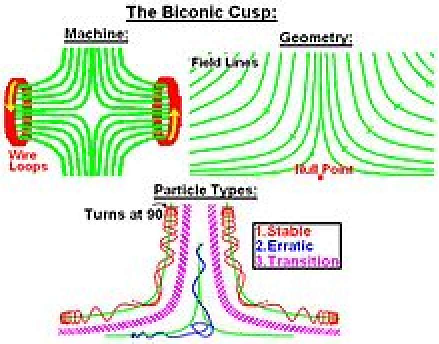

Figure 6.7 : Basic Biconic Cusp [138]. Particles in the 'stable' region start off with a sufficiently large magnetic moment that adiabatic invariance is a 'good' assumption, while particles in the 'erratic' region move too close to the field zero and eventually lose adiabaticity, destroying the mirror process.

of the quadrupole field are in the 'stable' region or the 'unstable' region (Fig. 6.7.), as it seems that there is no 'hard and fast' rule to calculate where the 'transition' region exists. Collisions may also play a deleterious role in the trapping process. Modeling these effects is outside of the scope of this thesis.

Experimental evidence of magnetic trapping

This method of magnetic trapping should work even in absence of cooling light. Thus, we decided to attempt this in our apparatus with the highest magnetic field gradients that we can currently obtain (b_{strong} = 115 G/cm along the strong axis and b_{weak} =57.5 G/cm along the weak axes) without any cooling lasers. We compare the difference in plasma evolution with and without the magnetic field for plasmas of identical initial spatial profiles and electron temperature ($T_e = 15.5\,\mathrm{K}$). In Fig. 6.8A we show the density in the center of the plasma as a function of time after photoionization. We observe that, while initially the two datasets match, after 100μs of evolution, we clearly see that ion loss is increasingly inhibited by the presence of the magnetic field. In Fig. 6.8B and C we show $n(x, y)$ after 310μs of evolution with and without the field to further demonstrate this effect.

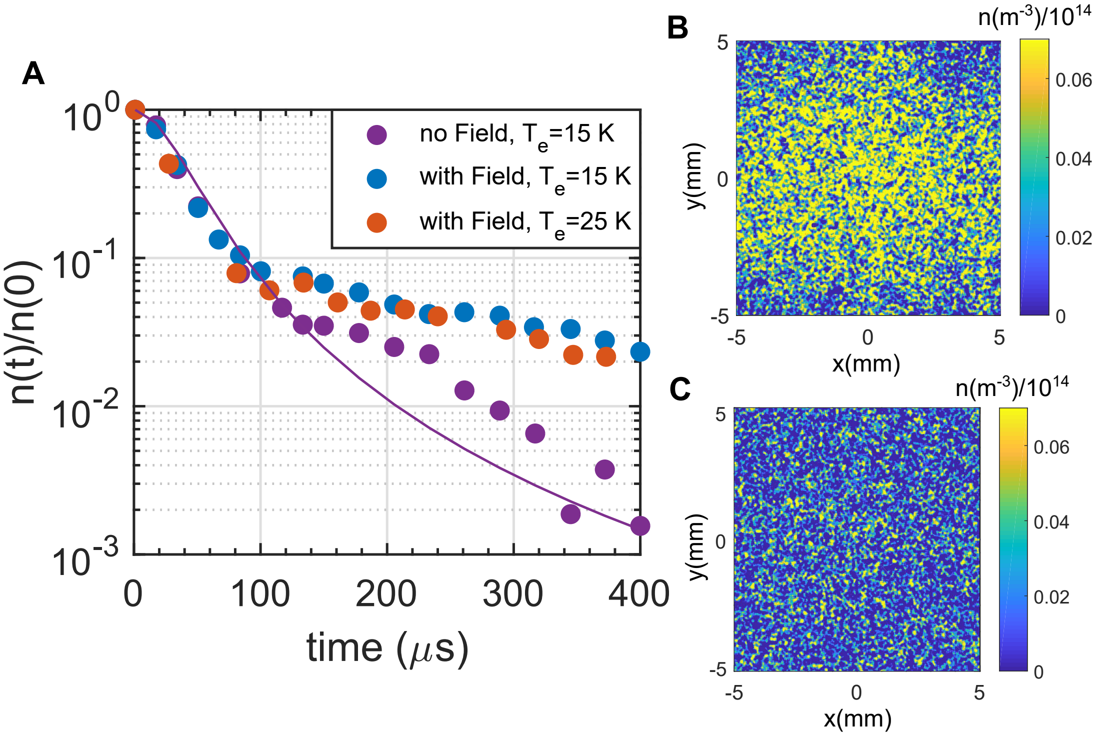

Figure 6.8 : (**A**): Log-linear plot of $n(t)/n(0)$ vs t for $T_e = 15\,\mathrm{K}$ with and without a magnetic field gradient of $b_{strong} = 115\,\mathrm{G/cm}$ and $b_{weak} = 57.5\,\mathrm{G/cm}$. We see some evidence of ion trapping, particularly at later times. We also obtained the evolution curve for $T_e = 25\,\mathrm{K}$ for the 'field-on' configuration. We also observe trapping in this case. This is evidence that we are, in fact, seeing trapped ions, not magnetically trapped Rydberg atoms produced by three body recombination because, if we were seeing Rydberg atoms, we would see ∼10x fewer ($25/15^{9/2} \sim 10$) for $T_e = 25\,\mathrm{K}$, which is clearly not the case. (**B**): $n(x, y)$ for $t = 310\mu$s for $T_e = 15\,\mathrm{K}$ with the field *on*. In the center of the trap we observe a density of $\sim 5 \times 10^{12}\,\mathrm{m}^{-3}$ ions. (**C**): $n(x, y)$ for $t = 310\mu$s for $T_e = 15\,\mathrm{K}$ with the field *off*. Here we observe very few, if any, ions. Thus, we interpret that the ions we observe in **B** result from magnetic trapping.

This is obviously a tantalizing result, as it indicates that we are indeed seeing some evidence of magnetic trapping. However, there are a few caveats. One is that we currently do not have the capability to determine whether or not electrons are also trapped; it is possible that we are only trapping the ion component. Another caveat is that what we are seeing may be magnetically trapped rydberg atoms resulting from three body recombination during the plasma evolution, which can also be observed through LIF on the D1 transition[16]. We investigated this possibility by increasing the electron temperature up to 25 K, for which the three body recombination should be suppressed by a factor of $(25/15)^{9/2}$=10 because the three body recombination rate depends on $T_e^{-9/2}$ (Sec. 2.4). We compare the resulting n vs t curves in these cases and find little overall difference in the observed 'trapped' fraction (Fig. 6.8A) after $t \gtrsim 300\mu$s evolution time. This does not completely rule out the possibility that we are observing Rydberg atoms, but it seems pretty unlikely that this is the case.

6.1.4 Summary

In this section, we have introduced a number of ways that magnetic fields can be used to improve upon the laser-cooling results we demonstrated in Ch. 5, which were achieved by using lasers in an optical molasses configuration. All of the techniques we have discussed use the same magnetic quadrupole field configuration that provides the MOT force used to confine the Sr atoms (Sec. 3.1).

One effect of the quadrupole field is to add an additional Zeeman shift that depends linearly on x. By using the antiMOT configuration, which, in absence of hydrodynamic expansion, would produce an anti-confining force, it is theoretically possible to cancel out the expansion-induced doppler shift, since it also depends linearly on x. In this case, the lasers will no longer inhibit the development of v_{Exp} (Fig. 6.1I), however, they will act to cool the plasma by providing a force $\vec{F} = -\beta\vec{w}$, where $\vec{w}$ is the 'thermal' portion of the total velocity ($\vec{v}$) of a given ion (e.g. $\vec{v} = \vec{v}_{Exp} + \vec{w}$), for all ions in the plasma (Fig. 6.1H). Unfortunately, the spatially dependent Zeeman shifts resulting from the presence of the magnetic fields present challenges to the LIF scheme employed for temperature measurements, so we were not able to test this in our apparatus.

Instead, we opted to test the antiMOT for the case where the magnetically-induced Zeeman shift is less than the expansion-induced Doppler shift for most of the plasma evolution time. In this case, the antiMOT should act to extend the region over which the confining force is effective, while the MOT configuration will further restrict this region to a small central portion of the plasma (Fig. 6.2B). The Zeeman shifts do not affect our ability to measure the density of the plasma $n(x, y)$ or the scattering rate $R_s(x, y)$ (see Sec. 5.1) using LIF techniques, and thus we were able to observe these effects. First, we observed that the region of plasma over which ions scatter photons from the cooling laser is larger in the antiMOT configuration (Fig. 6.3). Second, we observed that the expansion of the plasma was more successfully inhibited using the antiMOT configuration (Fig. 6.4), which we interpret as evidence that the confining force is more effective throughout a significant fraction of the plasma in the antiMOT than in the MOT, as predicted.

MOT forces can, in principle, be used to completely confine the plasma, similar to how they can be used to confine atoms. The challenge here is that, unlike atoms, the thermal electron pressure in the plasma results in a strong expansion force. To confine the plasma, the MOT force must be greater than the expansion force. We find that it is theoretically possible in our apparatus to provide such a force that can be active over a range $\sim 2\sigma_0$. However, the electron temperatures required are quite low ($T_e \lesssim 5\,\mathrm{K}$), and thus the need to avoid three body recombination requires very low densities. The ability to confine a *neutral* plasma is a tantalizing prospect for a number of reasons. First, it will allow for cooling to occur over a much greater timeframe (we are currently limited to $\sim 100\mu$s by the rapid expansion), which should enable the achievement of stronger coupling (though, as we will see in Sec. 6.2.2, the coupling achievable is limited by electron-ion heating). Second, demonstrating the ability to confine a neutral plasma is a worthy goal in and of itself, as neutral plasma confinement is a topic of great interest, since it is a critical component in proposed fusion reactors.

One confinement scheme that has been previously studied in this context is the 'magnetic mirror machine'. In this scheme, a plasma is confined within a region of low magnetic field, which is surrounded on either side by regions of higher magnetic field. The confinement results from conservation of two adiabatic invariants; the total energy and the magnetic moment.

One of these mirror machines, known as the 'biconic cusp' (Fig. 6.7) uses a quadrupole field. We observe some evidence of magnetic confinement when the quadrupole field is left on throughout the plasma evolution, even without the cooling lasers (Fig. 6.8). However, we cannot confirm that the trapped plasma is neutral, as we currently have no ability to detect electrons in our apparatus. Nevertheless, this is a promising first step towards demonstration of plasma confinement. In principle, this confinement force should aid in any efforts to use a MOT force for neutral plasma confinement.

6.2 Increasing τ_{Exp} by Creating Bigger Plasmas

One of the main limits on how effective laser-cooling can be in a UNP is the time limit imposed by plasma expansion, which effectively limits t_{cool} to a few multiples of $\tau_{Exp} = \sqrt{m_i\sigma_0^2/k_BT_e}$. For $t \gg \tau_{Exp}$, the plasma has become so dilute ($n \propto (t/\tau_{Exp})^{-3}$) [21] that, even though Γ is increasing throughout the plasma expansion, the correspondingly low temperature become difficult to measure (for a given Γ, $T \propto n^{1/3}$). This is why we restricted our measurements to $t < 135\mu$s in Fig. 5.5, even though the model implies that Γ continues to increase beyond this point in time. For two plasmas of equal initial density but different τ_{Exp}, the one with higher τ_{Exp} will reach the minimum temperature measurable ($T_{min} \sim 50\,$mK) with LIF at a higher n, and therefore a higher Γ.

In this chapter, we consider the effect of increasing τ_{Exp} by increasing σ_0 while keeping $n_0 = 1.3 \times 10^{14}\,\mathrm{m}^{-3}$, $\beta = 5.2 \times 10^4\mathrm{s}^{-1}$, and $T_e = 15.5\,$K (these are the experimental parameters for the laser cooling data shown in Fig. 5.5). Our 'figures of merit' will be Γ as a function of density ($\Gamma(n)$) throughout the plasma evolution, the density at the time where $T = T_{min}$ as a function of σ_0 ($n_{Tmin}(\sigma_0)$), and the value of Γ at that time as a function of σ_0 ($\Gamma(\sigma_0)$). We will also discuss how electron-ion heating ultimately limits the Γ that can be achieved at a given density.

However, one can ask the question: why not just keep N_i the same when increasing σ_0 and simply work at lower n_0? This, however, would defeat the purpose of increasing τ_{Exp}, which is to reach T_{min} at the highest density possible, and thus reach the maximum possible value of Γ measurable with LIF techniques. The upper limit of Γ that can be achieved in a UNP of initial density n_0 is $\Gamma_{max} = (T_{DIH}(n_0)/T_{min})\,\Gamma_{DIH}$, where $\Gamma_{DIH} \sim 3$ is the value of Γ after DIH (Sec. 2.2.2) and $T_{DIH}(n_0)$ is the temperature after DIH. For $n_0 = 1.3 \times 10^{14}$, $\Gamma_{max} = 27.3$, and thus there is room for improvement above the value of 11 measured in Sec. 5.2. If σ_0 is doubled without increasing N_i, then n_0 is reduced by a factor of 8, T_{DIH} is reduced by a factor of 2 ($T_{DIH} \propto n^{1/3}$) and thus $\Gamma_{max} = 13.7$. Since this is similar to the value of Γ we have already achieved, these parameters cannot result in a significant increase in achievable Γ. This example illustrates why increasing τ_{Exp} by increasing σ_0 should be coupled with a corresponding increase in N_i in order to keep n_0 the same.

This however raises another question: why not just increase n_0 by increasing N_i while keeping σ_0 constant? Assuming β remained the same, we would then reach T_{min} at a greater density. However, it turns out that β becomes lower as the temperature increases (see Fig. 4.7), and therefore the larger value of T_{DIH} achieved with greater n_0 will diminish the cooling effectiveness during the early stages of the plasma evolution. Furthermore, as we will see in Sec. 6.2.2, the electron-ion heating rate strongly limits the level of Γ achievable at high n.

This is why, in order to demonstrate the benefits achievable by increasing τ_{Exp}, we hold n_0 constant at $1.3 \times 10^{14}\,\mathrm{m}^{-3}$ for which $T_{DIH} \sim 0.41\,\mathrm{K}$, as in the experimental data presented in Fig. 5.5. This represents a 'sweet spot' in the initial density: low enough such that T_{DIH} is not so high as to make cooling ineffective during the initial stages of the plasma evolution, but high enough such that T_{min} can, in principal, be achieved at a high enough density for Γ to be substantial.

Finally, it may seem as though an alternate way of increasing τ_{Exp} would be to decrease T_e, however, T_e cannot be arbitrarily lowered due to three body recombination (Sec. 2.4), so increasing σ_0 is the only way to increase τ_{Exp}.

6.2.1 Results from Hydrodynamic Model Solutions

To determine the effect of increasing τ_{Exp} on the values of Γ achievable through laser cooling, we use Eqs. 5.2- 5.6. For simplicity, we consider the case of a *spherically-symmetric* plasma for which the cooling force is distributed evenly across all three axes (e.g., we assume $\vec{F} = -\frac{\beta}{3}\vec{v}$ throughout the cloud, where the factor of 1/3 is due to the cooling force being split evenly among the axes). The plasma will thus remain spherically symmetric throughout the evolution, and therefore the solution for $\sigma(t)$

from these equations represents the size of the plasma along all axes.

The parameter c, which relates to the inefficiencies in expansion retardation resulting from the diminished cooling force for regions with $|v_{Exp}| > |\delta/k|$, is the only remaining free parameter. In Figs. 6.9-6.11 we consider the evolution of T_i, n_i, and Γ_i for various σ_0 for $c = 0$ (e.g. no expansion slowing), $c = 0.6$ (the value measured from fitting the 1D cooling data in Ch. 5, see Sec. 5.5), and $c = 1$ (e.g. 'full' expansion slowing). We see that, as c increases, the cooling lasers do an increasingly good job of retarding the expansion (bottom left corners of Figs. 6.9-6.11). This has the counter-intuitive effect of resulting in Γ vs t/τ_{Exp} curves that *seem* less favorable with increasing c and σ_0 (top right corner of Figs. 6.9-6.11). However, as we will explain in Sec. 6.2.2, this is due to the fact that electron-ion heating is more effective at higher n. Plotting Γ vs n (bottom right corner of Figs. 6.9-6.11) by cross-referencing the $\Gamma(t)$ curve (top right) and $n(t)$ curve (bottom left), makes it clear that it is *always* advantageous to increase τ_{Exp} by increasing σ_0.

From these figures, we can obtain $n_{Tmin}(\sigma_0)$ and $\Gamma_{Tmin}(\sigma_0)$, the values of n and Γ at the time in the evolution for which $T = T_{min} = 50\,\mathrm{mK}$, which are shown in Fig. 6.12. In both plots, it is clear that a point of diminishing returns is reached at $\sigma_0 \sim 5\,\mathrm{mm}$. Moreover, this is *not* because the plasma is reaching $\Gamma_{max} = 27.3$. Instead, the peak Γ achievable appears to be ~ 15. As we will show in the next section, the diminishing returns observed here stem from electron-ion heating.

6.2.2 Limit on Γ due to Electron-Ion Heating

The electron-ion heating term was introduced in Sec. 2.3.1. We reproduce it below:

$$(\partial_t T_i)_{EI} \approx \gamma_{e,i} T_e \equiv \left(2\sqrt{\frac{2}{3\pi}}\Gamma_e^{3/2}\omega_{pe}\frac{m_e}{m_i}\ln\left[1 + 0.4\Gamma_e^{-3/2}\right]\right) T_e \tag{6.12}$$

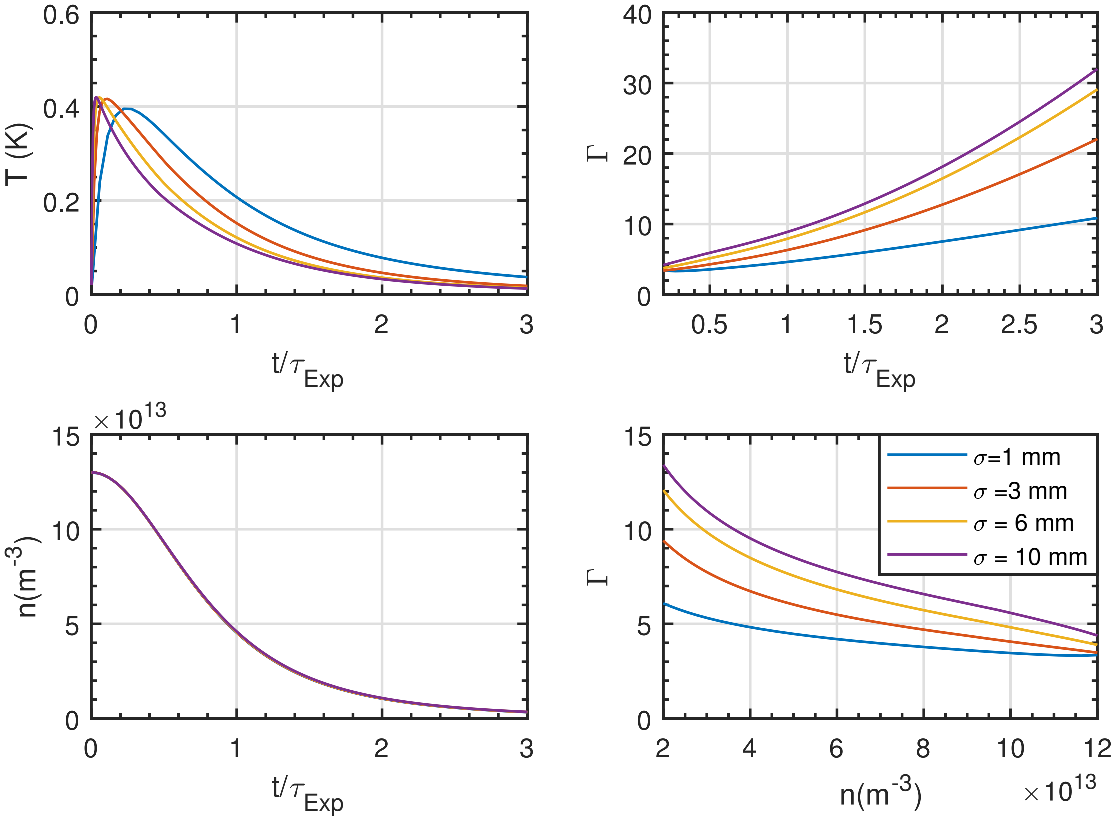

Figure 6.9 : Plots demonstrating how cooling effectiveness varies with σ_0 for $c = 0$ (e.g. assuming that the lasers do not retard the plasma expansion at all) for $n_0 = 1.3 \times 10^{13} \mathrm{m}^{-3}$, $T_e = 15.5\,\mathrm{K}$, and $\beta/3 = 1.7 \times 10^4\,\mathrm{s}^{-1}$, which is the effective cooling rate along each axis for the isotropic cooling assumption considered here. These are the same parameters as the experimental data shown in Fig. 5.5. All plots are obtained by numerically solving Eqs. 5.2- 5.6. Top left: T vs t/τ_{Exp} (τ_{Exp} changes with σ_0 through $\tau_{Exp} = \sqrt{m_i \sigma_0^2 / k_B T_e}$). Top right: Γ vs t/τ_{Exp}. Bottom left: n vs t/τ_{Exp}. Since $c = 0$, all $n(t)$ curves are identical. Bottom right: Γ vs n, obtained by cross-referencing $\Gamma(t)$ (top right) and $n(t)$ (bottom left). Here we see that increasing σ increases the value of Γ observed at a given density n during the plasma evolution.

and thus the total time derivative for the ion temperature, with all terms included, becomes:

$$\partial_t T_i = -\frac{\beta}{3} T_i - 2\gamma T_i + \gamma_{e,i} T_e \tag{6.13}$$

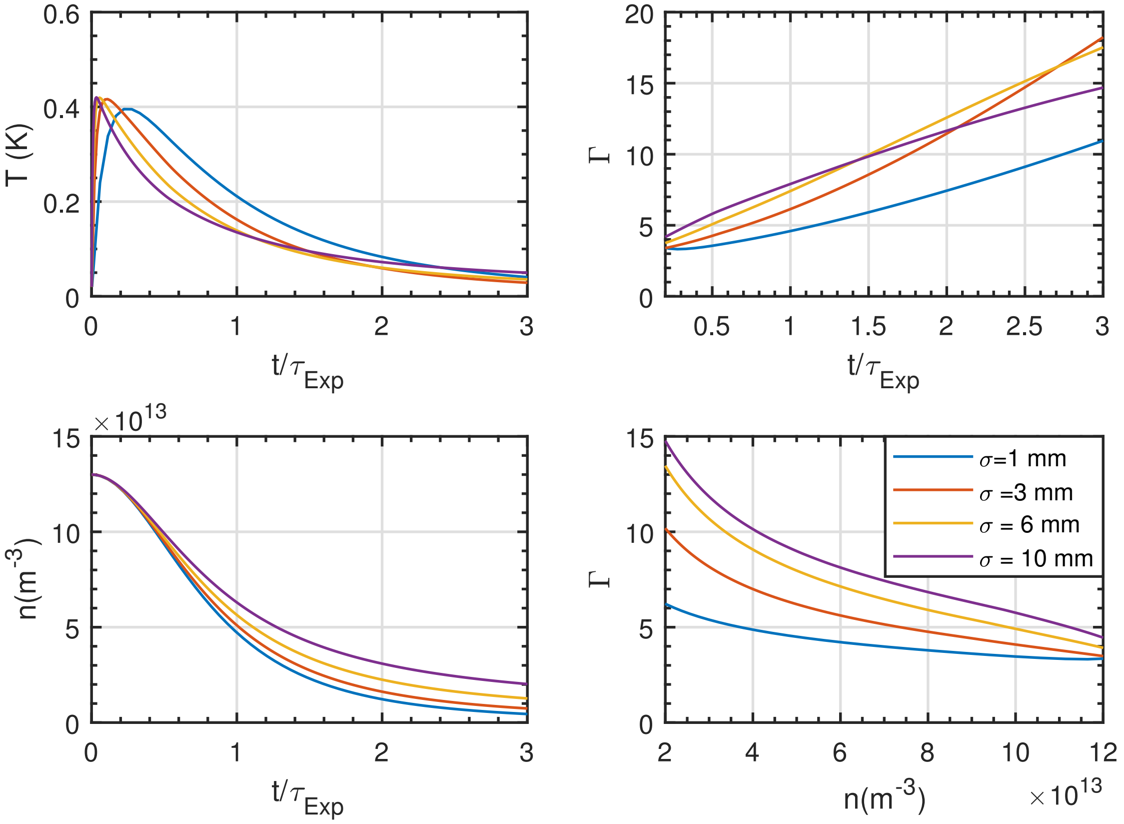

Figure 6.10 : Same plots as Fig. 6.9 taken for the same parameters except for c, which is set to 0.6 (this is the value of best fit for the experimental results in Fig. 5.5). Here we see that the density evolution is clearly affected by the cooling beams. Due to the increased electron-ion heating at higher n, this makes the Γ vs t curve at the highest σ_0 value *appear* suboptimal at later times (top right). However, when we plot Γ vs n, we again clearly see that, in fact, the value of Γ observed at a given density n always increases with σ_0.

For most relevant cases, $2\gamma \lesssim 10^3 \ll \beta/3$, and therefore we ignore the adiabatic cooling term $(-2\gamma T_i)$ and just consider the laser-cooling and electron-ion heating terms. We can easily solve for $T_{i,eq}$, the ion temperature for which the two remaining terms cancel:

$$T_{i,eq} = \frac{3\gamma_{e,i}T_e}{\beta} \tag{6.14}$$

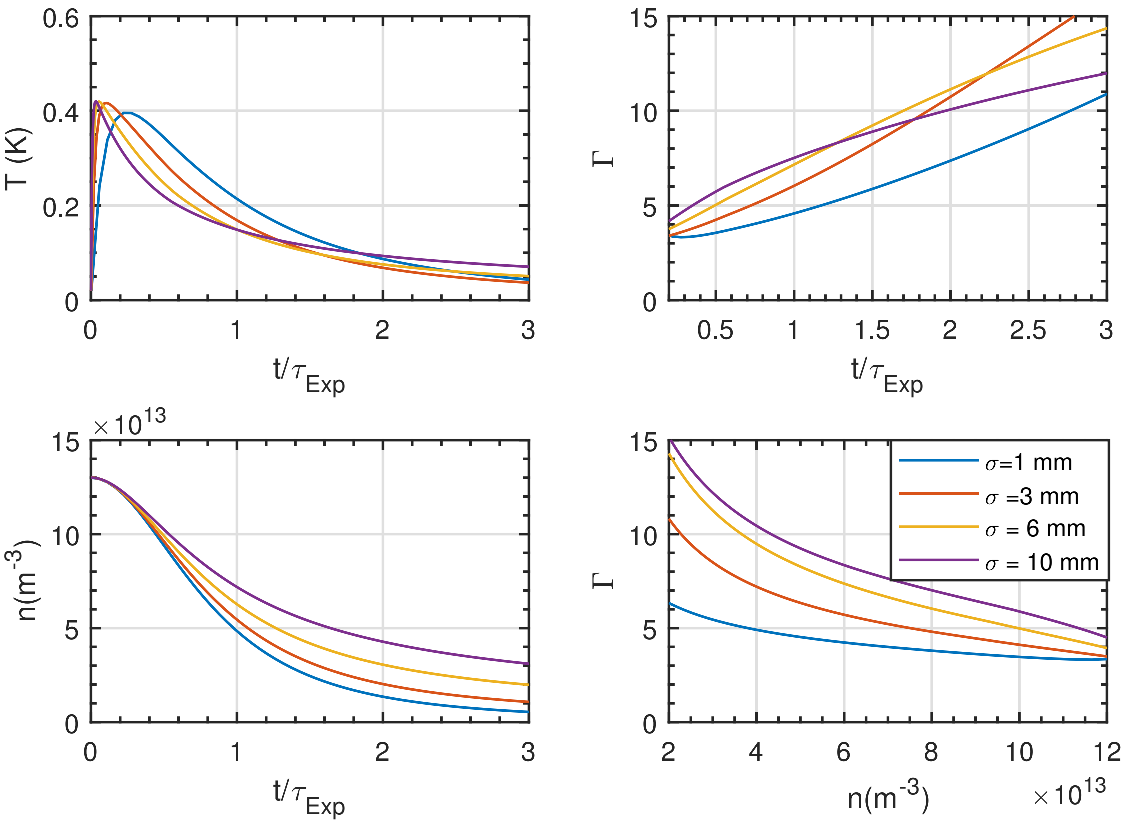

Figure 6.11 : Same plots as Fig. 6.9 taken for the same parameters except for c, which is set to 1 (this is the maximum value expected for c). Again, here we see that the density evolution is clearly affected by the cooling beams. As in Fig. 6.10, this makes the Γ vs t curve at the highest σ_0 value *appear* suboptimal at later times (top right). However, when we plot Γ vs n, we again clearly see that, in fact, the value of Γ observed at a given density n always increases with σ_0.

Substituting in the expression for $\gamma_{e,i}$, we have:

$$T_{i,eq} = 2\sqrt{\frac{2}{3\pi}}\frac{m_e}{m_i}\ln\left[1+0.4\Gamma_e^{-3/2}\right]\frac{3}{\beta}\omega_{pe}\Gamma_e^{3/2}T_e \tag{6.15}$$

Substituting $T_e = e^2/4\pi\epsilon_0 a k_B \Gamma_e$, we have

$$T_{i,eq} = 2\sqrt{\frac{2}{3\pi}}\left(\frac{4\pi}{3}\right)^{1/3}\frac{m_e}{m_i}\frac{e^2}{4\pi\epsilon_0 k_B}\Gamma_e^{1/2}\ln\left[1+0.4\Gamma_e^{-3/2}\right]\frac{3}{\beta}\omega_{pe}n^{1/3} \tag{6.16}$$

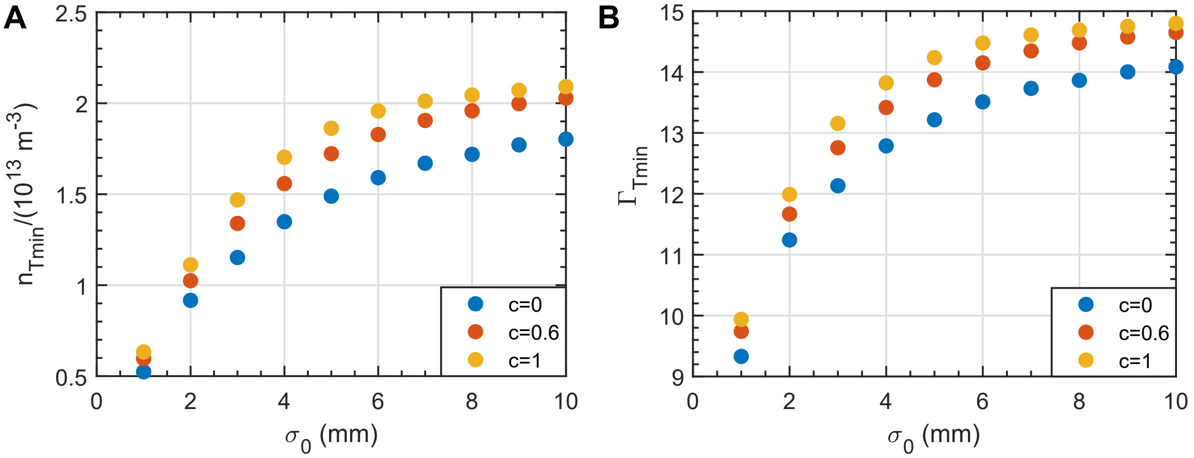

Figure 6.12 : (**A**): The density at the point in the plasma evolution when $T = T_{min} = 50\,\mathrm{mK}$ (n_{Tmin}) vs. σ_0. We see that, for all c, n_{Tmin} increases with σ_0. This density also increases with c. However, it seems that, for maximum σ_0 and c, the value of this density seems to converge to $\sim 2 \times 10^{13}\,\mathrm{m}^{-3}$. In Sec. 6.2.2, we determine that this is due to electron-ion heating (Fig. 6.13). (**B**): The value of Γ when $T = T_{min}$ (Γ_{Tmin}). Similarly to n_{Tmin}, this value increases with both σ_0 and c, but appears to converge to ~ 15 as c and σ_0 are maximized. This is also due to electron-ion heating, as we illustrate later in Fig. 6.13B.

Finally, substituting in $\omega_{pe} = \sqrt{e^2 n/m_e \epsilon_0}$, $\Gamma_e = 0.1$ (as previously discussed, TBR ultimately 'thermostats' Γ_e to approximately 0.1, see Sec. 2.4), and substituting in the parameters for the Sr$^+$ ion gives, one can show:

$$T_{i,eq}(\mathrm{K}) = 10\left(\frac{10^3\mathrm{s}^{-1}}{\beta}\right)\left(\frac{n}{10^{14}\mathrm{m}^{-3}}\right)^{5/6} \tag{6.17}$$

A corresponding formula for Γ_{eq} can also be derived:

$$\Gamma_{eq} = 0.125\left(\frac{\beta}{10^3\mathrm{s}^{-1}}\right)\left(\frac{10^{14}\mathrm{m}^{-3}}{n}\right)^{1/2} \tag{6.18}$$

In Fig. 6.13, we reproduce the plots of $\Gamma(n)$ from the bottom right corner of Figs. 6.9- 6.11 alongside a corresponding plot of $T(n)$. We also plot $\Gamma_{eq}(n)$ and $T_{eq}(n)$ for $\beta = 5.2 \times 10^4\,\mathrm{s}^{-1}$ in thick black lines. We clearly observe that, as the plasma expands and the density lowers, the cooling lasers will act to decrease T until $T = T_{eq}$, after which T simply follows T_{eq} as the density continues to be reduced by expansion. For larger plasmas, the expansion timescale is slow, and thus T converges to T_{eq} at a higher density. Thus, this plot illustrates both the benefit of going to larger σ_0 and the ultimate limit that electron-ion heating sets on the value of Γ and T achievable at a given density n. The low values of Γ_{eq} achievable at high n provide another reason why moving to higher n is not necessarily desirable, in addition to the expected reduction in β for T_{DIH} that accompany higher n, as discussed in the beginning of this section. Finally, for reasonable n, $T_{eq} \gg T_{Doppler}$, where $T_{Doppler} = \hbar\gamma_{SP}/2k_B \sim 500\mu\mathrm{K}$ is the Doppler limit (see Sec. 4.4.3). Therefore, the limit on T_i is *not* determined by the Doppler limit, but rather by a balance between the electron-ion heating rate and the optical-molasses induced cooling rate.

From the results in Fig. 6.13 we can clearly see that, for $\beta = 5.2 \times 10^4\,\mathrm{s}^{-1}$, the maximum possible density n for which $T_{min} = 50\,\mathrm{mK}$ can be achieved is $2 \times 10^{13}\,\mathrm{m}^{-3}$ and the corresponding value of Γ is 15 (this is also why we observed 'diminishing returns' when plotting Γ_{Tmin} and n_{Tmin} vs σ_0 in Fig. 6.12; they are simply converging towards these values as σ_0 and c are increased). Thus, increasing the size without either increasing β or decreasing T_{min} limits observable Γ to 15 or less. Decreasing T_{min} could be accomplished by making LIF measurements more sensitive, which can in principle be accomplished by using a transition with a narrower natural linewidth, or by using two-photon spectroscopy. Alternately, it may be possible to measure Γ directly by measuring transport coefficients, such as the self-diffusion coefficient, and comparing the measurements to MD results: we discuss this approach in greater detail in Chapter 8.

To increase β substantially, one would likely need to implement a laser-cooling

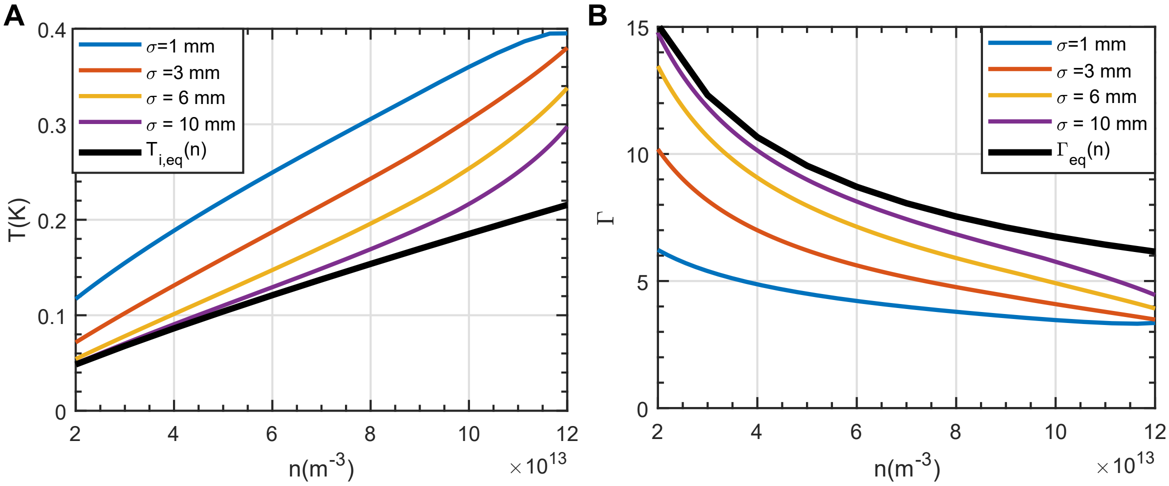

Figure 6.13 : Plots of T (**A**) and Γ (**B**) vs n for model data from Fig. 6.10. We also plot $T_{i,eq}$ and Γ_{eq} from Eqs 6.17 and 6.18, respectively. We observe that, as density decreases during the plasma evolution in the presence of the cooling lasers, T and Γ approach the values suggested by $T_{i,eq}$ and Γ_{eq}. For larger plasmas ($\sigma_0 = 10\,\mathrm{mm}$), the plasma interacts with the cooling lasers for a longer time before reaching a given density n, and therefore we see the T and Γ values approach $T_{i,eq}$ and Γ_{eq} at fairly high n. In contrast, for smaller plasmas ($\sigma = 1\,\mathrm{mm}$), the temperature and coupling have not yet reached $T_{i,eq}$ and Γ_{eq} for the densities considered here. Finally, examining the $T_{i,eq}$ curve, it is clear that the maximum value of n for which $T_{min} = 50\,\mathrm{mK}$ can be achieved is $\sim 2 \times 10^{13}\,\mathrm{m}^{-3}$, explaining why we observed n_{Tmin} to converge to this value in Fig. 6.12A. Similarly, we can see that the maximum value of Γ achievable at this density is $\sim$ 15, explaining why we observe that Γ_{Tmin} converges to 15 in Fig. 6.12B.

scheme other than optical molasses. There are a number of cooling schemes that use coherent processes in combination with spatially varying light shifts and optical pumping into dark states that can achieve forces greater than those achievable using optical-molasses [141, 81, 142]. However, these schemes typically have capture velocities v_c' even lower than the capture velocity for optical-molasses cooling (v_c), and as such are only effective for systems that have temperatures low enough such that thermal velocities $v_T < v_c'$; these cooling techniques will also only be effective in regions with $v_{Exp} < v_c'$. One possibility is to start off by cooling the plasma with optical-molasses up until T is low enough such that $v_T < v_c'$, at which point we would switch to whichever coherent process-based cooling scheme we attempt to implement. Another possible complicating factor is that, due to the reliance on dark states, it is possible that collisions will prevent these sort of cooling schemes from working in a plasma system for the reasons discussed in Sec. 4.5. Due to the benefits that can be achieved with greater cooling, it is still worthwhile to test whether these schemes can be effectively implemented in UNPs.

6.3 Summary and Outlook

In this chapter we have discussed a number of pathways for improving upon the laser-cooling results presented in Chapter 5. First, in Sec. 6.1, we focused on ways that we can use magnetic quadrupole fields to improve both laser-cooling and plasma confinement. Then, in Sec. 6.2, we discussed how increasing τ_{exp} can improve the values of Γ that can be achieved before the ion temperature becomes too low to accurately measure with LIF. Finally, we demonstrated that electron-ion heating, and not the Doppler limit, sets the ultimate limit on achievable values of T and Γ for a given n. Given a cooling rate β, one can determine the minimum (maximum) possible value of T (Γ) for a given density using Eq. 6.17 (Eq. 6.18). These equations result from balancing electron-ion heating and laser-cooling. For $\beta = 5.4 \times 10^4\,\mathrm{s}^{-1}$ (the highest we have measured in our apparatus), we demonstrated that the maximum possible density n for which $T_{min} = 50\,\mathrm{mK}$ can be achieved is $n = 2 \times 10^{13}\,\mathrm{m}^{-3}$, and the corresponding value of Γ is 15. To study plasmas of higher Γ, we must either reduce T_{min} by improving our diagnostics, or we must find a cooling scheme that produces a larger value of β.

However, even though our current values of β and T_{min} limit us to $\Gamma < 15$, laser-cooled UNPs are strongly coupled enough for measurements of transport coefficients in this regime to serve as a test of new theoretical models of strongly coupled plasma dynamics. There are a number of different techniques that have been proposed for the measurement of these quantities, but they can generally be split into two categories. The first category of techniques involve the direct measurement of transport properties by, for example, the application of external forces. These are discussed in Chapter 8. The second category, which we discuss in the next chapter, rely on measuring the relaxation of spin-velocity correlations, which can be induced by velocity-dependent optical-coupling of the spin states. If the correlations are induced in a certain way, their subsequent relaxation may be directly related to autocorrelation functions of powers of the velocity, from which transport coefficients can be derived. Some of these techniques have already been used to measure the self-diffusion coefficient for $\Gamma \leq 4$; applying these techniques to more strongly coupled plasmas and to new transport coefficients will greatly improve our knowledge of strongly coupled plasmas.

Chapter 7

Optical Pump-Probe Measurements of Velocity Autocorrelation Functions and Transport Quantities

In this chapter, we will discuss a set of techniques for measuring transport quantities (e.g. self-diffusion, viscosity, etc.) by creating and then observing the decay of spin-velocity correlations. Under certain circumstances, the decay of the correlations can be directly related to autocorrelation functions of powers of the velocity, where the auto-correlation function for the nth velocity power ($Z_n(t)$) is defined as:

$$Z_n(t) \equiv \sum_{i=x,y,z} \frac{\langle v_i^n(t) v_i^n(0)\rangle - \langle v_i^n\rangle^2}{\langle v_i^n(0) v_i^n(0)\rangle - \langle v_i^n\rangle^2} \tag{7.1}$$

where v_i represents the velocity along the i axis, the brackets $\langle\rangle$ represent an average over all particles, and Z_n has been normalized such that $Z_n(0) = 1$. The negative terms in the numerator and denominator are needed in order for Z_n to converge to 0 for even powers.

The auto-correlation functions are important measures of the microscopic dynamics of a given system. They can also be related to transport coefficients which govern macroscopic behaviors, like diffusion and viscosity, through a set of relationships known as 'Green-Kubo' formulas [92, 91]. For example, the self-diffusion coefficient D is related to Z_1 by:

$$D = \frac{k_B T}{m} \int_0^\infty Z_1(t) dt \tag{7.2}$$

Any tool that can be used to measure transport quantities in strongly coupled plasmas is of great interest for a number of reasons. First, these quantities are not well studied experimentally in the regime of $\Gamma > 1$, and so presently their values are determined from state-of-the-art MD simulations [100, 57], which have little or no experimental validation. These quantities are important input parameters for simulations of inertial confinement fusion (ICF) plasmas. Such simulations help guide the design of ICF experiments, and therefore it is critical that they are as accurate as possible. Second, new theoretical models for extending kinetic theory into the strongly coupled regime make predictions for the values of these parameters, and measurements can therefore serve as a test of these models.

In Sec. 7.1, we will demonstrate how 'pumping' lasers tuned to either the D1 or D2 Sr^+ transitions can be used to create correlations between spin and velocity, along with how LIF can be used to measure the relaxation of the correlations when the pumping lasers are turned off. These correlations can be generally expressed by considering the v-dependent probability for a given particle to be in the $|\uparrow\rangle$ state after the pumping stage, which we call $P_\uparrow(v)$. In Sec. 7.2 we use an MD code (see Appendix A) to test a theorem (see appendix of [39]) claiming that, for $P_\uparrow(v) = c_0 + c_n v^n$, the decay of the nth moment of the velocity distribution of the tagged subset $\langle v^n(t)\rangle_\uparrow$ can be related to Z_n by the following equation:

$$Z_n(t) = \frac{\langle v^n(t)\rangle_\uparrow - \langle v^n\rangle_{\text{all}}}{\langle v^n(0)\rangle_\uparrow - \langle v^n\rangle_{\text{all}}} \equiv M_n(t) \tag{7.3}$$

where we have defined $M_n(t)$, a normalized and offset form of the nth moment, and $\langle\rangle_{\text{all}}$ indicates an average over all ions regardless of spin state (this should simply be an average over a maxwellian, and a time-independent quantity, because the optical pumping schemes generally do not effect the overall distribution function). In other words, if the spin-velocity correlations are of form $P_{\uparrow}(v) = c_0 + c_n v^n$, then the relaxation curve of the *normalized and offset nth moment of the tagged subset* is directly proportional to Z_n. This is what we mean we we say that the relaxation of spin-velocity correlations can be used to measure Z_n, and therefore transport quantities through Green-Kubo formulas, under certain conditions.

However, optical pumping schemes cannot be used to create distributions that are *exactly* of the form $P_{\uparrow}(v) = c_0 + c_n v^n$. In Sec. 7.3 we examine which optical pumping schemes should most effectively replicate the needed form of $P_{\uparrow}(v)$ for $n = 1$ and $n = 2$. We then use the MDQT code described in Chapter 4 to test whether or not the decay of the resulting spin-velocity correlations successfully reproduce velocity-autocorrelation functions. For $n = 1$, we also test pumping schemes that clearly result in spin-velocity correlations that differ from the needed form of $P_{\uparrow}(v)$, the results are shown to diverge from Z_1, as expected. We also discuss how these techniques have been implemented experimentally in the past to measure D for $\Gamma \leq 4$, and how they can be implemented in the future for measurements of both D and η_l, the longitudinal viscosity, in laser-cooled plasmas for which $\Gamma \sim 11$ can be achieved (Chapter 5).

7.1 Creating, and Observing Decay of, Spin-Velocity Correlations Through Optical Pumping

.

The ground state of the Sr^+ ion is $^2\mathrm{S}_{1/2}$, and thus has two m_j sublevels, which we denote as $|\uparrow\rangle$ and $|\downarrow\rangle$. Without optical pumping, all ions, regardless of their velocity, have an equal likelihood of being in the $|\uparrow\rangle$ state or the $|\downarrow\rangle$ state. However, if lasers that couple these states to some excited manifold (for example, lasers corresponding to the D1 line, which couple states in the $^2\mathrm{S}_{1/2}$ manifold to states in the $^2\mathrm{P}_{1/2}$ manifold) are introduced, it can be made either more or less likely for an ion with velocity v to be in the $|\uparrow\rangle$ state; in other words, spin-velocity correlations can be developed.

An example of a pumping scheme that produces spin-velocity correlations is illustrated in Fig. 7.1. In this scheme, counter-propagating, red-detuned, circularly-polarized lasers operating on the D1 transition irradiate the plasma for a time $t_{pump} \sim 100\,\mathrm{ns}$. After the pumping process, we find that an ion moving in a direction opposite to the propagation of the σ^+ laser (e.g. with $v_x > 0$, see Fig. 7.1A) is more likely to be in the $|\uparrow\rangle$ state, and vice versa for an ion moving with $v_x < 0$. This is because the combination of red-detuning and the doppler-shift make it more likely for a $|\downarrow\rangle$ ion with $v_x > 0$ to absorb from the σ^+ laser, and thus have the chance to convert to $|\uparrow\rangle$ via decay from the P state, than it is for a $|\uparrow\rangle$ ion to absorb from the σ^- laser and convert to $|\downarrow\rangle$. The resulting $P_\uparrow(v)$ immediately after pumping is displayed in Fig. 7.1D; this curve comes from solutions to the time-dependent OBE equations.

After the lasers are turned off, the population of ions in the $|\uparrow\rangle$ state has mean velocity $\langle v\rangle_\uparrow > 0$. By waiting a time t after pumping lasers are turned off before imaging with σ^- polarized LIF light (such that only $|\uparrow\rangle$ ions scatter photons), we can obtain $f_\uparrow(v,t)$, the velocity distribution of ions in the $|\uparrow\rangle$ state at a time t. After measuring $f_\uparrow(v,t)$ for various t, one can obtain $\langle v(t)\rangle_\uparrow = \int_{-\infty}^{\infty} v f_\uparrow(v,t)\,dv$, which will relax towards zero due to collisions with the $|\downarrow\rangle$ population. This procedure is illustrated for in Fig. 7.1C.

For the pumping parameters in Fig. 7.1 ($\delta_{pump}/2\pi = -20\,\mathrm{MHz}$, $\Omega = 1.3\gamma_{SP}$) we

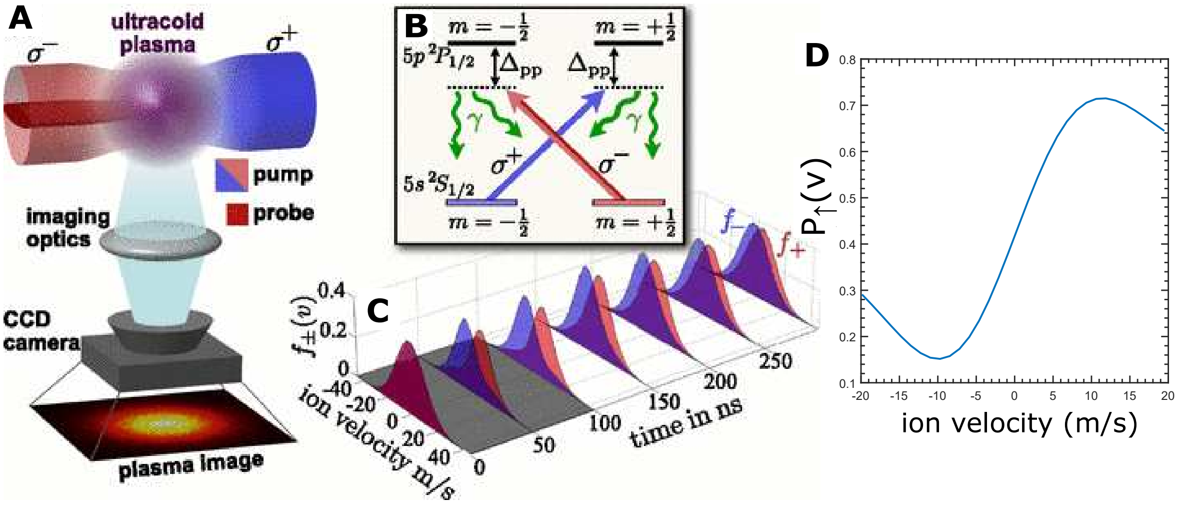

Figure 7.1 : **A-C** are adapted from [40]. **A**: In the pump stage, the plasma is irradiated by counter propagating red-detuned circularly-polarized beams of opposite polarization tuned to the $\mathrm{S}_{1/2} \rightarrow \mathrm{P}_{1/2}$ transition (see **B** for level diagram). This results in a correlation between spin and velocity, as ions in $|\uparrow\rangle$ are more likely to be moving towards the right, and vice versa for $|\downarrow\rangle$, as in **C**. The probability of an ion with spin v being in the $|\uparrow\rangle$ state is shown in **D**, and is derived from OBE solutions where $\Omega = 1.3\gamma$ and $\delta = 2\pi \times 20\,\mathrm{MHz}$ reflect the conditions in [39]. After the pumping laser is turned off, the velocity distributions collisionally relax towards equilibrium (**C** for $t > 100\,\mathrm{ns}$). If $P(v)$ matches certain conditions, the relaxation of the nth moment of the $|\uparrow\rangle$ velocity distribution function ($f_\uparrow(v,t)$) can be related to the autocorrelation function of v^n (Eq. 7.3).

find that, for $|v| \lesssim 6\,\mathrm{m/s}$, $P_\uparrow(v)$ is approximately linear (Fig. 7.1D). If we assume that the non-linear dependence of $P_\uparrow(v)$ on v outside of this region does not affect the measurement, we can expect that $\langle v\rangle_\uparrow(t)$ can be related to Z_1 by Eq. 7.3. We use MD results to demonstrate the validity of Eq. 7.3 in Sec. 7.2, while in Sec. 7.3.1 we use the MDQT code to show that, despite the fact that this optical pumping scheme will always result in ‘outer regions’ of $|v|$ for which $P_\uparrow(v)$ does not depend linearly on v, Eq. 7.3 appears to apply for this pumping scheme if Ω and δ_{pump} are chosen judiciously. By Eq. 7.2, this means that the optical pumping scheme in Fig. 7.1 can be used to measure D [39].

Another pumping scheme is illustrated in Fig. 7.2. In this scheme only one laser, tuned to resonance with the D2 line, irradiates the plasma. The laser propagates along the x axis and has σ^- polarization. Ions with low $|v_x|$ will be rapidly pumped into the $|\downarrow\rangle$ state while ions with high $|v_x|$ will be pumped more slowly as they are doppler shifted off of resonance. By pumping for a relatively short time, one winds up with a $P_\uparrow(v)$ curve that has a minimum at $v = 0$. For certain combinations of Ω and Doppler broadened linewidth ($\sigma_f = kv_T$) the resulting $P_\uparrow(v)$ curve can be approximated by a quadratic over a wide range in v/v_T, as indicated in Fig. 7.2B. Thus, we can potentially use this pumping scheme to measure Z_2 using the relation in Eq. 7.3. In Sec. 7.3.2, we use the MDQT code to verify that M_2 measured with this pumping scheme agrees well with Z_2. We will also discuss how $Z_2(t)$, and thus $M_2(t)$, can be used to measure the longitudinal viscosity.

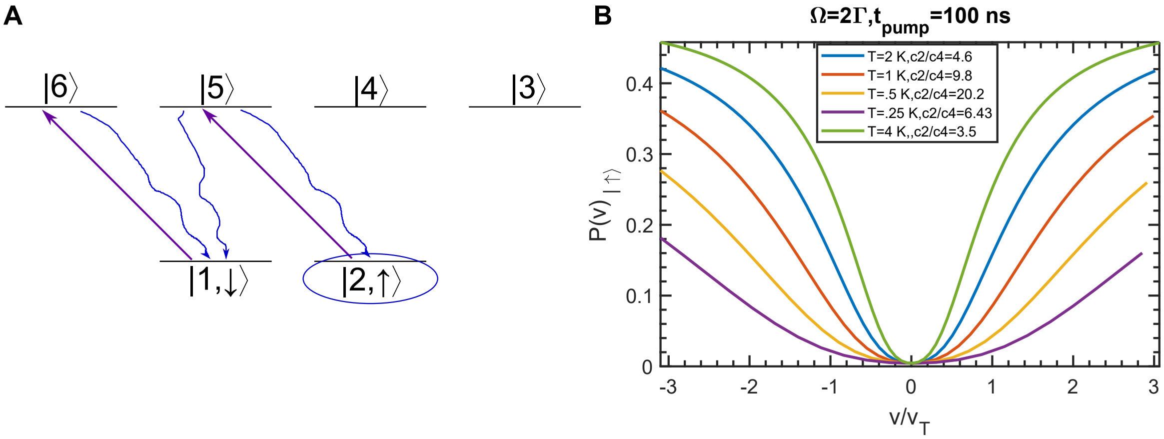

Figure 7.2 : (**A**): Level diagram including optical coupling lasers used for obtaining $P_\uparrow(v) \propto v^2$. By pumping ions out of $|\uparrow\rangle$ through exciting the $S_{1/2} \rightarrow P_{3/2}$ (numbered ket states correspond to those in Fig. 4.3B) transition with an on-resonance laser, we preferentially remove ions with near zero velocity, as ions with non-zero velocity will be Doppler shifted out of resonance and less likely to be pumped. (**B**): Resulting $P_\uparrow(v/v_T)$ for $\Omega = 2$ and $t_{pump} = 100\,\text{ns}$ at various T. The legend indicates the measured ratio of the coefficients from a fit of $P_\uparrow(v/v_T) = c_0 + c_2v^2 + c_4v^4$ to each curve. For $T = 500\,\text{mK}$, the curve is very well described by a quadratic.

We note here that these optical pump/probe techniques can be employed at any point during the plasma evolution. In particular, they can be employed after a laser-cooling (or laser-heating) stage, and therefore can be used to measure Z_n and associated transport-coefficients for $0.8 \leq \Gamma \leq 11$, according to the results shown in Fig. 5.5.

7.2 Using MD Simulations to Verify Eq. 7.3 for Ideal Pumping Schemes

It is impossible to use optical-pumping schemes to create a probability function that is *exactly* of the form $P_{\uparrow}(v) = c_0 + c_n v^n$. Thus, we need a way to test if the non-ideality causes any issues with the identification of $M_n(t)$ with auto-correlation functions. We can do this with our MDQT code, and we present those results in Sec. 7.3.

However, for comparison purposes, we must first obtain 'control' simulation data where the tagging *is* ideal. We do this by first generating an equilibrated plasma with a given Γ and κ by using a Monte Carlo approach [143] followed by a few hundred timesteps of MD with a thermostat (see Appendix A). After this is done, we can choose to tag particles and calculate the velocity moments of the tagged subsets at each timestep. We create four tagged subsets:

- Subset 1: If $v_x > 3v_T$ (note: $v_T/a\omega_{pi} = 1/\sqrt{3\Gamma}$), the particle is automatically tagged. If $v_x < -3v_T$, the particle is automatically not tagged. Otherwise, ions are tagged with probability $P(v) = 0.5 + \frac{1}{6}\frac{v_x}{v_T}$. Creates $P(v) \propto v$ in region bounded by $\pm 3v_T$.

- Subset 2: If $|v_x| > 3v_T$, ions are tagged with probability 0.5. Otherwise, ions are tagged with probability $P(v) = \frac{1}{18}\left(\frac{v}{v_T}\right)^2$. Creates $P(v) \propto v^2$ in region bounded by $\pm 3v_T$.

- Subset 3: If $v_x > 3v_T$, the particle is automatically tagged. If $v_x < -3v_T$, the particle is automatically not tagged. Otherwise, ions are tagged with probability $P(v) = 0.5 + \frac{1}{54}\left(\frac{v_x}{v_T}\right)^3$. Creates $P(v) \propto v^3$ in region bounded by $\pm 3v_T$.
- Subset 4: If $|v_x| > 3v_T$, ions are tagged with probability 0.5. Otherwise, ions are tagged with probability $P(v) = \frac{1}{162}\left(\frac{v}{v_T}\right)^4$. Creates $P(v) \propto v^4$ in region bounded by $\pm 3v_T$.

$P(v)$ for each subset is illustrated in Fig. 7.3.

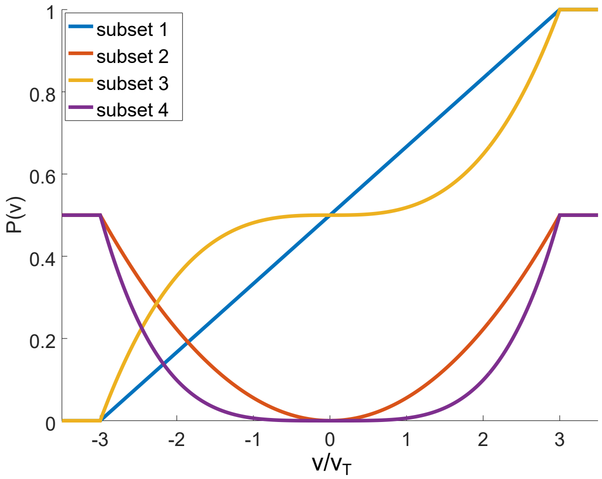

Figure 7.3 : $P(v)$ for the subsets defined in the text.

We then compare $M_1(t)$ for the odd subsets to $Z_1(t)$, which can also be measured in the simulation. We see that, although both tagged moments agree reasonably well with the VAF, the agreement is better for $P(v) \propto v$ (subset 1), as expected (Fig. 7.4A and B). On the other hand, comparing $M_3(t)$ for the odd subsets to $Z_3(t)$, we clearly see better agreement for $P(v) \propto v^3$ than for $P(v) \propto v$ (Fig. 7.4C and D).

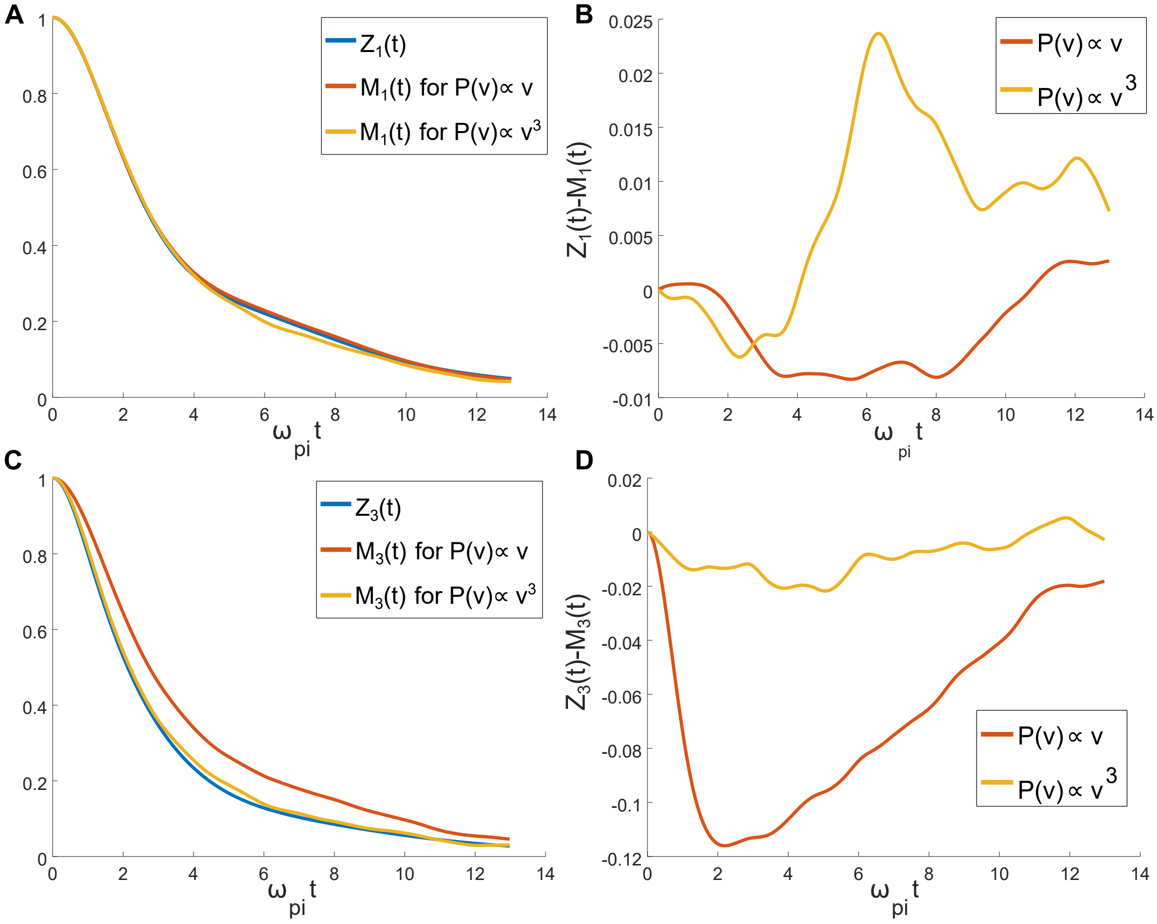

Figure 7.4 : **A**: Comparison of $Z_1(t)$ with $M_1(t)$ calculated from 'odd' subsets. Subset 1 ($P(v) \propto v$) more closely matches $Z_1(t)$, as can be seen in **B**, which plots $Z_1(t) - M_1(t)$ for each subset. **C**: Comparison of $Z_3(t)$ with $M_3(t)$ calculated from 'odd subsets'. Clearly subset 3 ($P(v) \propto v^3$) matches more closely, as can be seen in **D**.

The data from the even moments are compared in Fig. 7.5, and we again see better agreement with the autocorrelation function for power n when the tagging probability $P(v) \propto v^n$.

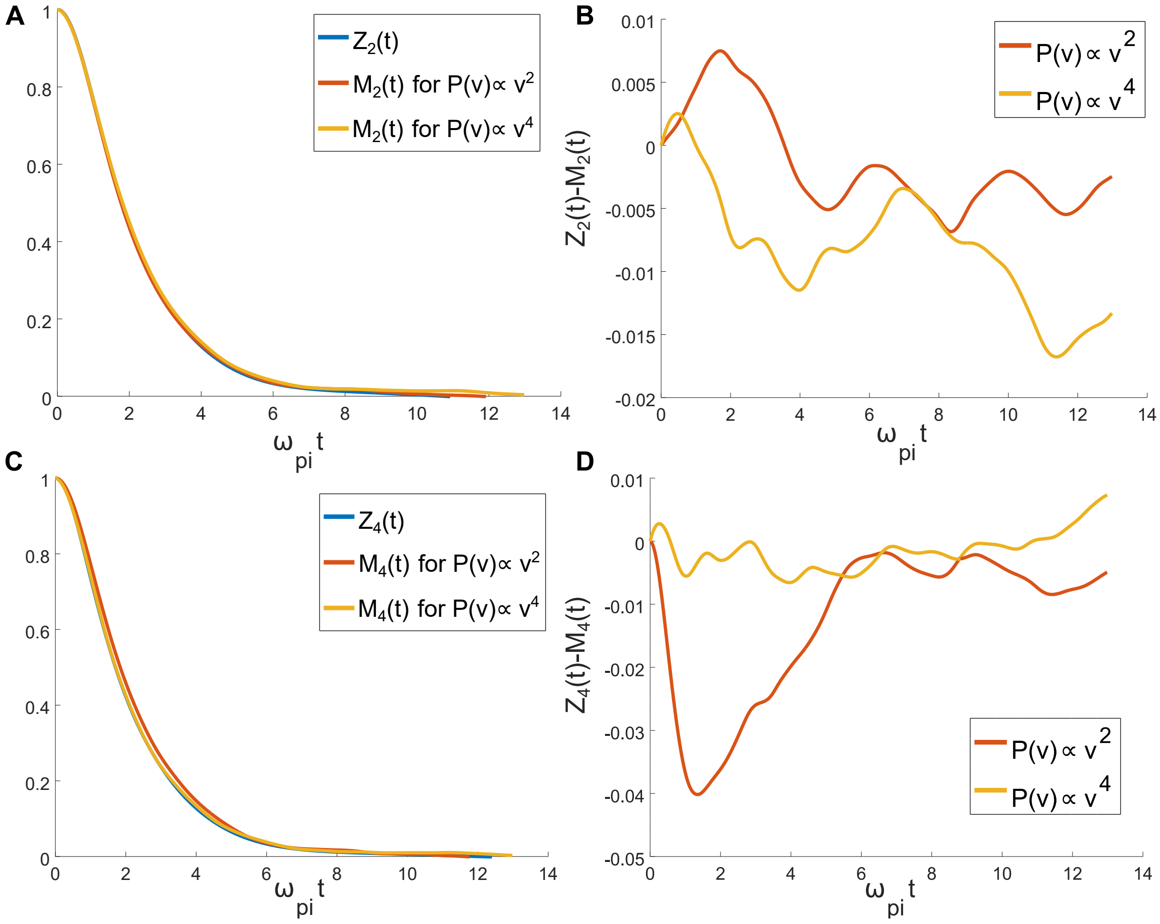

Figure 7.5 : **A**: Comparison of $Z_2(t)$ with $M_2(t)$ calculated from 'even' subsets. Subset 2 ($P(v) \propto v^2$) matches slightly better, as can be seen in **B**, which plots $Z_2(t) - M_2(t)$ for each subset. **C**: Comparison of $Z_4(t)$ with $M_4(t)$ calculated from 'even subsets'. Clearly subset 4 ($P(v) \propto v^4$) matches more closely, as can be seen in **D**.

7.3 Using the MDQT Code to Test Applicability of Eq. 7.3 for Optical Pumping Based Tagging Schemes

We can use the MDQT code to simulate the pump-probe experiments illustrated in Fig. 7.1 and Fig. 7.2 by taking the following steps:

- Create an equilibrated plasma with a given Γ and κ using the approach outlined in Appendix A.

- Use the QT implementation to simulate the optical pumping for time t_p.
- After t_p, turn off the lasers and let the system evolve for time t. Then, collapse all the wavefunctions (e.g. place each ion in either the $|\uparrow\rangle$ or $|\downarrow\rangle$ state with probability $|\langle\uparrow|\psi_i\rangle|^2$ and 1-$|\langle\uparrow|\psi_i\rangle|^2$, respectively) and record the desired velocity moment ($M_1(t)$ for the scheme illustrated in Fig. 7.1, $M_2(t)$ for the scheme illustrated in Fig. 7.2) of the ions in the $|\uparrow\rangle$ state.

The simulation allows us to test the applicability of Eq. 7.3 to pump-probe schemes with arbitrary pumping parameters (e.g. Ω, δ_{pump}, etc.) for plasmas with any set of values of Γ, κ, and n.

7.3.1 Testing Optical Pumping Scheme for Measuring $Z_1(t)$

We use the MDQT code to simulate this scheme (Fig. 7.1) for a plasma with $n = 2\times10^{14}$, $\kappa = 0.5$, and $\Gamma = 3$, which gives a temperature of $T \sim 520\,\mathrm{mK}$. The simulation is performed with pumping parameters (**a**: $\Omega = 1.3$, $\delta = -1$, $t_{pump} = 50\,\mathrm{ns}$), which are similar to the parameters used in a measurement of Z_1 performed by our lab in 2016 [39], along with (**b**: $\Omega = 0.7$, $\delta = -0.4$, $t_{pump} = 50\,\mathrm{ns}$) and (**c**: $\Omega = 0.7$, $\delta = -2.5$, $t_{pump} = 50\,\mathrm{ns}$). In Fig. 7.6A we show $P_\uparrow(v)$, determined by propagating the OBEs for these parameters up to 50 ns, vs. v/v_T for a 520 mK plasma. This is to illustrate the deviations from linearity in $P_\uparrow(v)$ that we expect in each case. We see that **b** is only linear over a small portion of v/v_T, and therefore we expect deviations between $M_1(t)$ and $Z_1(t)$ in this case. Although **c** and **a** both appear to be approximately linear over similarly sized region, we see that for **c** $P_\uparrow(v)$ sharply deviates from 0.5 *outside* of the linear region, and therefore a large portion of the $\langle v\rangle_\uparrow$ signal will come from these non-linear regions. Therefore we would expect **a** to perform the best.

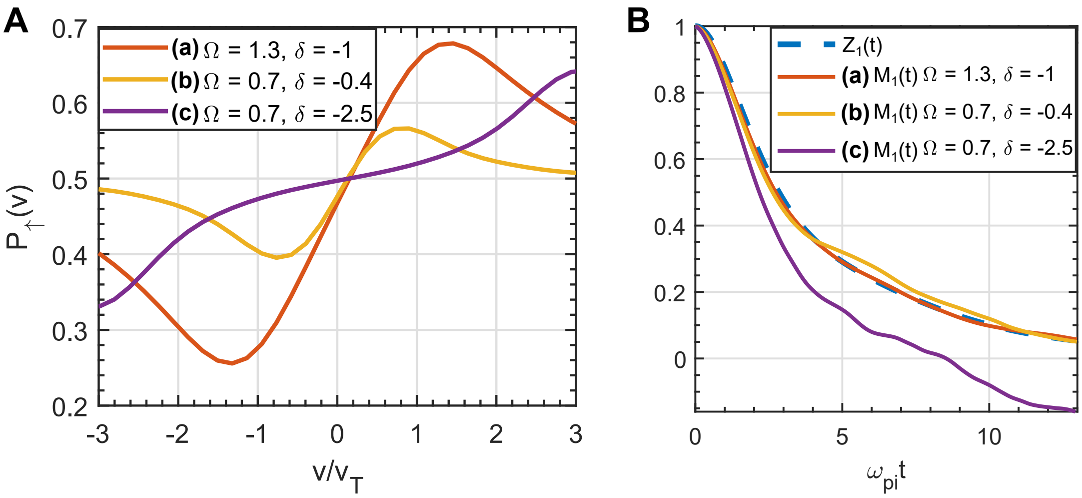

Figure 7.6 : **A**: OBE solutions for $P_{\uparrow}(v)$ vs. v/v_T ($T = 520\,\mathrm{mK}$) after pumping for 50 ns for various Ω and δ (letter labels in the legend correspond to those in the text). We see that if δ is too small (yellow) the function is linear only over $|v/v_T| < 0.5$ while if δ is too large (purple) the function begins to diverge from linearity for $v \sim v_T$ in such a way that the majority of the $\langle v \rangle_{\uparrow}$ signal will come from ions *outside* of the linear region. For $\delta = 1$ and a fairly large Rabi frequency $\Omega = 1.3$, the function is linear over a region $v \sim 1.4 v_T$, and, moreover, the strongest divergences from 0.5 are within the linear region, and thus most of the $\langle v \rangle_{\uparrow}$ signal will come from ions *within* the linear region. **B**: Results for $M_1(t)$ for the conditions in **A** plotted alongside $Z_1(t)$. As expected, the parameters of $\Omega = 1.3$ and $\delta = -1$ result in the best match between $M_1(t)$ and $Z_1(t)$.

The results in Fig. 7.6B verify that **a** does indeed perform the best, since its resulting $M_1(t)$ curve matches $Z_1(t)$ much more closely than the other two. This is despite the fact that the parameters of **a** result in a $P_{\uparrow}(v)$ curve that is only linear for $|v| \lesssim v_T$ (fig 7.6A). Thus, we find that the condition $P_{\uparrow}(v) \propto v$ in order for M_1 to be an accurate measure of $Z(t)$ is not that strict.

As we discussed in the introduction to this chapter, the ability to measure $Z_1(t)$ accurately is very important because it can be directly related to D through Eq. 7.2. Moreover, when plotted vs. scaled time ($\omega_{pi} t$), all $Z_1(t)$ of the same Γ and κ collapse onto the same universal curve $Z_1(\Gamma, \kappa, \omega_{pi} t)$. In this way, Z_1 is an inherent property of all plasmas of the same Γ and κ, and thus measurements of $Z_1(t)$ using UNPs can be directly related to $Z_1(t)$ of high density plasmas of comparable Γ and κ. This is another example of the ‘universality’ of these systems, a concept we introduced in Sec. 2.2.2.

We can also define a ‘universal’ value of the diffusion coefficient expressed in natural plasma units, $D^* = D/a^2\omega_{pi}$. In this case, we find

$$D^* = \frac{k_B T/m}{\omega_{pi} a^2} \int_0^\infty Z_1(t)\, dt = \frac{1}{3\Gamma} \int_0^\infty Z_1(\Gamma, \kappa, \omega_{pi} t)\, d\,(\omega_{pi} t) \tag{7.4}$$

where in the last step we use the relation $\frac{k_B T/m}{\omega_{pi}^2 a^2} = 1/3\Gamma$. Thus, we see that D^* is determined solely by Γ and κ and, as with Z_1, measurements of D^* in a UNP are directly generalizable to any other strongly coupled plasmas of similar Γ and κ. This is generally true of all transport coefficients.

Thus, by using LIF to measure $M_1(t)$ after optical pumping, ion density n_i (and thus ω_{pi}), and ion temperature T_i (and thus Γ), and by obtaining electron temperature T_e from the ionizing laser wavelength (and thus κ), one can obtain a measurement of $Z_1(\omega_{pi} t)$ for a UNP of Γ and κ. D^* can be determined by numerically integrating the experimentally measured $Z_1(\omega_{pi} t)$ curve using Eq. 7.4. We have done this in UNPs in the regime $\Gamma \leq 4$, which have not been laser-cooled, and we display the resulting $D^*(\Gamma)$ measurements (there is weak dependence on κ) in Fig. 7.7 along with curves representing phenomenological fits to MD results and some curves corresponding to various theoretical predictions for D^*, which are explained in the caption. Using laser-cooled UNPs, we hope to extend these measurements to $\Gamma \gtrsim 10$.

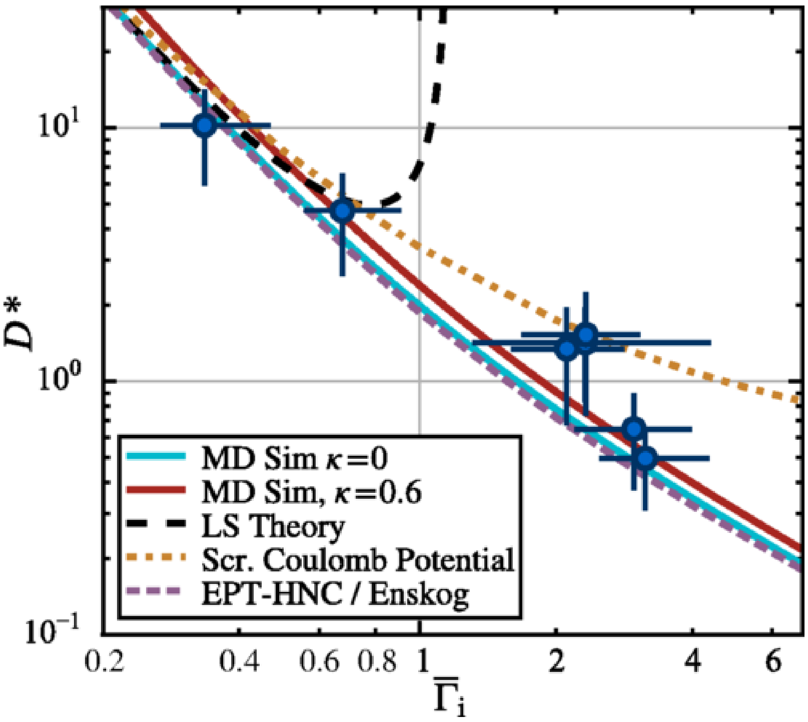

Figure 7.7 : Plot of normalized self-diffusion coefficient D^* vs. Γ measured in non-laser-cooled UNPs. We also show phenomenological fits to MD results for both $\kappa = 0$ and $\kappa = 0.6$ using solid lines [56]; there is very little difference between the two (all of our experimental data is taken for $\kappa < 0.6$). Dashed lines come from various theoretical predictions for D^*. The black dashed line represents the Landau-Spitzer theory, which does not factor in short-range correlations (aka 'conventional' kinetic theory). We see that this prediction clearly diverges from both our experimental data and the MD results. The orange and purple dashed lines indicate new theoretical predictions [47] which attempt to take short-range correlations into account through modification of the Boltzmann collision operator.

7.3.2 Testing Optical Pumping Scheme for Measuring $Z_2(t)$

We also use the MDQT code to simulate the optical pump-probe scheme described in Fig. 7.2 for the same values of Γ, κ, and n used in Sec. 7.3.1. We use $\Omega = 2\gamma_{SP}$, $t_{pump} = 100\,\text{ns}$ and $\delta = 0$, since the OBE solutions shown in Fig. 7.2 indicate that $P_\uparrow(v)$ is well described by a quadratic for these parameters. In Fig. 7.8 we show the MDQT results for $M_2(t)$ alongside $Z_2(t)$; the agreement is quite good.

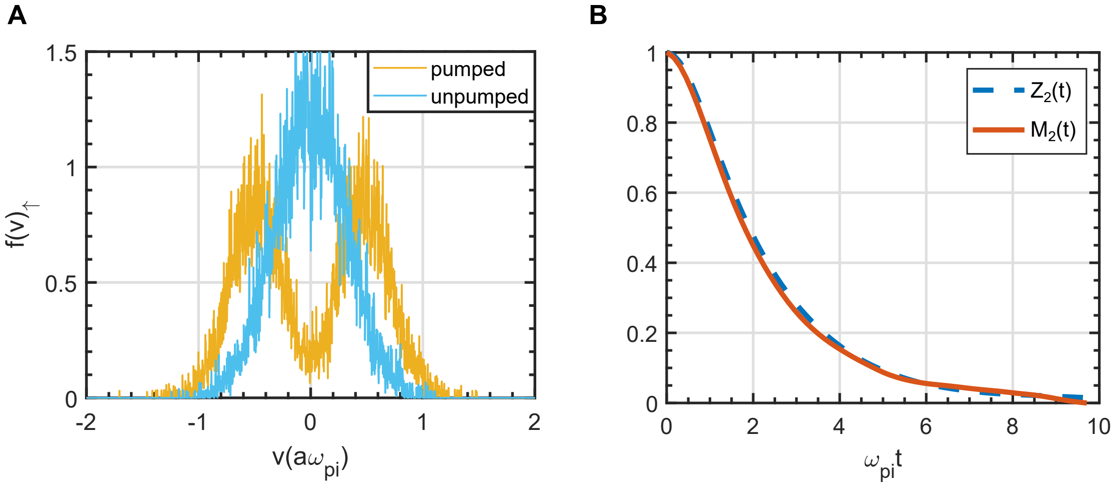

Figure 7.8 : (**A**): Velocity distribution of the $|\uparrow\rangle$ state with and without optical pumping for the MDQT simulation described in the text. The distributions are normalized to unit area. (**B**): Comparison of $M_2(t)$ and $Z_2(t)$ for the MDQT simulation described in the text.

Similarly to Z_1, it is also true that $Z_2(\omega_{pi}t)$ is universal in Γ and κ. Further, it can also be related to a transport coefficient using a Green-Kubo relation. Specifically, it can be used to determine the longitudinal viscosity. The rest of this section is dedicated to this Green-Kubo relation and a discussion on longitudinal viscosity.

Viscosity describes the resistance of a fluid to flow. The type of viscosity that is most commonly discussed in scientific discussion, and even in layman discussion, is shear viscosity η_s, which describes the resistance of a fluid to the application of a shear flow. The damping rate of an induced shear wave, for example, is proportional to η_s [43]. We discuss shear viscosity in greater detail in Sec. 8.3.

However, it turns out that η_s is quite difficult to measure experimentally via Green-Kubo techniques. The *longitudinal* viscosity, η_l, which describes resistance to 1D compression waves, is much more straightforwardly measured via a spin-tagging technique. These terms are related through the equation $\eta_l = 4\eta_s/3 + \eta_b$, where η_b

is the bulk viscosity that arises when considering resistance to 3D expansion or compression. For strongly coupled plasmas $\eta_b \sim 0.008\eta_s$ [144] and is therefore typically neglected, implying $\eta_l = 4\eta_s/3$.

The Green-Kubo relation for η_l is given by [43]:

$$\eta_l = \frac{1}{Vk_BT}\int_0^\infty C_l(t) \tag{7.5}$$

where $C_l(t)$ is known as the longitudinal current correlation function, which is defined as

$$C_l(t) = \langle(\Pi_{xx}(t) - \bar{\Pi}_{xx})(\Pi_{xx}(0) - \bar{\Pi}_{xx})\rangle \tag{7.6}$$

where Π_{xx} is the diagonal component of the stress tensor

$$\Pi_{xx}(t) = \sum_{i=1}^{N}\left[mv_{ix}v_{ix} - \frac{1}{2}\sum_{j\neq i}^{N}\frac{x_{ij}x_{ij}}{r_{ij}}\frac{\partial\phi(r_{ij})}{\partial r_{ij}}\right] \tag{7.7}$$

and $\bar{\Pi}_{xx}$ refers to the long term equilibrium value around with Π_{xx} fluctuates.

The current correlation function can thus be broken up into three terms: a term related to the autocorrelation of "kinetic terms" (e.g. $v_{ix}(t)v_{ix}(t)v_{ix}(0)v_{ix}(0)$), a "potential term" $\frac{1}{2}\sum_{j\neq i}^{N}\frac{x_{ij}(t)x_{ij}(t)}{r_{ij}(t)}\frac{\partial\phi(r_{ij}(t))}{\partial r_{ij}(t)}\frac{1}{2}\sum_{j\neq i}^{N}\frac{x_{ij}(0)x_{ij}(0)}{r_{ij}(0)}\frac{\partial\phi(r_{ij}(0))}{\partial r_{ij}(0)}$, and terms that couple potential and kinetic terms. The first term can be determined directly with knowledge of the auto-correlation function for v^2 (i.e. $Z_2(t)$), and can thus be related to a measurement of $M_2(t)$ using optical pump-probe as in Fig. 7.8. Unfortunately, there is no simple way to measure the other terms that contribute to C_l. However, it is expected that the terms coupling the potential and kinetic contributions are always negligible[47], and therefore we are only 'missing' the potential term.

The ability to measure the kinetic term is valuable for a number of reasons. First, for $\Gamma < 5$, the viscosity is almost entirely determined by the kinetic term, as demonstrated in Fig. 7.9. (NOTE: this figure is from a paper that measures η_s, however, as discussed previously the two viscosities are directly related to one another, and we expect them to behave similarly.) Second, MD simulations indicate that there is a minimum in the viscosity at $\Gamma \sim 20$ corresponding to when the dominant term crosses over from the kinetic to the potential term. By coupling a measurement of the kinetic term using our spin-tagging technique with a direct measurement of the full viscosity, which we propose in Sec. 8.3, we can elucidate the role of the potential term. Third, one of the latest proposals to extend kinetic theory to strong coupling is the 'effective potential theory' discussed in [47]; this is responsible for the theory curves in Fig. 7.9 and in Fig. 7.7. However, this theory only captures the kinetic contributions, and therefore a direct measurement of that term will serve as a test of the theory.

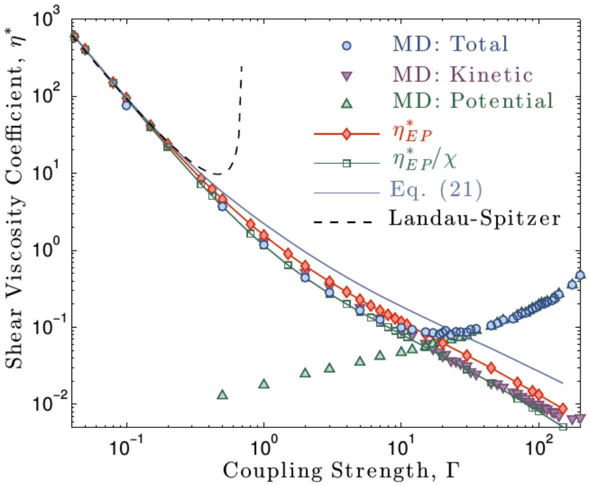

Figure 7.9 : Determination of kinetic and potential contributions to viscosity using Green-Kubo relations. The effective potential theory used to generate the three theory curves (η_{EP}, η_{EP}/χ, and 'Eq. (21)') attempt to calculate the kinetic contribution only. Thus, a measurement of the kinetic contribution would serve as a good test of this theory. Adapted from [47].

As with D, we can define a 'normalized' viscosity $\eta_l^* = \eta_l/mna^2\omega_{pi}$. The kinetic portion of Eq. 7.5 can then be written:

$$\begin{aligned}
\eta^*_{l,kin} &= \frac{N}{mnVa^2\omega_{pi}k_BT}\int_0^\infty m^2\left[\langle v_i(t)^2v_i(0)^2\rangle - v_T^2\langle v_i(t)^2\rangle - v_T^2\langle v_i(0)^2\rangle + v_T^4\right]\,dt \\
&= \frac{N}{mnVa^2\omega_{pi}k_BT}\int_0^\infty m^2\left[\langle v_i(t)^2v_i(0)^2\rangle - v_T^4\right]\,dt \\
&= \frac{m\left[\langle v_i(0)^2v_i(0)^2\rangle - v_T^4\right]}{a^2\omega_{pi}k_BT}\int_0^\infty Z_2(t)\,dt \\
&= \frac{m\left(3v_T^4 - v_T^4\right)}{a^2\omega_{pi}^2k_BT}\int_0^\infty Z_2(\omega_{pi}t)\,d(\omega_{pi}t) \\
&= \frac{2}{3\Gamma}\int_0^\infty Z_2(\omega_{pi}t)\,d(\omega_{pi}t)
\end{aligned} \tag{7.8}$$

where in the first step we use $\bar{\Pi}_{xx,kin} = mv_T^2$, in the second step we use the fact $\langle v_i(t)^2\rangle = v_T^2$ for all time assuming a maxwellian, in the third step we used Eq. 7.1, in the fourth step we substituted in $\langle v^4\rangle = 3v_T^4$, which again assumes a maxwellian velocity distribution, and in the last step we used the relations $v_T = \sqrt{k_BT/m}$ and $\frac{k_BT/m}{a^2\omega_{pi}^2} = 1/3\Gamma$.

From Eq. 7.8, it is clear that one can derive $\eta^*_{l,kin}$ from a measurement of $Z_2(t)$, while the MDQT results displayed in Fig. 7.8 demonstrate that $Z_2(t)$ can be accurately measured by obtaining $M_2(t)$ using the pump-probe scheme illustrated in Fig. 7.2. Thus, it should be possible to measure $\eta^*_{l,kin}$ in a UNP using this pump-probe technique. We have yet to study this in our experiment; this is something we hope to accomplish in the future, as there is a dearth of measurements of viscosity in strongly coupled plasmas.

Chapter 8

Direct Measurements of Transport Quantities Through Application of Laser Forces

In the previous chapter, we discussed how some transport quantities can be measured through *indirect* means, via optical pump-probe experiments in which autocorrelation functions of powers of velocity, $Z_n(t)$, are measured. Through Green-Kubo formulas, integrals of form $\int_0^\infty Z_n(t)\,dt$ can be used to obtain the transport quantities.

In contrast, in this chapter we will propose techniques for the *direct* measurement of transport quantities. For example, in Sec. 8.3, we will discuss a technique in which optical forces are used to create a shear flow. The subsequent dissipation of the flow can be used to measure the coefficient of shear viscosity.

We will focus on four transport quantities

- ν: The temperature anisotropy relaxation rate (also often referred to as the 'collisional equipartition rate'), introduced in Sec. 4.6.1, is the subject of Sec. 8.1.
- D: The self-diffusion coefficient, introduced in the previous chapter, is the subject of Sec. 8.2.
- η_s: The shear-viscosity coefficient, also introduced in the previous chapter, is the subject of Sec. 8.3
- K: The thermal conductivity, introduced in Sec. 5.1, is the subject of Sec. 8.4.

Knowledge of these quantities is critical for understanding the dynamics of any system, including strongly coupled plasmas. However, kinetic theories that attempt to generate these quantities from the microscopic dynamics of plasma collisions fail for $\Gamma \gtrsim 1$ due to the development of short-range correlations. Direct measurements of these quantities in a higher Γ system, such as a laser-cooled UNP, will help enhance our knowledge of plasmas in this regime.

8.1 Anisotropy Relaxation Rate

8.1.1 How Large of a Temperature Anisotropy can be Established?

In Sec. 5.3, we observed that laser-cooling along one axis of the cloud (the x-axis) resulted in the cooling of all thermal degrees of freedom (Fig. 5.6). This behavior was also observed in the MDQT simulation in Sec. 4.6.1 (Fig. 4.14). However, we see in the simulation results that a small level of temperature anisotropy of $\sim 30\,\mathrm{mK}$ should develop during the cooling process. If the lasers are turned off at some point during the cooling process, then we should observe the temperature isotropize at a rate ν, which we define as the temperature anisotropy relaxation rate.

Specifically, for a plasma with a temperature along the laser-cooling (or laser-heating) axis T_x, and temperature perpendicular to that axis $T_{y,z}$, the equations governing the temperature evolution are

$$\partial_t T_x = -\beta T_x + 2\nu(T_{y,z} - T_x) \tag{8.1}$$

$$\partial_t T_{y,z} = -\nu(T_{y,z} - T_x) \tag{8.2}$$

where $\beta > 0$ indicates laser-cooling and $\beta < 0$ indicates laser-heating. Here we ignore the effect of the correlation temperature (we discuss this effect in Sec. 4.6.1). If we assume that $T_x = T_{y,z} = T_0$ when the laser is turned on (which we define as $t = 0$), then these equations have an analytical solution:

$$T_x(t) = T(0)\exp\left[-\frac{t}{2}(\beta + 3\nu)\right]\left[\cosh\left(\frac{t\alpha}{2}\right) - \frac{\beta - 3\nu}{\alpha}\sinh\left(\frac{t\alpha}{2}\right)\right] \tag{8.3}$$

$$T_{y,z}(t) = T(0)\exp\left[-\frac{t}{2}(\beta + 3\nu)\right]\left[\cosh\left(\frac{t\alpha}{2}\right) + \frac{\beta + 3\nu}{\alpha}\sinh\left(\frac{t\alpha}{2}\right)\right] \tag{8.4}$$

where $\alpha = \sqrt{\beta^2 + 2\beta\nu + 9\nu^2}$. This is obviously a somewhat complicated expression, but the basic behavior is that, after a short period of time over which a temperature anisotropy is established, the two temperatures fall or rise (depending on whether cooling or heating) together (See Fig. 8.1A-C) with $\frac{T_x}{T_y}_{t\to\infty}$ as a constant given by:

$$\frac{T_x}{T_y}_{t\to\infty} = \frac{\alpha - \beta - \nu}{2\nu} \tag{8.5}$$

Results from MD simulations indicate that $\nu \approx 0.1\omega_{pi}t$ [137]. So, in order to determine what levels of temperature anisotropy we should be able to establish, we plot $T_x(t)$ and T_y for laser-**heating** with $\beta = -5.2 \times 10^4\,\mathrm{s}^{-1}$ (measured in Ch. 5.), $n = 4 \times 10^{13}\,\mathrm{m}^{-3}$ (we choose a relatively low density in order to have a relatively large ratio $\beta/\nu = 0.6$, since $\frac{T_x}{T_y}_{t\to\infty}$ increases with β/ν), and various $\Gamma(t = 0)$ (which sets $T(t = 0)$) in Fig. 8.1A-C. These plots are derived using Eqs 8.3 and 8.4. We also show $\frac{T_x}{T_y}(t)$(Fig. 8.1D), $T_y(t) - T_x(t)$ (Fig. 8.1E), and $T_y - T_x(t = 8\mu\mathrm{s})$ vs Γ (Fig. 8.1F), where we choose 8μs since this is approximately when T_x/T_y saturates.

From Fig. 8.1F we see that the expected temperature anisotropy $T_y - T_x$ ranges from $\sim$ 200 mK ($\Gamma = 1$) to $\sim$ 40 mK ($\Gamma = 5$). Measuring a 40 mK difference is pretty difficult using LIF, but, measuring differences of 100 mK or greater should be relatively easy. Since $\Gamma \sim 3$ after DIH, we will opt to heat the plasma (thus decreasing Γ) before measuring anisotropy in order to work in the high $T_y - T_x$ regime. Ultimately

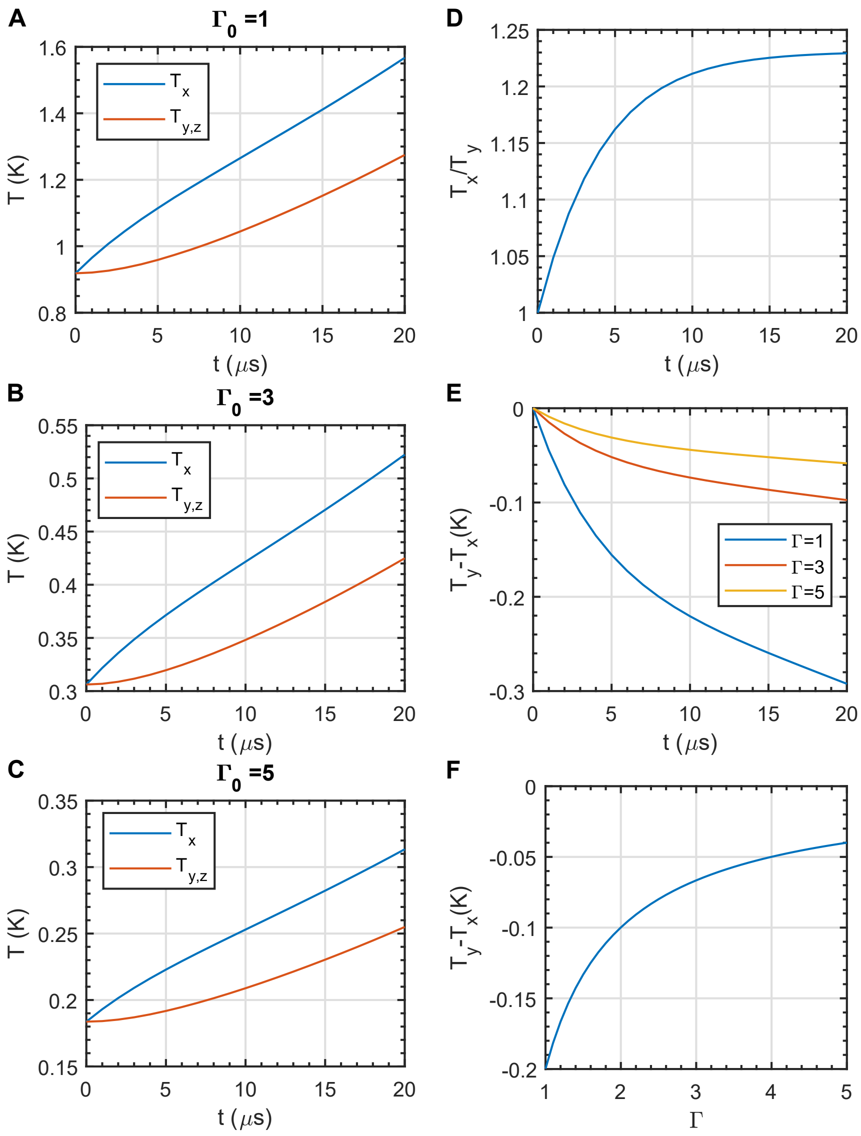

Figure 8.1 : (**A-C**): Plots of Eqs. 8.3 and 8.4 for $n = 4 \times 10^{13}\,\mathrm{m}^{-3}$, $\beta = -5.2 \times 10^4\,\mathrm{s}^{-1}$, and $\nu = 0.1\omega_{pi}$ for (**A**): $\Gamma_0 = 1$, $T_0 = 0.93\,\mathrm{K}$, (**B**): $\Gamma_0 = 3$, $T_0 = 0.31\,\mathrm{K}$ and (**C**): $\Gamma_0 = 5$, $T_0 = 0.18\,\mathrm{K}$. (**D**): T_x/T_y. We see that it converges after roughly 10μs. (**E**): $[T_y - T_x]\,(t)$ for each Γ_0 plotted in (**A-C**). (**F**): $T_y - T_x$ at $t = 8\mu$s as a function of Γ. We see that, for $\Gamma \leq 2$, anisotropy levels of 100 mK or greater could be achieved. In contrast, for $\Gamma \sim 5$, the anisotropy achievable for these parameters is only 40 mK. This will make anisotropy measurements at high Γ more difficult.

we want to measure ν as a function of Γ, and thus we will eventually need to attempt to study anisotropy relaxation for higher Γ, however for an initial test it makes sense to try at low Γ.

In principle, one could measure ν by laser-heating or laser-cooling the plasma along x and then measuring $T_x(t)$ and $T_y(t)$ curves and fitting them using Eqs 8.3 and 8.4 with ν as the fitting parameter. However, this would rely on the assumption of perfect knowledge of β. Although we have developed what seems to be a good tool for estimating β (see Sec. 5.1), it would be better to measure ν in a β independent way.

This can be done by first establishing an anisotropy, then turning off the laser-heating or cooling beams and observing the subsequent convergence of $T_{y,z}$ and T_x. For $\beta = 0$, it is clear from Eqs. 8.1-8.2 that

$$\partial_t(T_x - T_y) = -3\nu(T_x - T_y) \tag{8.6}$$

and therefore, by creating an anisotropy and then subsequently measuring $\left[T_x - T_y\right](t)$ and fitting to an exponential decay, we can measure ν in a β independent way. We show results from initial tests of this technique in Sec. 8.1.3. In the next section, we will introduce MD results of temperature anisotropy relaxation.

8.1.2 Molecular Dynamics Simulations of Temperature Anisotropy Relaxation

We use MD simulations to study relaxation of temperature anisotropies that are created in two ways:

- *Slow* anisotropy creation, in which we simulate anisotropy establishment through laser-cooling or laser-heating. In order to keep these simulations relatively simple, we assume that the force is of form $\vec{F} = -\beta/2m\left(\vec{v}\cdot\hat{x}\right)\hat{x}$ for all $\vec{v}$. We test two different cases: one where only the x axis is cooled or heated, and another where the x axis is heated with a force $\vec{F} = \beta/4m\,(\vec{v}\cdot\hat{x})\,\hat{x}$ while the y and z axes are cooled with forces $\vec{F} = -\beta/8m\,(\vec{v}\cdot\hat{y})\,\hat{y}$ and $\vec{F} = -\beta/8m\,(\vec{v}\cdot\hat{z})\,\hat{z}$. In the latter, the total thermal energy $T = T_x/3 + 2T_{y,z}/3$ is largely unaffected by the laser forces, which help make this technique and the next technique a bit more analogous, while the former is analagous to what we will actually study experimentally in Sec. 8.1.3, in which we apply laser-heating along only the x axis.

- *Instantaneous* anisotropy creation in which, at some time during the simulation, anisotropy is created in a previously isotropic plasma by instantaneously increasing velocities along one axis and decreasing them along the other two. Specifically, we consider the case where, at $t = 0$, $v_x \rightarrow v_x\sqrt{1+\epsilon}$ and $v_{y,z} \rightarrow v_{y,z}\sqrt{1-\epsilon/2}$. This results in $T_x \rightarrow T_x(1+\epsilon)$ and $T_{y,z} \rightarrow T_{y,z}(1-\epsilon/2)$. Thus, the total thermal energy $T = T_x/3 + 2T_{y,z}/3$ remains constant. We record T_x and $T_{y,z}$ after $t = 0$. This is *not* possible in our apparatus, as it would basically require $\beta \gg \nu$, which is impossible for reasonable density. However, this is how anisotropy relaxation is studied in MD literature [137], and thus it is worth obtaining these results as well in order to compare with the more 'realistic' anisotropy simulation performed by the previous method.

First, we compare MD data taken using the first technique (with forces applied along both axes) to MD data taken using the second technique for $\Gamma = 3$, $\kappa = 0.5$, and $n = 4 \times 10^{13}\,\mathrm{m}^{-3}$. For the first technique, we choose $\beta = 5.2 \times 10^{4}\,\mathrm{s}^{-1}$ and the force application time to be 10μs. For the second technique, we choose $\epsilon = 0.15$. The results are shown in Fig. 8.2. (NOTE: All references to 'instantaneous' MD data in figures *other than Fig. 8.2* are to results from [137], whereas Fig. 8.2 refers to our own

MD simulation. All ‘slow’ MD data is obtained from our own simulations).

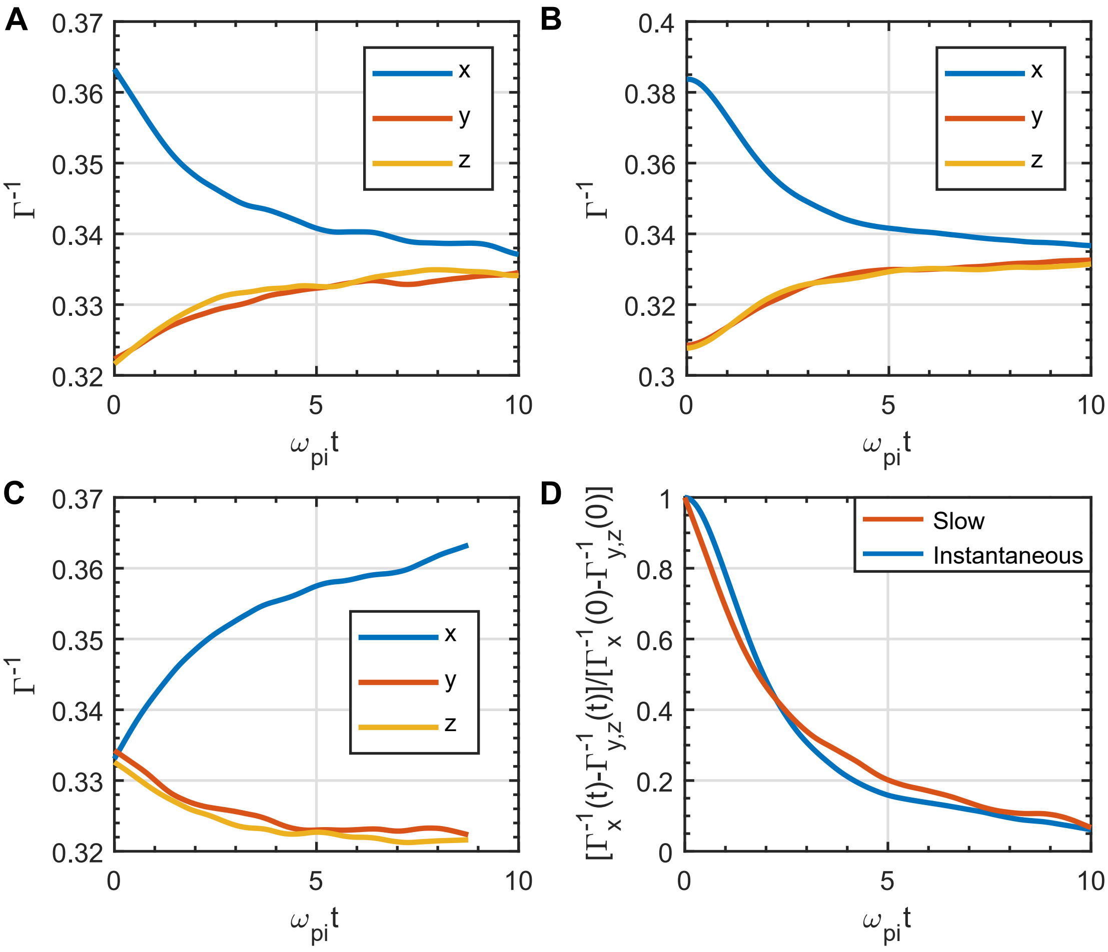

Figure 8.2 : (**A**): Anisotropy relaxation in ‘plasma units’ Γ^{-1} vs $\omega_{pi}t$, with the color corresponding to the temperature along a given axis indicated in the legend, for the case where the anisotropy is ‘slowly’ established by heating along the x axis (rate $\beta/2$) and cooling along the other two axes (rate $\beta/4$) for 10μs. For this simulation, we choose $\beta = 5.2 \times 10^4\,\mathrm{s}^{-1}$, $n = 4 \times 10^{13}\,\mathrm{m}^{-3}$, $\Gamma = 3$, and $\kappa = 0.5$. (**B**): Same conditions as **A**, but for the case where anisotropy is ‘instantaneously’ established with $\epsilon = 0.15$. Here we clearly observe a smooth ‘rollover’ at early times, which we do not see in **A**. (**C**): Plot of $\Gamma^{-1}(\omega_{pi}t)$ during the ‘slow’ anisotropy establishment preceding the relaxation stage shown in **A**. (**D**): Plot of $\left[\Gamma_x^{-1} - \Gamma_y^{-1}\right](t)$, normalized such that curve begins at 1 for $t = 0$, for both cases. We observe a number of differences between the two anisotropy relaxation curves. We observe the early time ‘rollover’ only in the ‘instantaneous’ case. It also appears that the decay is a little bit slower for the ‘slow’ case. This will cause relaxation rates, ν, measured from MD data to differ depending on how the anisotropy is established (see Fig. 8.4).

The primary feature to note is that the $T_x - T_y$ decay curves differ slightly between the two techniques (Fig. 8.2D). Specifically, for instantaneous establishment of anisotropy, the subsequent relaxation curve has a slow 'rollover' for early times ($\omega_{pi}t \leq 1$) before the relaxation becomes much more rapid for $\omega_{pi}t = 1{-}4$. This is similar to the behavior of velocity-autocorrelation functions for $\Gamma > 1$ (see Fig. 7.6B). The timescale of the rollover is set by the correlation time for fluctuating forces [39, 131], which is roughly one order of magnitude faster than the relaxation phenomenon that is being observed (see Fig. 7.6B).

In contrast, for slow establishment we do not see the rollover at early times for the β considered here. In this case, the correlations between fluctuating forces relax throughout the anisotropy establishment process. If the anisotropy establishment rate were increased, such that $\beta \gg \nu$, we would likely observe a rollover. We also observe that the relaxation rate appears to be a bit slower in the slow-establishment case than in the instantaneous establishment case.

This emphasizes the need to compare simulations and experiments that are as similar as possible. From these results, we observe that direct comparison between experimental temperature anisotropy data (which would necessarily be taken using a 'slow' establishment) and 'instantaneous' anisotropy data (which is what exists in most prior literature [137]) would be somewhat of an 'apples to oranges' comparison due to the differences between relaxation curves resulting from the different anisotropy establishment techniques.

In any case, in order to extract a 'relaxation' rate, the authors in [137] fit their 'instantaneous' MD results to exponential decay curves. However, by plotting $T_x - T_y$ on a log-linear plot, they observe that the relaxation curves ultimately diverge from an exponential decay curve at late time (Fig. 8.3A). Thus, they restrict their fits to the portion of the decay that appears exponential (roughly $\omega_{pi}t < 5$ for $\Gamma \geq 0.5$). Moreover, for data containing a 'roll over' they restrict the fit to $1 \leq \omega_{pi}t \leq 3$. They plot their measurements of ν vs Γ, along with a few theoretical plots (see Fig. 8.3B).

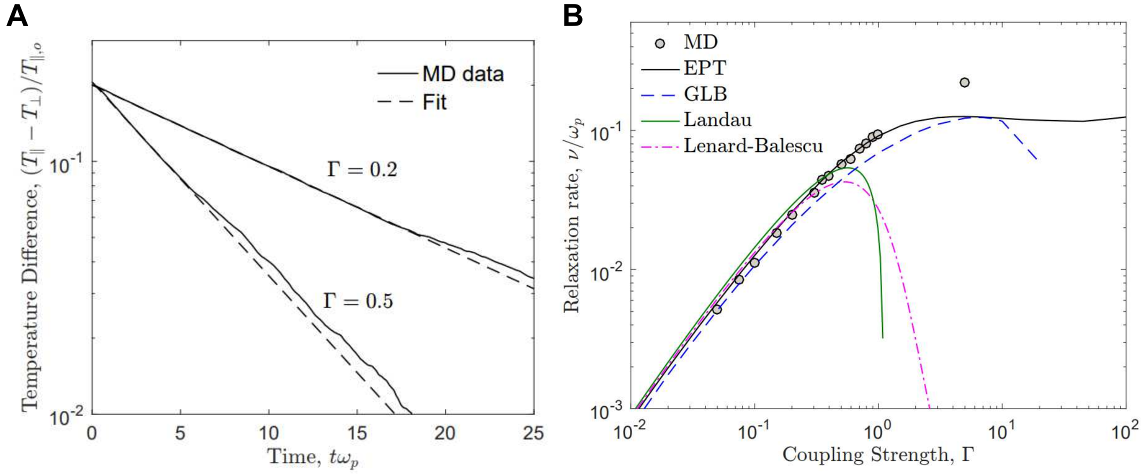

Figure 8.3 : (**A**): Observation of non-exponential decay in temperature anisotropy for late times for data from [137]. We see that, for $\Gamma = 0.5$, the curve diverges from an exponential fit for $\omega_{pi}t > 5$. (**B**): Measurements of $\nu/\omega_{pi}(\Gamma)$ obtained by fitting exponentials to temperature anisotropy within the region of time for which exponential decay is observed to be valid. Both figures adapted from [137].

We also observe this effect in our 'slow' MD data (Fig. 8.4A). Thus, we fit exponential decay curves to the portion of the data where $\omega_{pi}t < 2$ (we do not observe any roll-over at early times, so we are free to fit data even at $\omega_{pi}t = 0$). In Fig. 8.4B, we plot the fits for our 'slow' MD data along with the 'instant' MD and 'effective potential theory' (EPT) results from [137] (these are the same as in Fig. 8.3B).

For $\Gamma < 1$, both MD sets agree with the EPT theory. However, for $\Gamma = 5$, the instant data appears to diverge from the EPT results while the 'slow' MD data remains on the EPT curve. This is an interesting result, as it suggests that, for $\Gamma > 1$, the EPT theory, which is a method for extension of kinetic theory to the strongly coupled regime [47], describes the relaxation of temperature anisotropies

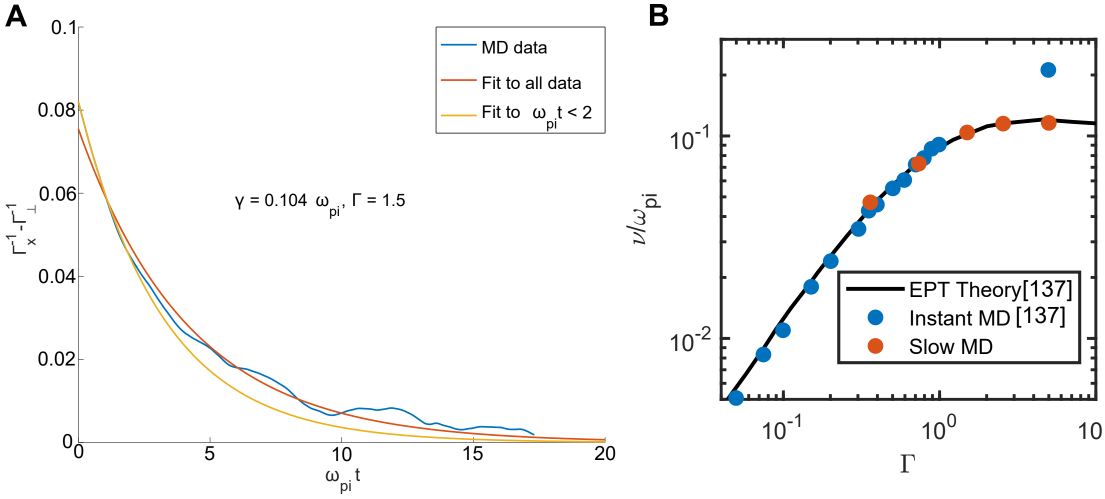

Figure 8.4 : (**A**): Observation of non-exponential decay in anisotropy relaxation curves for the 'slow' anisotropy establishment case. We clearly see good agreement between a fit to early data (yellow) and the early data itself (blue), whereas an exponential fit to all data (red) does not appear to characterize the relaxation. Thus, we fit the MD data within the region $\omega_{pi}t < 2$ to an exponential in order to obtain ν. (**B**): Plot of ν/ω_{pi} vs Γ. We compare our results, obtained with 'slow' anisotropy establishment, to 'instantaneous' anisotropy establishment results from [137]. We also plot a theoretical curve from [137] derived from 'effective potential theory' (EPT). Curiously, the 'slow' results at high Γ seem to match the EPT prediction, while the 'instantaneous' results do not.

which develop slowly but not ones that are developed instantaneously. Thus, we can conclude the EPT theory appears to well describe temperature anisotropy in physically relevant conditions in strongly coupled plasmas (at least for $\Gamma \leq 5$), since temperature anisotropies are typically *not* developed instantaneously.

To conclude: there appear to be substantial differences between temperature anisotropy relaxation curves depending on whether the anisotropy is developed 'instantaneously' or 'slowly'. The conditions in our experiment match the latter case, and so when comparing the anisotropy relaxation curves to MD data we must be careful to compare to the 'slow' MD data.

8.1.3 Preliminary Experimental Studies of Temperature Anisotropy Relaxation in a UNP

To test whether or not we could create observable temperature anisotropies by laser-cooling or heating UNPs, we took two sets of data. In the first set, we allowed the plasma to expand freely for 80μs before laser-cooling the cloud for 30μs, with beams propagating along the x axis. This resulted in a plasma with density $n = 5 \times 10^{13}\,\mathrm{m}^{-3}$ and $\Gamma = 2.7$ after laser-cooling. We then turn off the laser and immediately image the plasma, propagating the LIF beam along the x-axis with a camera gate width of 400 ns. We then repeat the process, but switch the LIF beam propagation axis to the y axis. We generate plots of T_x and T_y vs x, similar to the ones in Fig. 5.6. The temperature anisotropy, should it exist, would be centered in a small region about $x = 0$, as this is the region that experiences the most cooling (Sec. 5.1). Indeed, this is what we observe (Fig. 8.5A); the temperature along the cooling axis (T_x) is lower than the temperature perpendicular to the cooling axis (T_y) in the central region of the plasma.

In the second data set, we allowed the plasma to expand freely for 90μs before laser-heating the plasma for 30μs, again with beam propagation along the x axis. This resulted in a plasma with density $n = 4 \times 10^{13}\,\mathrm{m}^{-3}$ and $\Gamma = 1.45$ after laser-heating. We take LIF images in the same way as in the previous set. Here, we see that $T_x > T_y$ in the central, heated, region of the plasma, as expected (Fig. 8.5B).

In order to obtain accurate temperature anisotropy relaxation curves, we need to be able to resolve temperature differences to the $< 10\,\mathrm{mK}$ level. To make accurate measurements of $T_x - T_y$ at a given time t after the laser-cooling/heating is turned off, we obtain multiple independent measurements. This can be done in the following way: for a given dataset, we define the ‘heated’ (or cooled) region to be the central 3.25 mm

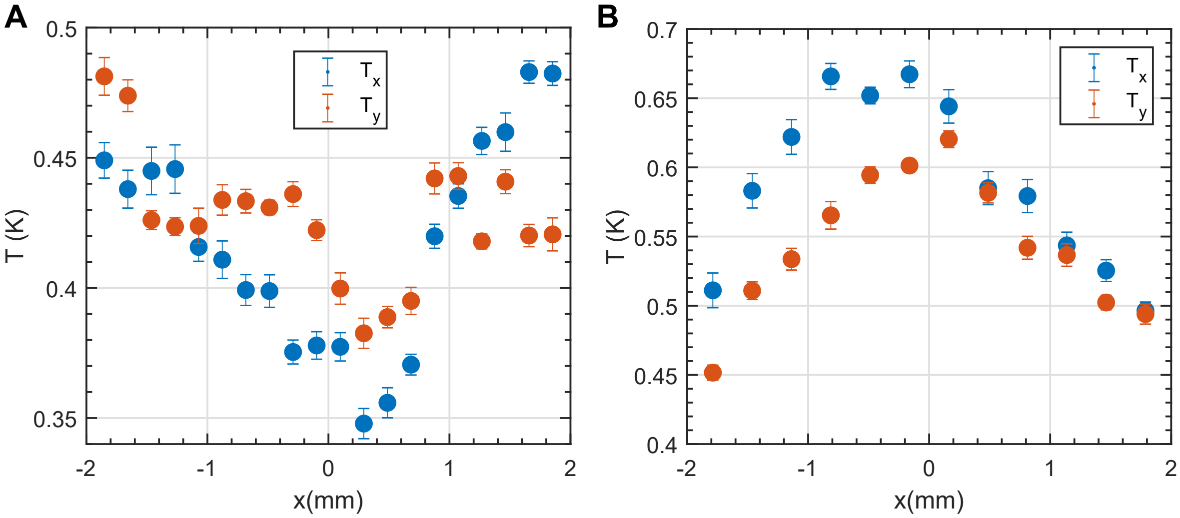

Figure 8.5 : (**A**): Observation of temperature anisotropy resulting from cooling the plasma along the x axis for 30μs after 80μs of free expansion. LIF data is taken within 400 ns after the cooling lasers are turned off. Here we observe that $T_x < T_y$ in the cooled central region, as expected. (**B**): Observation of temperature anisotropy resulting from heating the plasma along the x axis for 30μs after 90μs of free expansion. LIF data is taken within 400 ns after the heating lasers are turned off. Here we observe that $T_x > T_y$ in the heated central region, as expected.

X 3.25 mm portion of the plasma. We then break this region into 49 subregions of size 0.625 mm X 0.625 mm. T_x and T_y are obtained within each subregion by fitting the LIF data, providing 49 independent measurements of $T_x - T_y$. We then repeat this process for up to 5 cooling/heating runs, compiling up to 245 independent measurements of $T_x - T_y$ for a given time t after the 408 nm laser is turned off. These independent measurements are binned to create a histogram, which is then fitted to a normal distribution. The center of the fitted distribution provides the measurement of $T_x - T_y$ at time t, while we use the standard error $E = \sigma/\sqrt{N}$, where σ is the width of the fitted distribution and N is the number of independent measurements, to describe our uncertainty in this value. This process is illustrated in Fig. 8.6

We attempted to obtain an anisotropy relaxation curve $[T_x - T_y]\,(t)$ for the case

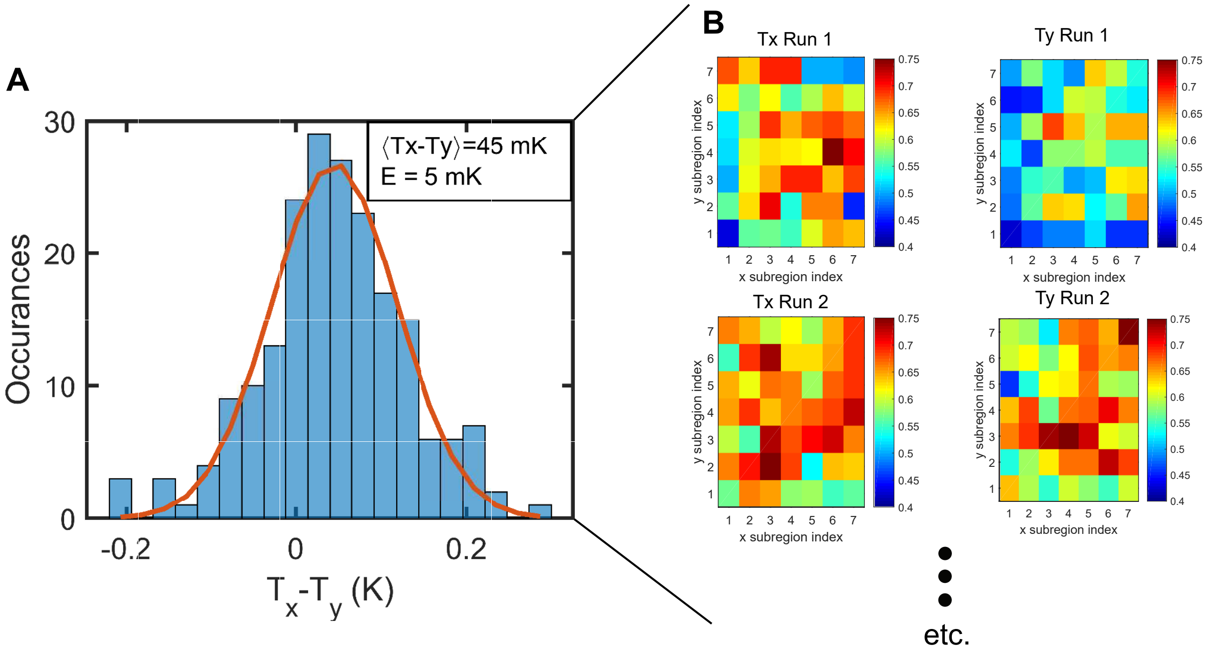

Figure 8.6 : (**A**) Histogram of occurrences of $T_x - T_y$ for LIF data taken within 400 ns after laser heating beams propagating along the x axis are turned off, along with a fit to a normal distribution (red). We see that the central value of $T_x - T_y$ is > 0, as expected for laser heating. The standard error is defined as $E = \sigma/\sqrt{N}$, where σ is the width of the normal distribution and N is the number of measurements. (**B**): Examples of datasets from which the histogram in **A** is derived. For each 'run', we obtain 49 independent measurements of T_x and T_y. By taking the difference, we obtain 49 independent measurements of $T_x - T_y$. We repeat this for as many runs as we want in order to accumulate enough data to obtain an accurate $T_x - T_y$ measurement.

where we laser-heat the plasma for 30μs after 90μs of free expansion. Unfortunately, for this data set we observed a β of only $3 \times 10^4\,\mathrm{s}^{-1}$ (compare to the $5.2{\times}10^4\,\mathrm{s}^{-1}$ observed in Ch. 5) from a fit of $T(t)$ during the laser-heating stage, which limits the level of anisotropy that can be achieved. Nevertheless, we did observe some evidence of temperature anisotropy relaxation (Fig. 8.7). However, the data does not quite match MD results and, furthermore, $T_x - T_y$ does not seem to be converging to 0 K as it should. Clearly, more work needs to be done, but this is a promising proof-of-concept. Future work would focus on solving the convergence issue, figuring out the best way to extract a value of ν from this data, and taking data at different values of Γ and n.

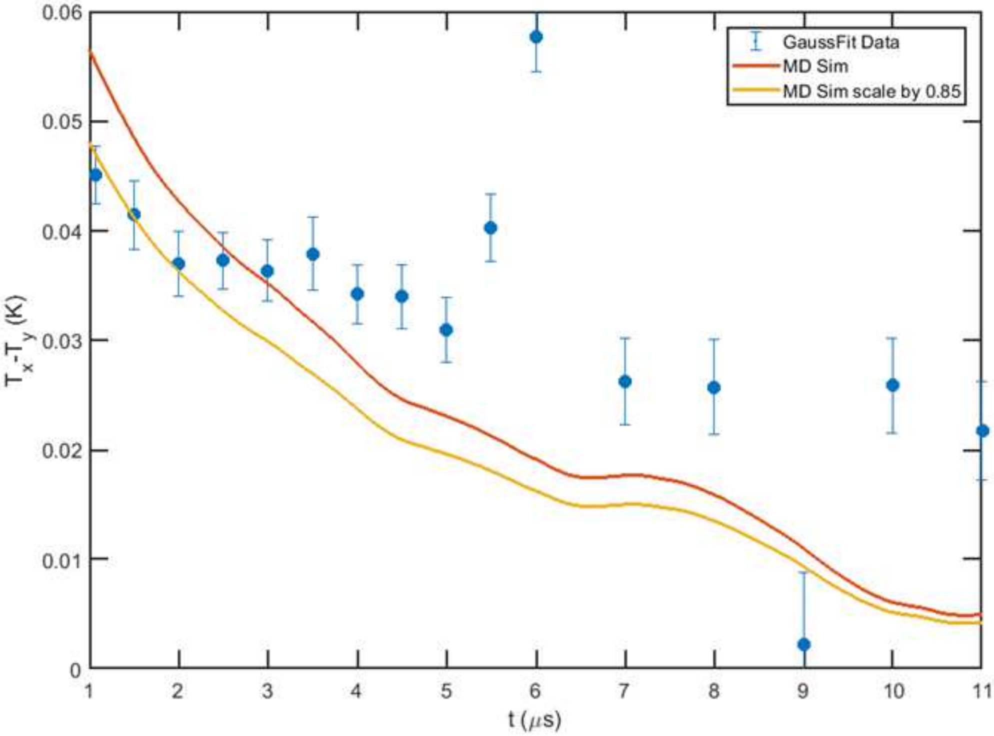

Figure 8.7 : Preliminary experimental measurement of temperature anisotropy relaxation (blue), where each data point and errorbar is obtained in the manner described in Fig. 8.6. For this data set, we allow the cloud to free expand for 90μs before heating for 30μs. We measure $n = 4 \times 10^{13}\,\mathrm{m}^{-3}$ and $\beta = 3 \times 10^{4}\,\mathrm{s}^{-1}$; we use these as inputs in the 'slow' MD code to obtain the MD results in red. In yellow, we plot the MD results rescaled to best match the data for early time t. We observe that, outside of a few outlier points, the anisotropy does appear to be decreasing in the experiment. However, it seems to either be converging towards 0 K anomalously slowly (with respect to the MD results), or converging to a non-zero value. More work needs to be done, but this is a promising proof-of-concept.

8.2 Self Diffusion

In his paper on Brownian motion, Einstein defined the diffusion coefficient D for a system of particles with density n surrounded by some uniform background fluid as [145]:

$$\frac{\partial n}{\partial t} = D\nabla^2 n. \tag{8.7}$$

We note here that D is typically called the 'self-diffusion coefficient' in the case where the 'background fluid' consists of particles of the same type as those whose diffusion is being considered (for example, if we are considering Sr^+ ions diffusing through a cloud consisting of other Sr^+ ions, as is the case in UNPs assuming that the effect of electron-ion collisions on ion diffusion is negligible due to the low mass of the electrons). For 1D diffusion, Einstein found that for an initial density given by a Dirac delta function at the origin, the solution to this equation is [145]:

$$n(x,t) = \frac{1}{4\pi Dt}\exp\left[-\frac{x^2}{4Dt}\right] \tag{8.8}$$

From this, we can see that for an arbitrary initial density distribution $n_0(x')$ the solution becomes

$$n(x,t) = \int_{-\infty}^{\infty} n_0(x')\exp\left[-\frac{(x-x')^2}{4Dt}\right] dx' \tag{8.9}$$

Thus, if we are able to instantaneously select some group of ions at some time $t = 0$, image their initial density distribution ($n_{tag,0}(x)$), and then follow the density distribution of that group as it evolves in time ($n_{tag}(x,t)$), we can use Eq. 8.9 to determine D from those measurements. This can be accomplished using the 408 nm laser. If the plasma is illuminated with 408 nm light, but no repumpers are on (no

1033 nm or 1092 nm), all ions will rapidly decay into the metastable D states. For a realistic scattering rate $R_s = 0.2\gamma_{SP}$, 99% of the ions will decay to D states within 2μs of illumination. Ions in these states will not be observed using LIF, as they must be in the S state to scatter 422 nm light.

Thus, by illuminating all of the plasma except for a small region defined by $|x| < w$ (we call this the 'tagged' region) for $t \sim 1-2\mu$s starting at time t_{pump} and subsequently imaging at time t_{probe}, we can observe the diffusion of the 'tagged' ions. I term this 'bright diffusion' (Fig. 8.8). Conversely, you can illuminate the cloud with a thin 408 nm beam and observe how the 'outer' ions fill in the pumped out hole in the center, which I term 'dark diffusion' (Fig. 8.8). In this case, all ions *outside* of $|x| < w$ are 'tagged' (e.g., the 'tagged' subset will always refer to the *visible* ions).

It's very important to note that this tagging **does not** actually affect the ion density profile; it simply results in some ions becoming 'dark' to the LIF laser in a spatially dependent manner. This is similar to how the tagging schemes described in Ch. 7 did not effect the overall plasma distribution function, but instead made atoms with certain velocities more likely to scatter LIF light from a circularly polarized probe beam [39, 40].

In Fig. 8.8B, we show the $n_{tag,0}(x)$ curves that would result from this tagging scheme, while in Fig. 8.8C we show the $n_{tag}(x, t = 10\mu\text{s})$ curves for both light and dark diffusion for a few different values of D^* (the normalized self-diffusion coefficient, defined in 7.4) calculated using Eq. 8.9 for $n_{total} = 10^{14}\,\text{m}^{-3}$ and $w = 20\mu$m. We choose values of D^* roughly within the range expected for $\Gamma \sim 3$ (Fig. 8.9). The n_{total} indicates the actual density of the plasma, including both the 'tagged' and untagged ions. We also note here that we are assuming that the plasma is effectively uniform, which is valid for $\sigma_0 \gg w$. This is true in this example since for typical

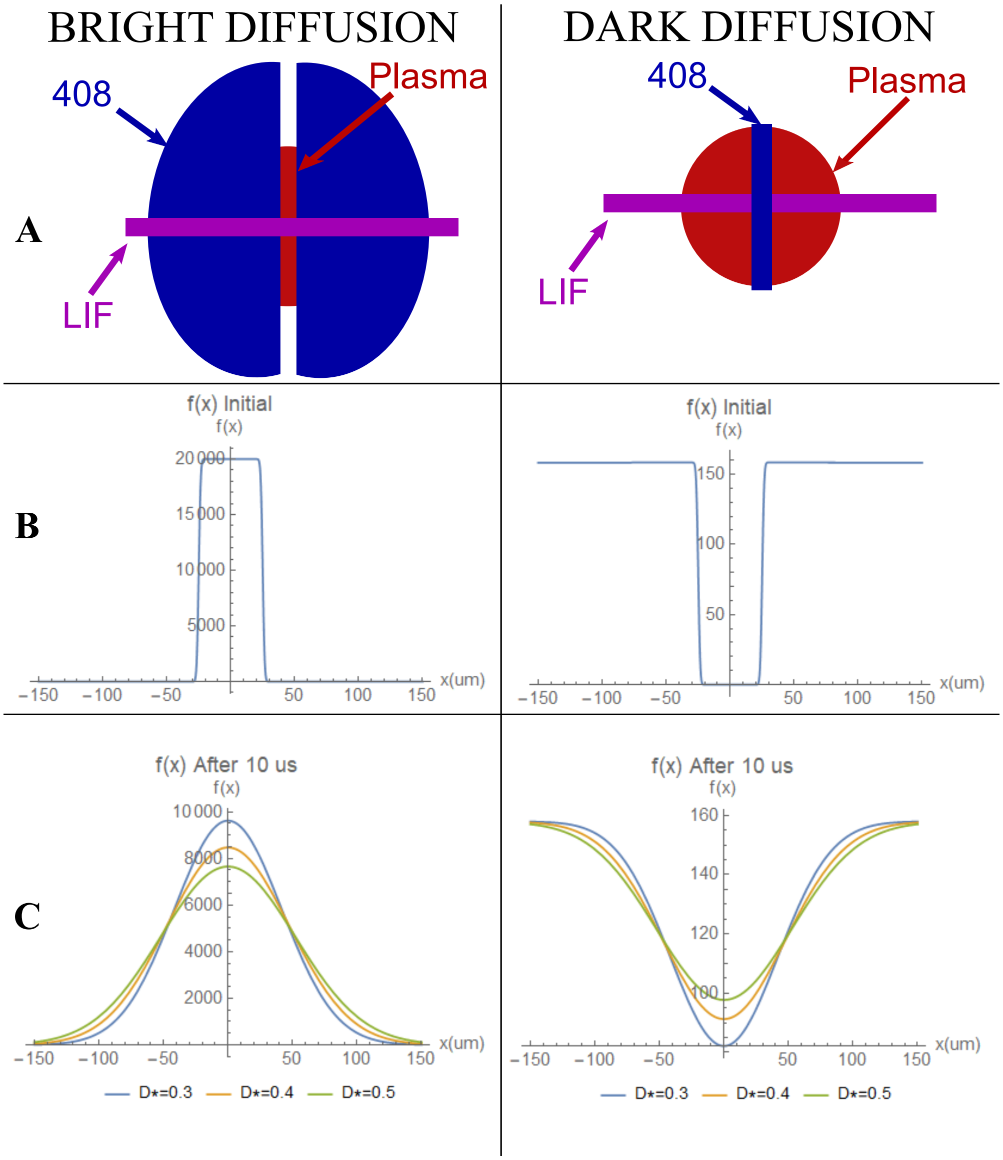

Figure 8.8 : (**A**): Mockup of schemes for bright and dark diffusion (all beams directed "into" page). In bright diffusion, all ions except those with $|x| \leq w$ are pumped into D states by a 408 nm beam with a dark sheet. In dark diffusion, a small uniform 408 nm beam is imaged onto the ions, 'untagging' the central region. (**B**): Initial distributions of 'tagged' ions after pumping ($w = 20\mu$m). (**C**): Distribution after 10 μs evolution time for different D^* for $n = 10^{14}$m^{-3} obtained by solving Eq. 8.9. Discrimination between different D^* is clearly achievable, indicating that this technique has the potential to measure D^* with reasonable accuracy.

UNP experiments $\sigma_0 \geq 1\,\mathrm{mm}$.

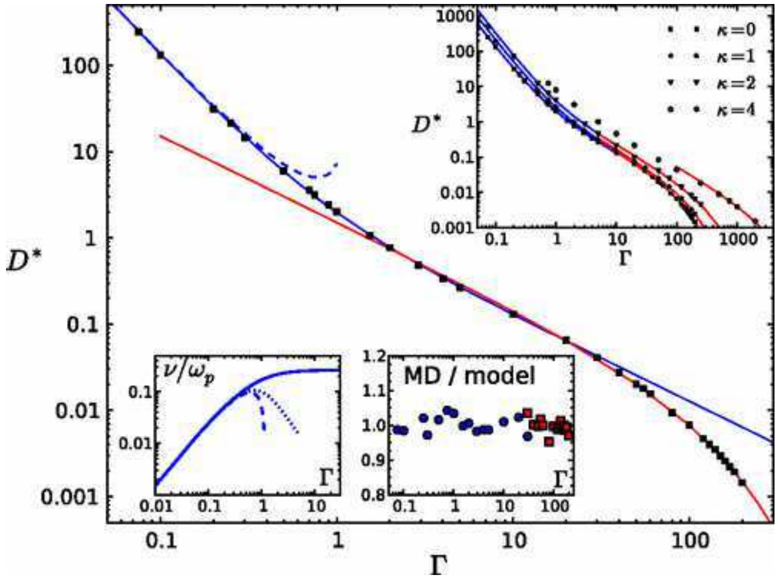

Figure 8.9 : MD results for $D^*(\Gamma)$ along with phenomenological fits [56] for $\kappa = 0$. Top Right Inset: $D^*(\Gamma)$ for various κ. Bottom Left Inset: MD results for measurement of velocity relaxation rate [40]. Bottom Center Inset: D^*_{MD}/D^*_{Fit} vs Γ; this demonstrates the (lack of) difference between the MD result and the phenomenological fit. Figure adapted from [56]

The width of $n_{tag}(x,t)$ clearly depends on D^* in a measurable way based on Fig. 8.8C. Thus, experimentally measuring the evolution of this width can give us a measurement of D^*. In Fig. 8.10 I plot $\sigma_{tag}(t)$, the gaussian width of $n_{tag}(x,t)$ for the case where $n_{tag,0} \propto \exp\left[-x^2/2\sigma^2_{tag,0}\right]$, $n_{total} = 10^{14}\,\mathrm{m}^{-3}$, and $\sigma_{tag,0} = 50\mu\mathrm{m}$ for a variety of different values of D^*. One could imagine placing some experimentally measured data for plasmas with **known** Γ on this plot (e.g., where we've measured Γ using LIF) and use it to determine $D^*(\Gamma)$. One could also imagine doing the same, but for $\sigma_{tag}(t)$ data in a plasma of **unknown** Γ (for example, if it is too cold to measure Γ after many 100's of μs of laser cooling has resulted in $T < T_{min} \sim 50\,\mathrm{mK}$, see Ch. 6), and using MD results [56] for $D^*(\Gamma)$ (I include some from Fig. 8.9 in the legend) to back out a measurement of Γ.

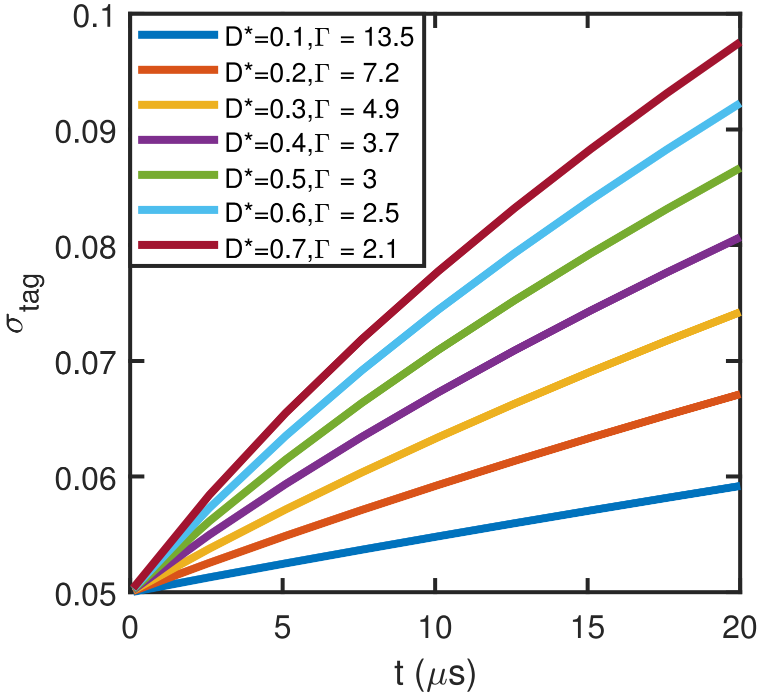

Figure 8.10 : σ_{tag} vs t for bright diffusion with an initial distribution of visible ions $n_{tag,0} = \exp\left[-x^2/(2\sigma_{tag,0}^2)\right]$ where $\sigma_{tag,0} = 50\mu$m. By measuring $\sigma_{tag}(t)$ after pumping and fitting the resulting curve to this model for D^*, we can measure D^* for a given Γ, giving $D^*(\Gamma)$. Conversely, we can fit D^* and then use MD results (e.g.[47]) to effectively 'measure' Γ; useful in cases where Γ is not easily measurable (i.e. when $T \leq T_{min} = 50\,$mK).

In order to do this measurement, the width of $n_{tag,0}$ must be small in order to observe appreciable evolution of $n_{tag}(x,t)$ relative to $n_{tag,0}$ in the desired timeframe of $t_{diff} \sim 10\mu$s (we need to observe evolution on a timescale $t_{diff} \ll \tau_{Exp}$, as this proposal assumes a non-expanding plasma). Thus, the width of either the bright or dark feature in the 408 nm beam must be small (e.g. $w \leq 50\mu$m). This is definitely physically doable; the Rayleigh length of a 408 nm laser with a 50μm waist is 2 cm, small enough for the feature to be resolved over the length of the plasma (20μm is a little dicier, as this gives a Rayleigh length of 3 mm). One could imagine having a narrow wire (AWG 44 has a nominal diameter of 50μm, for example) bisect the beam (similarly to the experiment in [26]); this can then be imaged onto the plasma using a set of relay optics for a 'bright diffusion' scheme.

The other important question is: can LIF imaging resolve these narrow features? In principle, the answer is yes; in previous experiments a 4x objective was successfully used to boost the camera resolution from 13μm (the pixel size of the CCD) to 3.3μm [119], which should be enough to measure $\sigma_{tag}(t) \geq 20\mu$m with sufficiently high resolution for a measurement of D^* according to Fig. 8.10.

To summarize: in principle, we can tag a small region of ions by making everything outside of this region dark to the LIF light. This is done by irradiating the plasma with a 408 nm laser containing a 'dark slit' of width $w \leq 50\mu$m in its center; anything outside of this region is rapidly pumped into a D state, which is dark to LIF ('bright diffusion', see Fig. 8.8A). Alternately, one can selectively 'untag' ions in the center by irradiating the plasma with a 408 nm beam with a narrow x-axis waist (w); this will result in ions with $|x| < w$ becoming 'dark' to the LIF light ('dark diffusion', see Fig. 8.8A). In either case, the subsequent evolution of the tagged particles can be used to directly obtain D^*. We can perform these measurements at different Γ by laser-cooling or laser-heating before the tagging stage, allowing for a measurement of $D^*(\Gamma)$ in the range $0.8 \leq \Gamma \leq 11$ that is, thus far, accessible by applying laser-forces (Sec. 5.2). Conversely, for plasmas where we can't measure Γ using LIF (e.g. for cases where $T < T_{min}$), we can use reliable MD results to back out Γ from the measurement of D^*.

8.3 Shear Viscosity

In Sec. 5.4, we demonstrated that optical forces are large enough to provide observable shifts in the expansion velocity of the plasma (Fig. 5.7C). This suggests that optical forces may be used to induce a variety of plasma fluid flow patterns. Inducing a shear flow can allow for measurements of the shear viscosity, which, for plasmas of $\Gamma > 1$, is relatively uncertain because few experimental measurements have been performed in this regime. One particular aspect of interest is the minimum in shear viscosity at $\Gamma \sim 20$ observed in MD simulations (Fig. 8.11) [57]. This is associated with the transition into the 'Yukawa liquid' regime, which is where most of the latest theoretical extensions of kinetic theory to strongly coupled systems begin to fail [47]. However, this aspect of shear viscosity has not yet been studied, despite its relevance in models of astrophysical systems in this regime of Γ [8]. Laser-cooled UNPs are very close to reaching this regime, and so it is worth thinking about how shear viscosity can be measured in such systems.

In Fig. 8.12A, we illustrate one such proposal in which counter-propagating beams with a 'hard edge' at $y = 0$ irradiate opposite sides of the plasma. Ions with $y < 0$ are thus irradiated by a beam propagating along the $-x$-axis while ions with $y > 0$ are irradiated by a beam propagating along the $+x$-axis. This force profile $F_x(y)/m$ is illustrated in Fig. 8.12B for the case where each beam creates a force of magnitude $F = \hbar k \gamma_{SP}/4$ (in other words, for $R_s = 0.25\gamma_{SP}$, the highest scattering rates we have observed). We also assume that the beam is sufficiently power-broadened (or otherwise broadened) in frequency such that all ions irradiated by the beam experience equal optical forces (e.g., $\gamma_{total} \gg kv$, where γ_{total} is the total laser linewidth with all broadening mechanisms accounted for and v represents the largest relevant ion-velocity).

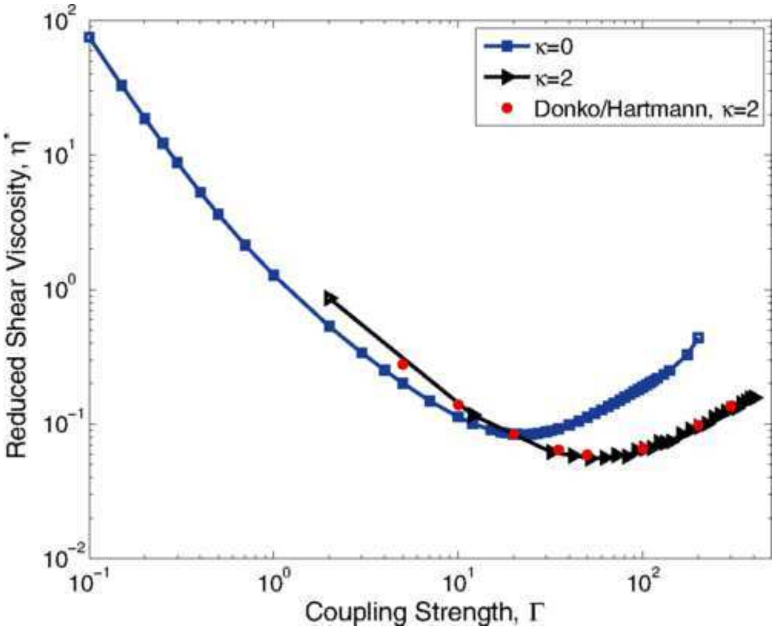

Figure 8.11 : Molecular Dynamics results for η_s^* [57]. We see that there is a viscosity minimum at $\Gamma \sim 20$ for $\kappa = 0$. Moreover, we see a large variation between the results for $\kappa = 0$ and $\kappa = 2$; since we will be typically working with $\kappa = 0.5$, it is important to keep this in mind, as measurements for this κ would likely fall in between these two curves.

The subsequent evolution of the shear flow $u_x(y, t = 0)$, where $u_x(y,t) = \int_{-\infty}^{\infty} f(v_x, y)\, dv_x$ is the mean velocity along the x-axis of all ions at y at time t, is determined by the viscous flow equation [43]:

$$\frac{\partial u_x}{\partial t} = \frac{\eta_s}{m_i n}\frac{\partial^2 u_x}{\partial y^2} + \frac{F_x(y)}{m} \tag{8.10}$$

where η_s is the shear viscosity and $\eta_s/m_i n$ is often referred to as the 'kinematic viscosity'. In Fig. 8.12C we plot solutions of Eq. 8.10 for the force profile in Fig. 8.12B for a variety of $\eta_s^* = \eta_s/mna^2\omega_{pi}$ (see Sec. 7.3.2) for $t = 20\mu$s and $n = 10^{14}\,\mathrm{m}^{-3}$. The observed shear flow depends on η_s^*, and thus if the shear flow is measured with high enough resolution, and F, n, and Γ are known to a sufficiently high degree of accuracy,

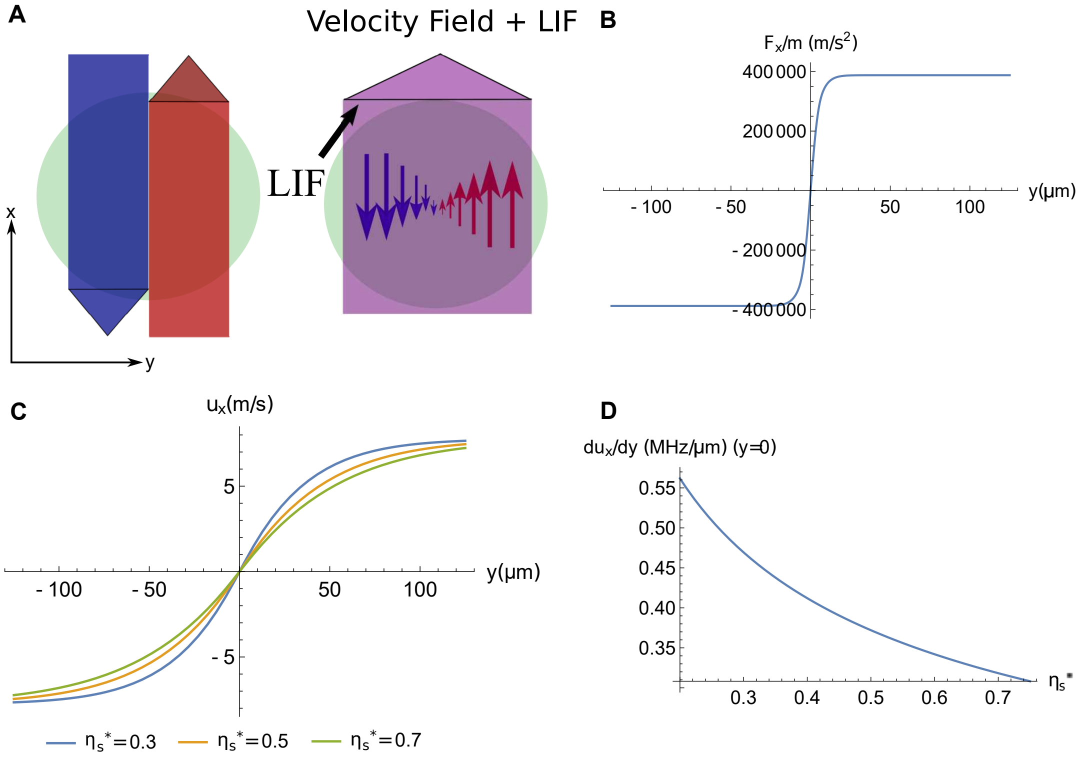

Figure 8.12 : (**A**): Illustration of experimental proposal discussed in text. LEFT: Two resonant 408 nm lasers pass through the plasma on opposite sides such that, for $y < 0$, the laser force is along $-x$, and for $y > 0$, the force is along $+x$. RIGHT: The optical forces creates a shear flow, illustrated with the blue and red arrows. The LIF propagates along the x axis, and therefore can be used to measure $u_x(y)$ through the induced spatially dependent doppler shift. (**B**): Illustration of $F_x(y)$ generated from this laser configuration. (**C**): $u_x(y, t = 20\mu\text{s})$ determined from solving Eq. 8.10 with initial conditions $u_x(y, 0) = 0$ for the force profile in **B**. (**D**): $\frac{du_x}{dy}\Big|_{y=0}$ vs η_s^* after the shear-flow has been applied for 20μs. We plot this quantity in 'Doppler units' of MHz/μm to illustrate the frequency and spatial resolution needed to extract a measurement of η_s^*

one can determine $\eta_s^*(\Gamma)$ from the shear flow measurement. An example of a figure of merit one could use is the slope $\frac{du_x}{dy}\Big|_{y=0}$ (Fig. 8.12D), where in this case we plot $\frac{du_x}{dy}\Big|_{y=0}$ in 'Doppler-Units' of MHz/μm to indicate the level of resolution we would need to achieve using LIF.

However, similarly to the temperature anisotropy measurement techniques proposed in Sec. 8.1, we would prefer to measure η_s^* in a way that does not require perfect knowledge of the force profile $F_x(y)$. This can be done by first establishing a shear flow $u_x(y, t = 0)$ using optical forces and then turning off the forces and measuring the subsequent $u_x(y, t)$. If the initial shear flow is 'steep' enough, the dissipation of the shear flow is experimentally observable. We do *not* need to know the exact force profile $F_x(y)$ that produced $u_x(y, t = 0)$; all that is needed is the ability to measure $u_x(y, t = 0)$ and $u_x(y, t)$ with sufficient resolution. The evolution of $u_x(y, t)$ depends on η_s^* through Eq. 8.10, and thus measuring $u_x(y, t)$ can provide a measurement of η_s^*.

We examine this approach in Fig. 8.13 for two cases, one with a 'steep' initial shear flow (plots on the left hand side) and one with a 'shallow' initial shear flow (plots on the right hand side) for $n = 10^{14}\,\mathrm{m}^{-3}$. In both cases, the initial flow is of the form

$$u_x(y, t = 0) = \frac{\Delta u}{1 + \exp\left[-y/k\right]} - \frac{\Delta u}{2} \tag{8.11}$$

For the 'steep' flow case, $k = 10\mu$m and for the 'shallow' flow case $k = 50\mu$m. In both cases we choose $\Delta u = 10\,\mathrm{m/s}$, comparable to the shear flow velocities we believe can be achieved with optical forces (see Fig. 8.12C). These initial conditions are shown in Fig. 8.13A. In Fig. 8.13B, we show $u_x(y, t = 10\mu\mathrm{s})$ for various η_s^*, which are obtained by solving Eq. 8.10 for $F_x(y) = 0$ with initial condition $u_x(y, t = 0)$. We can clearly see that the initially 'steep' flow results in a much stronger variation in the subsequent flow with η_s^*, and thus greater signal with which to fit for η_s^*. Finally, in Fig. 8.13C, we plot $\left.\frac{du}{dy}\right|_{y=0}(t)$ for various η_s^* for each case. We see that, in both cases, the decay rate of the shear flow is proportional to η_s^*, with larger η_s^* leading to faster decay. Thus, by measuring the decay rate for a known initial shear flow, η_s^*

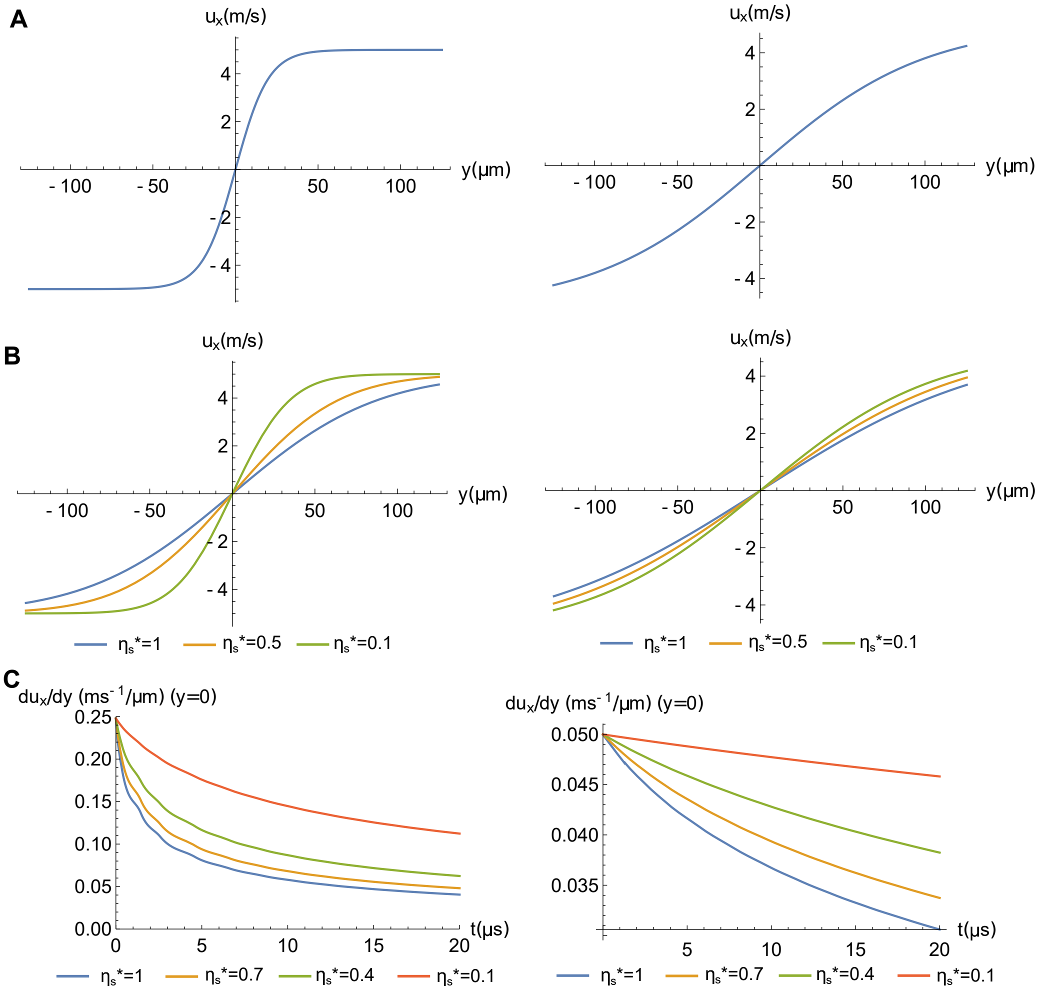

Figure 8.13 : (**A**):LEFT: Initial conditions $u_x(y, t = 0)$ for 'steep' shear flow ($k = 10\mu$m and $\Delta u = 10\,$m/s in Eq. 8.11). RIGHT: Initial conditions for 'shallow' shear flow ($k = 50\mu$m and $\Delta u = 10\,$m/s). (**B**): LEFT: $u_x(y, t = 10\mu\text{s})$ for various η_s^* for the case of 'steep' initial conditions. RIGHT: Same as LEFT, but for 'shallow' initial conditions. We can see here that the differences between the flow patterns for different η_s^* are much harder to resolve. (**C**): LEFT: $\left.\frac{du_x}{dy}\right|_{y=0}$ vs t for various η_s^* for the 'steep' initial conditions. We see that the rate at which the flow dissipates is proportional to η_s^*, with high η_s^* resulting in faster dissipation. By measuring the dissipation decay with high enough resolution, one could measure η_s^* by fitting a decay curve. RIGHT: Same as LEFT but for 'shallow' initial flow gradient. We see similar results, but the resolution that would be required to distinguish between the curves of different η_s^* is much higher than in the 'steep' case.

can be determined.

Next, let's consider the resolution required in order to measure η_s^* in this way. From Fig. 8.13b, we see that one would need a spatial resolution of $\sim 10\mu$m or less. This is difficult, but in principle achievable by increasing the resolution of the ICCD camera to 3.3μm with a 4x objective, as described in Sec. 8.2. The required velocity resolution depends on the steepness of the shear flow. In the 'steep' case, we can see from Fig. 8.13(b-c) that a resolution of $\sim 1\,$m/s (this corresponds to a spectral resolution of 2 MHz) per 10μm is required to distinguish between shear flow decay curves. In the 'shallow' case, a resolution of $\sim 0.1\,$m/s (200 kHz) is required. A resolution of $\sim 1\,$MHz has been demonstrated in previous measurements of the VAF performed using our apparatus [40]. In principle, resolution of $\sim 100\,$kHz may be achievable, however, this has not been demonstrated in our current apparatus. The main limiting factor is the width of the LIF transition (20.213 MHz). This emphasizes the importance of creating as steep of an initial shear flow as possible in order to measure η_s^* accurately.

This measurement can be conducted at any point during the plasma evolution, with the caveat that one will want the shear flow relaxation timescale to be $\ll \tau_{Exp}$. It could also be performed after laser-cooling or heating the plasma, allowing for a measurement of η_s^* as a function of Γ, which we can compare to MD results (Fig. 8.11) or theoretical predictions (Fig. 7.9).

To summarize: If counter-propagating beams irradiate opposite sides of the plasma such that ions with $y < 0$ experience a force towards $-x$, and ions with $y > 0$ experience a force towards $+x$, a shear flow should result. If the force gradient around $y = 0$ is sufficiently sharp, this will hopefully result in a 'sharp' shear flow such as the example on the left hand side of Fig. 8.13, from which measurements of

η_s^* can be made by considering the subsequent dissipation of the flow after the laser forces are extinguished. Even if the flow is somewhat more 'shallow' (right hand side of Fig. 8.13), η_s^* may still be measurable with sufficient resolution.

Although the measurement would be challenging for these reasons, it is still worth attempting since there is a dearth of measurements of shear viscosity in strongly coupled plasmas, and thus any attempt to measure this quantity should extend our knowledge of shear flow dissipation in these systems.

8.4 Thermal Conductivity

We introduced the concept of thermal conductivity in Sec. 5.1 in order to explain the stability of the spatial gradients observed in the temperature of a laser-cooled plasma; the thermal conductivity of a UNP (K) is simply too low to result in thermal equilibration over a length of $\sim 1\,\mathrm{mm}$ in a time frame of $\sim 100\mu\mathrm{s}$. However, if we are able to generate thermal gradients over a smaller length, we could conceivably measure K in a similar manner to how we proposed to measure η_s in the previous section.

Similar to D and η_s, the thermal conductivity in strongly coupled plasmas is typically expressed in 'natural' plasma units: $K^* = K/nk_B\omega_{pi}a^2$. If we substitute this expression into the 1D heat equation (Eq. 5.1), and add a spatially dependent cooling/heating term $-\beta(y)T$, we find:

$$\frac{\partial T(y,t)}{\partial t} = \frac{2K^*\omega_{pi}a^2}{5}\frac{\partial^2 T(y,t)}{\partial y^2} - \beta(y)T(y,t) \tag{8.12}$$

MD results for $K^*(\Gamma)$ are shown in Fig. 8.14.

We will want to use a $\beta(y)$ profile that results in a relatively steep thermal gradient. This can be done by applying a cooling force ($\beta > 0$) for $y < 0$ and a heating force

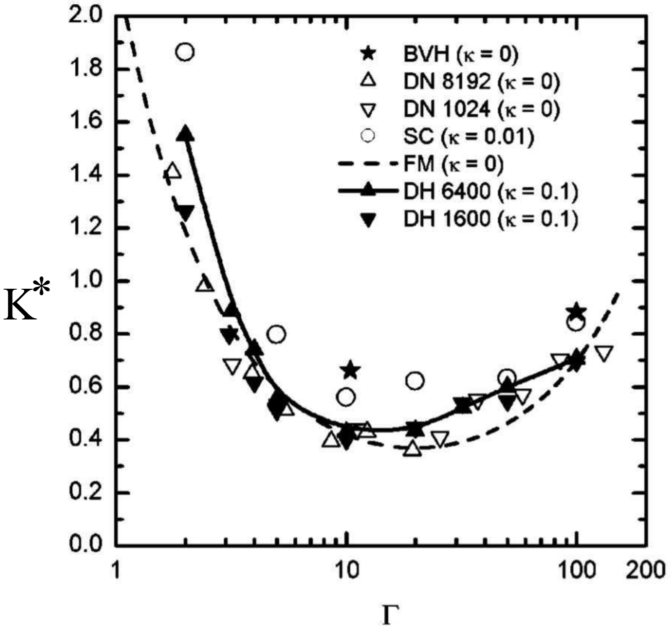

Figure 8.14 : MD results for K^*. We see that there is a relatively high level of uncertainty even in the MD results; experimental measurements of K^* would thus be quite valuable. Figure adapted from [58].

($\beta < 0$) for $y > 0$, as in Fig. 8.15A. We assume that the maximum $|\beta|$ we can apply to either side of the cloud is $\beta_{max} = 1.7 \times 10^4\,\mathrm{s}^{-1}$, which is one third of the maximum value stated in Ch. 5, with the factor of 1/3 resulting from the rapid temperature anisotropy relaxation (we assume that the forces will be applied for $t \gg \nu^{-1}$, where ν is the anisotropy relaxation rate discussed in Sec. 8.1). In Fig. 8.15B-D, we illustrate the resulting $\beta(y)$, solutions to Eq. 8.12 for K^* relevant to $\Gamma = 1 - 10$ (see Fig. 8.14 [58]) for $t = 20\mu$s where initially $T = 0.5\,\mathrm{K}$ throughout the plasma and $n = 10^{14}\,\mathrm{m}^{-3}$, and dT/dy vs K^* for $t = 20\mu$s, respectively. These figures are analogous to those presented in Fig. 8.12 for the shear viscosity measurement proposal.

Similarly to the viscosity measurement proposal, we would prefer to measure thermal conductivity without needing exact knowledge of the laser-forces. If a thermal

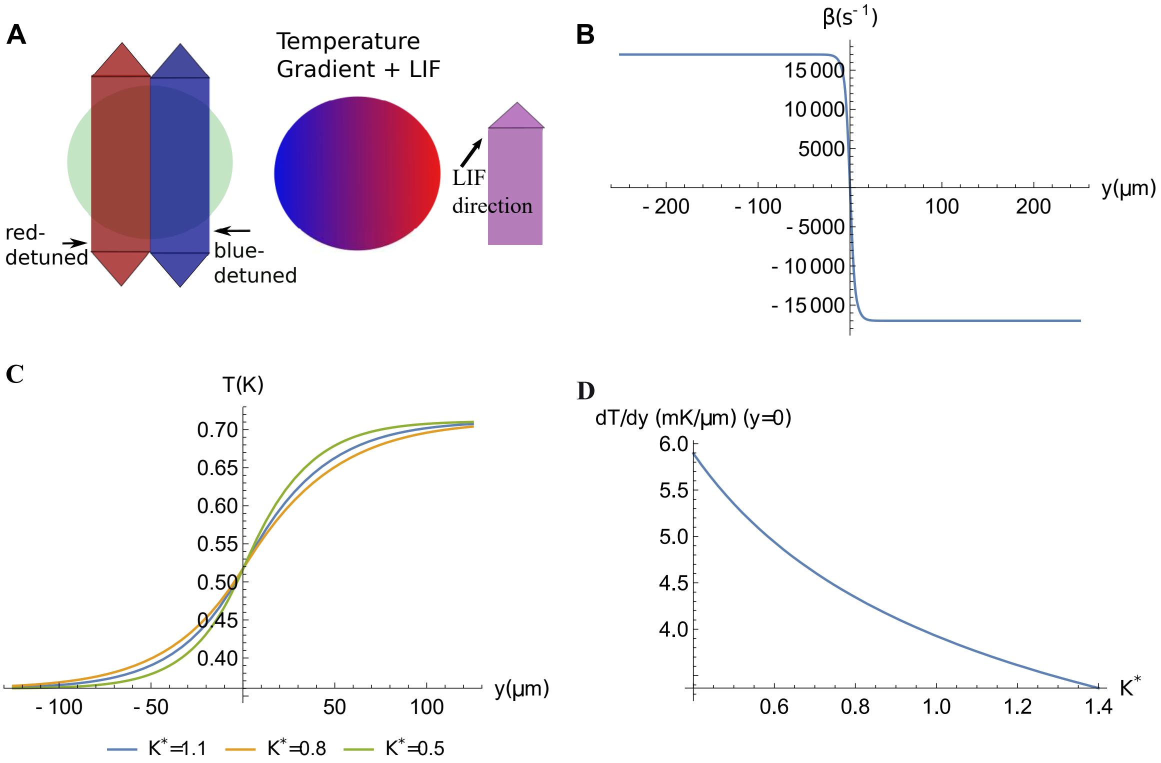

Figure 8.15 : (**A**): Illustration of experimental proposal discussed in text. LEFT: Two sets of detuned counter-propagating 408 nm lasers pass through the plasma on opposite sides. The lasers propagating along x for $y < 0$ are red detuned and thus cool the plasma, while the ones propagating along x for $y > 0$ are blue detuned and thus heat the plasma. RIGHT: The optical forces creates a thermal gradient (blue is cold, red is hot). The spatially resolved LIF imaging technique can be used to measure this spatial variation in T. (**B**): Illustration of $\beta(y)$ generated from this laser configuration. (**C**): $T(y, t = 20\mu\text{s})$ determined from solving Eq. 8.12 with initial conditions $T(y, 0) = 0.5$ for the $\beta(y)$ profile in **B**. (**D**): $\left.\frac{dT}{dy}\right|_{y=0}$ vs η_s^* after the lasers have been on for 20μs. This provides an idea of the level of spatio-thermal resolution one needs to accurately determine K^* using this technique.

gradient is somehow established through the application of optical forces, the dissipation of the gradient can be related to the thermal conductivity of the system, again in exact analogy to the shear viscosity proposal. This analogy carries over to Fig. 8.16, in which we show the dissipation of ‘steep’ and ‘shallow’ thermal gradients for various K^*; the plots shown in Fig. 8.16A-C are exactly analogous to those in Fig. 8.13A-C.

The initial thermal gradient profiles are of the form:

$$T(y, t = 0) = \frac{\Delta T}{1 + \exp\left[-y/k\right]} - \frac{\Delta T}{2} \tag{8.13}$$

for $k = 10\mu$m (left hand side of Fig. 8.16) and $k = 50\mu$m (right hand side of Fig. 8.16), and a value of ΔT of 0.4 K, comparable to what we observe in Fig. 8.15 for reasonable heating and cooling parameters. This equation is exactly the same as Eq. 8.11, with ΔT replacing Δu.

We see that the variation of the thermal gradient dissipation with K^* is again much easier to resolve in the 'steep' gradient case, similarly to how the variation of shear flow dissipation with η_s^* was more easily resolved for the 'steep' shear flow case. With good enough resolution, in principle K^* can be determined in either case by examining the decay rate in $\left.\frac{dT}{dy}\right|_{y=0}$, with higher K^* implying a faster decay (Fig. 8.16C).

In practice, this measurement will be quite difficult, as it will require the ability to resolve temperature variations on the scale of ~ 10 mK over a length scale of 10's of μm. However, even measurements of K^* with relatively high uncertainty made in the strongly coupled plasma regime are desirable, as the value of this parameter is not well known for $\Gamma > 1$. Even the MD data displayed in Fig. 8.14 have relatively high uncertainty. Any experimental input would be valuable.

To summarize: If one half of the plasma is cooled with red-detuned counter-propagating lasers, and the other half is heated with blue-detuned counter-propagating lasers, a thermal gradient should be established (Fig. 8.15). If that thermal gradient is sufficiently steep, it may be possible to measure K^* by turning off the lasers after the gradient is established and subsequently measuring the rate at which the gradient dissipates. This rate increases with K^* (Fig. 8.16C), and thus

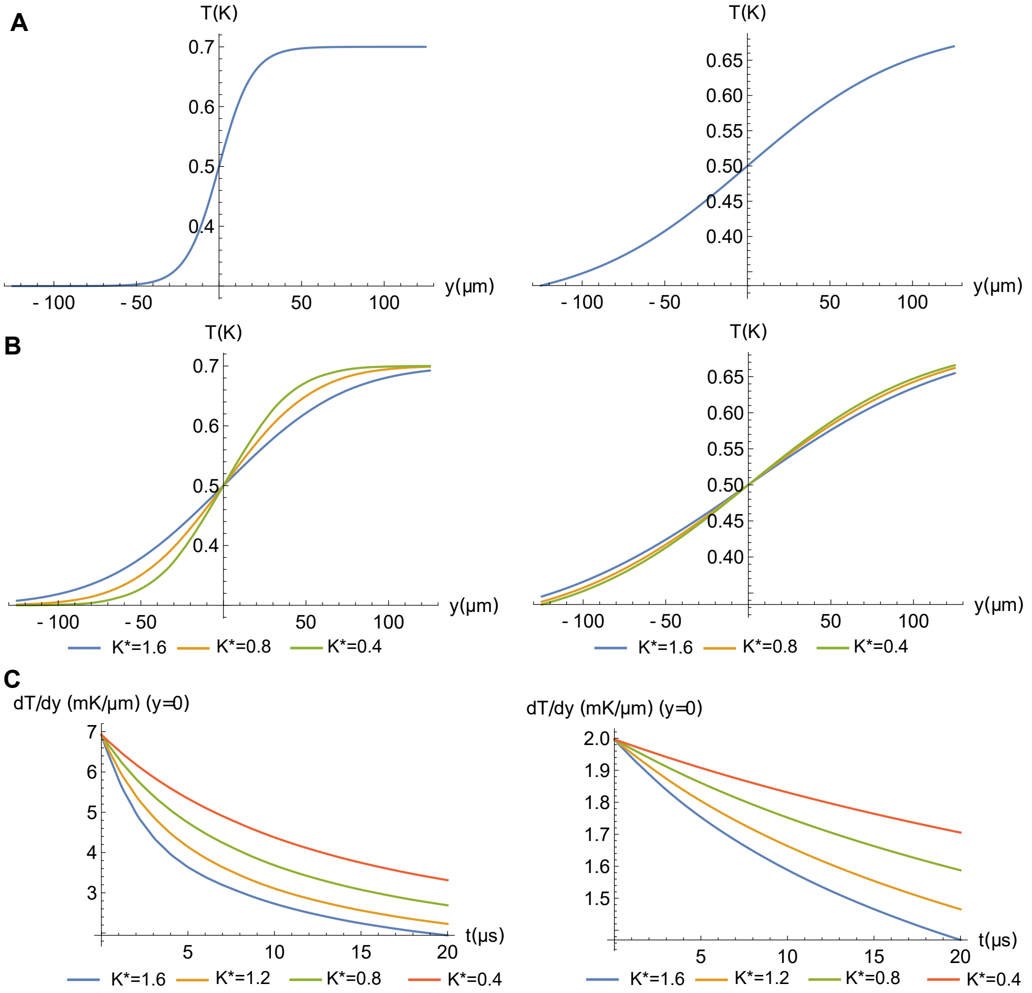

Figure 8.16 : (**A**):LEFT: Initial conditions $T(y, t = 0)$ for 'steep' thermal gradient ($k = 10\mu$m and $\Delta T = 0.4\,$K in Eq. 8.13). RIGHT: Initial conditions for 'shallow' thermal gradient ($k = 50\mu$m and $\Delta T = 0.4\,$K). (**B**): LEFT: $T(y, t = 10\mu$s) for various K^* for the case of 'steep' initial conditions. RIGHT: Same as LEFT, but for 'shallow' initial conditions. We can see here that the differences between thermal gradients for different K^* are much harder to resolve. (**C**): LEFT: $\left.\frac{dT}{dy}\right|_{y=0}$ vs t for various K^* for the 'steep' initial conditions. We see that the rate at which the thermal gradient dissipates is proportional to K^*, with high K^* resulting in faster dissipation. By measuring the dissipation decay with high enough resolution, one could measure K^* by fitting a decay curve. RIGHT: Same as LEFT but for 'shallow' initial thermal gradient. We see similar results, but the resolution that would be required to distinguish between the curves of different K^* is much higher than in the 'steep' case.

measuring the rate with a reasonable degree of accuracy should allow one to obtain a measurement of K^*.

8.5 Summary

Throughout this thesis, we have seen that optical forces can exert a significant effect on UNP behavior. These forces are strong enough to cool or to heat the plasma (Sec. 5.1) and they can also have observable impacts on the expansion dynamics (Sec. 5.4).

In this chapter, we introduced a number of proposals for measuring transport coefficients through use of these strong optical forces. Almost all of the techniques in this chapter (excluding the proposal for measuring self-diffusion) use optical forces to generate states which, in absence of the force application, would be out of equilibrium states, and thus subsequently relax towards equilibrium after the forces are extinguished. These out of equilibrium states include:

- A state in which there is a temperature anisotropy, which isotropizes after the forces are removed. The rate at which the plasma isotropizes is the 'temperature anisotropy relaxation rate' ν (Sec. 8.1)

- A state that exhibits shear flow, with a 'transition range' of $\sim 100\mu$m, which dissipates after the forces are removed. The rate at which the shear flow dissipates is proportional to the shear viscosity η_s^* (Sec. 8.3)

- A state that contains a thermal gradient, with a 'transition range' of $\sim 100\mu$m, which dissipates after forces are removed. The rate at which the thermal gradient dissipates is proportional to the thermal conductivity K^* (Sec. 8.4)

Of these, we only have preliminary experimental data from an implementation of the proposal to measure ν (Fig. 8.7); we include the other proposals in this thesis to help motivate future studies.

We have also proposed a technique that uses 'spatial' optical tagging (in contrast to the 'velocity' tagging discussed in Ch. 7) as a tool to measure the self-diffusion coefficient D^* (Sec. 8.2). We demonstrate that, for small, but realistically achievable, tagging regions ($\sim 50\mu$m), the diffusion rate could be measured by observing the rate at which the tagged ions diffuse through the plasma (Fig. 8.10).

All of these proposals represent ways in which the transport quantity is being measured directly, as opposed to through a statistical relation such as a Green-Kubo formula. These approaches can be thought of as complimentary, as any tool to measure transport in strongly coupled plasmas will aid in our understanding of these complex systems.

Chapter 9

Conclusion

In this thesis, we presented the first ever demonstration of laser-cooling in a neutral plasma system. Thus, neutral plasmas join the ever growing list of systems in which laser-cooling has been implemented; this list includes neutral atoms [79, 78], trapped ions [77, 146], diatomic [80] and triatomic [81] molecules, solids [82], and mesoscopic systems [84]. The application of laser-cooling in these systems has led to a number of ground breaking advances in physics, such as the achievement of quantum degeneracy [85, 86, 87, 70], implementation of quantum computation schemes [89], and Wigner crystallization in trapped non-neutral plasmas [49], just to name a few. We hope that the laser-cooling of neutral plasmas will lead to similarly important advances.

Laser-cooling has been a goal within the ultracold neutral plasma community for quite some time, with the first theoretical papers modeling laser cooling of a UNP [72, 73, 61] being written within 5 years of the first experimental realization of a UNP in 1999 [3]. However, it had not been successfully implemented before the demonstration presented in this thesis. This is because of the many challenges associated with laser-cooling a neutral plasma, such as the high level of inter-particle collisionality and the rapid electron-driven hydrodynamic expansion. Despite these challenges, we were able to demonstrate laser-cooling in a UNP, through which a coupling of $\Gamma = 11(1)$ was achieved, the highest ever observed in a UNP system.

The most immediate impact of this result will be to allow researchers to apply pre-existing techniques for measuring transport quantities, such as the self-diffusion coefficient D^* [39], to more strongly coupled plasmas. Obtaining accurate measurements of transport quantities in this regime will help benchmark theories for describing dynamics of strongly coupled plasmas. Due to the lack of experimental measurements of these quantities, the main method for testing these theories is molecular dynamics (MD) simulation. Both the simulation and theory are currently unchecked by experiment. Laser-cooled UNPs can rectify this. Improved knowledge of these quantities may also improve simulations of plasmas relevant to inertial confinement fusion, which are in the strongly coupled regime for a portion of their evolution. Transport quantities such as thermal conductivity K^* are important for understanding the evolution of these laser-produced plasmas, and are thus typically obtained from state-of-the-art MD simulations [100], results of which are used as inputs into the simulation codes. Bolstering these MD data with experimental measurements can help expand our knowledge of these potentially world-changing fusion experiments.

Further down the line, we can imagine using these laser scattering forces in a number of different ways. For example, in this thesis we observed that the laser-cooling force also results in an observable retardation of the plasma expansion. It is possible that, by adding a magnetic quadrupole field, one could completely confine the plasma in a 'Plasma MOT' in a similar way to how atomic MOTs are used to confine atoms. Confining the neutral plasma would open the door to a number of interesting experiments. In particular, it would allow for cooling to be applied over an indefinitely long time, in principle allowing for laser-cooled UNPs to reach the Wigner Crystallization threshold of $\Gamma \geq 172$ [49, 61].

Laser forces could potentially be used to temporarily force the plasma into a state which, in absence of the applied forces, would be an out-of-equilibrium state. For example, laser-forces of sufficient strength may induce a shear flow in the plasma, which, upon extinguishing the laser-forces, will dissipate on a timescale determined by the coefficient of shear viscosity. Thus, using lasers to ‘poke’ and ‘prod’ the plasma may allow for direct measurement of transport coefficients.

We have also demonstrated a powerful tool for the simulation of plasmas irradiated by laser fields that couple the internal states of the ion; the ‘MDQT’ code, which augments a MD simulation of plasma evolution with a quantum trajectories approach to both the evolution of the ion’s quantum state and the resulting optical force. We have demonstrated the ability of this tool to simulate laser-cooling in a UNP, with results that largely match the results of our experimental implementation of laser-cooling. This code is a potential first step towards the development of a multiscale code for the evolution of an expanding plasma irradiated by coupling lasers, with the MDQT code operating on the lowest scale and a hydrodynamic or kinetic code governing the macroscopic plasma evolution. We hope that the results presented in this thesis motivate the pursuit of such an approach, as there are some results we observe, such as the bifurcation of laser-heated plasmas, which would only be able to be modeled by a multiscale simulation.

The results presented in this thesis are the first steps of a journey towards greater understanding of strongly coupled plasma systems through laser-cooling. The next few steps are clear, but we can only guess where the road will lead from there. We have hinted at some possible directions in this conclusion, however, we hope that there will also be completely unforeseen advances resulting from this new development.

Appendices

Appendix A

Simulation of Equilibrated Plasmas Using a Combined Monte Carlo and Molecular Dynamics Approach

In this thesis we have made frequent references to molecular dynamics simulations. These simulations fall into two categories:

- Method 1: Simulation of plasmas with randomly distributed ion positions and all ion velocities set to 0. This effectively simulates the initial conditions of a UNP immediately after photoioinization. This was used to simulate DIH (Sec. 2.2.2, see Fig. 2.5 and [36]). The laser-cooling simulations presented throughout Chapter 4 were also performed in an MD simulation with these initial conditions. This is why we see DIH oscillations in Fig. 4.14, for example.
- Method 2: Simulations of plasmas initialized in an equilibrium state defined by Γ and κ (e.g., with the right level of spatial correlations $g(r, \Gamma, \kappa)$ (see Sec. 2.2.3) and with velocities obtained from a gaussian distribution with width determined by $\sqrt{\Gamma^{-1}}$ (Γ^{-1} is the equivalent of T in scaled plasma units, see Sec. 4.3)). The simulation results presented throughout Chapter 7, along with those in Sec. 8.1.2, used this technique.

Importantly, the quantum trajectories approach can be implemented in both methods.

DIH ensures that simulations using the first method will always equilibrate to $\Gamma \sim 3$ (Fig. 2.6). If we want to use simulations of this form to measure equilibrium transport quantities, such as the self-diffusion coefficient D^* or the velocity auto-correlation function $Z_1(t)$, at arbitrary Γ, we would need to adjust Γ after equilibration. In principle, this is what is done during the QT laser-cooling stage, however, this can take quite a long simulation time. It is *much* faster to use established simulation techniques to first generate a plasma in an equilibrium state and then measure its transport quantities.

This motivated us to develop a tool to perform the second 'type' of plasma MD simulation. This tool will be quite helpful for future studies of transport in laser-cooled plasmas. For example, in the future we will want to be able to compare measurements of $Z_1(t)$ made in laser-cooled (or heated) plasmas of Γ ranging from 0.8 to 10 using the technique discussed in Sec. 7.1 to MD results, and thus the ability to use equilibrium MD simulations to quickly generate $Z_1(t)$ for arbitrary Γ will be quite helpful. This type of simulation was also useful for testing the pump-probe tagging scheme discussed in Chapter 7, as out-of-equilibrium effects present in the first 'type' of simulation may result in defects in measurements of Z_n that persist even at $\sim 30\omega_{pi}t$ after the start of the simulation, hampering comparison between the M_n and Z_n measurements (See Fig. A.1).

The rest of this appendix is dedicated to describing how we implement the second approach using a combined molecular dynamics and monte carlo [143] simulation.

The first step is to 'arrange' the particles in a way such that they reproduce the equilibrium level of spatial correlations, typically parameterized by the pair-correlation function $g(r)$, which generally depends on Γ and κ. This can be done using a 'Monte Carlo' technique known as the 'Metropolis method' (we note that, in this method we use periodic boundary conditions for situations where particles move outside of the simulation region, and the minimum image convention to calculate the

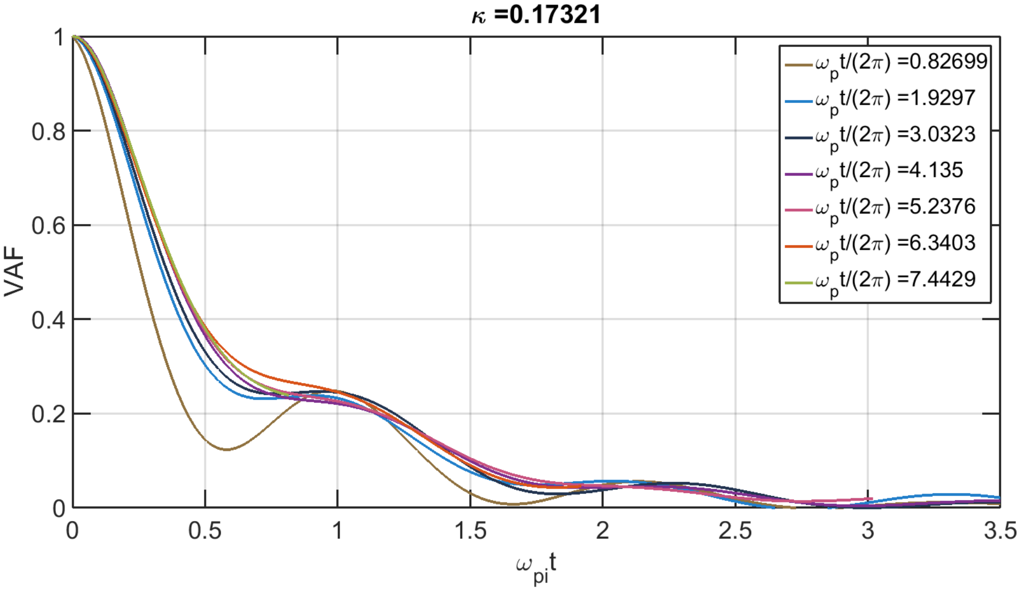

Figure A.1 : $Z_1(t)$ (aka the VAF) recorded starting at different times after the start of an MD simulation initialized with motionless ions in random positions (aka 'method 1' in the text). We clearly see that the curve depends on what time we start recording $Z_1(t)$. This would *not* be the case in an equilibrated system, for which we would instead expect $Z_1(t)$ to always be the same no matter what time we begin 'recording' it. This makes using 'method 1' problematic for tests of optical tagging schemes described in Ch. 7, as one needs to wait a long time ($\omega_{pi}/2\pi \sim 5$) for the VAF to converge. This is why we used 'method 2' for the MD data in Ch. 7.

total potential energy U. We will also be working in 'natural' plasma units (length normalized by a, time by ω_{pi}^{-1}, etc.). These techniques are described in Sec. 4.3) [143]. In the Metropolis method, the following steps are performed:

- The initial positions of the particles are assigned. It doesn't really matter how this is done; common choices are to either initialize with random positions or in a lattice configuration.

- Calculate the total potential energy of the system, U_{init}, in this configuration (for a Yukawa OCP we have $U = \sum_{ij} U_{ij} = \frac{1}{2}\sum_{i,j}\frac{1}{r_{ij}}\exp\left[-\kappa r_{ij}\right]$.).

- Pick one particle, i, at random
- Change its position from $\vec{r_i}$ to $\vec{r_i'} = \vec{r_i} + \Delta\vec{r}$, where $\Delta\vec{r}$ is randomly chosen from within a sphere of radius δr (δr is chosen by the user; we typically pick $\delta r = 0.3a$).
- Calculate U_{new}, the potential energy of the system after making this change in particle i's position.
- Roll a 'dice' picking a random number c between 0 and 1.
- If $c <$min$\{1$,exp$[-(U_{new} - U_{old})/(\Gamma^{-1})]\}$, 'accept' the move (note: k_BT is replaced by Γ^{-1} because we are working in plasma units). If the move is not accepted, move the particle back to $\vec{r_i}$
- Go back to step 3 and repeat for some user defined number of steps

Basically, if the move lowers the energy, it is automatically accepted. If it doesn't, then the move is accepted conditionally with a temperature-dependent probability. To see how this can possibly work, consider the two extreme cases of $T = \infty$ and $T = 0$. If $T = \infty$ (e.g. $\Gamma = 0$), every move is accepted. This will result in, after enough steps, a completely random distribution of particles, as expected for $T = \infty$. If $T = 0$ ($\Gamma = \infty$), only moves that lower the potential energy are accepted, and eventually the system will find its lowest energy state.

Importantly, this method satisfies what's known as 'detailed balance', which is satisfied when a move is as likely as its reverse. For example, consider moving from state n to state m. Detailed balance implies that:

$$Acc(n \to m)Choose(n \to m)P(n) = Acc(m \to n)Choose(m \to n)P(m) \tag{A.1}$$

where Acc is the probability of accepting the move, $P(n)$ is the likelihood of the system being in state n and $Choose$ is the likelihood of choosing a given move. The likelihood of choosing any move is completely random, and so the $Choose$ on each side cancels out. $P(n)$ is determined by the boltzmann distribution in whatever ensemble you've chosen, for the basic microcanonical ensemble this probability is just $\frac{1}{Z}\exp\left[-U_n/(\Gamma^{-1})\right]$.

Let's consider what happens for a move from $n \rightarrow m$ where $U_m > U_n$. $Acc(n \rightarrow m)$ is $\exp\left[-(U_m - U_n)/(\Gamma^{-1})\right]$ while $Acc(m \rightarrow n)$ is 1 (see step 7 of Metropolis algorithm). $P(m)/P(n)$ is also $\exp\left[-(U_m - U_n)/(\Gamma^{-1})\right]$. Thus, Eq. A.1 is satisfied. This is clearly true for a move where $U_n > U_m$ as well.

We typically run simulations with $\sim 3000 - 5000$ particles; for these system sizes, we typically find that 10^5 steps are sufficient for convergence of $g(r)$ (Fig. A.2). This can be accomplished quite quickly (within a few minutes) even on a laptop computer.

After the initial, 'equilibrated', positions are determined in this way, we choose ion velocities from a thermal distribution of width $v_T/(a\omega_{pi}) = 1/\sqrt{3\Gamma}$.

In principle, these steps are sufficient to result in a completely equilibrated plasma. However, just to be safe we also add an 'equilibrative' MD stage after the Metropolis method is completed. In this stage we propagate MD with a timestep of $t_{step} = 0.003\omega_{pi}t$. However, during the time step we give each ion a probability $\nu_{coll}t_{step}$ to have a 'collision' with a 'bath' particle. If this happens, the velocity of the ion is 'redrawn' from the thermal distribution. This is known as an 'Anderson thermostat' [127]. We typically set $\nu_{coll} = \omega_{pi}/5$ and evolve the plasma with this thermostat for 500 timesteps.

Afterwards, we turn off the 'thermostat' and allow the MD simulation to evolve freely. This is the starting point for the QT implementation of spin-tagging discussed

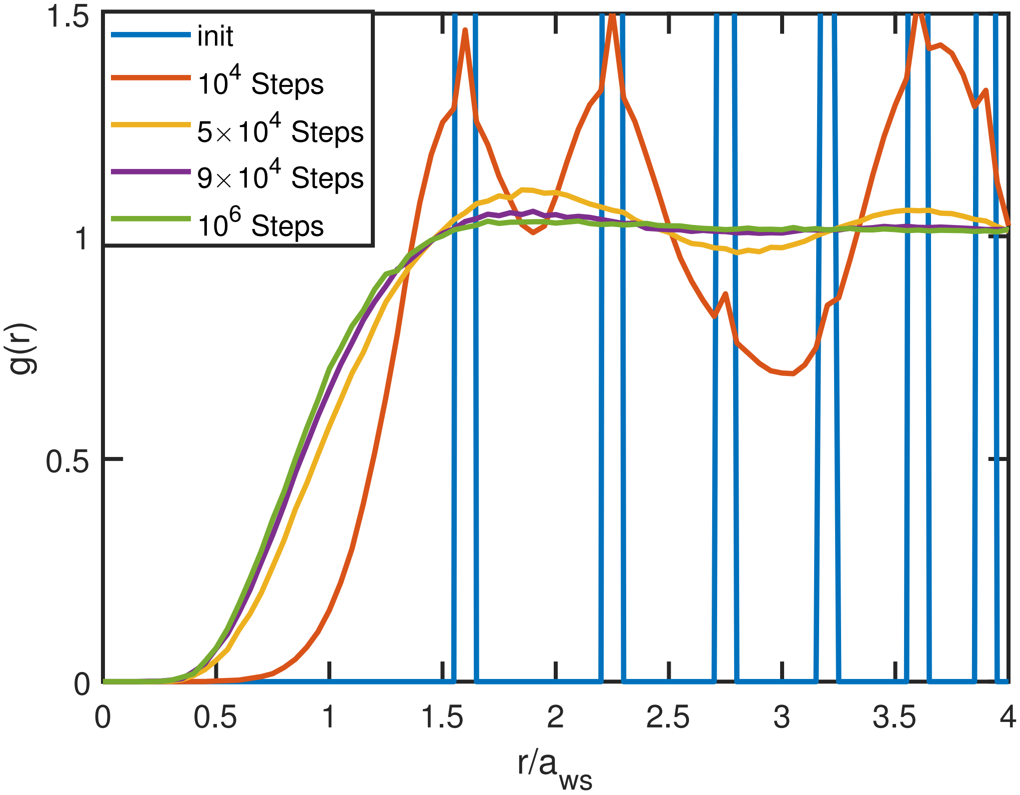

Figure A.2 : Convergence of $g(r)$) towards its equilibrium value for $\Gamma = 3$ and $\kappa = 0.5$ as a function of number of steps of the Metropolis Algorithm. The system is initialized in a cubic lattice (hence why $g(r)$ is initially 'spiky'). After $\sim 10^5$ steps of the Metropolis algorithm, the system has converged towards its equilibrium state (there appears to be very little difference between 9×10^4 steps and 10^6 steps).

in Ch. 7 and for the temperature anisotropy studies discussed in Sec. 8.1.2.

Bibliography

[1] T. C. Killian, T. Pattard, T. Pohl, and J. M. Rost. Ultracold neutral plasmas. *Phys. Rep*, 449:77, 2007.

[2] M. Lyon and S. L. Rolston. Ultracold neutral plasmas. *Rep. Prog. Phys.*, 80:017001, 2017.

[3] T. C. Killian, S. Kulin, S. D. Bergeson, L. A. Orozco, C. Orzel, and S. L. Rolston. Creation of an ultracold neutral plasma. *Phys. Rev. Lett.*, 83:4776, 1999.

[4] D. Ciampini, M. Anderlini, J. H. Muller, F. Fuso, O. Morsch, J. W. Thomsen, and E. Arimondo. Photoionization of ultracold and bose-einstein-condensed rb atoms. *Phys. Rev. A.*, 66:043409, 2002.

[5] E. A. Cummings, J. E. Daily, D. S. Durfee, and S. D. Bergeson. Fluorescence measurements of expanding strongly coupled neutral plasmas. *Phys. Rev. Lett.*, 95:235001, 2005.

[6] C. E. Simien, Y. C. Chen, P. Gupta, S. Laha, Y. N. Martinez, P. G. Mickelson, S. B. Nagel, and T. C. Killian. Using absorption imaging to study ion dynamics in an ultracold neutral plasma. *Phys. Rev. Lett.*, 92:143001, 2004.

[7] T. C. Killian. Ultracold neutral plasmas. *Science*, 316:705, 2007.

[8] S. Ichimaru. Strongly coupled plasmas: high-density classical plasmas and degenerate electron liquids. *Rev. Mod. Phys*, 54:1017, 1982.

[9] M. S. Murillo. Strongly coupled plasma physics and high energy-density matter. *Physics of Plasmas*, 11:2964, 2004.

[10] B. A. Remington, R. P. Drake, and D. D. Ryutov. Experimental astrophysics with high power lasers and z pinches. *Rev. Mod. Phys*, 78:755, 2006.

[11] R. O. Dendy. *Plasma Dynamics.* Oxford University Press, 1990.

[12] J. P. Morrison, C. J. Rennick, J. S. Keller, and E. R. Grant. Evolution from a molecular rydberg gas to an ultracold plasma in a seeded supersonic expansion of no. *Phys. Rev. Lett.*, 101:205005, 2008.

[13] M. P. Robinson, B. Laburthe Tolra, M. W. Noel, T. F. Gallagher, and P. Pillet. Spontaneous evolution of rydberg atoms into an ultracold plasma. *Phys. Rev. Lett.*, 85:4466, 2000.

[14] A. Walz-Flannigan, J. R. Guest, J. H. Choi, and G. Raithel. Cold-rydberg-gas dynamics. *Phys. Rev. A.*, 69:063405, 2004.

[15] M. Robert de Saint-Vincent, C. S. Hofmann, H. Schempp, G. Gunter, S. Whitlock, and M. Weidemuller. Spontaneous avalanche ionization of a strongly blockaded rydberg gas. *Phys. Rev. Lett.*, 110:045004, 2013.

[16] P. McQuillen, X. Zhang, T. Strickler, F. B. Dunning, and T. C. Killian. Imaging the evolution of an ultracold strontium rydberg gas. *Phys. Rev. A.*, 87:013407, 2013.

[17] T. Niedeprum, O. Thomas, T. Manthey, T. M. Weber, and H. Ott. Giant cross section for molecular ion formation in ultracold rydberg gases. *Phys. Rev. Lett.*, 115:013003, 2015.

[18] G. Bannasch, T. C. Killian, and T. Pohl. Strongly coupled plasmas via rydberg blockade of cold atoms. *Phys. Rev. Lett.*, 110:253003, 2013.

[19] D. Jaksch, J. I. Cirac, P. Zoller, S. L. Rolston, R. Cote, and M. D. Lukin. Fast quantum gates for neutral atoms. *Phys. Rev. Lett.*, 85:2208, 2000.

[20] J. Castro, P. McQuillen, and T. C. Killian. Ion acoustic waves in ultracold neutral plasmas. *Phys. Rev. Lett.*, 105:065004, 2010.

[21] S. Laha, P. Gupta, C. E. Simien, H. Gao, J. Castro, T. Pohl, and T. C. Killian. Experimental realization of an exact solution to the vlasov equations for an expanding plasma. *Phys. Rev. Lett.*, 99:155001, 2007.

[22] P. McQuillen, T. Strickler, T. K. Langin, and T. C. Killian. Ion temperature evolution in an ultracold neutral plasma. *Physics of Plasmas*, 22:033513, 2015.

[23] X. L. Zhang, R. S. Fletcher, S. L. Rolston, P. N. Guzdar, and M. Swisdak. Ultracold plasma expansion in a magnetic field. *Phys. Rev. Lett.*, 100:235002, 2008.

[24] J. P. Morrison, N. Saquet, and E. R. Grant. Classical scaling and the correspondence between the coupled rate equation and molecular dynamics models for the evolution of ultracold neutral plasma. *J. Phys. B*, 45:025701, 2012.

[25] R. S. Fletcher, X. L. Zhang, and S. L. Rolston. Using three-body recombina-

tion to extract electron temperatures of ultracold plasmas. *Phys. Rev. Lett.*, 99:145001, 2007.

[26] P. McQuillen, J. Castro, S. J. Bradshaw, and T. C. Killian. Emergence of kinetic behavior in streaming ultracold neutral plasmas. *Physics of Plasmas*, 22:043514, 2015.

[27] P. McQuillen, J. Castro T. Strickler, S. J. Bradshaw, and T. C. Killian. Ion holes in the hydrodynamic regime in ultracold neutral plasmas. *Physics of Plasmas*, 20:043516, 2013.

[28] R. S. Fletcher, X. L. Zhang, and S. L. Rolston. Observation of collective modes of ultracold plasmas. *Phys. Rev. Lett.*, 96:105003, 2006.

[29] X. L. Zhang, R. S. Fletcher, and S. L. Rolston. Observation of an ultracold plasma instability. *Phys. Rev. Lett.*, 101:195002, 2008.

[30] K. A. Twedt and S. L. Rolston. Electronic detection of collective modes of an ultracold plasma. *Phys. Rev. Lett.*, 108:065003, 2012.

[31] T. M. Wilson, W. Chen, and J. L. Roberts. Density-dependent response of an ultracold plasma to few-cycle radio-frequency pulses. *Phys. Rev. A.*, 87:013410, 2013.

[32] W. Chen, C. Witte, and J. L. Roberts. Observation of a strong-coupling effect on electron-ion collisions in ultracold plasmas. *Phys. Rev. E.*, 96:013203, 2017.

[33] S. Laha, Y. C. Chen, P. Gupta, C. E. Simien, Y. N. Martinez, P. G. Mickelson, S. B. Nagel, and T. C. Killian. Kinetic energy oscillations in annular regions of ultracold neutral plasmas. *Eur. Phys J. D*, 40:51, 2006.

[34] S. D. Bergeson, A. Denning, M. Lyon, and F. Robicheaux. Density and temperature scaling of disorder-induced heating in ultracold plasmas. *Phys. Rev. A.*, 83:023409, 2011.

[35] M. Lyon, S. D Bergeson, and M. S. Murillo. Limit of strong ion coupling due to electron shielding. *Phys. Rev. E.*, 87:033101, 2013.

[36] T. K. Langin, T. Strickler, N. Maksimovic, P. McQuillen, T. Pohl, D. Vrinceanu, and T. C. Killian. Demonstrating universal scaling for dynamics of yukawa one-component plasmas after an interaction quench. *Phys. Rev. E.*, 93:023201, 2016.

[37] C. F. Driscoll, K. S. Fine, and J. H. Malmberg. Reduction of radial losses in a pure electron plasma. *The Physics of Fluids*, 29:2015, 1986.

[38] F. Anderegg, D. H. E. Dubin, T. M. O'Neil, and C. F. Driscoll. Measurement of correlation-enhanced collision rates. *Phys. Rev. Lett.*, 102:185001, 2009.

[39] T. S. Strickler, T. K. Langin, P. McQuillen, J. Daligault, and T. C. Killian. Experimental measurement of self-diffusion in a strongly coupled plasma. *Phys. Rev. X.*, 6:021021, 2016.

[40] G. Bannasch, J. Castro, P. McQuillen, T. Pohl, and T. C. Killian. Velocity relaxation in a strongly coupled plasma. *Phys. Rev. Lett.*, 109:185008, 2012.

[41] J. P. Hansen, E. L. Pollock, and I. R. McDonald. Velocity autocorrelation function and dynamical structure factor of the classical one-component plasma. *Phys. Rev. Lett.*, 32:277, 1974.

[42] T. Ott, M. Bonitz, L. G. Stanton, and M. S. Murillo. Coupling strength in

coulomb and yukawa one-component plasmas. *Physics of Plasmas*, 21:113704, 2014.

[43] J. P. Hansen and I. R. McDonald. *Theory of Simple Liquids with Applications to Soft Matter*. Academic Press, 2013.

[44] L. D. Landau. Kinetic equation for the coulomb effect. *Phys. Z. Sowjetunion*, 10:154, 1936.

[45] L. Spitzer. *Physics of Fully Ionized Gases*. Interscience, New York, 1967.

[46] L. G. Stanton and M. S. Murillo. Ionic transport in high-energy-density matter. *Phys. Rev. E.*, 93:043203, 2016.

[47] S. D. Baalrud and J. Daligault. Modified enskog kinetic theory for strongly coupled plasmas. *Phys. Rev. E.*, 91:063107, 2015.

[48] G. E. Morfill and A. V. Ivlev. Complex plasmas: An interdisciplinary research field. *Rev. Mod. Phys*, 81:1353, 2009.

[49] W. M. Itano, J. J. Bollinger, J. N. Tan, B. Jelenkovic, X. P. Huang, and D. J. Wineland. Bragg diffraction from crystallized ion plasmas. *Science*, 279:686, 1998.

[50] A. Mortensen, E. Nielsen, T. Matthey, and M. Drewsen. Observation of three-dimensional long-range order in small ion coulomb crystals in an rf trap. *Phys. Rev. Lett.*, 96:103001, 2006.

[51] D. H. E. Dubin and T. M. O'Neil. Trapped nonneutral plasmas, liquids, and crystals (the thermal equilibrium states). *Rev. Mod. Phys*, 71:87, 1999.

[52] H. Thomas, G. E. Morfill, V. Demmel, J. Goree, B. Feuerbacher, and D. Mohlmann. Plasma crystal: Coulomb crystallization in a dusty plasma. *Phys. Rev. Lett.*, 73:652, 1994.

[53] S. Hamaguchi, R. T. Farouki, and D. H. E. Dubin. Triple point of yukawa systems. *Phys. Rev. E.*, 56:4671, 1997.

[54] D. O. Gericke and M. S. Murillo. Disorder-induced heating of ultracold plasmas. *Contrib. Plasma Phys*, 43:298, 2003.

[55] Y. C. Chen, C. E. Simien, S. Laha, P. Gupta, Y. N. Martinez, P. G. Mickelson, S. B. Nagel, and T. C. Killian. Electron screening and kinetic-energy oscillations in a strongly coupled plasma. *Phys. Rev. Lett.*, 93:265003, 2004.

[56] J. Daligault. Diffusion in ionic mixtures across coupling regimes. *Phys. Rev. Lett.*, 108:225004, 2012.

[57] J. Daligault, K. O. Rasmussen, and S. D. Baalrud. Determination of the shear viscosity of the one-component plasma. *Phys. Rev. E.*, 90:033105, 2014.

[58] Z. Donko and P. Hartmann. Thermal conductivity of strongly coupled yukawa liquids. *Phys. Rev. E.*, 69:016405, 2004.

[59] P. Kaw and A. Sen. Low frequency modes in strongly coupled dusty plasmas. *Physics of Plasmas*, 5:3552, 1998.

[60] A. Diaw and M. S. Murillo. Generalized hydrodynamics model for strongly coupled plasmas. *Phys. Rev. E.*, 92:013107, 2015.

[61] T. Pohl, T. Pattard, and J. M. Rost. Coulomb crystallization in expanding laser-cooled neutral plasmas. *Phys. Rev. Lett.*, 92:155003, 2004.

[62] Z. Donko, G. J Kalman, and K. I. Golden. Caging of particles in one-component plasmas. *Phys. Rev. Lett.*, 88:225001, 2002.

[63] P. Makotyn, C. E. Klauss, D. L. Goldberger, E. A. Cornell, and D. S. Jin. Universal dynamics of a degenerate unitary bose gas. *Nature Phys.*, 10:116, 2014.

[64] R. Lopes, C. Eigen, A. Barker, K. G. H. Viebahn, M. Robert de Saint-Vincent, N. Navon, Z. Hadzibabic, and R. P. Smith. Quasiparticle energy in a strongly interacting homogeneous bose-einstein condensate. *Phys. Rev. Lett.*, 118:210401, 2017.

[65] C. Eigen, J. A. P. Glidden, R. Lopes, N. Navon, Z. Hadzibabic, and R. P. Smith. Universal scaling laws in the dynamics of a homogeneous unitary bose gas. *Phys. Rev. Lett.*, 119:250404, 2017.

[66] E. Shuryak. Strongly coupled quark-gluon plasma in heavy ion collisions. *Rev. Mod. Phys*, 89:035001, 2017.

[67] Y. Yanase, T. Jujo, T. Nomura, H. Ikeda, T. Hotta, and K. Yamada. Theory of superconductivity in strongly correlated electron systems. *Phys. Rep*, 387:1, 2003.

[68] M. Greiner, O. Mandel, T. Esslinger, T. W. Hansch, and I. Bloch. Quantum phase transition from a superfluid to a mott insulator in a gas of ultracold atoms. *Nature*, 415:40, 2002.

[69] M. S. Murillo. Using fermi statistics to create strongly coupled ion plasmas in atom traps. *Phys. Rev. Lett.*, 87:115003, 2001.

[70] B. DeMarco and D. S. Jin. Onset of fermi degeneracy in a trapped atomic gas. *Science*, 285:1703, 1999.

[71] M. Lyon, S. D. Bergeson, A. Diaw, and M. S. Murillo. Using higher ionization states to increase coulomb coupling in an ultracold neutral plasma. *Phys. Rev. E.*, 91:033101, 2015.

[72] S. G. Kuzmin and T. M. O'Neil. Numerical simulation of ultracold plasmas. *Physics of Plasmas*, 9:3743, 2002.

[73] A. P. Gavrilyuk, I. V. Krasnov, and N. Y. Shaparev. Laser cooling and wigner crystallization of resonant plasma in magneto-optical trap. *Laser Physics*, 8:653, 1998.

[74] A. P. Gavriliuk, I. L. Isaev, S. V. Karpov, I. V. Krasnov, and N. Y. Shaparev. Brownian dynamic of laser cooling and crystallization of electron-ion plasma. *Phys. Rev. E.*, 80:056404, 2009.

[75] T. W. Hansch and A. L. Schawlow. Cooling of gases by laser radiation. *Optics Communications*, 13:68, 1975.

[76] D. Wineland and H. Dehmelt. Proposed 10^{14} $\delta\nu < \nu$ laser fluorescence spectroscopy on $t1^{+}$ mono-ion oscillator iii. *Bull. Am. Phys Soc.*, 20:637, 1975.

[77] D. Wineland, R. Drullinger, and F. Walls. Radiation pressure cooling of bound-resonant absorbers. *Phys. Rev. Lett.*, 40:1639, 1978.

[78] S. V. Andreev, V. I. Balykin, V. S. Letokhov, and V. G. Minogin. Radiative slowing and reduction of the energy spread of a beam of sodium atoms to 1.5

k in an oppositely directed laser beam. *Pis'ma Zh. Eksp. Teor. Fis.*, 34:463, 1981.

[79] W. D. Phillips and H. Metcalf. Laser deceleration of an atomic beam. *Phys. Rev. Lett.*, 48:596, 1982.

[80] E. S. Shuman, J. F. Barry, and D. DeMille. Laser cooling of a diatomic molecule. *Nature*, 467:820, 2010.

[81] I. Kozyryev, L. Baum, K. Matsuda, B. L. Augenbraun, L. Anderegg, A. P. Sedlack, and J. M. Doyle. Sisyphus laser cooling of a polyatomic molecule. *Phys. Rev. Lett.*, 118:173201, 2017.

[82] R. I. Epstein, M. I. Buchwald, B. C. Edwards, T. R. Gosnell, and C. E. Mungan. Observation of laser-induced fluorescent cooling of a solid. *Nature*, 377:500, 1995.

[83] D. V. Seletskiy, S. D. Melgaard, S. Bigotta, A. D. Lieto, M. Tonelli, and M. Sheik-Bahae. Laser cooling of solids to cryogenic temperatures. *Nature Photonics.*, 4:161, 2010.

[84] M. Aspelmeyer, T. J. Kippenberg, and Florian. Marquardt. Cavity optomechanics. *Rev. Mod. Phys.*, 86:1391, Dec 2014.

[85] M. H. Anderson, J. R. Ensher, M. R. Matthews, C. E. Wieman, and E. A. Cornell. Observation of bose-einstein condensation in a dilute atomic vapors. *Science*, 269:198, 1995.

[86] C. C. Bradley, C. A. Sackett, J. J. Tollett, and R. G. Hulet. Evidence of bose-

einstein condensation in an atomic gas with attractive interactions. *Phys. Rev. Lett.*, 75:1687, 1995.

[87] K. B. Davis, M. O. Mewes, M. R. Andrews, N. J. van Druten, D. S. Durfee, D. M. Kurn, and W. Ketterle. Bose-einstein condensation in a gas of sodium atoms. *Phys. Rev. Lett.*, 75:3969, 1995.

[88] H. Haffner, C. F. Roos, and R. Blatt. Quantum computing with trapped ions. *Phys. Rep*, 469:155, 2008.

[89] N. M. Linke, D. Maslov, M. Roetteler, S. Debnath, C. Figgatt, K. A. Landsman, K. Wright, and C. Monroe. Experimental comparison of two quantum computing architectures. *Proc. Natl. Acad. Sci.*, 114:13, 2017.

[90] W. D. Phillips. Laser cooling and trapping of neutral atoms. *Rev. Mod. Phys*, 70:721, 1998.

[91] M. S. Green. Markoff random processes and the statistical mechanics of time dependent phenomena ii. irreversible processes in fluids. *J. Chem. Phys*, 22:398, 1954.

[92] R. Kubo. Statistical-mechanical theory of irreversible processes. i. general theory and simple applications to magnetic and conduction problems. *J. Phys. Soc. Jpn.*, 12:570, 1957.

[93] Thomas Langin. Universality in the equilibration of quenched yukawa one component plasmas. Master's thesis, Rice University, 2015.

[94] F. Robicheaux and J. D. Hanson. Simulated expansion of an ultra-cold, neutral plasma. *Physics of Plasmas*, 10:2217, 2003.

[95] D. Comparat, T. Vogt, N. Zahzam, M. Mudrich, and P. Pillet. Star cluster dynamics in a laboratory: electrons in an ultracold plasma. *Mon. Not. R. Astron. Soc.*, 361:1227, 2005.

[96] K. Morawetz, M. Bonitz, V. G. Morozov, G. Ropke, and D. Kremp. Short-time dynamics with initial correlations. *Phys. Rev. E.*, 63:020102, 2001.

[97] M. S. Murillo. Ultrafast dynamics of strongly coupled plasmas. *Phys. Rev. Lett.*, 96:165001, 2006.

[98] R. T. Farouki and S. Hamaguchi. Thermodynamics of strongly-coupled yukawa systems near the one-component-plasma limit. ii. molecular dynamics simulations. *J. Chem. Phys.*, 101:9885, 1994.

[99] S. Hamaguchi, R. T. Farouki, and D. H. E. Dubin. Phase diagram of yukawa systems near the one-component-plasma limit revisited. *J. Chem. Phys.*, 105:7641, 1996.

[100] J. Clérouin, P. Arnault, C. Ticknor, J. D. Kress, and L. A. Collins. Unified concept of effective one component plasma for hot dense plasmas. *Phys. Rev. Lett.*, 116:115003, 2016.

[101] S. G. Kuzmin and T. M. O'Neil. Numerical simulation of ultracold plasmas: How rapid intrinsic heating limits the development of correlation. *Phys. Rev. Lett.*, 88:065003, 2002.

[102] Z. Donko, P. Hartmann, and G. J Kalman. Strongly coupled plasma liquids. *arXiv*, 2002.

[103] T. Pohl, T. Pattard, and J. M. Rost. Kinetic modeling and molecular dynamics simulation of ultracold neutral plasmas including ionic correlations. *Phys. Rev. A.*, 70:033416, 2004.

[104] N. A. Krall and A. W. Trivelpiece. *Principles of Plasma Physics.* McGraw-Hill Inc., 1973.

[105] A. V. Baitin and K. M. Kuzanyan. A self-similar solution for expansion into a vacuum of a collisionless plasma bunch. *J. Plasma Phys.*, 59:83, 1998.

[106] D. S. Dorozhkina and V. E. Semenov. Exact solution of vlasov equations for quasineutral expansion of plasma bunch into vacuum. *PRL*, 81:2691, 1998.

[107] G. Dimonte and J. Daligault. Molecular-dynamics simulations of electron-ion temperature relaxation in a classical coulomb plasma. *Phys. Rev. Lett.*, 101:135001, 2008.

[108] P. Mansbach and J. Keck. Monte carlo trajectory calculations of atomic excitation and ionization by thermal electrons. *Phys. Rev.*, 181:275, 1969.

[109] T. Pohl, D. Vrinceanu, and H. R. Sadeghpour. Rydberg atom formation in ultracold plasmas: Small energy transfer with large consequences. *Phys. Rev. Lett.*, 100:223201, 2008.

[110] P. Gupta, S. Laha, C. E. Simien, H. Gao, J. Castro, T. C. Killian, and T. Pohl. Electron-temperature evolution in expanding ultracold neutral plasmas. *Phys. Rev. Lett.*, 99:075005, 2007.

[111] J. Castro, H. Gao, and T. C. Killian. Using sheet fluorescence to probe ion dy-

namics in an ultracold neutral plasma. *Plasma Phys. Control Fusion*, 50:124011, 2008.

[112] S. B. Nagel, C. E. Simien, S. Laha, P. Gupta, V. S. Ashoka, and T. C. Killian. Magnetic trapping of metastable ^{3}p$_2$ atomic strontium. *Phys. Rev. A.*, 67:011401, 2003.

[113] S. B. Nagel, P. G. Mickelson, A. D. Saenz, Y. N. Martinez, Y. C. Chen, T. C. Killian, P. Pellegrini, and R. Cote. Photoassociative spectroscopy at long range in ultracold strontium. *Phys. Rev. Lett.*, 94:084004, 2005.

[114] H. J. Metcalf and P. van der Straten. Laser cooling and trapping of atoms. *J. Opt. Soc. Am. B*, 20:887, 2003.

[115] W. Mende and M. Kock. Oscillator strengths of ba i and sr i rydberg transitions. *J. Phys. B: At. Mol. Opt. Phys.*, 29:655, 1996.

[116] S. U. Haq, S. Mahmood, M. A. Kalyar, R. Rafiq, R. Ali, and M. A. Baig. Photoionization cross section and oscillator strength distribution in the near-threshold region of strontium. *Eur. Phys. J. D*, 44:439, 2007.

[117] Jose Castro. Sheet fluorescence and annular analysis of ultracold neutral plasmas. Master's thesis, Rice University, 2009.

[118] Sampad Laha. *Ion Dynamics in Strongly Coupled Plasmas.* PhD thesis, Rice University, 2007.

[119] Patrick McQuillen. *High Resolution Measurement and Modeling of Ion Dynamics in an Ultracold Neutral Plasma.* PhD thesis, Rice University, 2015.

[120] J. E. Sansonetti. Wavelengths, transition probabilities, and energy levels for the spectra of rubidium (rb i through rb xxxvii). *J. Phys. Chem. Ref. Data*, 35:301, 2006.

[121] B. G. Lindsay, K. A. Smith, and F. B. Dunning. Control of long-term output frequency drift in commercial dye lasers. *Review of Scientific Instruments*, 62:1656, 1991.

[122] M. Lukin. *Modern Atomic and Optical Physics.* 2005.

[123] M. Fleischhauer, A. Imamoglu, and J. P. Marangos. Electromagnetically induced transparency: Optics in coherent media. *Rev. Mod. Phys*, 77:633, 2005.

[124] J. Dalibard, Y. Castin, and K. Molmer. Wave-function approach to dissipative processes in quantum optics. *Phys. Rev. Lett.*, 68:580, 1992.

[125] H. J. Carmichael. Quantum trajectory theory for cascaded open systems. *Phys. Rev. Lett.*, 70:2273, 1992.

[126] Clayton Simien. *Early Time Ion Dynamics and Progress Towards Laser Cooling in an Ultracold Neutral Plasma.* PhD thesis, Rice University, 2007.

[127] J. M. Haile. *Molecular Dynamics Simulation: Elementary Methods.* Wiley-Interscience, 1997.

[128] B. J. Alder and T. E. Wainwright. Studies in molecular dynamics. i. general method. *J. Chem. Phys.*, 31:459, 1959.

[129] A. Rahman. Correlations in the motion of atoms in liquid argon. *Phys. Rev.*, 136:A405, 1964.

[130] L. Verlet. Computer experiments on classical fluids. i. thermodynamical properties of lennard-jones molecules. *Phys. Rev.*, 159:98, 1967.

[131] J. P. Hansen, I. R. McDonald, and E. L. Pollock. Statistical mechanics of dense ionized matter. iii. dynamical properties of the classical one-component plasma. *Phys. Rev. A.*, 11:1025, 1975.

[132] R. T. Farouki and S. Hamaguchi. Spline approximation of 'effective' potentials under periodic boundary conditions. *Journal of Computational Physics*, 115:276, 1994.

[133] A. Denning, S. D. Bergeson, and F. Robicheaux. Measurement and simulation of laser-induced fluorescence from nonequilibrium ultracold neutral plasmas. *Phys. Rev. A.*, 80:033415, 2009.

[134] P. D. Lett, , W. D. Phillips, S. L. Rolston, C. E. Tanner, R. N. Watts, and C. I. Westbrook. Optical molasses. *Journal of the Optical Society of America B.*, 6:2084, 1989.

[135] J. Dalibard, S. Reynaud, and C. Cohen-Tannoudji. Potentialities of a new σ_+-σ_- laser configuration for radiative cooling and trapping. *J. Phys. B: At. Mol. Phys.*, 17:4577, 1984.

[136] J. R. Cannon. *The One-Dimensional Heat Equation.* Cambridge University Press, 1984.

[137] S. D. Baalrud and J. Daligault. Temperature anisotropy relaxation of the one-component plasma. *Contrib. Plasma Phys*, 57:238, 2017.

[138] H. Grad. *Containment in cusped plasmas systems*. New York: Courant Institute of Mathematical Sciences, New York University, 1961.

[139] ITER Group. Technical basis for the iter-feat final design report. *IAEA (Vienna)*, 2002.

[140] ALPHA-2 Group. Observation of the 1s-2s transition in trapped antihydrogen. *Nature*, 541:506, 2017.

[141] A. Aspect, J. Dalibard, A. Heidmann, C. Calomon, and C. Cohen-Tannoudji. Cooling atoms with stimulated emission. *Phys. Rev. Lett.*, 57:1688, 1986.

[142] V. Voitsekhovich, M. Danileiko, A. Negriiko, V. Romanenko, and L. Yatsenko. Observation of a stimulated radiation pressure of amplitude-modulated light on atoms.

[143] N. Metropolis, A. W. Rosenbluth, M. N. Rosenbluth, A. H. Teller, and E. Teller. Equations of state calculations by fast computing machines. *J. Chem. Phys.*, 21:1087, 1953.

[144] G. Salin and J. Caillol. Transport coefficients of the yukawa one-component plasma. *Phys. Rev. Lett.*, 88:065002, 2002.

[145] A. Einstein. On the movement of small particles suspended in a stationary liquid demanded by the molecular-kinetic theory of heat. *Ann. Phys. (Berlin)*, 17:549, 1905.

[146] W. Neuhauser, M. Hohenstatt, P. Toschek, and H. Dehmelt. Optical-sideband cooling of visible atom cloud confined in parabolic well. *Phys. Rev. Lett.*, 41:233, 1978.